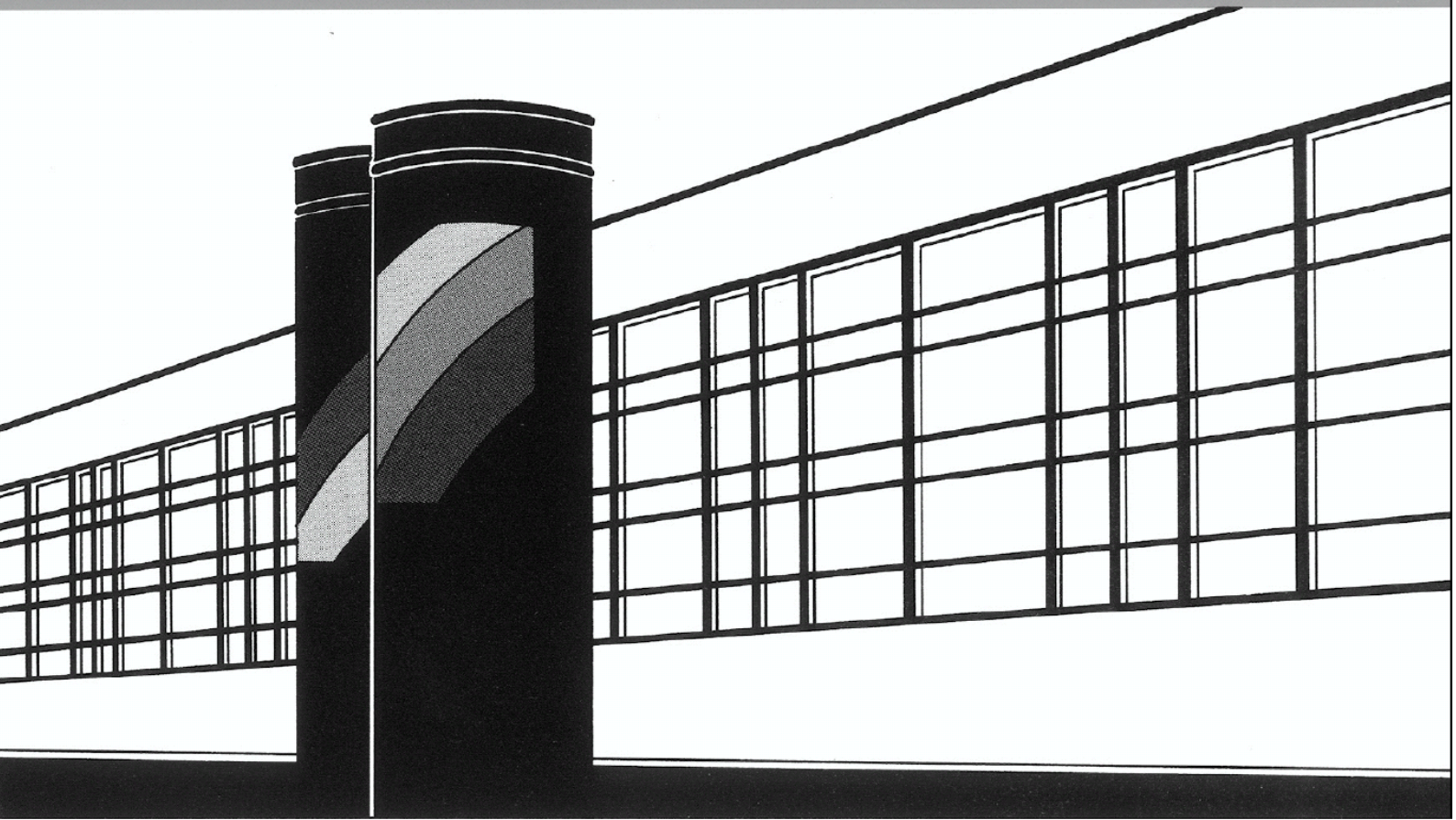


Universität Stuttgart



Institut für Wasser- und Umweltsystemmodellierung

Mitteilungen



Heft 273 Kilian Weishaupt

Model Concepts for Coupling Free Flow with
Porous Medium Flow at the Pore-Network Scale:
From Single-Phase Flow to Compositional Non-
Isothermal Two-Phase Flow

**Model Concepts for Coupling Free Flow with
Porous Medium Flow at the Pore-Network Scale:
From Single-Phase Flow to Compositional
Non-Isothermal Two-Phase Flow**

von der Fakultät Bau- und Umweltingenieurwissenschaften
und dem Stuttgart Research Centre for Simulation Technology der
Universität Stuttgart zur Erlangung der Würde eines
Doktor-Ingenieurs (Dr.-Ing.) genehmigte Abhandlung

vorgelegt von

Kilian Weishaupt

aus Wangen im Allgäu, Deutschland

Hauptberichter:

Prof. Dr.-Ing. Rainer Helmig

Mitberichter:

Prof. Dr. Ir. Majid Hassanizadeh

Prof. Dr.-Ing. Bernhard Weigand

Tag der mündlichen Prüfung: 12. März 2020

Institut für Wasser- und Umweltsystemmodellierung
der Universität Stuttgart
2020

Heft 273 **Model Concepts for Coupling
Free Flow with Porous Medium
Flow at the Pore-Network
Scale: From Single-Phase
Flow to Compositional Non-
Isothermal Two-Phase Flow**

von
Dr.-Ing.
Kilian Weishaupt

Eigenverlag des Instituts für Wasser- und Umweltsystemmodellierung
der Universität Stuttgart

D93 Model Concepts for Coupling Free Flow with Porous Medium Flow at the Pore-Network Scale: From Single-Phase Flow to Compositional Non-Isothermal Two-Phase Flow

Bibliografische Information der Deutschen Nationalbibliothek

Die Deutsche Nationalbibliothek verzeichnet diese Publikation in der Deutschen Nationalbibliografie; detaillierte bibliografische Daten sind im Internet über <http://www.d-nb.de> abrufbar

Weishaupt, Kilian:

Model Concepts for Coupling Free Flow with Porous Medium Flow at the Pore-Network Scale: From Single-Phase Flow to Compositional Non-Isothermal Two-Phase Flow, Universität Stuttgart. - Stuttgart: Institut für Wasser- und Umweltsystemmodellierung, 2020

(Mitteilungen Institut für Wasser- und Umweltsystemmodellierung, Universität Stuttgart: H. 273)

Zugl.: Stuttgart, Univ., Diss., 2020

ISBN 978-3-942036-77-1

NE: Institut für Wasser- und Umweltsystemmodellierung <Stuttgart>: Mitteilungen

Gegen Vervielfältigung und Übersetzung bestehen keine Einwände, es wird lediglich um Quellenangabe gebeten.

Herausgegeben 2020 vom Eigenverlag des Instituts für Wasser- und Umweltsystemmodellierung

Druck: DCC Kästl e.K., Ostfildern

Danksagung

Ich möchte mich im Folgenden bei all jenen bedanken, die mich bei der Anfertigung dieser Arbeit während der letzten Jahre begleitet haben. Dies gilt insbesondere für Rainer Helmig, auf dessen Unterstützung und fachlichen Rat ich mich jederzeit verlassen konnte. Seine begeisterte Persönlichkeit und positive Haltung haben mich durch manches Tal getragen und nachhaltig geprägt.

Besonders hervorheben möchte ich die außergewöhnlich gute Atmosphäre in der Arbeitsgruppe - ich bin sehr dankbar dafür, Teil dieses herausragenden Teams zu sein. Ohne die gegenseitige Unterstützung zu jeder Tages- und Nachtzeit, das gemeinsame Schaffen eines großartigen Softwareprojekts und den steten Nachschub an Kuchen und Gesprächsthemen wäre diese Arbeit nicht möglich gewesen – vielen Dank an alle Kollegen! Ein herzliches Dankeschön auch an Holger Class, der stets ein offenes Ohr für Fragen hatte und mir die Mitarbeit an interessanten Projekten, wie etwa der Höhlenforschung auf der Schwäbischen Alb, ermöglichte und an Bernd Flemisch für die Koordination von und Hilfestellung zu DuMu^x. Ein besonderer Dank gilt auch Prudence Lawday, Stefanie Siegert, Michelle Hartnick und David Werner für das Meistern bürokratischer und computertechnischer Hürden jedweder Art.

Herzlichen Dank an Bernhard Weigand für die Übernahme des Mitberichts und die fachliche Unterstützung. I would like to thank Majid Hassanizadeh for writing the report and for giving me the opportunity to come to Utrecht where I learned a lot about pore-scale interfaces. Thanks to Amir Raouf for joining our fruitful discussions there. Thanks to Vahid Joekar-Niasar for hosting me in Manchester and sharing his knowledge with me. Thanks to Alex Terzis, Ioannis Zarikos, Nikos Karadimitriou and Matthijs de Winter for introducing me to the world of micromodel experiments. Thanks to Guang Yang for his support on free-flow modeling. Thanks to Ivan Yotov for the discussions and the mathematical insights.

Ich danke der Deutschen Forschungsgemeinschaft (DFG) für die Förderung des Sonderforschungsbereichs 1313, in dessen Rahmen diese Arbeit entstanden ist.

Ein großes Dankeschön an meine Familie, die mir immer zur Seite stand.

Mein größter Dank gilt meiner wundervollen Frau Carina. Nur durch ihre bedingungslose Unterstützung, Geduld und aufmunternden Worte besonders in schwierigen Zeiten konnte ich mein Ziel verfolgen und diese Arbeit abschließen.

Contents

List of Figures	V
List of Tables	IX
Nomenclature	XI
Abstract	XVII
Zusammenfassung	XXI
1 Introduction	1
1.1 Motivation	1
1.2 Structure of the thesis	5
2 Fundamentals	7
2.1 Terms and definitions	7
2.1.1 Flow regimes	7
2.1.2 Scales	7
2.1.3 Phases and components	9
2.2 Thermodynamic basics	10
2.2.1 Chemical potential and fugacity	10
2.2.2 Local thermodynamic equilibrium	11
2.2.3 Phase composition and phase change	11
2.2.4 Mass and heat fluxes	13
2.3 Porous media	14
2.3.1 Contact angle and capillary pressure	16
2.3.2 Phase displacement processes	17
2.3.3 Evaporation from porous media	20

2.4	Pore-network modeling	23
2.4.1	Network representation	23
2.4.2	Constitutive laws	27
2.4.3	Model concepts for two-phase flow	35
3	Conceptual and numerical models for the individual sub-domains	39
3.1	(Navier-)Stokes model (free flow)	41
3.1.1	Conceptual model	41
3.1.2	Numerical model	44
3.2	Pore-network model (interface region)	45
3.2.1	Conceptual model for single-phase flow	45
3.2.2	Conceptual model for two-phase flow	47
3.2.3	Summary of pore-network models and primary variables	50
3.2.4	Numerical model	52
3.3	Darcy-scale model (bulk porous medium)	55
3.3.1	Conceptual model for single-phase flow	55
3.3.2	Conceptual model for two-phase flow	56
3.3.3	Numerical model	57
4	Coupling conditions	59
4.1	Free flow / pore-network model	60
4.2	Pore-network model / REV-scale model	68
5	Implementation and software	73
6	Code verification	77
6.1	Free-flow model	77
6.2	Dynamic two-phase pore-network model	81
7	Results and Discussion I: single-phase flow	85
7.1	Recalculation of single-phase flow micromodel experiments	85
7.1.1	Experimental setup	86
7.1.2	3D simulation results and comparison with micro-PIV experimental data	88
7.1.3	Dimensional reduction by inclusion of a wall friction term	95
7.1.4	Quasi-3D simulation results for the micromodel geometry	100

7.1.5	Numerical determination of pore-network model parameters	106
7.1.6	Application of the coupled model on the micromodel geometry	120
7.1.7	Further studies on structured porous geometries	126
7.2	Compositional single-phase flow over a random network	134
7.3	A three-domain example	140
8	Results and Discussion II: evaporation studies	143
8.1	Model comparison for a stagnant atmosphere and a homogeneous network with square-shaped throats	146
8.2	Influence of network heterogeneity	157
8.3	Influence of the throat cross-sectional shape	162
8.4	Evaporation into a moving atmosphere from a homogeneous network with square-shaped throats	166
9	Summary and Outlook	171
9.1	Summary	171
9.2	Outlook	174
A	Determination of corner half-angles for scalene triangles	177
B	Derivation of the Hagen-Poiseuille equation	181
	Bibliography	183

List of Figures

2.1	REV concept	8
2.2	Droplet of wetting fluid on a solid surface	16
2.3	Pore bodies and throats	18
2.4	Snap-off concept	19
2.5	Evaporation from porous media	21
2.6	Shape factor concept	26
2.7	Non-wetting phase conductances.	35
3.1	Conceptual coupled model	39
3.2	Illustration of the staggered-grid scheme.	44
3.3	Pore-network model entities	45
3.4	Application of the Box scheme for pore-network modeling	52
4.1	Interfaces for coupling the sub-models.	59
4.2	Pore cut into halves at the interface	60
4.3	Coupling free flow with the pore-network model	62
4.4	Pore-local slip conditions	63
4.5	Diffusion from pores	66
4.6	Coupling the pore-network model with the REV model	68
6.1	Results for the lid-driven cavity test	80
6.2	Phase distribution on a randomly generated pore network.	82
6.3	Capillary pressure-saturation curves (with constraint)	83
6.4	Capillary pressure-saturation curves (without constraint)	84
7.1	Micromodel geometry used for the micro-PIV measurements	87
7.2	3D simulation results	89
7.3	Velocity profiles at the channel inlet (3D simulation)	90

7.4	Experimental and numerical (3D) flow fields	92
7.5	Experimental and numerical (3D) velocity profiles	93
7.6	Experimental and numerical (3D) flow angles	94
7.7	Variation of channel aspect ratios	95
7.8	Influence of aspect ratio (maximum center-plane velocity)	96
7.9	Influence of aspect ratio (height-averaged velocity)	97
7.10	Channel with a bend	100
7.11	Quasi-3D flow field	101
7.12	Difference between the 3D and the quasi-3D velocity fields	101
7.13	Pressure and velocity in the channel (quasi-3D)	103
7.14	Horizontal velocity profiles over height	104
7.15	Vertical velocity profiles over length	105
7.16	Schematic depiction of the regular porous structure	106
7.17	Numerical determination of the conductance factors	108
7.18	Setups for assessing the PNM's accuracy	110
7.19	Comparison of horizontal volume flow rates	111
7.20	Comparison of vertical volume flow rates	112
7.21	Influence of the throat width on β_{pore}	115
7.22	Near-interface flow field for a throat perpendicular to the interface . .	116
7.23	Near-interface flow field for an inclined throat	117
7.24	Shear rates and pressure distribution at the interface	118
7.25	Pressure and velocity fields of the coupled model	121
7.26	Near-interface flow field for the coupled model (center)	121
7.27	Near-interface flow field for the coupled model (left)	122
7.28	Profiles of vertical velocity (coupled model)	123
7.29	Pore-local volume flow rates for the 3D, quasi-3D and coupled model	124
7.30	Horizontal velocity profiles and volumetric flow rates over height for the 3D, quasi-3D and coupled model	125
7.31	Setup overview for further studies on the coupled model	127
7.32	Pressure and velocity fields for the low-Re case	128
7.33	Pore-local volume flow rates for the low-Re case	129
7.34	Pressure and velocity fields for the high-Re case	130
7.35	Pore-local volume flow rates for the high-Re case	131
7.36	Setup for compositional flow over a random network	135
7.37	Velocity fields for compositional flow over a random network	136

7.38	Concentration fields for compositional flow over a random network . . .	138
7.39	Concentration fields and interface pressures for a three-domain setup	141
8.1	Setups for evaporation studies	145
8.2	Vapor concentration fields and saturation distribution for the isothermal model and the non-isothermal model	148
8.3	Pore-local evaporation rates and interface quantities for the isothermal model and the non-isothermal model	150
8.4	Global evaporation rates for the NCP models and the PVS models . .	151
8.5	Simulation statistics over time for the NCP models and the PVS models	153
8.6	Simulation statistics over time for different initial saturations	155
8.7	Network with randomly distributed pore body radii	157
8.8	Vapor concentration fields and saturation distribution for a random network	158
8.9	Global evaporation rates for a random network	159
8.10	Simulation statistics over time for a uniform network and a random network	160
8.11	Wetting-phase flow field in Ω^{PNM}	161
8.12	Global evaporation rates for square and circular throat cross sections	163
8.13	Diffusion at the interface during evaporation	164
8.14	Local evaporation rates for circular throats	164
8.15	Vapor concentration fields and saturation distribution	167
8.16	Global evaporation rates for air flow	168
8.17	Non-wetting phase flow in Ω^{PNM}	169
A.1	Randomly constructed triangles	179

List of Tables

3.1	Primary variables and balance equations of the different pore-network models.	51
6.1	Convergence test results for Stokes flow	79
6.2	Convergence test results for Navier-Stokes flow	80
7.1	Flow rates and accuracy of the quasi-3D model	99
7.2	Variation of porous structures	107
7.3	Upscaled conductance factors	109
7.4	Accuracy of the pore-network model	111
7.5	Setups for the numerical determination of β_{pore}	114
7.6	Setup overview for further studies on the coupled model	126
7.7	Simulation statistics for single-phase flow	132
7.8	Simulation statistics for single-phase flow (continued)	133
8.1	Simulation statistics for the NCP models and the PVS models	154
8.2	Simulation statistics for different initial saturations	156
8.3	Simulation statistics for a uniform network and a random network	161
8.4	Simulation statistics for different throat shapes	166
8.5	Simulation statistics for air flow	170

Nomenclature

Selected Acronyms

AM arc meniscus

NCP non-linear complementarity problem

PDMS polydimethylsiloxane

PIV particle image velocimetry

PNM pore-network model

PVS primary variable switch

REV representative elementary volume

TM terminal meniscus

Greek Letters

α_{FF} phase present in the free-flow domain

β corner half-angle [rad]

β_{pore} pore-scale interface slip coefficient [1/m]

$\Delta\{x, y, z\}$ grid cell size [m]

ΔG Gibbs free energy [J]

Δt	time step size	[s]
γ	interfacial tension	[N/m]
Γ^{FF}	interface between Ω^{FF} and Ω^{PNM}	
Γ^{REV}	interface between Ω^{REV} and Ω^{PNM}	
Γ_{box}	face of bulk-model box control volume on coupling interface	
Γ_i^{FF}	discrete free-flow coupling interface at pore body i	
λ	thermal conductivity	[W/(Km)]
μ	dynamic viscosity	[Pa s]
ν	kinematic viscosity	[m ² /s]
ω	linear ansatz function	
Ω^{FF}	free-flow domain	
Ω^{PNM}	pore-network model interface region domain	
Ω^{REV}	REV model bulk porous medium domain	
Φ	porosity	[-]
ϕ	chemical potential	[J]
ϱ	mass density	[kg/m ³]
ϱ_{mol}	molar density	[mol/m ³]
σ	free-flow cell face	
τ	tortuosity	[-]
$\theta_{\{\text{a,r}\}}$	contact angle (advancing/receding)	[rad]

Roman Letters

A	area	[m ²]
A_{ij}	throat cross-sectional area	[m ²]
C	control volume	
c	factor in wall friction term	[-]
$C_{\{x,y,z\}}^*$	staggered control volume	
c_s	solid specific heat capacity	[J/(kgK)]
Ca	capillary number	[-]
D	diffusion coefficient	[m ² /s]
\dot{e}_i	pore-local evaporation rate	[mm/d]
\dot{e}	total evaporation rate	[mm/d]
\mathbf{f}	momentum source/sink term	[kg/(m ² s ²)]
\mathbf{f}_{drag}	wall friction term	[kg/(m ² s ²)]
f	fugacity	[Pa]
\mathbf{g}	gravitational acceleration	[m/s ²]
G	shape factor	[-]
g_{ij}	conductance factor of throat ij	[m ² /(sPa)]
H	Henry constant	[Pa]
h	specific enthalpy	[J/kg]
h_Ω	domain height	[m]

\mathbf{j}_{diff}	diffusive flux vector	[kg/(m ² s)]
\mathbf{K}	intrinsic permeability	[m ²]
k_r	relative permeability	[-]
l_{ij}	length of pore throat ij	[m]
M	molecular mass	[g/mol]
m	mass	[kg]
\mathbf{n}	unit normal vector	[-]
n_{coord}	coordination number	[-]
n_{DOF}	number of degrees of freedom	[-]
n_{It}	number of Newton iterations	[-]
n_{mole}	number of moles	[-]
n_{wasted}	number of wasted Newton iterations	[-]
P	perimeter	[m]
p	pressure	[Pa]
p^κ	partial pressure of component κ	[Pa]
p_c	capillary pressure	[Pa]
p_{sat}^κ	saturation vapor pressure of component κ	[Pa]
$p_{c,e}$	entry capillary pressure	[Pa]
q	mass sink/source term	[kg/(m ³ s)]
q^κ	molar sink/source term	[mol/(m ³ s)]

q^e	energy sink/source term	[J/(m ³ s)]
Q_{ij}	volume flow in pore throat ij	[m ³ /s]
R	universal gas constant	[J/(molK)]
r	(inscribed) radius	[m]
r_{am}	arc meniscus curvature radius	[m]
r_i	inscribed radius of pore body i	[m]
r_{ij}	inscribed radius of pore throat ij	[m]
Re	Reynolds number	[-]
S	saturation	[-]
\mathbf{t}_k	basis vector of interface tangent plane	[-]
T	temperature	[K]
t	time	[s]
u	specific internal energy	[J/kg]
\mathbf{v}	velocity vector	[m/s]
v	velocity (scalar value)	[m/s]
V	volume	[m ³]
w_{ij}	throat width	[m]
\mathbf{x}	spatial coordinate	[m]
X	mass fraction	[-]
x	mole fraction	[-]

Subscripts

α	phase index (w: wetting, n: non-wetting, s: solid, g: gaseous, l: liquid)
eff	effective
g	gas phase
i	quantity related to pore body i
ij	quantity related to pore throat ij connecting pore bodies i and j
l	liquid phase
n	non-wetting phase
pm	porous medium
s	solid phase
w	wetting phase

Superscripts

κ	component index
----------	-----------------

Operators and other symbols

$[\cdot]^{\text{FF}}$	free-flow interface quantity
$[\cdot]^{\text{PNM}}$	pore-network model interface quantity
$[\cdot]^{\text{REV}}$	REV model interface quantity
$\langle \cdot \rangle$	average
$ \cdot $	area or volume of geometric entity

Abstract

Coupled systems of free flow adjacent to a porous-medium appear ubiquitously in nature and in technical applications. Examples for interface-driven transport and exchange processes include soil evaporation, fuel cell water management or food drying. Understanding the complexity of pore-scale mechanisms is paramount to build efficient and reliable mathematical and numerical models.

Typically, averaged models based on the concept of a representative elementary volume (REV) approach are chosen to overcome the enormous computational demand of solving these types of systems on the pore scale. This leads, however, to a loss of detail for certain sub-scale processes which might critically affect the global system behavior.

Model In this work, we propose a novel hybrid approach which combines models of different scales in order to increase the level of detail for the description of flow and transport processes at the interface between free flow and the porous medium at a comparatively low computational cost.

The central feature is a pore-network model representing the transition region between the porous matrix and the free flow. This model locally resolves pore-scale processes on a simplified yet equivalent porous geometry which makes it comparatively efficient.

The coupled model comprises up to three computational domains: the free-flow region where the (Navier-)Stokes equations are solved, the transition zone described by the pore-network model and an optional bulk porous domain accounted for by Darcy's law.

We present and discuss coupling conditions to ensure thermodynamic consistency. Following a monolithic coupling approach, the fluxes of mass, momentum and energy across the domain interfaces are preserved implicitly while no coupling iterations are required. In order to resolve flow and transport processes beyond capillary equilibrium

states, a fully implicit dynamic pore-network model is employed. The inherently stable and oscillation-free staggered-grid (MAC) scheme is used for the spatial discretization of the free-flow domain.

Taking advantage of its multi-model coupling facilities, we use the open-source porous media simulator DuMu^x for the implementation of the coupled model.

We present numerical results for models of different physical complexity, ranging from single-phase flow to non-isothermal compositional two-phase flow.

Results for single-phase flow Micro-PIV experiments on a microfluidic device were first recalculated in high three-dimensional detail using the open-source CFD tool OpenFOAM. Having assured physical consistency, these numerical results were then used as reference solutions for further simulations. First, a dimensional reduction was performed by considering a wall friction term which allows a two-dimensional simulation of the micromodel at considerably lower computational costs. The maximum deviation from the three-dimensional reference solution was only around 10%. Afterwards, the porous domain of the micromodel was accounted for by a pore-network model, further lowering the computational costs, while all relevant fluxes could be accurately resolved.

A novel concept for describing local pore-scale slip velocities is presented for which a parameter β_{pore} was determined numerically. The smaller the porous structures under consideration, the more accurate this approach.

An example of compositional single-phase flow over a random pore network revealed the formation of concentration boundary layers at the interface, depending on the Reynolds number in the free-flow channel, and the establishment of preferential flow paths in the network. A bulk porous medium region was afterwards added below the pore-network domain for demonstration purposes.

Results for two-phase flow Special attention was given to the simulation of evaporation. Here, non-isothermal, two-phase and two-component flow in the pore network was considered. At first, all simulations were done for a resting gas atmosphere in the free-flow domain. Two different approaches for the pore-network, the primary variable switch (PVS) method and the non-linear complementarity problem (NCP) approach were compared. The NCP method clearly outperformed the PVS approach which

suffered from strong numerical instabilities due to the frequent trigger of the switch mechanism. Only the NCP model was able to simulate the full range of saturation from one to zero.

We found a strong influence of the throat cross-sectional shape on the local and overall evaporation behavior. Rectangular throats facilitate wetting-phase layer flow in their corners which helps to sustain a rather constant evaporation rate for a long time due to the presence of liquid water at the porous medium's surface. In contrast to that, no layer flow is possible in circular throats where the evaporation rate drops immediately once a throat gets invaded by the air phase and evaporation is then limited by diffusion. An increased local evaporation rate was found for singular pores where all neighboring pores had fallen dry before. Here, evaporation changes from a mainly one-dimensional to a two-dimensional process.

Adding heterogeneity to the network did not influence the global evaporation rate while it strongly impaired the numerical performance due to local (both temporal and spatial) peaks of liquid flow within the network.

Finally, air flow in the free-flow region was induced which led to a considerably different evaporation behavior, both in terms of the invasion pattern within the network and the temporal evolution of the global evaporation rate. Air penetrating the network formed pathways for advective vapor transport, thereby temporally increasing the evaporation rate. In this case, evaporation was no longer only diffusion-controlled but also governed by advection. This increase of physical complexity resulted in an increase of CPU time.

Zusammenfassung

Gekoppelte Systeme mit freier Strömung über einem porösen Medium lassen sich vielerorts sowohl in der Natur als auch bei technischen Anwendungen finden. Das Austrocknen von Böden durch Verdunstung, Wassermanagement in Brennstoffzellen oder die industrielle Trocknung von Lebensmitteln sind nur einige Beispiele, bei denen Transport- und Austauschprozesse an Grenzflächen eine wichtige Rolle spielen. Für die Entwicklung von effizienten und zuverlässigen Modellen ist ein Verständnis dieser porenskaligen Mechanismen entscheidend.

Üblicherweise werden jedoch gemittelte Modelle auf Basis von repräsentativen Elementarvolumen (REV) verwendet, da eine diskrete, porenskalige Beschreibung des Systems die gegenwärtigen Rechenkapazitäten übersteigt. Hierbei können kleinskalige Prozesse jedoch oft nicht mehr hinreichend genau aufgelöst werden, obwohl diese möglicherweise einen großen Einfluss auf das gekoppelte System haben.

Modell In dieser Arbeit wird ein neuartiges hybrides Modellkonzept vorgestellt, welches auf der Kombination von verschiedenskaligen Submodellen beruht und vergleichsweise wenig rechenintensiv ist. Dennoch können porenskalige Effekte und Prozesse am Übergang zwischen freier Strömung und porösem Medium abgebildet werden. Diese Zone wird von einem Poren-Netzwerk-Modell beschrieben, welches das Kernelement des vorgestellten Modellkonzepts darstellt. Hierbei werden porenskalige Prozesse diskret auf einer vereinfachten, aber äquivalenten Porengeometrie abgebildet, was das Modell vergleichsweise effizient macht.

Das gekoppelte Modell besteht aus bis zu drei Rechengebieten: Auf dem Gebiet der freien Strömung werden die (Navier-)Stokes-Gleichungen gelöst. Die Übergangsregion wird mittels eines Poren-Netzwerk-Modells beschrieben und auf dem optionalen Gebiet des erweiterten porösen Mediums abseits der Grenzregion gilt das Gesetz von Darcy.

Thermodynamisch konsistente Kopplungsbedingungen werden präsentiert und erörtert. Dank einer monolithischen Kopplungsstrategie werden die Flüsse von Masse, Impuls und Energie über die Grenzflächen implizit erhalten. Des Weiteren sind keine Kopplungsiterationen nötig. Um Fließ- und Transportprozesse auch abseits von kapillaren Gleichgewichtszuständen beschreiben zu können, wird ein voll-implizites dynamisches Poren-Netzwerk-Modell verwendet. Für die freie Strömung kommt das staggered-grid Diskretisierungsverfahren zum Einsatz, welches von Natur aus stabil und frei von Oszillationen ist. DuMu^x, ein quelloffenes Simulationstool für poröse Medien, bietet umfangreiche Möglichkeiten zur Modellkopplung und wird in dieser Arbeit verwendet.

Die Komplexität der präsentierten numerischen Beispiele reicht von Einphasenströmung bis hin zu Zweiphasenströmung mit Stoff- und Energietransport.

Ergebnisse für Einphasenströmung: Zunächst wurden experimentelle Ergebnisse von Mikro-PIV Messungen mit einem dreidimensionalen numerischen Modell mithilfe von OpenFOAM, einem quelloffenen CFD Tool, hochaufgelöst nachgerechnet. Die Simulationsergebnisse sind physikalisch konsistent mit den Messdaten und dienen daher als Referenzlösung für weitere numerische Untersuchungen.

Hierbei wurde zunächst eine Dimensionsreduktion des Modells durchgeführt. Unter Berücksichtigung eines zusätzlichen Wandreibungsterms war es möglich, das dreidimensionale Modellgebiet zweidimensional zu berechnen und somit den Rechenaufwand erheblich zu senken. Die dabei auftretenden maximalen Abweichungen von der Referenzlösung betragen nur etwa 10%. Anschließend wurde das Poren-Netzwerk-Modell verwendet, um die poröse Struktur des Mikromodells abzubilden. Dies verringerte den Rechenaufwand weiter, wobei maßgebliche Flüsse weiterhin relativ genau abgebildet wurden.

Parameter für ein neuartiges Konzept für die Beschreibung porenskaliger Gleitgeschwindigkeiten wurden numerisch bestimmt. Dieses Konzept lieferte umso genauere Ergebnisse, je feiner die porösen Strukturen des Modellgebiets sind.

Ein numerisches Beispiel für Einphasenströmung mit Komponententransport zeigte die Bildung von Konzentrationsgrenzschichten über dem porösen Medium, welche von der Reynoldszahl in der freien Strömung abhängen. Zusätzlich bildeten sich bevorzugte Fließwege im Poren-Netzwerk aus. Für Demonstrationszwecke wurde in einer weiteren

Simulation ein zusätzliches Gebiet für das poröse Medium abseits der Grenzregion am unteren Ende des Poren-Netzwerks hinzugefügt.

Ergebnisse für Zweiphasenströmung: Besonderes Augenmerk wurde auf die Simulation eines Verdunstungsprozesses gelegt. Hierbei wurde nicht-isotherme Zwei-Phasen-Strömung mit Komponententransport im Poren-Netzwerk betrachtet. Zunächst wurden alle Simulationen für eine ruhende Gas-Atmosphäre über dem Netzwerk durchgeführt.

Für das Poren-Netzwerk-Modell wurden zwei verschiedene Modellansätze verglichen. Hierbei handelt es sich zum einen um eine Methode mit wechselbaren Primärvariablen (primary variable switch, PVS), und zum anderen um eine Methode, bei der ein zusätzliches nicht-lineares Problem (non-linear complementarity problem, NCP) gelöst wird. Das NCP-Modell war dabei dem PVS-Ansatz deutlich überlegen, da Letzteres durch ein häufiges Wechseln des Primärvariablensatzes zu numerischen Instabilitäten neigte. Zudem war nur das NCP-Modell in der Lage, die volle Bandbreite an Sättigungen von eins bis null zu simulieren.

Es zeigte sich, dass die Querschnittsgeometrie der Porenhäule einen maßgeblichen Einfluss, sowohl lokal als auch global, auf den Verdunstungsprozess hat. Rechteckige Porenhäule erlauben der benetzenden Phase, Filme in den Ecken auszubilden. Über diese Filme entsteht ein Fluss, welcher eine hohe Verdunstungsrate über längere Zeit aufrechterhalten kann, was durch das Vorhandensein von flüssigem Wasser an der Oberfläche des porösen Mediums begründet ist. Im Gegensatz dazu kann sich kein Film und somit kein Fluss in runden Porenhäulen bilden. Hier fällt die Verdunstungsrate sprunghaft ab, sobald die nicht-benetzende Phase in den Porenhals eingedrungen ist, da der Prozess dann diffusionslimitiert ist. Die lokale Verdunstungsrate einzelner Poren steigt, wenn diese von ausgetrockneten Nachbarporen umgeben sind. Hierbei wandelt sich das Verdunstungsverhalten von einem hauptsächlich eindimensionalen zu einem zweidimensionalen Diffusionsprozess.

Ein heterogenes, zufällig erzeugtes Poren-Netzwerk wies dieselbe globale Verdunstungsrate wie sein gleichförmiges Pendant auf, allerdings stieg der numerische Aufwand durch das Auftreten (zeitlich und räumlich) begrenzter starker Flüsse der Flüssigphase innerhalb des Netzwerks.

Zum Schluss wurde ein Luftstrom oberhalb des Poren-Netzwerks angelegt, was den Verdunstungsprozess deutlich änderte. Dies betraf sowohl das Muster, mit welchem das Netzwerk von der Luftphase durchdrungen wurde, als auch den zeitlichen Verlauf der globalen Verdunstungsrate. Die eindringende Luft erzeugte Fließwege für advektiven Wasserdampftransport, was die Verdunstungsrate vorübergehend stark ansteigen ließ. In diesem Fall war der Verdunstungsprozess nicht nur diffusionsbestimmt, sondern auch stark durch Advektion beeinflusst. Diese erhöhte physikalische Komplexität spiegelte sich auch in einem Zuwachs an Rechenaufwand wider.

1 Introduction

1.1 Motivation

Coupled systems of free flow adjacent to a porous medium are pervasive in technical, biological and environmental contexts. Evaporation from soils is driven by interface-related phenomena that arise from the interaction of atmospheric flows with the porous medium [e.g., Or et al., 2013, Vanderborght et al., 2017, Fetzer et al., 2017]. Incorporating the effects of hydrogeological and atmospheric coupling is essential for the development of accurate weather forecasting models [e.g., Benoit et al., 2000, Bauer et al., 2015, Powers et al., 2017]. Transpiration cooling [e.g., Dahmen et al., 2014, Lindner et al., 2016], fuel cell water management [e.g., Gurau and Mann, 2009], heat exchange systems [e.g., Yang et al., 2018], food processing [e.g., McMinn and Magee, 1999, Verboven et al., 2006, Defraeye et al., 2016] and drying processes in general [e.g., Defraeye, 2014] are examples where free and porous medium flow interact in technical systems. Exchange processes between blood vessels and the surrounding tissue are governed by coupled flow within the human body [e.g., Chauhan et al., 2011, Quarteroni et al., 2017].

REV-scale modeling approaches The importance of such coupled systems for industry, medicine and agriculture has therefore been a driving force for lively research, including experimental, theoretical and numerical investigations. Model development for these systems is a challenging task due to the multitude of physical processes involved and the wide range of spatial and temporal scales on which they occur. Pore-scale studies explicitly resolving the geometrical features of the permeable medium [e.g., Chandesris et al., 2013] are computationally expensive and thus only feasible for rather small domains. Modeling larger systems therefore requires *upscaling* such that

pore-scale quantities and processes are accounted for in an averaged sense [Whitaker, 1999], following the concept of a *representative elementary volume* (REV) [Bear, 1972].

A variety of coupled models featuring an averaged description of the porous medium have been developed during the last decades. Generally speaking, two classes [Goyeau et al., 2003] of coupled models can be discerned: the *single-domain* and the *two-domain approach*. The former was first introduced by Brinkman [1949] and Neale and Nader [1974] who employed a single set of equations valid for both the free flow and the porous domain. The transition between the flow domains is realized by a spatial variation of material parameters which can be either continuous (smooth interface region) or abrupt (sharp interface).

Obviating the need to postulate explicit coupling conditions is a great advantage of considering a smooth transition between free flow and porous medium because all relevant thermodynamic properties are conserved implicitly. However, the choice of material parameters at the transition zone strongly affects the general behavior of the coupled system while their experimental determination can be challenging if not impossible for certain configurations [Goyeau et al., 2003]. Assessing the transition zone thickness, which tends to be in the range of some grain diameters [Jamet et al., 2008], adds another difficulty to this method.

The two-domain approach relies on domain decomposition, i.e., different governing equations hold in the free flow and in the porous domain. For instance, the *Navier-Stokes equations* may be used in the free-flow part while *Darcy's* or *Forchheimer's* law accounts for the porous medium. Conceptual challenges arise due to the different order of the partial differential equations employed in both sub-domains. Appropriate coupling conditions need to be formulated at the interface between the two domains in order to ensure thermodynamic consistency [Hassanizadeh and Gray, 1989].

These conditions are commonly formulated [e.g., Layton et al., 2002, Mosthaf et al., 2011, Fetzer, 2018, Schneider et al., 2020] on a sharp, so-called simple interface devoid of thermodynamic properties, i.e., no mass, momentum or energy is stored. A notable exception to this is presented by Baber et al. [2016] who considered drop formation and detachment on a sharp interface. While enforcing mass conservation and the continuity of normal stress [Layton et al., 2002] across the interface is rather straight-forward, difficulties arise for the treatment of the tangential shear stress. Based on experimental observations, Beavers and Joseph [1967] proposed a semi-empirical stress condition,

which was later simplified by Saffman [1971] by neglecting the comparatively low flow velocity in the porous medium. Mikelić and Jäger [2000] used homogenization to mathematically justify this condition, followed by others employing a variety of different strategies [e.g., Ochoa-Tapia and Whitaker, 1995a,b, Chandesris and Jamet, 2008]. A key issue related to the Beavers-Joseph-Saffman (BJS) condition is its dependence on a material parameter describing the geometrical interface properties. This parameter needs to be determined experimentally or numerically. Yang et al. [2019] showed that the parameter may depend on the flow field and that the validity of the BJS condition is impaired for flow not parallel to the interface. Furthermore, the forthright application of the BJS condition for multi-phase flow [e.g., Mosthaf et al., 2011] remains questionable. Two-domain models may also feature a smooth transition zone of finite thickness, as presented, e.g., by Ochoa-Tapia and Whitaker [1995a,b] and Discacciati et al. [2016].

Pore-network modeling and hybrid-dimensional models All REV-scale approaches describe the porous medium, including the region close to the interface to the free flow, by nature only in an averaged sense. While providing the possibility to model larger domains, pore-scale effects such as local saturation distribution patterns [Shahraeeni et al., 2012] or other sub-scale characteristics like preferential flow paths causing non-Fickian transport behavior [Most et al., 2016] may not be captured in sufficient detail. These effects, however, can influence the global system behavior, thus leading to discrepancies between numerical results and experimental observations.

In contrast to REV-scale approaches, *pore-network models* (PNM) resolve the pore-scale characteristics of the permeable medium, albeit in a strongly simplified form, which still results in a rather low computational demand. First introduced by Fatt [1956a,b,c], their primary use was (and to large parts, still is today) the prediction of upscaled material parameters [e.g., Reeves and Celia, 1996, Oren et al., 1998, Blunt et al., 2002, Nuske, 2014], which was fostered by the advent of advanced CT-imaging technologies [e.g., Cnudde and Boone, 2013] providing computational networks from digitalized rock samples.

Pore-network models have also been used to gain a better understanding of pore-scale processes involved in, e.g., drying [e.g., Laurindo and Prat, 1998, Yiotis et al., 2007, Prat, 2011], technical applications such as fuel cells [e.g., Gostick, 2013, Qin, 2015] and

food processing [e.g., Ho et al., 2013], or capillary hysteresis [e.g., Joekar-Niasar et al., 2008] and reactive transport in porous media [e.g., Raoof et al., 2010]. Considering their rather simple and efficient nature, pore-network models yield relatively accurate results [Oostrom et al., 2016, Babaei and Joekar-Niasar, 2016] compared to computationally more expensive models.

A recent class of so-called hybrid-dimensional models [Scheibe et al., 2015] aims at combining the efficiency of macro-scale models with the local predictive accuracy of pore-scale approaches, such as pore-network models. Balhoff et al. [2007, 2008], Arbogast et al. [2007], Chu et al. [2012] and Mehmani and Balhoff [2014] coupled classical Darcy-type models to pore-network models for (compositional) single-phase flow, partly using mortar techniques. Sheng and Thompson [2013] present a Darcy-PNM coupling for two-phase flow. Beyhaghi et al. [2016] and Xu and Pillai [2016] simulated the drying of a porous medium by coupling a pore-network model to a free-flow domain.

Contribution of this work In this work, we develop model concepts for coupled free flow over a porous medium, using a pore-network model for the description of the interface region. The physical complexity of the coupled models presented ranges from stationary single-phase flow in all domains to compositional, non-isothermal two-phase flow in the porous medium. The model concept involves up to three computational sub-domains: (1) a region of free flow, where the (Navier-)Stokes equations hold, (2) an interface region described by a pore-network model and (3) an optional bulk porous domain used for regions of lower process intensity where we employ a classical REV-scale approach.

The main focus of this work is set on the coupling between free flow and the pore-network model, for which we also provide a comparison with experimental data for single-phase flow. In the works of Beyhaghi et al. [2016] and Xu and Pillai [2016], a commercial solver for single-phase flow was used to generate a steady-state velocity field for the free-flow region. Based on this field, vapor transport in the free-flow region was iteratively coupled to vapor transport within the pore network, where an invasion-percolation algorithm was used to determine the liquid phase distribution. The model therefore only considers capillary equilibrium points, thereby assuming the dominance of capillary forces over viscous ones, which limits the model's general applicability.

In contrast to that, we aim at the temporal resolution of the relevant processes by employing a dynamic pore-network model and a fully coupled, fully implicit model concept where no coupling iterations are required and mass, momentum and energy fluxes across the interfaces are preserved implicitly. This means that, e.g., the flow and pressure field within the pore network dynamically affects the free-flow domain and vice versa. We furthermore present, to our knowledge, the first attempt of using a fully coupled, fully implicit non-isothermal, two-phase and two-component pore-network model, while usually, decoupled or sequential approaches both with respect to phase redistribution [e.g., Joekar-Niasar et al., 2010a] and vapor transport [e.g., Qin, 2015] are employed.

The goal of this work is to provide a first step towards the accurate yet still computationally feasible description of pore-scale processes for coupled systems of free flow and porous media, focusing at the interface region between the two model domains.

1.2 Structure of the thesis

Having motivated the topic, the next chapter introduces some fundamental concepts for modeling porous media systems. Special attention is given to pore-network models. Chapter 3 explains the mathematical and numerical concepts used in the different sub-domains while Chapter 4 focuses on the coupling conditions. Chapter 5 discusses the implementation of the coupled model. Numerical results are presented in Chapters 7 and 8, where Section 7.1 includes a comparison with experimental data. We conclude with Chapter 9 where we also discuss potentials and perspectives for further model development.

2 Fundamentals

2.1 Terms and definitions

2.1.1 Flow regimes

Fluid flow can be characterized using the dimensionless *Reynolds number*

$$Re = \frac{vd_{\text{char}}}{\nu}, \quad (2.1)$$

where v is a characteristic velocity, d_{char} a characteristic length scale and ν the kinematic viscosity of the fluid.

Inertia forces can be neglected for very slow, *creeping* flow ($Re < 1$). This is usually a valid assumption for natural porous media systems. *Laminar* flow is characterized by parallel, non-crossing streamlines and may potentially exhibit some inertial effects. Further increasing the flow velocity will lead to a transition to *turbulent* flow which occurs under certain conditions specific to the system under consideration. Turbulence is characterized by a high amount of mixing and the transfer of kinetic energy from larger to smaller eddies where it eventually dissipates into heat. Turbulent flow will not be considered in this work.

2.1.2 Scales

Systems of coupled free and porous medium flow feature processes that occur over a wide range of *spatial and temporal scales*.

Spatial scales The movement and behavior of individual molecules as well as intermolecular interactions are described on the *molecular scale*. Averaging over a sufficient number of molecules yields *continuum-scale* quantities such as density, pressure or viscosity. The latter are defined on every point in space the continuum occupies. Many mathematical models for the description of flow and transport, including the ones used in this work, are based on the formulation of conservation equations on the continuum scale. The *pore scale* or *micro scale* is defined by an exact geometrical description of the solid and void space within a porous medium. *Pore-network models* (PNM, see 2.4) consider a discrete, simplified description of the pore space. The properties of a sufficiently large volume of the porous medium, the representative elementary volume (REV), may be averaged which gives rise to *REV-scale* quantities like porosity or permeability [Bear, 1972, Whitaker, 1999]. The size of an REV (Fig. 2.1) depends on the quantity of interest. Its lower bound is found if a further increase of the averaging volume's size does not affect the value of the averaged quantity anymore. The REV has to be large enough to even out pore-scale fluctuations while a maximum size should not be exceeded in order capture *macro-scale* heterogeneities.

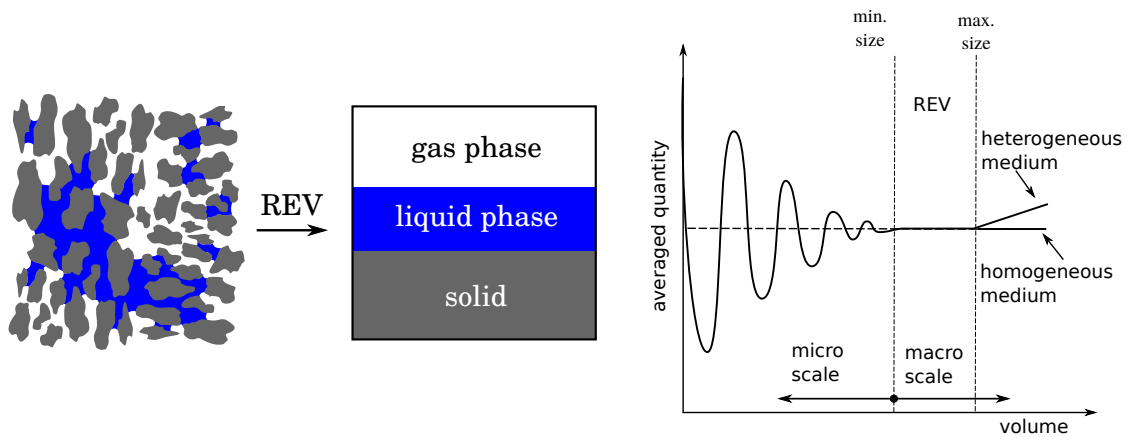


Figure 2.1 – REV concept. Left: averaging of pore-scale properties, right: exemplary REV size for some averaged quantity (after Helmig [1997] and Bear [1972]).

Temporal scales The *temporal scale* of a process determines the validity of the assumption of local thermodynamic equilibrium (see 2.2.2). While flow and transport processes on the pore scale, such as *Haines jumps* [e.g., Armstrong et al., 2015], may occur on temporal scales of the order of milliseconds, REV-scale phenomena are usually much slower, ranging from hours to years, such as the drainage of a core sample or

tracer transport experiments in the field. Furthermore, turbulent flow exhibits small-scale temporal fluctuations which either need to be resolved discretely by means of *direct numerical simulation* (DNS) or treated in an upscaled sense, e.g., by employing *Reynolds-averaged Navier-Stokes* (RANS) models [e.g., Fetzner, 2018].

2.1.3 Phases and components

Phases A phase α is defined as a continuum with homogeneous physical properties and a certain state of aggregation (solid, liquid, supercritical, gaseous) which is given by the thermodynamic state variables pressure p and temperature T . On the continuum scale, multiple phases are separated by sharp interfaces over which discontinuities of the above-mentioned physical properties occur. Several liquid and solid phases may coexist but there can only be one gas phase because gases are inherently miscible.

Components Phases consist of one or more components κ which can be either pure chemical species (e.g., nitrogen) or a mixture of species such as air (pseudo component). The physical properties of a phase can be influenced by its composition. A component may be present in multiple phases and phase transition processes such as evaporation and condensation facilitate the migration of a component from one phase to another.

Mole and mass fractions The composition of a phase can be defined in terms of mole or mass fractions.

The mole fraction x_α^κ relates the number of moles $n_{\text{mole},\alpha}^\kappa$ of component κ in phase α to the total number of moles $n_{\text{mole},\alpha}$ in the same phase:

$$x_\alpha^\kappa := \frac{n_{\text{mole},\alpha}^\kappa}{n_{\text{mole},\alpha}} = \frac{n_{\text{mole},\alpha}^\kappa}{\sum_{\kappa'} n_{\text{mole},\alpha}^{\kappa'}} . \quad (2.2)$$

If only one component κ is present $x_\alpha^\kappa = 1$. In analogy, the mass fraction X_α^κ is a ratio of component masses. It can be computed from the mole fraction x_α^κ as follows:

$$X_\alpha^\kappa := \frac{x_\alpha^\kappa M^\kappa}{M_\alpha} = \frac{x_\alpha^\kappa M^\kappa}{\sum_{\kappa'} x_\alpha^{\kappa'} M^{\kappa'}} . \quad (2.3)$$

Here, M^κ is the component's molecular weight while M_α is the phase-averaged molecular weight. By definition, the sum of mole or mass fractions within one phase α has to equal one:

$$\sum_{\kappa} x_{\alpha}^{\kappa} = \sum_{\kappa} X_{\alpha}^{\kappa} := 1 . \quad (2.4)$$

The phase *molar density* $\varrho_{\text{mol},\alpha} = \frac{n_{\text{mole},\alpha}}{V_{\alpha}}$ quantifies the number of moles per volume of α and can be transferred to the phase *mass density*:

$$\varrho_{\alpha} = \frac{m_{\alpha}}{V_{\alpha}} = \varrho_{\text{mol},\alpha} \sum_{\kappa} x_{\alpha}^{\kappa} M^{\kappa} . \quad (2.5)$$

2.2 Thermodynamic basics

In the following, some thermodynamic essentials for compositional and non-isothermal (multi-phase) flow are covered.

2.2.1 Chemical potential and fugacity

The chemical potential of a component κ in phase α is given by

$$\phi_{\alpha}^{\kappa} = \frac{\partial \Delta G}{\partial n_{\text{mole},\alpha}} . \quad (2.6)$$

The *Gibbs free energy* ΔG is a measure for the maximum reversible work a thermodynamic system under isothermal and isobaric conditions ($T = \text{const.}$, $p = \text{const.}$) can perform.

The *fugacity* f_{α}^{κ} is a function of ϕ_{α}^{κ} and can be seen as the tendency of a component κ to “escape” from a mixture. While $\phi_{\alpha}^{\kappa} \rightarrow \infty$ for non-present components, $f_{\alpha}^{\kappa} \rightarrow 0$, which makes the latter a favorable primary variable for numerical models. The fugacity of a pure *ideal gas* (Eq. (2.7)) equals the gas phase pressure. More details on the calculation of f_{α}^{κ} can be found in Lauser [2014].

2.2.2 Local thermodynamic equilibrium

According to Helmig [1997], thermodynamic equilibrium is a triple of mechanical, thermal and chemical equilibrium. *Thermal equilibrium* implies that all phases of a system feature the same temperature. Phases in *chemical equilibrium* have the same chemical potentials and hence no net component transfer from one phase to another takes place. This also implies that $f_\alpha^\kappa = f^\kappa$. In order to reach *mechanical equilibrium*, the mechanical forces at the interface between phases have to balance out. For multi-phase systems in porous media, pressure jumps due to capillary forces occur (see Section 2.3.1). Local thermodynamic equilibrium is a requirement for many REV-scale models. It is usually satisfied if the processes occur on a sufficiently large time scale. Advanced model concepts have been developed to handle local-thermodynamic non-equilibrium, e.g., if the solid and liquid phase locally exhibit different temperatures [e.g., Nuske, 2014].

2.2.3 Phase composition and phase change

Under the assumption of thermodynamic equilibrium, the *phase composition* is uniquely defined by its thermodynamic state variables and one does not have to explicitly account for kinetic phase transition processes.

Gas phase composition (Dalton's Law) The density of an ideal gas only depends on its pressure p_g and temperature T_g , as given by the corresponding equation of state, the *Ideal Gas Law*:

$$\varrho_g = \frac{p_g M_g}{RT_g}. \quad (2.7)$$

$R \approx 8.3146 \text{ J}/(\text{molK})$ is the universal gas constant and the M_g molar mass of the gas.

According to *Dalton's Law* and assuming that Eq. (2.7) also holds for mixtures, the total gas phase pressure p_g can be written as the sum of all *partial pressures* p_g^κ :

$$p_g = \sum_{\kappa} p_g^\kappa. \quad (2.8)$$

The partial pressure is defined as the theoretical pressure value in case the pure substance κ would occupy the entire available volume of the mixture (i.e., there are no interactions with other species' molecules). From this it follows that

$$p_g^\kappa = f^\kappa = p_g x_g^\kappa . \quad (2.9)$$

Liquid phase composition (Raoult's Law and Henry's Law) For mixtures, the partial pressure p_g^κ of a component κ within the gas phase g is related to the component's mole fraction within the liquid phase x_1^κ via Raoult's Law or Henry's Law, depending on whether κ is the major (solvent) or minor (solute) component within the liquid phase l.

Raoult's Law can be used if κ is the major component ($x_1^\kappa \rightarrow 1$):

$$p_g^\kappa = f^\kappa = x_1^\kappa p_{\text{sat}}^\kappa . \quad (2.10)$$

Here, p_{sat}^κ is the saturated vapor pressure. It is defined as the pressure of a vapor phase in thermodynamic equilibrium with its pure condensed (i.e., liquid or solid) phase in a closed system.

If κ is a solute ($x_1^\kappa \rightarrow 0$), *Henry's Law* can be applied:

$$p_g^\kappa = f^\kappa = x_1^\kappa H . \quad (2.11)$$

The Henry coefficient H is a measure for the solubility of κ in l. Combining Eqs. (2.4), (2.9) and (2.11) fully defines the phase composition for local thermodynamic equilibrium.

2.2.4 Mass and heat fluxes

Diffusion In this work, molecular diffusion within a fluid phase α is described by *Ficks's* first law:

$$\mathbf{j}_{\text{diff},\alpha}^{\kappa} = -D_{\alpha}^{\kappa} \varrho_{\alpha} \nabla X_{\alpha}^{\kappa} . \quad (2.12)$$

This law holds for binary (two-component) systems where the minor component (solute) is highly diluted such that its concentration does not affect the binary molecular diffusion coefficient D_{α}^{κ} . Note that different formulations of Fick's law exist, each one valid for a certain frame of reference. As the Navier-Stokes equations and consequently Darcy's law yield mass-averaged velocities [Taylor and Krishna, 1993, Bear, 1972], we use the mass-fraction based formulation as presented above in the context of fluid mechanics, yielding a mass flux. As a consequence, diffusion driven by a concentration gradient may also give rise to an advective flux for species of different molecular weight.

The sum of all diffusive fluxes within one phase α is always zero:

$$\sum_{\kappa} \mathbf{j}_{\text{diff},\alpha}^{\kappa} := 0 . \quad (2.13)$$

Eq. (2.12) may be also applied to multi-component systems if the individual solutes' concentrations are sufficiently low and if one solute's presence does not affect the diffusive behavior of another solute. If these requirements are met, each solute is assumed to behave as a binary system with the solvent with a specific binary diffusion coefficient. Otherwise, Maxwell-Stefan diffusion [e.g., Krishna and Wesselingh, 1997] has to be considered. Eq. (2.12) can be derived from this more comprehensive model. In this work, only binary diffusion is considered.

Distortions and fluctuations of the transporting velocity field lead to *dispersion* which is a process phenomenologically similar to diffusion, i.e., smearing out concentration gradients. Replacing D_{α}^{κ} in Eq. (2.12) by

$$D_{\alpha,\text{eff}}^{\kappa} = D_{\alpha}^{\kappa} + D_{\alpha,\text{disp}}^{\kappa}(\mathbf{v}_{\alpha}) \quad (2.14)$$

allows to incorporate the velocity-dependent effects of dispersion [Bear, 1972] which is, however, not considered in this work.

Heat conduction The diffusive flux of heat driven by a temperature gradient ∇T_α is given by *Fourier's* law:

$$\mathbf{j}_{\text{heat},\alpha} = -\lambda_\alpha \nabla T_\alpha . \quad (2.15)$$

Here, λ_α is the thermal conductivity of either a solid, liquid or gaseous phase.

2.3 Porous media

A porous medium is a material which includes void spaces (pores) and a solid matrix (e.g., grains in a soil). The *porosity* Φ relates the volume of the void space V_{void} to the total volume of an REV which includes both the solid matrix and the pores:

$$\Phi := \frac{V_{\text{void}}}{V_{\text{REV}}} . \quad (2.16)$$

The *saturation* is a measure of how much pore volume V_{void} is filled by a given fluid phase α :

$$S_\alpha := \frac{V_\alpha}{V_{\text{void}}} . \quad (2.17)$$

Per definition, the sum of all saturations has to equal one:

$$\sum_{\alpha} S_\alpha := 1 . \quad (2.18)$$

If the void spaces are connected with each other, fluids may flow from one pore to another and the porous medium is called *permeable*. When flow processes are of interest, usually only this *effective* porosity (which is often smaller than the total porosity) is considered.

Darcy [1856] experimentally quantified the resistance of soils to fluid flow and found a linear relation between the applied potential gradient and the resulting flow rate.

Darcy's law is a simplified momentum balance valid only for creeping flow ($Re_{\text{pore}} < 1$, based e.g., on the main grain diameter). If inertial forces within the porous medium cannot be neglected, Darcy's law should be replaced by the non-linear *Forchheimer* equation [Whitaker, 1996, Nield et al., 2006]. In this work, we will only consider creeping porous medium flow.

Tortuous pathways due to the presence of the solid matrix or other fluid phases slow down diffusion in porous media. Adapting the effective diffusion coefficient

$$D_{\alpha,\text{pm}}^{\kappa} = D_{\alpha}^{\kappa} \tau \Phi S_{\alpha} \quad (2.19)$$

accounts for this with $\tau = \Phi^{1/3} S_{\alpha}^{7/3}$ being the tortuosity factor [Millington, 1959, Helmig, 1997].

Under local thermal equilibrium, it is sufficient to calculate a single conductive heat flux (see Eq. (2.15)) considering an effective thermal conductivity which incorporates the thermal properties of the solid and fluid phases within the porous medium. Among others, Somerton et al. [1974] suggest an empirical relation

$$\lambda_{\text{pm}} = \lambda_{\text{dry}} + \sqrt{S_w} (\lambda_{\text{sat}} - \lambda_{\text{dry}}) \quad (2.20)$$

where $\lambda_{\text{dry}} = \lambda_s^{1-\Phi} \lambda_n^{\Phi}$ and $\lambda_{\text{sat}} = \lambda_s^{1-\Phi} \lambda_w^{\Phi}$ are the bulk thermal conductivities of a completely dry and a completely saturated porous medium. The subscripts s, w and n refer to the solid, wetting and non-wetting phase as described in the next section.

Multi-phase flow processes in porous media exhibit an increased level of physical complexity due to the presence of capillary forces that originate from micro-scale phenomena but govern the macro-scale system behavior. This subject is addressed in the following sections, following largely Blunt [2017].

2.3.1 Contact angle and capillary pressure

Interfacial tension The driving force of all capillary effects in porous media is *interfacial tension* and the tendency of a system to minimize its free energy. Interfacial tension is a measure for the work W required to increase the interfacial area A between two phases:

$$\gamma = \frac{\partial W}{\partial A} . \quad (2.21)$$

It is the work needed to overcome the intermolecular cohesive forces within a single phase in order to create a new interface where the molecules of one phase interact with those of the other phase. The term *surface tension* describes the interfacial tension of a solid or liquid phase with its pure gas phase.

Wettability and contact angle (Young Equation) The term *wettability* refers to a fluid's tendency to spread on a solid surface. Striving for an energetically favorable state, the *wetting* phase prefers to coat the solid's surface while the *non-wetting* phase tries to minimize the area in contact with the solid.

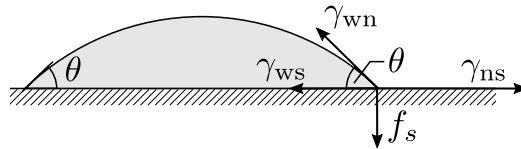


Figure 2.2 – Droplet of wetting fluid on a solid surface. f_s is the solid bonding force on the contact line [Hassanizadeh and Gray, 1993].

Figure 2.2 shows a droplet of wetting fluid (gray) placed on a horizontal solid surface. It is surrounded by the non-wetting phase (white). At the triple line where the fluid phases are in contact with the solid, a *contact angle* θ can be found which accounts for the local balance of horizontal forces, the *Young equation*:

$$\gamma_{ns} = \gamma_{ws} + \cos(\theta)\gamma_{wn} . \quad (2.22)$$

Here, γ_{ns} , γ_{ws} and γ_{wn} are the interfacial tensions between the non-wetting phase and the solid, the wetting phase and the solid, and the wetting phase and the non-wetting phase, respectively. For the latter, the subscript wn can be omitted. By convention, the contact angle θ is usually measured through the denser fluid phase (e.g., water in a water/air system). Wetting fluids feature contact angles below 90° .

Capillary pressure (Young-Laplace Equation) As seen in Fig. 2.2, the interface between the wetting and the non-wetting phase is curved which minimizes the interfacial area. This curvature gives rise to a pressure jump between the two fluids, the *capillary pressure*, defined as

$$p_c := \gamma \left(\frac{1}{r_1} + \frac{1}{r_2} \right) = \gamma \kappa . \quad (2.23)$$

A derivation of Eq. (2.23), commonly known as *Young-Laplace equation*, can be found, e.g., in Blunt [2017]. $\kappa = \left(\frac{1}{r_1} + \frac{1}{r_2} \right)$ is the total curvature of the interface where the principal radii of curvature r_1 and r_2 are identical for spherical geometries.

Under equilibrium conditions [Hassanizadeh and Gray, 1993], a balance of interfacial forces results in

$$p_c = p_n - p_w , \quad (2.24)$$

where p_n and p_w are the pressures of the non-wetting and wetting phase, respectively.

2.3.2 Phase displacement processes

The fluid configuration and phase distribution within a porous medium is the result of the system trying to minimize its free energy. A change in this configuration usually occurs in discrete steps, each one representing a local energy minimum. The replacement of the wetting phase by the non-wetting phase is called *drainage* while the opposite process, where the non-wetting phase is receding, is called *imbibition*. For the discussion of phase displacement, it is useful to classify the pore space into *pore bodies* and

pore throats, as shown in Fig. 2.3. One pore body is separated from another by a local constriction, the pore throat.

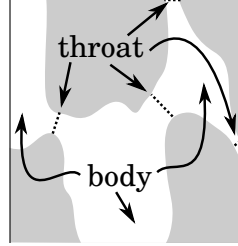


Figure 2.3 – Pore bodies and throats. Large void spaces correspond to pore bodies which are separated by constrictions (pore throats, dashed lines).

Drainage For energetic considerations, a certain threshold capillary pressure, the so-called *entry capillary pressure* $p_{c,e}$ has to be overcome before the non-wetting phase can invade a pore during drainage. According to Eq. (2.24), this can be realized by either increasing p_n , i.e., pushing the non-wetting phase into the medium, or decreasing p_w by applying a suction pressure to the wetting phase. As indicated by Eq. (2.23), wider pores featuring a lower $p_{c,e}$ are invaded first while the narrowest throats are the restricting factor for drainage. A meniscus may traverse several pores in a single invasion event if the downstream pores have a lower $p_{c,e}$ than the primarily invaded one (Haines jump). For non-circular pore geometries, the wetting phase may still be present in form of a wetting layer residing in the pore's corners once it has been invaded by the non-wetting phase which will then be present at the center of the pore.

Imbibition Two different processes lead to the displacement of the non-wetting phase during imbibition. If there are layers of wetting fluid in the corners of the pore, a decrease of the capillary pressure p_c caused, e.g., by an increase of p_w can lead to a *swelling of the layers*, accompanied by a decrease of the curvature of the *arc menisci* (see Fig. 2.4). Provided the wetting layers are connected throughout the porous medium, this uniformly increases S_w . The wetting layers can swell until they touch at the narrowest point in the pore geometry, the pore throat. Once this happens, the triple line of solid, wetting and non-wetting phase vanishes, i.e., the non-wetting phase loses contact to the solid phase and becomes unstable. This *snap-off* engenders two *terminal menisci* across the pore throat. The latter is then filled rapidly by the wetting phase while the non-wetting phase becomes disconnected and retreats to the two adjacent

pore bodies. This in turn can lead to *trapping*, i.e., parts of the non-wetting phase become severed from the bulk phase and thus immobile.

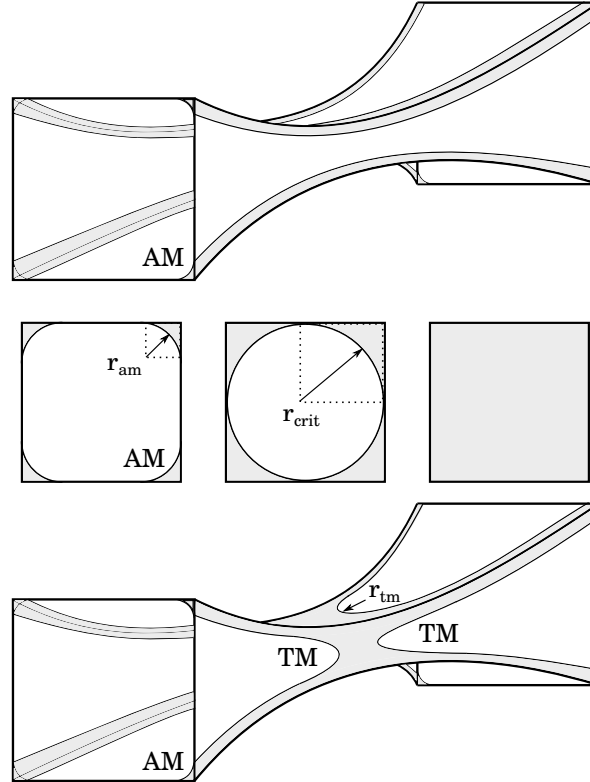


Figure 2.4 – Snap-off concept. Illustration of a throat before (top) and after (bottom) snap-off occurred. The center drawings show the swelling of the wetting layers until $r_{am} \geq r_{crit}$. Terminal menisci are marked with TM, arc menisci with AM. Adapted from Blunt [2017].

The second imbibition mechanism is called *piston-like advancement*. Here, the pore throat is completely filled by the wetting phase, i.e., a terminal meniscus moves along the pore and throat. This generally leads to a sharper and more distinct wetting front compared to layer swelling. The movement of the meniscus is limited by the widest cross-sections in the pore space, the pore bodies. Here, the capillary forces driving the imbibition process are smallest and thus p_c needs to fall below a critical value in order to allow the meniscus to pass the pore body (e.g., by increasing p_w). This value can be calculated similarly as $p_{c,e}$ by considering an energy balance. Piston-type advancement is basically a reversed drainage process featuring a higher level of complexity, depending both on the pore geometry and on the current fluid configuration. The filling behavior of a pore body is controlled by the number of adjacent throats n that are still occupied

by the non-wetting phase. This is called *cooperative pore filling* or I_n mechanism. For I_0 , the non-wetting phase can only escape through a single throat while for I_3 , three different throats are available for the non-wetting phase to leave the pore. For each mechanism, a different critical threshold pressure holds.

Piston-type advancement leads to less trapping than layer swelling. Both processes are competing with each other and depend on the pore-space geometry and wettability of the solid. Layer swelling and snap-off are favored for high aspect ratios between pore bodies and pore throats, sharp corners in the pore geometry (there are no wetting layers in circular throats) and low contact angles. In contrast, piston-like advancement is favored if there is a high degree of connectivity between the pore bodies, allowing the non-wetting phase to escape a pore being filled by the wetting phase. Only imbibition due to layer swelling and snap-off will be considered in this work.

Hysteresis Due to the different nature of the processes involved in drainage and imbibition, a repeated increase and decrease of the saturation by ΔS_α will generally not result in the same pore-scale fluid configuration which also means that the local capillary pressures and consequently the global, averaged one will not be equal before and after the repeated change of saturation. This phenomenon is called *hysteresis* [Helmig, 1997]

2.3.3 Evaporation from porous media

Evaporation from porous media is governed by the evaporating liquid's thermodynamic properties, the ambient conditions and the properties of the porous medium itself. The driving force of evaporation is the vapor pressure gradient which renders the process diffusion-dominated [e.g., Brutsaert, 2013, Or et al., 2013].

As already mentioned in the context of Raoult's law (Eq. (2.10)), the saturated vapor pressure p_{sat}^κ of component κ corresponds to the equilibrium gas phase pressure $p_g^\kappa = p_g$ if a pure liquid phase is considered with κ as the only component. Lord Kelvin [Thomson, 1872, Class, 2007] observed that p_{sat}^κ is decreased for gas atmospheres above

concave surfaces, such as liquid menisci of wetting fluids in porous media. The eponymous equation

$$p_{\text{sat,Kelvin}}^\kappa = p_{\text{sat}}^\kappa \exp\left(-\frac{p_c M^\kappa}{\rho_l R T}\right) \quad (2.25)$$

accounts for this by considering the capillary pressure p_c . Fetzer [2018] showed that the evaporative behavior on the REV scale does not depend strongly on Eq. (2.25) for $p_c < 1 \times 10^6$ Pa. Nevertheless, we will always consider Eq. (2.25) in this work.

The *evaporation rate* \dot{e} describes the mass flux of vapor leaving the porous medium. Based on its temporal development (see Fig. 2.5), two different main stages of evaporation can be distinguished. A consistently high initial evaporation rate designates *stage-I* [e.g., Lehmann et al., 2008] or the *constant-rate period* (CRP) [e.g., Yiotis et al., 2007], where the evaporating liquid is still present at the surface of the porous medium. Here, only the atmospheric demand, i.e., the ambient partial pressure gradient, is the limiting factor. The evaporation rate may already drop during stage-I [e.g., Shahraeeni et al., 2012, Or et al., 2013], as a consequence of the system striving towards an equilibrium state and the evaporative cooling effect [Mosthaf et al., 2014] lowering p_{sat}^κ .

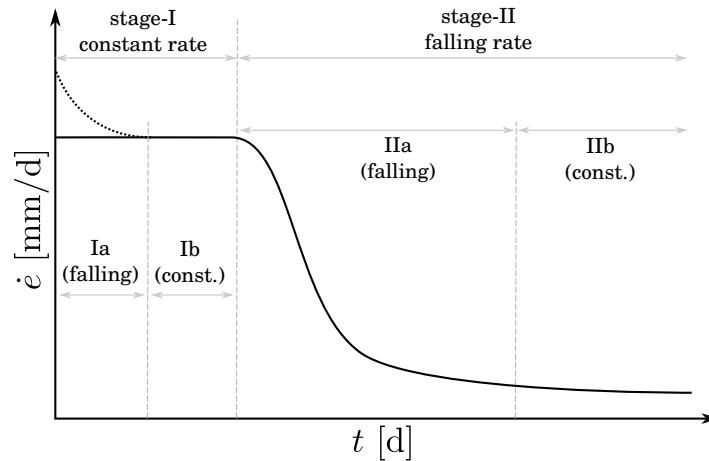


Figure 2.5 – Evaporation from porous media. Temporal evolution of an exemplary evaporation rate with different stages, after Mosthaf et al. [2014] and Fetzer [2018].

At the end of stage-I, the evaporative demand exceeds the capillary potential transporting or “pumping” liquid from deeper regions of the porous medium to its surface. At this point, the first pores at the surface fall dry, i.e. the fluid menisci recede into the porous medium. Liquid vapor thus has to be transported by diffusion from the inside of the porous domain towards the surface which considerably slows down the evaporation process. This marks *stage-II* or the falling-rate period (FRP) [e.g., Shokri and Or, 2011]. Shahraeeni et al. [2012] and Or et al. [2013] report a counteracting phenomenon which can help to prolong the duration of stage-I, i.e., maintain a relatively high level of the evaporation rate: as singular pores fall dry, the local evaporation rates of the neighboring pores increase since the diffusion of vapor changes from a one-dimensional (perpendicular to the surface of the porous medium) to a three-dimensional characteristic (forming local spheres of strong vapor pressure gradients around the pores).

Chauvet et al. [2009] showed that the drying behavior of porous media on the REV scale resembles the evaporation characteristics of a single square-shaped capillary tube. In a circular tube, the meniscus of the evaporating liquid phase immediately recedes into the tube (corresponding to stage-II evaporation). While in an angular tube, the meniscus also recedes, liquid films in the corners of the tube establish a path through which the (wetting) liquid is transported by capillary action to the entrance of the tube, where strong vapor pressure gradients account for a high evaporation rate (corresponding to stage-I evaporation). We refer to Prat [2011] for the discussion of further pore-scale effects related to evaporation.

2.4 Pore-network modeling

The following chapter introduces pore-network models [e.g., Fatt, 1956a,b,c, Oren et al., 1998, Blunt et al., 2002, Xiong et al., 2016] since those will be used to describe the interface region between free flow and bulk porous medium.

2.4.1 Network representation

The fundamental idea of pore-network modeling is a simplified yet physically equivalent representation of the pore structure using the concept of pore bodies and pore throats. The continuous void space of a porous medium is segmented into discrete pore bodies which are separated from each other by local constrictions, the pore throats, over which fluid flow between the bodies occurs (see Fig. 2.3). The center of a pore body is defined as the point which features the greatest distance to the solid wall locally while the throat can be seen as the surface with a local minimum distance to the solid wall [Blunt, 2017]. A network representation of a porous medium is defined by its topology and geometry [Joekar-Niasar and Hassanizadeh, 2012a]. The topology describes the spatial arrangement of the pore bodies and their interconnectivity via pore throats. The *coordination number* n_{coord} specifies how many other pore bodies (and thus, pore throats) are connected to a given pore body. Higher coordination numbers usually result in greater network permeability. The network topology and its degree of connectivity can be described mathematically in terms of *Minkowski* functionals and *Euler* characteristics [Blunt, 2017]. The network geometry is given by the sizes and shapes of the pores which commonly includes the use of simplified idealized geometries as described in more detail later.

Network generation A pore network can be either extracted from a given three-dimensional image of a porous medium or generated synthetically based on stochastic properties inherent to the medium of interest.

An example of the latter approach is given by Raouf and Hassanizadeh [2009]. Starting from a regular lattice of pore bodies featuring coordination numbers of 26, the connecting pore throats are deleted randomly with a probability specified for each of the 13

possible directions. Using an optimization algorithm, the statistical properties of real porous media could be recovered.

In the following, different network extraction techniques from image data are summarized. Three-dimensional voxel images of porous media can be either obtained directly from micro-CT or synchrotron X-ray imaging [Cnudde and Boone, 2013, Wildenschild and Sheppard, 2013] of a cylindrical sample, or by stochastic reconstruction from a two-dimensional thin section image such as presented, e.g., by Bakke and Øren [1997] where the sedimentary and diagenetic formation process of the medium was considered. The extraction of a network from the 3D image corresponds to a direct mapping [Xiong et al., 2016], i.e., the pore bodies in the network will be arranged irregularly following the actual topology of the porous material. Three different extraction methods are commonly used. (1) The medial axis skeletonization [e.g., Lindquist et al., 1996, Prodanović et al., 2007] yields a graph of connected lines, the skeleton, which runs through the center of the void space, maintaining the maximum possible distance to the walls. The method exactly preserves the pore throat topology in theory but suffers from the finite resolution of the voxel data and ambiguities in finding pore body locations which here are defined as the junctions of the skeleton and not necessarily the widest parts of the void space [Blunt, 2017]. (2) The maximal ball algorithm developed by Silin and Patzek [2006] aims at recovering the pore bodies more accurately. Spheres are placed in the void space and grown until they intersect with a solid wall which then defines them as maximal balls. The centers of the largest spheres, the ancestors, will coincide with the pore body centers. All spheres completely encased by a larger sphere are neglected, those overlapping with a larger sphere are assigned to the same family, headed by the ancestor maximal ball. Spheres belonging to two different families will be found at constrictions, the pore throats. Like before, the method suffers from the limited image resolution and the distinction between pore body and throat is made rather arbitrarily due to the discrete nature of the input data. Furthermore, very small pores might be spuriously identified close to rough solid walls [Blunt, 2017]. (3) Lastly, the watershed algorithm [e.g., Jiang et al., 2007, Gostick, 2017] is based on a distance map which stores the discrete distance from each void voxel to the nearest solid wall. After determining the gradient of the distance map, pore body centers can be found at the local maxima while pore throat centers are located at the saddle points. From each void-space voxel, a streamline following the local gradient is started which finally ends at a position where the gradient takes a value of zero, i.e., a pore body or throat

center. Voxels with streamlines ending at the center of a pore body are assigned to the latter. If the streamline ends at a pore-throat center, the corresponding starting-point voxel belongs to the pore-throat plane separating two pore bodies or, in other terms, watersheds [Blunt, 2017].

Each of the above-mentioned extraction methods applied to the same image data will result in a different network with partly substantially different topological and geometric properties [Bhattad et al., 2011, Baychev et al., 2019]. Interestingly, the upscaled single-phase permeability of the network seems to be rather insensitive to the chosen method.

Idealized geometries and shape factor The complex void space geometries are usually transferred to more simple, idealized shapes that are chosen such that relevant geometrical properties governing the pore-scale fluid flow behavior are preserved as good as possible. Joekar-Niasar and Hassanizadeh [2012a] and Joekar-Niasar et al. [2010b] extensively summarize the use of different idealized geometries for both pore bodies and pore throats. Their findings are briefly presented here.

Pore bodies are usually represented as spheres [e.g., Koplik and Lasseter, 1985] or cubes [e.g., Mogensen and Stenby, 1998] but other geometries may be used, too, such as truncated octahedrons [Joekar-Niasar and Hassanizadeh, 2011] or prolate spheroids [Joekar-Niasar et al., 2010b]. Most often, all pore bodies of the entire network feature the same type of geometry. Some models do not explicitly distinguish between pore bodies and pore throats. Instead, pore throats with a constriction at the center and wider openings are employed. The intersections of these “composite pores” [Joekar-Niasar and Hassanizadeh, 2012a] may then be considered as pore bodies, though lacking a distinct geometrical description.

Idealized pore throats can be either represented as converging and diverging ducts, such as biconical tubes [e.g., Reeves and Celia, 1996], or as prismatic channels with a constant cross-sectional area and shape, which has been used more commonly. Circles [e.g., Koplik and Lasseter, 1985], rectangles [e.g., Joekar-Niasar et al., 2010a] or triangles [e.g., Oren et al., 1998] are frequently chosen as idealized cross-sectional shape. The key feature of the angular types is that they permit the formation of wetting layers within the corners of the throat, once it has been invaded by the non-wetting phase. This ensures the connectivity of the wetting phase throughout the entire network,

where either a single type of cross-sectional shape [e.g., Joekar-Niasar et al., 2010a] or a mixture of different types [e.g., Patzek, 2000] may be assigned to the pore throats.

The widely used concept of a so-called *shape factor* proposed by Mason and Morrow [1991] relates the throat's cross-sectional area A to its perimeter P and can be seen as a sort of hydraulic radius:

$$G = \frac{A}{P^2} . \quad (2.26)$$

This factor allows the analytic computation of throat conductance values and threshold capillary pressures, which are essential for the description of multi-phase flow [Blunt, 2017]. Valvatne and Blunt [2004] have chosen the type of idealized shape based on the actual geometry's shape factor, where $0 < G < \sqrt{3}/36$ corresponds to a scalene triangle, $G = \sqrt{3}/36$ to an equilateral triangle, $G = 1/16$ to a rectangle and $G = 1/4\pi$ to a circle, which also marks the maximum possible value of G . As illustrated in Fig. 2.6, higher values of G indicate smoother shapes.

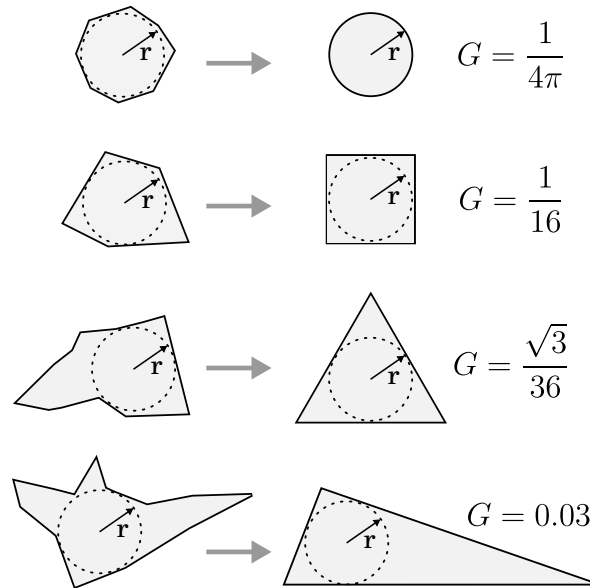


Figure 2.6 – Shape factor concept. Illustration of different void space geometries mapped to simpler idealized shapes. Apart from the circle ($G = 1/4\pi$), both the actual geometry and the simplified shape feature exactly the same shape factor G and inscribed radius r whereas the respective areas may differ. Adapted from Valvatne and Blunt [2004] and Blunt [2017].

Choosing an appropriate representative shape also fixes the number of corners and

the associated corner half-angles ($\beta = \pi/4$ and $\beta = \pi/6$ for squares and equilateral triangles, respectively). For scalene triangles, a non-unique triple of corner half-angles has to be found such that G is preserved (see Appendix A).

Apart from circles, rectangles or triangles, star-shaped polygons [e.g., Man and Jing, 2000] and other geometries have been used to idealize pore throats. Joekar-Niasar et al. [2010b] employed hyperbolic polygons with different numbers of vertices which may feature curved sides and allow a more continuous distribution of shapes for $G \geq \sqrt{3}/36$. While requiring more complex analytic expressions for the description of the geometries and the determination of threshold capillary pressures, the authors reported a closer approximation of experimental results for a glass-bead packing using the hyperbolic polygons when compared to models limited to circular shapes or ordinary polygons.

2.4.2 Constitutive laws

Threshold capillary pressures and phase distribution As explained in Section 2.3.2, the narrowest regions of the porous medium, i.e., the pore throats, are the limiting elements for drainage. Here, an entry capillary pressure $p_{c,e}$ needs to be overcome before the meniscus can pass the throat. For circular throat cross sections, this can be simply derived from Eq. (2.23) where now both principal radii of curvature are equal:

$$p_{c,e} = \frac{2\gamma \cos(\theta_r)}{r_{ij}} . \quad (2.27)$$

Since the wetting fluid is displaced, one has to consider the receding contact angle θ_r . r_{ij} is the inscribed radius of the pore throat ij connecting pore bodies i and j .

For non-circular throats, the calculation of $p_{c,e}$ becomes more involved. Here, wetting layers may be present in the corners of the throat only if

$$\beta + \theta_r < \pi/2 , \quad (2.28)$$

where β is the corner half angle [Blunt, 2017]. For a rectangular throat with $\beta = \pi/4$ for instance, this means that the wetting phase can only be present in the corner if

$\theta_r \leq \pi/4$ in order to keep a positive capillary pressure, i.e., a concave arc meniscus. The capillary pressure within that layer is then given by

$$p_c = \frac{\gamma}{r_{\text{am}}} , \quad (2.29)$$

where r_{am} is the radius of the arc meniscus as shown in Fig. 2.4. Here, only this radius is considered; the curvature along the length of the throat is very large and therefore neglected.

Mason and Morrow [1991] and Ma et al. [1996] derived an analytical expression for the entry capillary pressure of irregular throat cross sections based on the *Mayer-Stowe-Princen* (MSP) method [Mayer and Stowe, 1965, Princen, 1969a,b, 1970]. Here, an energy balance for displacing the wetting phase is considered which equates the curvature of the arc meniscus with the one of the invading fluid's terminal meniscus. Oren et al. [1998] generalized this approach for arbitrary cross-sectional shapes:

$$p_{c,e} = \frac{\gamma \left(1 + 2\sqrt{\pi G}\right) \cos(\theta_r) F_d(\theta_r, G)}{r_{ij}} , \quad (2.30)$$

$$F_d(\theta_r, G) = \frac{1 + \sqrt{1 + 4GE / \cos^2(\theta_r)}}{1 + 2\sqrt{\pi G}} , \quad (2.31)$$

$$E = \pi - 3\theta_r + 3 \sin(\theta_r) \cos(\theta_r) - \frac{\cos^2(\theta_r)}{4G} . \quad (2.32)$$

$F_d(\theta_r, G)$ is a dimensionless correction factor which becomes 1 for $\theta_r = 0$. Equation (2.32) only holds if a wetting layer is present in every corner of the throat. Blunt [1997] provides an expression for $p_{c,e}$ if this requirement is not met.

The critical minimum capillary pressure relevant for imbibition occurs at the widest regions of the porous medium, the pore bodies, as shown in Section 2.3.2. For piston-like advance, Eq. (2.30) can be used after replacing the receding contact angle θ_r with the advancing one θ_a and the throat radius r_{ij} with the inscribed pore body radius r_i .

In the case of cooperative pore filling, no exact expression for the threshold capillary pressure exists. Instead, various approximations were proposed, such as by Blunt [1998]:

$$p_c(I_n) = \frac{2\gamma \cos(\theta_a)}{r_i} - \gamma \sum_{m=1}^n b_m x_m . \quad (2.33)$$

Here, n is the number of throats adjacent to the pore through which the non-wetting phase can escape. The coefficients b_m are “arbitrary” [Blunt, 1998] and $x_m \in [0, 1]$ are random numbers. Blunt [2017] suggests to chose b_m as the approximate inverse value of a mean throat radius, except for $b_1 = 0$ such that the I_1 filling characteristic (Section 2.3.2) is preserved.

In contrast to the threshold capillary pressure described above, no energy balance is required for the determination of the snap-off capillary pressure relevant for layer swelling. Instead, the critical radius of curvature and thus capillary pressure can be inferred from the throat’s geometry [Blunt, 2017],

$$p_{c,s} = \frac{\gamma \cos(\theta_a)}{r_{ij}} (1 - \tan(\theta_a) \tan(\beta)) , \quad (2.34)$$

where β is the corner half-angle.

Local capillary-pressure saturation relationship Pore-network models that evaluate pressure and saturation at pore bodies [e.g., Thompson, 2002, Joekar-Niasar et al., 2010a] require the formulation of a local capillary-pressure saturation relationship per pore body. This can be derived, under a number of assumptions, from pure geometrical considerations. Joekar-Niasar et al. [2010a] propose a simplified relation for a cubic pore body i with local saturation $S_{w,i}$:

$$p_{c,i}(S_{w,i}) = \frac{2\gamma}{r_i(1 - \exp(-6.83S_{w,i}))} . \quad (2.35)$$

A relation for truncated octahedrons can be found in Joekar-Niasar and Hassanizadeh [2012b].

Flow resistance Assuming creeping flow, pore-network models commonly employ linear laws for the approximation of the volumetric flow rate of phase α within the pore throat ij connecting the two neighboring pore bodies i and j :

$$Q_{\alpha,ij} = g_{\alpha,ij}(p_{\alpha,i} - p_{\alpha,j}). \quad (2.36)$$

The flow rate is proportional to the phase pressure drop ($p_{\alpha,i} - p_{\alpha,j}$) related to the pore body centers \mathbf{x}_i and \mathbf{x}_j and the throat conductance $g_{\alpha,ij}$. The latter incorporates the throat's geometry (e.g., length, shape, diameter) and the fluid properties (viscosity), as well as the capillary pressure dependent phase distribution in the case of two-phase flow. This approximation can be derived from the one-dimensional stationary Stokes equations. For the simplest case of single-phase flow in a circular tube, this results in the well-known Hagen-Poiseuille equation (see Appendix B)

$$Q_{ij} = \frac{\pi r_{ij}^4}{\underbrace{8\mu l_{ij}}_{g_{ij}}}(p_i - p_j), \quad (2.37)$$

where r_{ij} and l_{ij} are the throat's radius and length, respectively, while μ is the fluid's dynamic viscosity. For ease of exposition, the subscript α is dropped for single-phase flow here. Like Darcy's law, Eq. (2.37) is only valid for creeping flow ($Re < 1$). Inertia effects can be incorporated by using more advanced formulations in analogy to the Forchheimer equation [e.g., Balhoff and Wheeler, 2009, Veyskarami et al., 2017]. We will only consider creeping pore-network flow in this work.

Several (semi-) analytical relations for non-circular ducts can be found in the literature [e.g., Boussinesq, 1868, Proudman, 1914, Bruus, 2008], e.g.,

$$g_{ij} = \frac{0.4218h_{ij}^3w_{ij}}{12\mu l_{ij}} \quad (2.38)$$

for rectangular channels of width w_{ij} and height h_{ij} or

$$g_{ij} = \frac{0.45\sqrt{3}r_{ij}^4}{\mu l_{ij}} \quad (2.39)$$

for equilateral triangles with an inscribed radius r_{ij} . Extending the work of Oren et al. [1998], a generalized concept for different cross-sectional shapes was developed by Patzek and Silin [2001] who propose a linear scaling of the throat conductance with the previously discussed shape factor G in the case of single-phase flow:

$$g_{ij} = \frac{kA_{\text{tot},ij}^2 G}{\mu l_{ij}} . \quad (2.40)$$

Here, k is a proportionality constant which takes the values of 0.5 for circles, 0.5623 for squares, and 0.6 for equilateral triangles. The latter value also holds for isosceles triangles in close approximation. $A_{\text{tot},ij}$ is the total cross-sectional area of the throat.

If the pore bodies are rather large compared to the pore throats' dimensions, their contribution to flow resistance is commonly neglected [e.g., Joekar-Niasar et al., 2010a]. On the other hand, the pressure drop within the pore bodies may be relevant if both pores and throats are of comparable size and thus should be taken into account [e.g., Valvatne and Blunt, 2004]:

$$g_{ij}^* = (g_{ij}^{-1} + g_i^{-1} + g_j^{-1})^{-1} . \quad (2.41)$$

Equation (2.40) may be used to approximate the conductance factors within the pore bodies g_i and g_j . Mehmani and Tchelepi [2017] further extended this approach by segmenting the void space between one pore body center to another into a series of disks of equal thickness but potentially varying radius based on the maximum inscribed radius between the grains. Using Eq. (2.40) to calculate the conductance g_d of each disk, the integral conductance may then be expressed as:

$$g_{ij}^* = \left(\sum_{d=1}^{n_{\text{disc}}} g_d^{-1} \right)^{-1} . \quad (2.42)$$

Miao et al. [2017] developed a novel approach which goes beyond the use of a single shape parameter for the representation of the void space. Using machine learning, they identified a combination of different shape properties which govern the single-phase flow resistance.

More than one phase may be present in an angular throat. In this case, the wetting phase recedes to the throat's corners while the non-wetting phase occupies its central bulk void space. Fluid flow in all phases can be treated individually by assigning a corresponding phase conductance. An expression for the wetting layer conductance is given by Ransohoff and Radke [1988],

$$g_{w,ij} = \frac{r_{\text{am}}^2}{\mu_w l_{ij}} \sum_{\Lambda=1}^{n_{\text{corner}}} \frac{A_{w,\Lambda}}{\xi_{\Lambda}}, \quad (2.43)$$

where $r_{\text{am}} = \gamma/p_c$ is the radius of curvature of the arc menisci, $A_{w,\Lambda}$ the cross-sectional area of the wetting layer in corner Λ , μ_w the wetting-phase viscosity and ξ_{Λ} is a dimensionless resistance factor. The latter can be determined numerically by solving the stationary Stokes equations for a single wetting layer for a given corner geometry and phase configuration, i.e., contact angle and capillary pressure. Zhou et al. [1997] propose an analytical approximation of

$$\xi_{\Lambda} = \frac{12 \sin^2(\beta_{\Lambda})(1-B)^2(\psi_1 - B\psi_2)[\psi_3 + f_2 B\psi_2 - r_d(1 - f_1 B)]^2}{(1 - \sin(\beta_{\Lambda}))^2 B^2 [\psi_1 - B\psi_2 - (1-B)r_d^2]^3}, \quad (2.44)$$

where β_{Λ} is the half-angle of corner Λ and

$$\psi_1 = \cos^2(\beta_{\Lambda} + \theta_{\Lambda}) + \cos(\beta_{\Lambda} + \theta_{\Lambda}) \sin(\beta_{\Lambda} + \theta_{\Lambda}) \tan(\beta_{\Lambda}), \quad (2.45)$$

$$\psi_2 = 1 - \frac{\theta_{\Lambda}}{\pi/2 - \beta_{\Lambda}}, \quad (2.46)$$

$$\psi_3 = \frac{\cos(\beta_{\Lambda} + \theta_{\Lambda})}{\cos(\beta_{\Lambda})}, \quad (2.47)$$

$$B = (\pi/2 - \beta_{\Lambda}) \tan(\beta_{\Lambda}). \quad (2.48)$$

θ_{Λ} is the contact angle in corner Λ . As a parameter for the degree of roundness, $r_d = 0$ for sharp corners. The factors f_1 and f_2 correspond to boundary conditions. Between the wetting and the non-wetting phase, a no-slip ($f_2 = 1$), no-stress ($f_2 = 0$)

or intermediate condition ($0 < f_2 < 1$) may be assigned, depending on the fluids' viscosity ratio. For instance, if water is the wetting phase and air the non-wetting phase, a no-stress condition may be appropriate while a no-slip condition would be more realistic for a water/oil system [Blunt, 2017]. For the interface between the solid and the wetting phase, a no-slip condition is assumed and thus $f_1 = 1$.

Patzek and Kristensen [2001] revised the numerical determination of ξ_Λ developed by Ransohoff and Radke [1988] and propose an expression related to tabulated values which yields more accurate results compared to those obtained by Eq. (2.44). Focusing on viscous coupling effects, Xie et al. [2017] used a lattice Boltzmann method to derive improved expressions for the conductance of both the wetting phase layers in the throat's corners and non-wetting phase layers that are sandwiched between the wetting phase in the corners and the wetting phase in the center of the throat - a configuration that may arise in the case of intermediate-wet porous media.

The conductance of the non-wetting phase occupying the center of the throat is usually approximated with rather simple expressions which all yield more or less comparable results (see Fig. 2.7). According to Blunt¹, the bulk non-wetting phase conductance mainly depends on the phase's cross-sectional area and hydraulic diameter within the throat center while the influence of viscous shear stresses at the interface towards the wetting phase is commonly assumed to follow a no-slip condition. Thus, the accuracy of pore-network models is generally less sensitive to the approximation of the bulk non-wetting phase conductance compared to the one of the wetting phase layers in the corners. In the following, a selection of different expressions for $g_{n,ij}$ described in the literature is presented.

Blunt [1997] used an equation based on flow in a circular tube (see Eq. 2.37),

$$g_{n,ij} = \frac{\pi r_{\text{eff}}^4}{8\mu_n l_{ij}}, \quad (2.49)$$

where an effective radius is used for scaling with the actual cross-sectional area of the

¹Private communication on InterPore conference in Valencia, May 2019.

non-wetting phase $A_{n,ij}$:

$$r_{\text{eff}} = \frac{1}{2} \left(\sqrt{\frac{A_{n,ij}}{\pi}} + r_{ij} \right). \quad (2.50)$$

This approach has found application in a number of works [e.g., Mogensen and Stenby, 1998, Mogensen et al., 1999, Wang et al., 2015]. Singh and Mohanty [2003] define $r_{\text{eff}} = \frac{1}{2} \left(\sqrt{\frac{A_{n,ij}}{\pi}} + r_{ij} \right)$ which might be a typo with regard to the units of the sum.

Bakke and Øren [1997], Tørå et al. [2011] and Khayrat and Jenny [2017] used a slightly modified version of Eq. (2.49):

$$g_{n,ij} = \frac{r_{\text{eff}}^2 A_{n,ij}}{8\mu_n l_{ij}}. \quad (2.51)$$

Valvatne and Blunt [2004] simply scale the single-phase conductance factor as given by Eq. (2.40) with the fraction of the non-wetting phase area occupying the lumen:

$$g_{n,ij} = \frac{kA_{\text{tot},ij}^2 G}{\mu_n l_{ij}} \frac{A_{n,ij}}{A_{\text{tot},ij}} = \frac{kA_{\text{tot},ij} A_{n,ij} G}{\mu_n l_{ij}}. \quad (2.52)$$

Lastly, Blunt [2017] proposes

$$g_{n,ij} = \frac{kA_{n,ij}^2 G}{\mu_n l_{ij}}. \quad (2.53)$$

Figure 2.7 summarizes the results yielded by evaluating Eqs. (2.49) to (2.53) for a square (left) and equilateral triangle (right) cross section, assuming a contact angle of $\theta = 0$. r_{am}/r_{ij} is the ratio between the arc meniscus curvature and the throat's inscribed radius r_{ij} . $r_{\text{am}}/r_{ij} = 0$ corresponds to a situation where the non-wetting phase completely occupies the throat, i.e., $p_c \rightarrow \infty$. This point is marked with a square or triangle in the figures. All results are normalized by the single-phase conductance given by Eq. (2.40) at this point. The case where the arc meniscus radius approaches the throat's inscribed radius is given at $r_{\text{am}}/r_{ij} = 1$, a state which usually cannot be reached because snap-off would occur before.

For the square cross-section, only Eq. (2.49, Blunt A) deviates clearly from the single-phase value at $r_{\text{am}}/r_{ij} = 0$, while it exactly recovers the single-phase value at $r_{\text{am}}/r_{ij} = 1$, as does Eq. (2.51, Bakke). The observations are similar for the triangular throat cross-section. Here, Eq. (2.51, Bakke) overestimates the single-phase value at $r_{\text{am}}/r_{ij} = 0$. While Eq. (2.52, Valvatne) and Eq. (2.53, Blunt B) exactly reproduce the single-phase conductance for both geometries at $r_{\text{am}}/r_{ij} = 0$, the values for $r_{\text{am}}/r_{ij} \rightarrow 1$, corresponding to the single-phase conductance of a circular tube, are over- and underestimated, respectively.

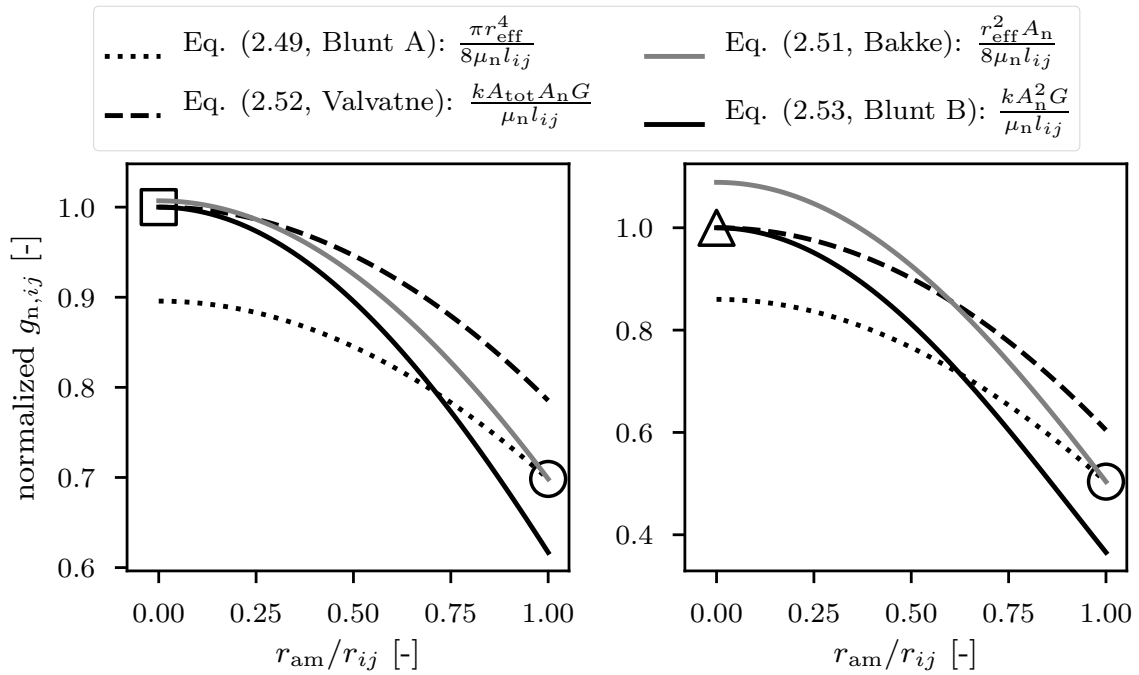


Figure 2.7 – Non-wetting phase conductances. Comparison of normalized non-wetting phase conductances for a square (left) and equilateral triangle (right) throat cross-section as given by Eqs. (2.49) to (2.53).

2.4.3 Model concepts for two-phase flow

Using the constitutive relations or local rules explained in the previous section, flow and transport can be simulated on a network. This is rather straightforward for single-phase flow whereas the situation becomes more complex if multiple phases are involved. This section briefly summarizes the different modeling approaches for two-phase flow

described in the literature. Such pore-network models can be generally divided into *quasi-static* and *dynamic models*.

Quasi-static PNM The first type of pore-network models is based on the assumption that the fluids within the pore space are at rest or, in other words, that there is no pressure gradient within the individual fluid phases. This implies that there is a constant capillary pressure throughout the entire fluid-fluid interface which corresponds to an externally applied global capillary pressure. A drainage or imbibition process can be modeled by incrementally increasing or decreasing this global pressure difference which will result in discrete saturation changes, corresponding to equilibrium states. Since fluid flow is not considered, only the critical threshold capillary pressures described in Section 2.4.2 are relevant for quasi-static models. Fluid configurations between the equilibrium states can not be modeled.

Drainage corresponds to an *invasion percolation* process where the bonds (throats) of the network are filled subsequently based on the ascending order of the entry capillary pressures, under the constraint that only throats adjacent to already filled throats or the inlet of the domain may be invaded. Invasion percolation also holds for imbibition with piston-type advance but here, the sites (pore bodies) are the limiting elements which means that smaller pores and their neighboring throats will be filled first. In contrast to invasion percolation, *percolation* allows a pore filling throughout the entire domain, regardless whether the newly filled element is connected to an already filled one or not. This corresponds to imbibition with layer-swelling which assumes a globally connected wetting phase via the pore throat corners [Blunt, 2017]. Quasi-static models have been used successfully for the prediction of rock properties such as capillary pressure-saturation curves [e.g., Oren et al., 1998, Valvatne and Blunt, 2004], but they are limited to situations where equilibrium conditions can be safely assumed or capillary forces dominate the system. This is given for low *capillary numbers*,

$$Ca = \frac{\mu v}{\gamma}, \quad (2.54)$$

where μ and v are the dynamic viscosity and the specific bulk flow rate, i.e., *Darcy* velocity (Section 2.3), of the invading phase and γ is the interfacial tension.

Dynamic PNM Dynamic pore-network models account for time-dependent phase displacement processes and are capable of modeling non-equilibrium capillary pressure states under the consideration of the fluid phases' viscosities. Dynamic models solve for pressure fields and phase fluxes based on the conservation of mass or volume, in close analogy to conventional Darcy-type models. Given their highly non-linear behavior and the requirement to capture both very slow and fast displacement processes, dynamic models are computationally more complex and resource intensive than quasi-static models [Blunt, 2017]. Joekar-Niasar and Hassanizadeh [2012a] extensively review the different types of solution strategies for dynamic two-phase pore-network models. They discern two general types of dynamic models: the first one assigns a *single pressure* to each pore body [e.g., Koplik and Lasseter, 1985, Mogensen and Stenby, 1998, Al-Gharbi and Blunt, 2005], assuming either the exclusive presence of a single phase or the concept of an equivalent pressure that accounts for both phases. While this approach decreases the computational complexity of the problem, Al-Gharbi and Blunt [2005] observed inconsistencies with respect to equivalent quasi-static simulation results for networks with angular cross sections. The second type of algorithm solves for an individual pressure field for each phase. This type of *two-pressure model* was first introduced by Thompson [2002], following a sequential solution strategy based on a decoupling between pressure and saturation and thus a faster solution of the linearized problems. This is very similar to the *IMPES* (implicit pressure, explicit saturation) method widely used in reservoir models [e.g., Chen et al., 2004]. Having solved for the pressures, the saturation field is updated explicitly, which requires very small time steps in order to maintain numerical stability. However, no close match to quasi-static results could be achieved and the method was unsuited for very low Ca . This was improved by Joekar-Niasar et al. [2010a] who introduced a semi-implicit saturation update in order to account for the highly non-linear nature of the processes. The model has found application in a number of other works [e.g., Qin, 2015, Khayrat and Jenny, 2017]. However, the efficiency of the model is still limited by the maximal admissible time step size which is governed by the filling dynamics of the pores at the saturation front [Bierbaum, 2019].

3 Conceptual and numerical models for the individual sub-domains

This chapter explains the mathematical models and the numerical discretization schemes used for the individual sub-domains. It is followed by a description of the interface conditions required for the coupling of the sub-models in Chapter 4 and an elaboration of the coupled model’s implementation in the open-source simulator DuMu^x (see Chapter 5). As shown in Fig. 3.1, the coupled model comprises up to three sub-domains: the free-flow domain Ω^{FF} , the interface region of the porous medium Ω^{PNM} and an optional bulk porous medium domain Ω^{REV} with low process activity.

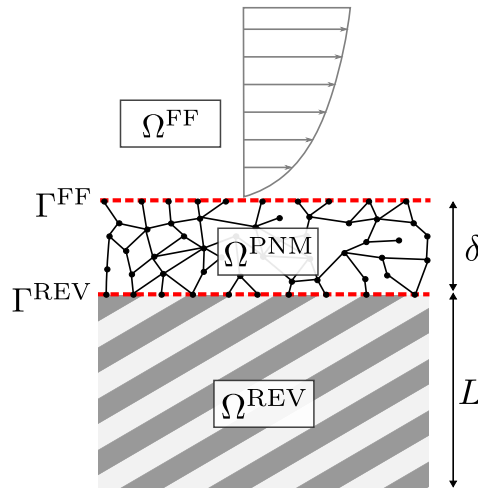


Figure 3.1 – Conceptual coupled model. Sketch of the coupled model comprising the three sub-domains Ω^{FF} , Ω^{PNM} and Ω^{REV} . The latter domain is optional. The domains are coupled at the interfaces Γ^{FF} and Γ^{REV} . δ and L are length scales.

Ω^{PNM} represents a “thin” interface region separating Ω^{FF} and Ω^{REV} , hence $\delta \ll L$. The thickness δ strongly depends on the coupled system under consideration and should

be determined experimentally or by means of a high-resolution simulation. It should probably at least cover the extent of an REV to meet the requirements of a “non-simple interface” [Hassanizadeh and Gray, 1989]. In future work, the possibility of estimating δ based on characteristics of the free flow (such as the boundary layer thickness) and the bulk porous medium (such as permeability or porosity) could be assessed. We assume that δ is in the order of several pore diameters.

The bulk porous medium domain Ω^{REV} is optional. As explained later in Section 4.2, formulating physically consistent coupling conditions between Ω^{PNM} and Ω^{REV} is challenging and not the focus of this work where we rather concentrate on the coupling between Ω^{FF} and Ω^{PNM} . We nevertheless present a first, somewhat tentative set of coupling conditions for the two porous-media models in the hope of providing a foundation on which future work can build.

The conceptual models and numbers of fluid phases considered in each sub-domain are:

- Ω^{FF} : (Navier-)Stokes, single-phase flow (1p)
- Ω^{PNM} : pore-network model, single-phase or two-phase flow (1p or 2p)
- Ω^{REV} : Darcy, single-phase or two-phase flow (1p or 2p)

Component transport and non-isothermal flow can be considered for all sub-domains. The fluid phases’ physical properties, such as density and viscosity, can be solution-dependent. The models are implemented in a way such that the influence of gravity can be incorporated or neglected. For all numerical results presented in this work, gravity is neglected.

Furthermore, we always consider laminar flow regimes in all sub-domains with creeping flow in the porous medium (Ω^{FF} and Ω^{REV}) while Re can be greater than one in Ω^{FF} .

A monolithic coupling approach (see Chapter 5) is followed in this work and the fully implicit backward Euler method is used for discretizing the coupled model in time. We therefore do not address temporal discretization for the individual sub-models. We employ a *Newton-Raphson* scheme to solve the potentially non-linear system of equations.

Treatment of solution-dependent parameters (secondary variables) All balance equations in the following sections are formulated in a general form such that fluid properties like density ϱ , viscosity μ , specific internal energy u , specific internal enthalpy h , heat conductivity λ or diffusion coefficients D do not have to be constant but may depend on the system's state, i.e., the current values of the respective primary variables. We will specify for each numerical example shown in Chapters 7 and 8 whether constant or solution-dependent quantities are used.

In order to avoid repetition, we briefly describe here how these solution-dependent parameters (secondary variables) are treated. We employ the `fluidsystem` framework of DuMu^x [Lauser, 2012] (see Chapter 5) which provides all necessary constitutive relations (see Chapter 2) for a wide range of different substances and mixtures. These may be either equations of state such as the *Ideal Gas Law* (Eq. (2.7)) or other supplementary empirical equations as well as tabulated values such as the industry standard IAPWS [Wagner and Pruß, 2002] for water.

3.1 (Navier-)Stokes model (free flow)

As explained above, only one single phase may be present in Ω^{FF} . If, for instance, air flow over a partly water-saturated soil is considered, water may only enter the free-flow region in gaseous form. For brevity, we neglect the phase subscript α in this section.

3.1.1 Conceptual model

Momentum balance The free flow in sub-domain Ω^{FF} is governed by the Navier-Stokes equations. The general transient and compressible form of the momentum balance for a single Newtonian fluid phase (e.g., gas or liquid) is given by

$$\frac{\partial(\varrho \mathbf{v})}{\partial t} + \nabla \cdot (\varrho \mathbf{v} \mathbf{v}^T) = \nabla \cdot [\mu(\nabla \mathbf{v} + \nabla \mathbf{v}^T) - \frac{2}{3}\mu(\nabla \cdot \mathbf{v})\mathbf{I}] - \nabla p + \varrho \mathbf{g} + \mathbf{f} . \quad (3.1)$$

Here, ϱ and $\mu = \varrho \nu$ are the phase mass density and dynamic viscosity while \mathbf{v} and p are the phase velocity and pressure. The dilatation term $\frac{2}{3}\mu(\nabla \cdot \mathbf{v})\mathbf{I}$ [Truckenbrodt, 1996] is neglected in this work. \mathbf{g} is the gravitational acceleration which can be set to zero

if gravity shall be neglected. \mathbf{f} represents an additional volume force which is usually zero.

Equation (3.1) simplifies to the stationary Stokes equations for creeping flow when neglecting the temporal derivative and the advective momentum flux term:

$$\nabla \cdot [\mu(\nabla \mathbf{v} + \nabla \mathbf{v}^T)] - \nabla p + \varrho \mathbf{g} + \mathbf{f} = 0 . \quad (3.2)$$

Stokes flow in channel-type domains with a slit-like cross section, such as Hele-Shaw cells with high aspect ratios between channel height h_Ω and width w , may be modeled on a two-dimensional grid, which drastically reduces the computational cost. Assuming a parabolic flow profile along the omitted coordinate's axis, Flekkøy et al. [1995] proposed a drag term which accounts for the wall friction of the virtual frontal and rearward boundary:

$$\mathbf{f}_{\text{drag}} = -c \frac{\mu}{h_\Omega^2} \mathbf{v} . \quad (3.3)$$

h_Ω is the virtual height of the model domain while c is a constant which determines whether the maximum velocity at the central plane of the channel at $0.5h_\Omega$ ($c = 8$) or the height-averaged one ($c = 12$) is recovered. This approach has been applied successfully for a number of different applications [Venturoli and Boek, 2006, Laleian et al., 2015, Kunz et al., 2015, Class et al., 2020] and provides the best accuracy for $h_\Omega \ll w$, as also shown later in Section 7.1.3. In the following, we will refer to this approach as *quasi-3D model*.

Mass/mole balance For flow of a pure fluid, the continuity equation

$$\frac{\partial(\varrho)}{\partial t} + \nabla \cdot (\varrho \mathbf{v}) = q \quad (3.4)$$

closes the system of equations given by Eq. (3.1) or Eq. (3.2), with q denoting a mass sink or source term.

For compositional flow, one molar balance equation is solved for each component κ :

$$\frac{\partial(x^\kappa \varrho_{\text{mol}})}{\partial t} + \nabla \cdot (x^\kappa \varrho_{\text{mol}} \mathbf{v} + \mathbf{j}_{\text{diff,mol}}^{\kappa,\text{FF}}) = q_\alpha^\kappa . \quad (3.5)$$

q^κ is a molar sink or source term while $\mathbf{j}_{\text{diff,mol}}^{\kappa,\text{FF}}$ is the diffusive molar flux, which is approximated by Fick's first law (see Eq. (2.12)) here:

$$\mathbf{j}_{\text{diff,mol}}^{\kappa,\text{FF}} = -\frac{1}{M^\kappa} \varrho D^\kappa \nabla X^\kappa . \quad (3.6)$$

Note that the mass-based form of Fick's first law is used because Eq. (3.1) yields a mass-averaged bulk velocity [Taylor and Krishna, 1993]. Therefore, the diffusive mass flux needs to be converted into a molar flux by division by M^κ .

Energy balance Non-isothermal systems require the formulation of an energy balance:

$$\frac{\partial(\varrho u)}{\partial t} + \nabla \cdot (h \varrho \mathbf{v}) + \sum_{\kappa} \nabla \cdot (\mathbf{j}_{\text{diff,mol}}^{\kappa,\text{FF}} h^\kappa) - \nabla \cdot (\lambda \nabla T) = q^e . \quad (3.7)$$

The storage term includes the solution-dependent specific internal energy u while the advective second term considers the specific phase enthalpy,

$$h = \sum_{\kappa} X^\kappa h^\kappa , \quad (3.8)$$

where h^κ is the specific enthalpy of a phase consisting only of component κ . $\mathbf{j}_{\text{diff,mol}}^{\kappa,\text{FF}} h^\kappa$ takes into account the molar diffusive energy transport. For non-compositional systems, this term is zero and $h = h^\kappa$.

The third term describes the conductive energy flux via Fourier's law (see Eq. (2.15)), where λ is the phase heat conductivity and T the phase temperature. q^e is an energy sink or source term.

3.1.2 Numerical model

The free-flow model is discretized in space using a staggered-grid finite volume approach, also known as MAC scheme [Harlow and Welch, 1965], which provides inherently stable and oscillation-free solutions without the need of any stabilization techniques [Versteeg and Malalasekera, 2007]. As shown in Fig. 3.2, scalar quantities like pressure, density or mole fractions are stored at the centers of the control volumes C of the primal grid \mathcal{G} , while the velocity degrees of freedom are located at the primary cells' faces around which dual-grid (\mathcal{G}^*) control volumes $C_{\{x,y,z\}}^*$ are constructed. Figure 3.2 shows a two-dimensional grid with C_x^* and C_y^* only.

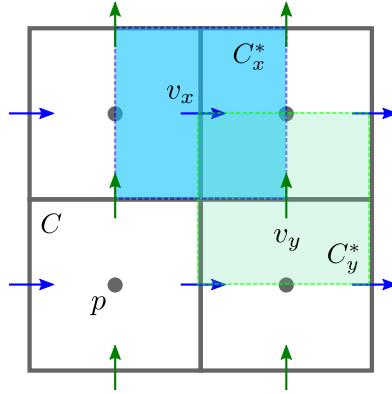


Figure 3.2 – Illustration of the staggered-grid scheme. Pressure degrees of freedom are located at the primal grid cell centers. Velocity degrees of freedom live on the primal grid's cell faces. The control volume for v_x is marked blue, the one for v_y green.

We refer to Schneider et al. [2020] for details on the discretized form of Eq. (3.1). The primary variables of the free-flow model are p and \mathbf{v} , supplemented by T and x^κ (for each component κ) in case of compositional non-isothermal systems.

3.2 Pore-network model (interface region)

In principle, the same balance equations already described for free flow also hold for the pore-network model employed in the interface region of the coupled model. Here, we present the semi-discrete equations applied to the lower-dimensional network elements. Fluxes are evaluated on throats while storage terms are located on the pore bodies on which also all primary variables are defined. In this work, we assume a constant and rigid pore geometry, i.e., no precipitation or dissolution of solid material [e.g., Raouf et al., 2012, Nogues et al., 2013] is considered. A summary of all primary variables for the different pore-network model varieties used in this work is given at the end of this section. Figure 3.3 summarizes all relevant pore body and pore throat dimensions.

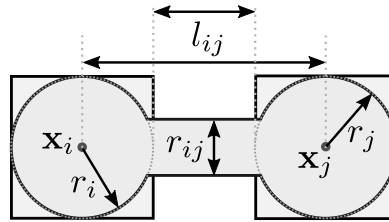


Figure 3.3 – Pore-network model entities. Schematic drawing of a pore throat ij and two pore bodies i and j with centers \mathbf{x}_i and \mathbf{x}_j . For cubic pore bodies, r_i and r_j correspond to the inscribed pore body radii. The length of the pore throat l_{ij} can optionally include the two adjacent pore body radii, depending on whether the pressure drop within the pore bodies is considered or not. r_{ij} is the pore throat (inscribed) radius.

3.2.1 Conceptual model for single-phase flow

Momentum balance As mentioned in Section 2.4.2 and in Appendix B, standard pore-network models consider a one-dimensional form of the stationary Stokes equations under the assumption of fully developed stationary, creeping laminar flow ($Re < 1$):

$$v_{ij} = \frac{1}{A_{ij}} Q_{ij} = \frac{1}{A_{ij}} g_{ij} (p_i - p_j + \Psi) . \quad (3.9)$$

The averaged phase velocity v_{ij} within throat ij is proportional to the discrete phase pressure difference between pore bodies i and j and a conductance term g_{ij} depending

on the throat geometry and the fluid viscosity (see Eq. (2.37)). The influence of gravity,

$$\Psi = \varrho \mathbf{g}(\mathbf{x}_i - \mathbf{x}_j) , \quad (3.10)$$

with $\mathbf{x}_i - \mathbf{x}_j$ being the distance vector between the centers of pore bodies i and j is usually neglected, as we do in this work.

An extensive discussion of g_{ij} can be found in Section 2.4.2. Q_{ij} and A_{ij} are the absolute phase volumetric flow and the phase cross-sectional area within the throat, which equals the entire throat cross-sectional area for single-phase flow.

Mass/mole balance For pure single-phase flow without component transport, a mass balance equation is formulated for each pore body i :

$$V_i \frac{\partial(\varrho_i)}{\partial t} + \sum_j (\varrho Q)_{ij} = (Vq)_i . \quad (3.11)$$

V_i is the pore body volume and the advective mass flow $(\varrho Q)_{ij}$ through throat ij can be based on the fluid phase density ϱ either of the upstream pore body i or j (upwinding) or on the respective averaged value. q_i is a mass sink or source term defined on pore body i .

For compositional systems, we formulate a mole balance for each component κ on each pore body i :

$$V_i \frac{\partial((x^\kappa \varrho_{\text{mol}})_i)}{\partial t} + \sum_j (x^\kappa \varrho_{\text{mol}} Q)_{ij} + \sum_j \left(j_{\text{diff,mol}}^{\kappa,\text{PNM}} A \right)_{ij} = (Vq^\kappa)_i . \quad (3.12)$$

As before, $(x^\kappa \varrho_{\text{mol}} Q)_{ij}$ can be evaluated either by upwinding or averaging. The discrete molecular diffusive flux through pore throat ij is given by Fick's first law:

$$j_{\text{diff,mol},ij}^{\kappa,\text{PNM}} = \frac{1}{M^\kappa} \frac{\varrho_i + \varrho_j}{2} \frac{D_i^\kappa + D_j^\kappa}{2} \frac{X_i^\kappa - X_j^\kappa}{l_{ij}} . \quad (3.13)$$

Here, D_i^κ is the molecular diffusion coefficient for component κ in pore body i , while X_i^κ is the respective mass fraction. The throat's length is given by l_{ij} .

Energy balance An energy balance is needed for non-isothermal systems:

$$V_i \frac{\partial((\varrho u)_i)}{\partial t} + \sum_j (\varrho h Q)_{ij} + \sum_j \left[A_{ij} \sum_\kappa \left(j_{\text{diff,mol}}^{\kappa,\text{PNM}} h^\kappa \right)_{ij} \right] + \sum_j \frac{\lambda_i + \lambda_j}{2} \frac{T_i - T_j}{l_{ij}} A_{ij} = (V q^e)_i . \quad (3.14)$$

The convective heat flow rate $(\varrho h Q)_{ij}$ is evaluated either by upwinding or averaging of the fluid density ϱ and specific phase enthalpy h (see Eq. (3.8)). q_i^e is a heat sink or source term defined on pore body i . The molecular diffusive energy transfer, which is zero for non-compositional systems, is taken into account by $j_{\text{diff,mol}}^{\kappa,\text{PNM}} h^\kappa$.

Note that only energy fluxes within the pore space (the fluid) are balanced here.

3.2.2 Conceptual model for two-phase flow

Momentum balance For two-phase flow, a momentum balance is formulated for each phase α :

$$v_{\alpha,ij} = \frac{1}{A_{\alpha,ij}} Q_{\alpha,ij} = \frac{1}{A_{\alpha,ij}} g_{\alpha,ij} (p_{\alpha,i} - p_{\alpha,j} + \Psi_\alpha) . \quad (3.15)$$

$A_{\alpha,ij}$ is the cross-sectional area of phase α within throat ij . The phase-specific conductance factor $g_{\alpha,ij}$ depends not only on the throat geometry and the fluid properties but also on the local phase distribution within the throat, i.e., the capillary pressure, as described in detail in Section 2.4.2. We neglect the influence of gravity $\Psi_\alpha = \varrho_\alpha \mathbf{g}(\mathbf{x}_i - \mathbf{x}_j)$ also for two-phase flow. If only one phase is present in the throat, the respective single-phase conductance value for the given throat geometry and fluid is used.

Mass/mole balance For immiscible fluids, one total mass balance is formulated for each phase α :

$$V_i \frac{\partial((\varrho_\alpha S_\alpha)_i)}{\partial t} + \sum_j (\varrho_\alpha Q_\alpha)_{ij} = (V q_\alpha)_i . \quad (3.16)$$

$S_{\alpha,i}$ is the local saturation in pore body i . A local capillary pressure-saturation relation $p_{c,i}(S_{w,i})$ (see Section 2.4.2) and $S_w + S_n = 1$ (Eq. (2.18)) are used to close the system.

If compositional two-phase flow is considered, a component balance is required for each component κ :

$$\begin{aligned} V_i \frac{\partial(\sum_\alpha (x_\alpha^\kappa \varrho_{\text{mol},\alpha} S_\alpha)_i)}{\partial t} + \sum_\alpha \sum_j (x_\alpha^\kappa \varrho_{\text{mol},\alpha} Q_\alpha)_{ij} \\ + \sum_\alpha \sum_j \left(j_{\text{diff,mol},\alpha}^{\kappa,\text{PNM}} A_\alpha \right)_{ij} = (V q^\kappa)_i . \end{aligned} \quad (3.17)$$

The diffusive fluxes are again described by Fick's first law:

$$j_{\text{diff,mol},\alpha,i,j}^{\kappa,\text{PNM}} = \frac{1}{M^\kappa} \frac{\varrho_{\alpha,i} + \varrho_{\alpha,j}}{2} \frac{D_{\alpha,i}^\kappa + D_{\alpha,j}^\kappa}{2} \frac{X_{\alpha,i}^\kappa - X_{\alpha,j}^\kappa}{l_{ij}} . \quad (3.18)$$

The constitutive relations Eqs. (2.7) to (2.11) and Eq. (2.4) close the system of equations, i.e., phase transfer processes such as evaporation or condensation are not modeled explicitly [Nuske, 2014], but implicitly accounted for under the assumption of a local thermodynamic equilibrium per pore body [Helmig, 1997].

Numerical problems arise if one of the phases vanishes, e.g., when the drying of soil is considered, as the two-phase system degenerates and S_α and x_α^κ of the vanished phase lose their physical meaning. A possible solution strategy is switching the local set of primary variables such that they remain physically meaningful [Class et al., 2002]. We will refer to this as *PVS* (primary variable switch) model in the remainder of the text. The mole fractions of the non-present phase α , though devoid of physical meaning, are still kept as secondary variables determined according to Section 2.2.3 and used as switching criterion:

$$\text{both phases present : phase } \alpha \text{ vanishes if } S_\alpha \leq 0 \quad (3.19a)$$

$$\text{only wetting phase w present : n appears if } \sum_\kappa x_n^\kappa \geq 1 \quad (3.19b)$$

$$\text{only non-wetting phase n present : w appears if } \sum_\kappa x_w^\kappa \geq 1 . \quad (3.19c)$$

PVS models can suffer from decreased numerical convergence behavior and oscillations if the switch is triggered and the number of present phases is about to change locally [Class and Helmig, 2002].

Another potentially more stable but computationally more involved approach requires solving for an additional constraint for each phase α [Lauser et al., 2011, Lauser, 2014]:

$$S_\alpha \left(1 - \sum_\kappa x_\alpha^\kappa \right) = 0 \quad \wedge \quad 1 - \sum_\kappa x_\alpha^\kappa \geq 0 \quad \wedge \quad S_\alpha \geq 0 . \quad (3.20)$$

This *NCP* (non-linear complementarity problem) model has a fixed set of primary variables which also includes the fugacities f^κ of all components κ . Eq. (3.20) is solved in terms of

$$\min(S_\alpha, 1 - \sum_\kappa x_\alpha^\kappa) = 0 \quad (3.21)$$

in this work, but other conditions, such as the *Fischer-Burmeister* [Fischer, 1992] function, fulfill Eq. (3.20), too. Equation (3.21) is piecewise linear but not continuously differentiable, which may pose further numerical challenges. Nevertheless, the NCP model can be superior to the PVS model for certain problem cases with a high degree of phase transition activity on the REV scale [Lauser et al., 2011]. We will therefore also compare the two concepts, applied to the pore-network model, in this work.

Table 3.1 summarizes the different sets of primary variables for all pore-network model varieties, including the PVS and the NCP model.

Energy balance The energy balance is given by:

$$\begin{aligned}
& V_i \frac{\partial (\sum_{\alpha} (\varrho_{\alpha} u_{\alpha} S_{\alpha})_i)}{\partial t} + \sum_{\alpha} \sum_j (\varrho_{\alpha} h_{\alpha} Q_{\alpha})_{ij} \\
& + \sum_{\alpha} \sum_j \left[A_{\alpha,ij} \sum_{\kappa} \left(j_{\text{diff,mol},\alpha}^{\kappa, \text{PNM}} h_{\alpha}^{\kappa} \right)_{ij} \right] \\
& + \sum_{\alpha} \sum_j \frac{\lambda_{\alpha,i} + \lambda_{\alpha,j}}{2} \frac{T_i - T_j}{l_{ij}} A_{\alpha,ij} = (Vq^e)_i .
\end{aligned} \tag{3.22}$$

For compositional systems, the molecular diffusive energy transport is taken into account by $j_{\text{diff,mol},\alpha}^{\kappa, \text{PNM}} h_{\alpha}^{\kappa}$. This flux is zero for immiscible fluids. In analogy to Eq. (3.8), the specific phase enthalpies depend on the composition:

$$h_{\alpha} = \sum_{\kappa} X_{\alpha}^{\kappa} h_{\alpha}^{\kappa} . \tag{3.23}$$

h_{α}^{κ} is the specific enthalpy of a phase purely consisting of component κ . $h_{\text{g}}^{\kappa} > h_{\text{l}}^{\kappa}$, hence the temperature drop during evaporation.

3.2.3 Summary of pore-network models and primary variables

Table 3.1 summarizes the sets of primary variables and balance equations for the different kinds of pore-network models considered in this work. Each model can be either isothermal or non-isothermal (ni), which extends the set of primary variables by T , assuming local thermal equilibrium between all fluid phases.

The single-phase flow model (1pnc) with n_{Comp} components features p and $n_{\text{Comp}} - 1$ mole fractions x^{κ} as primary variables, excluding the mole fraction of the phase's major component $\kappa^1 = \kappa^{\text{major}}$.

The PVS model has a different local (per pore body) set of primary variables for each phase state: If both phases are present (A), p_{n} , S_{w} and $n_{\text{Comp}} - 2$ mole fractions are the primary variables. This changes if one of the phases vanishes (B and C) and all the present phase's minor components and p_{n} become the new primary variables. We

require $p_c(S_w = 1) = 0$ by adapting Eq. (2.35) accordingly, thus $p_n = p_w$ if only the wetting phase is present.

Table 3.1 – Primary variables and balance equations of the different pore-network models. 1p: single-phase flow. 1pnc: single-phase flow with n_{Comp} components. 2p: two-phase flow. 2pnc PVS: two-phase flow with n_{Comp} components and primary variable switch; A: both phases present; B: only non-wetting phase present; C: only wetting-phase present. 2pnc NCP: two-phase flow with n_{Comp} components and non-linear constraint. κ^{major} is the major component of phase α . Non-isothermal (ni) models additionally feature the temperature (T) as primary variable.

model	primary variables	balance equations
1p(ni)	$p, (T)$	3.11, (3.14)
1pnc(ni)	$p, \{x^{\kappa_2}, \dots, x^{\kappa_{nC}}\}, (T)$	3.12, (3.14)
2p(ni)	$p_n, S_w, (T)$	3.16, (3.22)
2pnc(ni) PVS	A: $p_n, S_w, \{x_w^{\kappa_3}, \dots, x_w^{\kappa_{nC}}\}, (T)$	3.17, (3.22)
	B: $p_n, \{x_n^{\kappa_2}, \dots, x_n^{\kappa_{nC}}\}, (T)$	
	C: $p_n, \{x_w^{\kappa_2}, \dots, x_w^{\kappa_{nC}}\}, (T)$	
2pnc(ni) NCP	$p_n / p_w, S_w, \{f^{\kappa_1}, \dots, f^{\kappa_{nC}}\}, (T)$	3.17, 3.20, (3.22)

Example: We consider a liquid/gas two-phase system with *water* and the pseudocomponent *air* as components (2p2c). We assume that the liquid phase is the wetting phase w with water as the main component, while air is the main component of the non-wetting gas phase n. For state A (both phases present), the primary variables are p_n and S_w (there is no third component). For state B (only gas phase n present), the primary variables are p_n and x_n^{water} . For state C (only liquid phase w present), the primary variables are p_n and x_w^{air} .

The original NCP model of Lauser et al. [2011] has a permanently fixed set of primary variables which is p_n, S_w and the fugacities f^κ of all components. Applied to the above-mentioned example, this means that the number of primary variables is increased by two, compared to the PVS model.

During preliminary numerical studies on evaporation (Chapter 8), the Newton algorithm failed to converge for S_w approaching zero. To remedy this, we also introduced a primary variable switch for the NCP model, replacing p_n by p_w as primary variable if S_w falls below a given threshold and vice versa. We found that this very simple

mechanism does not impair the numerical robustness of the model, in contrast to the PVS model where initial saturations of the appearing phases need to be guessed rather arbitrarily in case of a switch event [Class et al., 2002]. For sake of simplicity, we will continue to use the term *NCP model* even though the modified version of it is meant.

3.2.4 Numerical model

The *Box* method [Huber and Helmig, 2000] is used to spatially discretize the pore-network model. This finite volume scheme is node centered, i.e., a control volume is associated to each grid node on which the balance equations are formulated. Each control volume is divided into sub-control volumes over the faces of which the fluxes are evaluated, which makes the scheme locally mass conservative. In the context of pore-network modeling, the one-dimensional grid elements represent the pore throats while the grid vertices correspond to the pore bodies. Figure 3.4 shows an example network with five pore bodies and five pore throats. Each pore body corresponds to a control volume which is split into n_{coord} sub-control volumes, with n_{coord} being the coordination number. Pore i is connected to four other pores and therefore features four sub-control volumes. The vertical line at the center of the throat ij is the sub-control volume face over which the flux between pore i and pore j is evaluated.

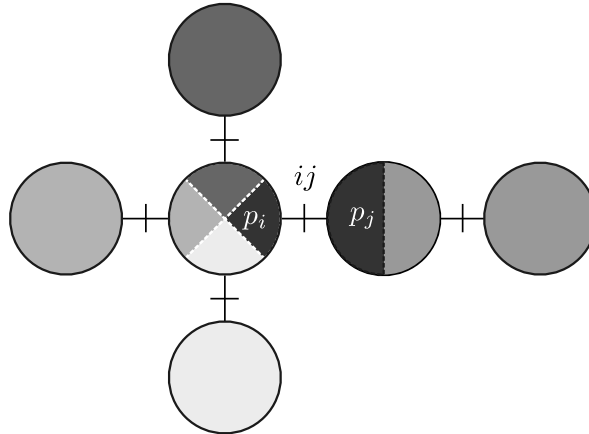


Figure 3.4 – Application of the Box scheme for pore-network modeling. The fluid pressures p are located at the centers of the pore bodies. Each pore body corresponds to a control volume, subdivided into n_{coord} sub-control volumes.

In the following, we will briefly discuss the numerical model for two-phase flow. A dynamic and fully coupled approach (see Section 2.4.3) is chosen such that both saturations and pressures are solved for simultaneously, using the Newton-Raphson method. The time step size is chosen adaptively based on the convergence behavior of the non-linear solver (see Eq. (5.2) in Chapter 5).

The highly non-linear and non-smooth nature of the constitutive laws (see Section 2.4.2) renders the numerical solution of two-phase problems challenging. After each Newton iteration, the invasion state of each throat is checked. If the throat was not invaded in the previous time step and if one of the capillary pressures of the adjacent pore bodies is greater than the entry capillary pressure $p_{c,e}$ (see Eq. (2.30)), the throat is marked as invaded and the set of constitutive laws for describing fluid flow is adapted accordingly. This means, e.g., that an initially water-filled rectangular throat might become invaded after a Newton iteration and its non-wetting phase conductance $g_{n,ij}$ jumps from zero to a certain value while the wetting phase conductance drastically decreases as the phase now retreats to the corners of the throat. The opposite process (snap-off) occurs if both of the pore-body capillary pressures fall below $p_{c,s}$ (see Eq. (2.34)) and the throat was invaded in the previous time step. If an invasion or snap-off event occurs, we force the Newton scheme to do at least one additional iteration before the solution is considered to be converged. Nevertheless, numerical instabilities, e.g., in the form of oscillating invasion/snap-off states within consecutive Newton iterations may occur, leading to failing time steps and a necessary decrease of the time step size (see Eq. (5.2)).

We therefore employ some measures aiming at the improvement of the numerical stability and accuracy of the scheme.

Regularization In analogy to REV-scale models [e.g., Fetzer, 2018], the local capillary-pressure saturation curve (see Eq. (2.35)) is regularized for very high and low saturations. The curve is further modified such that $p_{c,i}(S_{w,i} = 1) = 0$.

Limitation of admissible saturation change If the change of saturation within a pore body between two consecutive time steps is larger than a given threshold (e.g., 30%), the time step will be rejected and repeated with a reduced time step size.

Limitation of admissible deviation from entry capillary pressure at invasion event

If a pore throat gets invaded and the capillary pressure of the upstream pore body $p_{c,i}$ deviates by more than a given threshold from the throat's entry capillary pressure $p_{c,e}$ (e.g., 1%), the time step will be rejected and repeated with a reduced time step size. The rationale is that invasion events require small time steps to accurately describe the temporal evolution of the phase pressure change. If Δt is too large, $p_{c,i}$ will be considerable lower than $p_{c,e}$ due to a temporal peak of fluid flow directly after the invasion event which relaxes the system.

The latter two heuristic measures may lead to an increased number of rejected time steps during the occurrence of local invasion events but facilitate increased time step sizes during the rest of the simulation while maintaining an acceptable degree of accuracy.

3.3 Darcy-scale model (bulk porous medium)

Considering a standard REV-scale approach, the optional bulk porous domain is described by the same physical models employed for Ω^{PNM} (see Table 3.1). One or two phases may be present.

3.3.1 Conceptual model for single-phase flow

Momentum balance Darcy's law (Section 2.3) yields the REV-scale velocity which is a volume flux:

$$\mathbf{v} = -\frac{\mathbf{K}}{\mu}(\nabla p - \varrho \mathbf{g}) . \quad (3.24)$$

\mathbf{K} is the *intrinsic permeability* and a property of the porous medium alone. Since the latter may feature anisotropic (i.e., orientation-dependent) flow resistance, the permeability is a tensorial quantity in general.

Mass/mole balance The mass balance for a pure fluid includes the porosity Φ in the storage term:

$$\Phi \frac{\partial(\varrho)}{\partial t} + \nabla \cdot (\varrho \mathbf{v}) = q . \quad (3.25)$$

The same is true for the molar balances formulated for each component κ if a miscible system is considered:

$$\Phi \frac{\partial(x^\kappa \varrho_{\text{mol}})}{\partial t} + \nabla \cdot (x^\kappa \varrho_{\text{mol}} \mathbf{v} + \mathbf{j}_{\text{diff}}^{\kappa, \text{REV}}) = q^\kappa . \quad (3.26)$$

q and q^κ are sink or source terms.

Fick's first law yields the diffusive fluxes:

$$\mathbf{j}_{\text{diff}}^{\kappa, \text{REV}} = -\frac{1}{M^\kappa} D_{\text{pm}}^\kappa \varrho \nabla X^\kappa . \quad (3.27)$$

Energy balance We assume local thermal equilibrium for non-isothermal systems.

$$\Phi \frac{\partial(\varrho u)}{\partial t} + (1 - \Phi) \frac{\partial(\varrho_s c_s T)}{\partial t} + \nabla \cdot (h \varrho \mathbf{v}) - \nabla \cdot (\lambda_{\text{pm}} \nabla T) = q^e . \quad (3.28)$$

Here, the storage terms include both the fluid and solid phases' contributions. ϱ_s and c_s are the solid's density and heat capacity. The effective heat conductivity λ_{pm} (Eq. (2.20)) is given by Somerton et al. [1974]. In contrast to the models for Ω^{FF} and Ω^{PNM} , the contribution of the component enthalpy flux (see, e.g., Eq. (3.7)), is not treated explicitly for the bulk porous medium as it is already included in λ_{pm} [Class, 2007].

3.3.2 Conceptual model for two-phase flow

Momentum balance Darcy's extended law for two-phase flow,

$$\mathbf{v}_\alpha = - \frac{k_{r,\alpha} \mathbf{K}}{\mu_\alpha} (\nabla p_\alpha - \varrho_\alpha \mathbf{g}) , \quad (3.29)$$

yields an REV-scale velocity per phase α . The *relative permeability* $k_{r,\alpha}$ is a function of the saturation and incorporates the effect of fluids mutually blocking each other's pathways through the porous medium.

Mass/mole balance For non-compositional systems, a mass balance per phase α is formulated:

$$\Phi \frac{\partial(\varrho_\alpha S_\alpha)}{\partial t} + \nabla \cdot (\varrho_\alpha \mathbf{v}_\alpha) = q_\alpha . \quad (3.30)$$

Compositional systems require the formulation of a mole balance per component κ :

$$\Phi \frac{\partial(\sum_\alpha (x_\alpha^\kappa \varrho_{\text{mol},\alpha} S_\alpha))}{\partial t} + \sum_\alpha \nabla \cdot (x_\alpha^\kappa \varrho_{\text{mol},\alpha} \mathbf{v}_\alpha) + \sum_\alpha \nabla \cdot (\mathbf{j}_{\text{diff},\alpha}^{\kappa,\text{REV}}) = q^\kappa . \quad (3.31)$$

The diffusive flux is again given by Fick's first law:

$$\mathbf{j}_{\text{diff},\alpha}^{\kappa,\text{REV}} = -\frac{1}{M^\kappa} D_{\alpha,\text{pm}}^\kappa \varrho_\alpha \nabla X_\alpha^\kappa. \quad (3.32)$$

As already described for the two-phase pore-network model (Section 3.2.2), a capillary pressure-saturation relation $p_c(S_w)$ and $S_w + S_n = 1$ (Eq. (2.18)) are needed to close the system.

Energy balance Assuming local thermal equilibrium, the energy balance is given by

$$\Phi \frac{\partial(\sum_\alpha (\varrho_\alpha u_\alpha S_\alpha))}{\partial t} + (1 - \Phi) \frac{\partial(\varrho_s c_s T)}{\partial t} + \sum_\alpha \nabla \cdot (h_\alpha \varrho_\alpha \mathbf{v}_\alpha) - \nabla \cdot (\lambda_{\text{pm}} \nabla T) = q^e. \quad (3.33)$$

3.3.3 Numerical model

Like Ω^{PNM} (see Section 3.2.4), the bulk porous domain Ω^{REV} is spatially discretized using the Box method [Huber and Helmig, 2000]. For further details on applying this method on the REV scale, we refer to [e.g., Mosthaf et al., 2014].

Having discussed the individual sub-models, we will elaborate on the coupling conditions in the next chapter.

4 Coupling conditions

Appropriate coupling conditions are required to ensure the continuity of mass, momentum and energy at the interfaces between the sub-models [Hassanizadeh and Gray, 1989]. The following sections explain these conditions for the interface between free flow and pore-network model Γ^{FF} and the interface between the Darcy REV-scale model and the pore-network model Γ^{PNM} . The free-flow model always features single-phase flow and the phase index α is dropped when no ambiguity is imminent. Two fluid phases may exist in the pore-network model and the REV-scale model. The index α_{FF} corresponds to the phase present in the free-flow region. For instance, $\alpha_{\text{FF}} = \text{g}$ if evaporation from soil into a gas atmosphere is considered. The superscripts FF, PNM and REV refer to the interfacial quantities of the free-flow domain, the pore-network model and the Darcy model respectively. \mathbf{n} is a unit vector normal to the coupling interface, pointing outside the own model domain. For instance, all quantities of $[\rho \mathbf{v} \cdot \mathbf{n}]^{\text{FF}}$ correspond to the free-flow domain, evaluated at the coupling interface.

Figure 4.1 shows the three model domains and the two coupling interfaces.

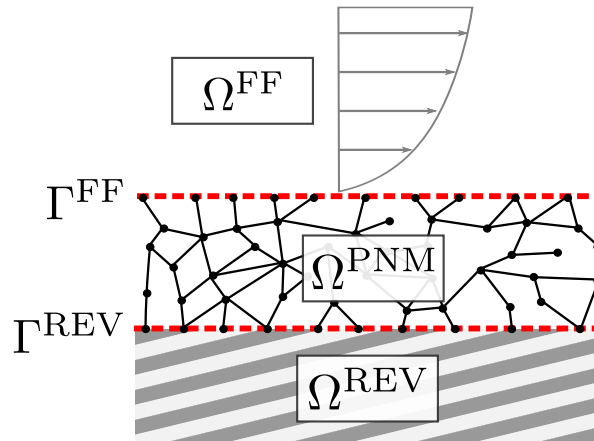


Figure 4.1 – Interfaces for coupling the sub-models. Γ^{FF} separates Ω^{FF} and Ω^{PNM} while Γ^{REV} separates Ω^{PNM} and Ω^{REV} .

All coupling conditions are formulated for creeping ($Re < 1$), laminar flow at the interfaces. We follow largely Mosthaf et al. [2011] with certain adaptations made to account for the pore-scale coupling. The spatial extent of Ω^{PNM} is briefly discussed in Chapter 3.

4.1 Free flow / pore-network model

REV-scale coupled models [e.g., Layton et al., 2002, Mosthaf et al., 2011] consider the exchange of mass, momentum and energy across the entire coupling interface Γ^{FF} , i.e., the common surface between the free-flow and porous-medium model. In contrast to that, the free-flow and the pore-network models are only coupled at discrete locations, the pore-scale coupling interfaces Γ_i^{FF} which are associated with each pore body i intersecting with the boundary of the free-flow domain (Fig. 4.2). These pore bodies are assumed to be cut in half by the interface and only the interior part of the volume is considered. We assume that the coordination number of pore bodies connected to the free-flow domain is always one, i.e., only one pore throat is connected to them.

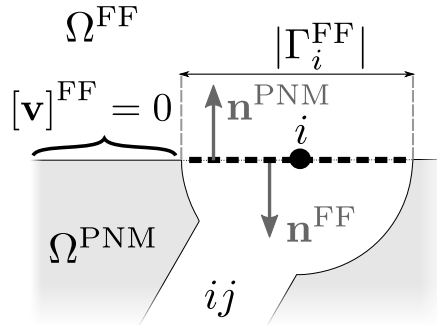


Figure 4.2 – Pore cut into halves at the interface. The discrete coupling interface Γ_i^{FF} (black dashed line) is associated to pore body i which is connected to a single throat ij . The unit normal vectors \mathbf{n} point towards the neighboring domain. We assume no-slip/no-flow conditions with $[\mathbf{v}]^{\text{FF}} = 0$ above the solid matrix shown in gray, next to the coupling pore.

At the location of solid grains (no intersecting pore body), a no-slip/no-flow condition for the free flow is assumed, as indicated for the gray solid part in Fig. 4.2.

Total mass balance For non-compositional systems, we require the continuity of the total mass flux across the interface:

$$[\varrho_{\alpha_{\text{FF}}} \mathbf{v}_{\alpha_{\text{FF}}} \cdot \mathbf{n}]^{\text{PNM}} = -[\varrho \mathbf{v} \cdot \mathbf{n}]^{\text{FF}} . \quad (4.1)$$

As explained earlier, the subscript α_{FF} is dropped for the free-flow model as there is only one phase. Any phase other than α_{FF} cannot leave or enter the pore-network model.

Equation (4.1) is reformulated in terms of an equivalent, discrete mass sink or source term for pore body i at the local interface Γ_i^{FF} :

$$[(Vq)_i]^{\text{PNM}} = \sum_{\sigma \in \Gamma_i^{\text{FF}}} [(\varrho \mathbf{v} \cdot \mathbf{n})_{\sigma} |\sigma|]^{\text{FF}} . \quad (4.2)$$

Here, the discrete free-flow velocities \mathbf{v} at the free-flow cell faces σ with normal \mathbf{n} pointing towards the interface are considered. $|\sigma|$ is the area of a free-flow cell face and $\sum_{\sigma \in \Gamma_i^{\text{FF}}} [|\sigma|]^{\text{FF}} = |\Gamma_i^{\text{FF}}|$. The density ϱ is determined by upwinding, i.e., either the free-flow or pore-network value is taken based on the direction of flow.

The implementation of Eq. (4.2) is visualized on the left pore body in Fig. 4.3. The free-flow grid cell sizes are chosen such that they are perfectly aligned with Γ_i^{FF} , i.e., they are flush with the borders of the interface pore. Any number > 0 of free-flow cells per boundary pore may be chosen.

Momentum balance We require mechanical equilibrium at the interface, yielding

$$\begin{aligned} & [(\varrho \mathbf{v} \mathbf{v}^T + p \mathbf{I} - \mu(\nabla \mathbf{v} + \nabla \mathbf{v}^T)) \cdot \mathbf{n}]^{\text{FF}} \\ & = - \left[(\varrho \mathbf{v} \mathbf{v}^T + p \mathbf{I} - \mu(\nabla \mathbf{v} + \nabla \mathbf{v}^T))_{\alpha_{\text{FF}}} \cdot \mathbf{n} \right]^{\text{PNM}} . \end{aligned} \quad (4.3)$$

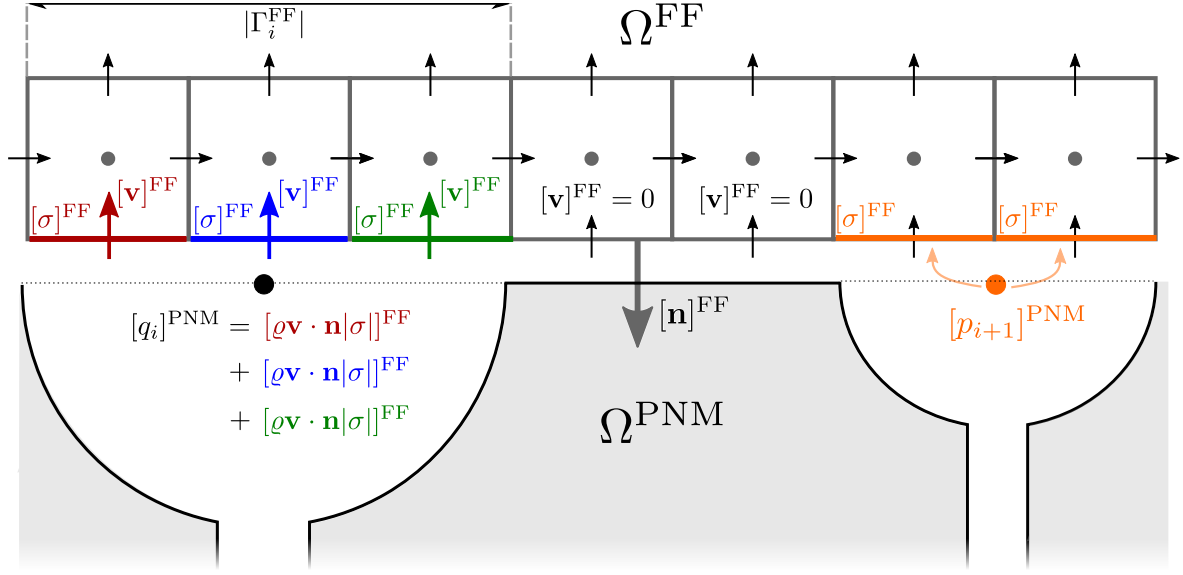


Figure 4.3 – Coupling free flow with the pore-network model. Implementation of the single-phase flow coupling conditions between the free-flow model and the pore-network model in normal direction of the coupling interface. One pore body i can be coupled to an arbitrary number of free-flow cell faces σ (here: three on the left and two on the right).

Assuming creeping flow ($Re < 1$) and the continuity of viscous forces across the interface, the coupling condition for the normal component of Eq. (4.3) simplifies to

$$[p]^{\text{FF}} = [p_{\alpha_{\text{FF}}}]^{\text{PNM}} \quad \text{on } \Gamma_i^{\text{FF}}. \quad (4.4)$$

We recall that Eq. (2.36), which yields the discrete volume flow per pore throat in the pore-network model, is based on the volume integration of the stationary Stokes equations as shown in Appendix B. Contrary to Darcy-type models [Whitaker, 1999, Layton et al., 2002], the pore body pressure of the pore-network model has thus the same physical meaning as the pressure of the free-flow model.

Equation (4.4) can be seen as a Neumann-type coupling condition for the free-flow momentum balance. As mentioned above, we assume the continuity of normal viscous forces at the interface. The term $[(\mu(\nabla \mathbf{v} + \nabla \mathbf{v}^T) \cdot \mathbf{n}) \cdot \mathbf{n}]^{\text{FF}}$ therefore still needs to be taken into account by the free-flow model, approximated only by quantities of Ω^{FF} ,

as the pore-network model does not readily provide any velocity gradient information. The implementation of Eq. (4.4) is illustrated on the right pore body in Fig. 4.3.

We consider two different approaches to account for the tangential momentum transfer from the pore-network model to the free-flow domain. The first, simple approach (Fig. 4.4a) [Weishaupt et al., 2019a] directly applies the tangential component of the pore-body interface velocity as slip condition for the free-flow domain:

$$[\mathbf{v} \cdot \mathbf{t}_k]^{\text{FF}} = \begin{cases} [\mathbf{v}_{\alpha\text{FF}} \cdot \mathbf{t}_k]^{\text{PNM}}, & k \in \{0, \dots, d-1\} \quad \text{on } \Gamma_i^{\text{FF}} \\ 0 & \text{else .} \end{cases} \quad (4.5)$$

\mathbf{t}_k , $k \in \{0, \dots, d-1\}$ is the basis of the interface's tangent plane.

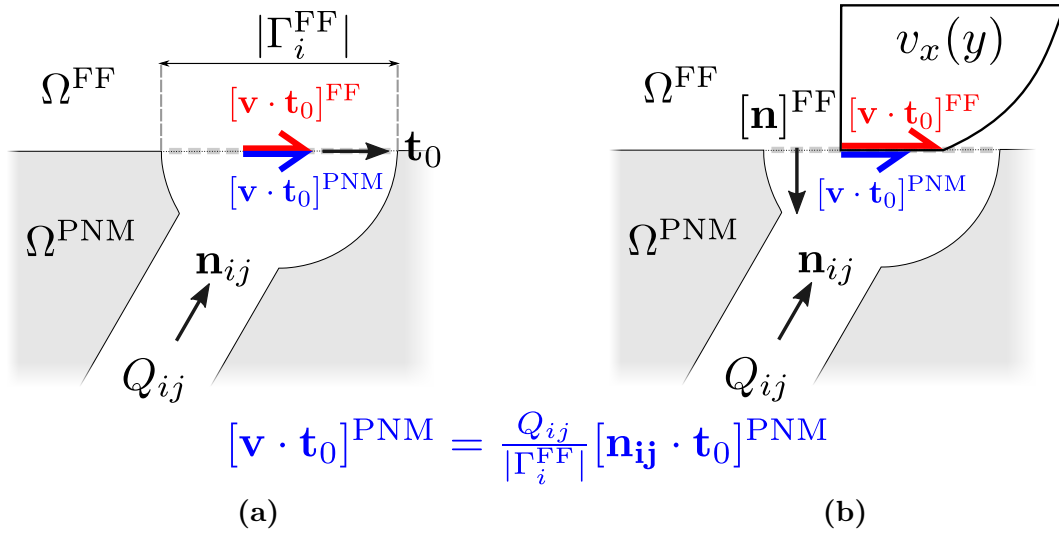


Figure 4.4 – Pore-local slip conditions. Illustration of the two possible interface conditions for $[\mathbf{v} \cdot \mathbf{t}_k]^{\text{FF}}$. Left: simple condition (Eq. (4.5)) assigning the pore-body tangential velocity at the interface directly. Right: slip condition allowing $[\mathbf{v} \cdot \mathbf{t}_k]^{\text{FF}} \neq [\mathbf{v}_{\alpha\text{FF}} \cdot \mathbf{t}_k]^{\text{PNM}}$ (Eq. (4.9)).

The tangential component of the pore-body interface velocity is approximated as

$$[\mathbf{v}_{\alpha\text{FF}} \cdot \mathbf{t}_k]^{\text{PNM}} = \frac{Q_{\alpha\text{FF},ij}}{|\Gamma_i^{\text{FF}}|} [\mathbf{n}_{ij} \cdot \mathbf{t}_k]^{\text{PNM}} . \quad (4.6)$$

$Q_{\alpha_{\text{FF}},ij}$ is the volume flow through pore throat ij while $|\Gamma_i^{\text{FF}}|$ is the area of the discrete coupling interface. \mathbf{n}_{ij} is a unit normal vector parallel to the throat's central axis and pointing towards the interface. Note that this is a simplification which does not take into account potential deflection effects of the fluid flow leaving the pore throat and entering the pore body (Fig. 4.4). We furthermore assume that phase α_{FF} completely occupies Γ_i^{FF} , neglecting potential two-phase effects directly at the interface. Note that Eq. (4.6) does not impair mass conservation as it is only used for the approximation of the tangential momentum transfer.

The disadvantage of this approach is that pore throats intersecting orthogonally with the interface ($\mathbf{n}_{ij} \perp [\mathbf{t}_k]^{\text{FF}}$) will always feature a no-slip condition with $[\mathbf{v}_{\alpha_{\text{FF}}} \cdot \mathbf{t}_k]^{\text{PNM}} = 0$ at the intersection since $[\mathbf{n}_{ij} \cdot \mathbf{t}_k]^{\text{PNM}} = 0$.

To remedy this, the second approach for the tangential momentum transfer condition (Fig. 4.4b) [Weishaupt et al., 2019b] approximates the slip velocity on Γ_i^{FF} by revisiting Eq. (4.3) and assuming the continuity of tangential shear stresses across the interface:

$$[(-\mu(\nabla \mathbf{v} + \nabla \mathbf{v}^T) \cdot \mathbf{n}) \cdot \mathbf{t}_k]^{\text{FF}} = [(\mu(\nabla \mathbf{v}_{\alpha_{\text{FF}}} + \nabla \mathbf{v}_{\alpha_{\text{FF}}}^T) \cdot \mathbf{n}) \cdot \mathbf{t}_k]^{\text{PNM}}. \quad (4.7)$$

Instead of trying to calculate the shear rate $\nabla \mathbf{v}_{\alpha_{\text{FF}}} + \nabla \mathbf{v}_{\alpha_{\text{FF}}}^T$ in the one-dimensional pore throats where only uniform, averaged fluxes along the center-line of the throats are defined, we propose a simple parametrization

$$[(-\nabla \mathbf{v} + \nabla \mathbf{v}^T) \cdot \mathbf{n}) \cdot \mathbf{t}_k]^{\text{FF}} = \beta_{\text{pore}} ([\mathbf{v} \cdot \mathbf{t}_k]^{\text{FF}} - [\mathbf{v}_{\alpha_{\text{FF}}} \cdot \mathbf{t}_k]^{\text{PNM}}) \quad (4.8)$$

in close analogy to the widely-used Beavers-Joseph interface slip condition for REV-scale models [Beavers and Joseph, 1967]. The main difference here is that the slip coefficient β_{pore} is now defined locally per local intersection Γ_i and not an averaged quantity of the entire porous medium's interface.

Our new coupling condition for the tangential component of the free-flow velocity thus reads

$$[\mathbf{v} \cdot \mathbf{t}_k]^{\text{FF}} = \begin{cases} v_{\text{slip},k} & \text{on pore throat ,} \\ 0 & \text{else ,} \end{cases} \quad (4.9)$$

with

$$v_{\text{slip},k} = \frac{1}{\beta_{\text{pore}}} [(-(\nabla \mathbf{v} + \nabla \mathbf{v}^T) \cdot \mathbf{n}) \cdot \mathbf{t}_k]^{\text{FF}} + [\mathbf{v}_{\alpha_{\text{FF}}} \cdot \mathbf{t}_k]^{\text{PNM}} . \quad (4.10)$$

We will numerically determine β_{pore} for various sizes of Γ_i , as shown later in Section 7.1.5. This approach may be comparable to the work of Bae and Kim [2016] who likewise used numerical data to determine an effective slip parameter, yet for non-creeping flow. We furthermore note that there exist analytical solutions to related problems, such as presented by Moffatt [1964] and Jeong [2001], which, however, often base on a number of assumptions and prerequisites that might not always be met in this work.

Chemical equilibrium and mole flux conservation For compositional flow, we require the conservation of the individual component fluxes across the interface for each component κ :

$$[(x^\kappa \varrho_{\text{mol}} \mathbf{v} + \mathbf{j}_{\text{diff,mol}}^\kappa)_{\alpha_{\text{FF}}} \cdot \mathbf{n}]^{\text{PNM}} = -[(x^\kappa \varrho_{\text{mol}} \mathbf{v} + \mathbf{j}_{\text{diff,mol}}^\kappa) \cdot \mathbf{n}]^{\text{FF}} . \quad (4.11)$$

As before, Eq. (4.11) is implemented as a sink or source term for component κ at interface pore body i :

$$[(Vq)_i^\kappa]^{\text{PNM}} = \sum_{\sigma \in \Gamma_i^{\text{FF}}} [(\{x^\kappa \varrho_{\text{mol}} \mathbf{v} + \mathbf{j}_{\text{diff,mol}}^\kappa\} \cdot \mathbf{n})_\sigma |\sigma|]^{\text{FF}} . \quad (4.12)$$

We assume local chemical equilibrium [Mosthaf et al., 2011] within a pore body and at the interface,

$$[X^\kappa]^{\text{FF}} = [X_{\alpha_{\text{FF}}}^\kappa]^{\text{PNM}} \quad \text{on } \Gamma_i^{\text{FF}}, \quad (4.13)$$

which serves as a Dirichlet-type coupling condition for the free-flow model.

As illustrated in Fig. 4.5, the diffusive molecular flux $\mathbf{j}_{\text{diff,mol}}^\kappa$ is approximated using the mass fraction gradient within the free-flow domain directly at the interface:

$$[\mathbf{j}_{\text{diff,mol}}^\kappa \cdot \mathbf{n}]^{\text{FF}} = -\frac{1}{M^\kappa} [D^\kappa \varrho]^{\text{FF}+1} \frac{[X^\kappa]^{\text{FF}} - [X^\kappa]^{\text{FF}+1}}{0.5[\Delta h]^{\text{FF}+1}}. \quad (4.14)$$

Here, the superscript $\text{FF} + 1$ denotes the quantities of the first free-flow grid cell adjacent to the interface, while $0.5[\Delta h]^{\text{FF}+1}$ is the distance between the interface and said grid cell's center. In the presence of multiple phases within the pore body at the interface, e.g., in the context of water evaporation, we assume that all phase-transfer processes occur within the pore body under local thermodynamic equilibrium. This means that liquid water vaporizes in the pore body and only the diffusive and advective flux of water vapor within the gas phase is considered for the mass transfer between the pore-network model and the free-flow model.

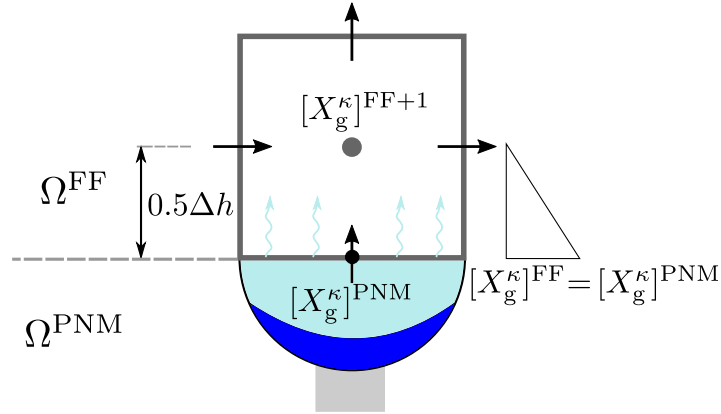


Figure 4.5 – Diffusion from pores. Implementation of the diffusive flux calculation for the coupling of free flow and the pore-network model. The liquid (dark blue) and gaseous (light blue) phase within the pore body are in thermodynamic equilibrium.

Energy balance For non-isothermal flow, we require the conservation of energy fluxes across the interface:

$$\begin{aligned} & \left[\left((h\rho\mathbf{v})_{\alpha_{\text{FF}}} + \sum_{\kappa} (\mathbf{j}_{\text{diff,mol}}^{\kappa} h^{\kappa})_{\alpha_{\text{FF}}} - \lambda_{\alpha_{\text{FF}}} \nabla T \right) \cdot \mathbf{n} \right]^{\text{PNM}} \\ & = - \left[\left(h\rho\mathbf{v} + \sum_{\kappa} (\mathbf{j}_{\text{diff,mol}}^{\kappa} h^{\kappa}) - \lambda \nabla T \right) \cdot \mathbf{n} \right]^{\text{FF}} . \end{aligned} \quad (4.15)$$

For non-compositional systems, the molecular diffusive energy transfer $\mathbf{j}_{\text{diff,mol}}^{\kappa} h^{\kappa}$ is zero.

Like the mass fluxes described above, the energy flux between the two sub-models is implemented in terms of an equivalent sink or source term for pore body i at the local interface Γ_i^{FF} :

$$[(Vq^e)_i]^{\text{PNM}} = \sum_{\sigma \in \Gamma_i^{\text{FF}}} \left[\left(\left\{ h\rho\mathbf{v} + \sum_{\kappa} (\mathbf{j}_{\text{diff,mol}}^{\kappa} h^{\kappa}) - \lambda \nabla T \right\} \cdot \mathbf{n} \right)_{\sigma} |\sigma| \right]^{\text{FF}} . \quad (4.16)$$

As discussed earlier in the context of diffusive mass exchange between the sub-models, we assume that the phase present in the free-flow domain α_{FF} fully occupies the coupling interface Γ_i^{FF} and therefore, all diffusive, conductive and convective energy transfer only occurs through phase α_{FF} . The conductive heat transfer is calculated in analogy to Eq. (4.14) and Fig. 4.5 as we demand local thermal equilibrium at the coupling interface.

$$[T]^{\text{FF}} = [T]^{\text{PNM}} \quad \text{on } \Gamma_i^{\text{FF}} \quad (4.17)$$

serves as a Dirichlet-type coupling condition for the free-flow model.

4.2 Pore-network model / REV-scale model

As mentioned in the beginning of this section, the conditions for coupling Ω^{PNM} with Ω^{REV} should be regarded as a starting point for further conceptual model development. While enforcing flux continuity across the coupling interface is universally valid, conceptual questions arise for the other conditions demanding the continuity of primary variables such as p and x^κ at the interface. We will discuss this in more detail in the following. The conditions presented here are furthermore specialized for using the Box scheme [Huber and Helmig, 2000] in Ω^{REV} and require modification for other spatial discretization schemes.

Total mass balance The continuity of the total mass flux across the interface is required for non-compositional systems:

$$\int_{\Gamma_{\text{box},k}} [\varrho_\alpha \mathbf{v}_\alpha \cdot \mathbf{n}]^{\text{REV}} d\Gamma = - \sum_{i \in \Gamma_{\text{box},k}} \left[V_i \frac{\partial(\varrho_{\alpha,i})}{\partial t} + \sum_j (\varrho Q)_{\alpha,ij} \right]^{\text{PNM}}. \quad (4.18)$$

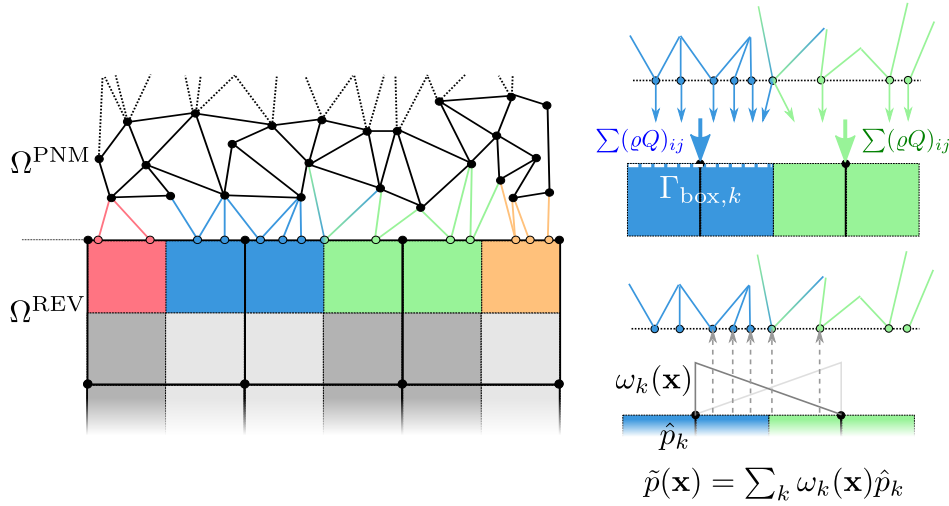


Figure 4.6 – Coupling the pore-network model with the REV model. Implementation of the coupling conditions between the pore-network model and the REV-scale model.

This condition evaluates a cumulative mass flux entering or leaving all pore bodies

i associated with the face of a REV-model box (i.e., control volume) $\Gamma_{\text{box},k}$ at the interface. Hence, it is a Neumann flux condition for the REV model. The right-hand side of Eq. (4.18) is identical to the mass balance equation for the single-phase pore-network model (Eq. (3.11)) excluding the source term. This means that any imbalance in said equation can be seen as a flux entering or leaving the pore across the domain boundary, i.e., the coupling interface [Mosthaf et al., 2014].

For an incompressible fluid, evaluating the Neumann flux term boils down to summing up the mass fluxes of all throats connected to the pores on $\Gamma_{\text{box},k}$, as shown in the upper right part of Fig. 4.6. We note the conceptual similarity to, e.g., Mehmani and Balhoff [2014]. If a pore body i is associated with multiple box faces, the flux is distributed equally.

Momentum balance For sake of simplicity, we assume the continuity of phase pressures at the coupling interface, thus ignoring the conceptual discrepancy regarding the definition of (averaged) pressures at different scales [Nordbotten et al., 2007, 2008, Korteland et al., 2009]:

$$[p_\alpha]^{\text{PNM}} = [p_\alpha]^{\text{REV}} . \quad (4.19)$$

This rather bold (and in many cases, probably incorrect) simplification can be found throughout the literature [e.g., Balhoff et al., 2007, 2008, Mehmani and Balhoff, 2014, Zenyuk et al., 2015] and definitively needs revision in future work. We see this simplified coupling condition as a starting point for further model development.

Exploiting the linear ansatz functions of the Box discretization scheme, we can interpolate the value of the REV-scale pressure for each pore body intersecting with the coupling interface:

$$[p_\alpha]^{\text{REV}} = \tilde{p}_\alpha(\mathbf{x}_i) = \sum_k \omega_k(\mathbf{x}_i) \hat{p}_{\alpha,k} . \quad (4.20)$$

Here, \mathbf{x}_i is the location of pore body i at the interface, ω_k is a linear ansatz function and $\hat{p}_{\alpha,k}$ is the discrete REV-scale pressure of phase α at node k of the primal mesh of

Ω^{REV} (see lower left part of Fig. 4.6). Eq. (4.20) serves as internal Dirichlet condition for Ω^{PNM} .

Chemical equilibrium and mole flux conservation Following the same reasoning as for the total mass balance, we enforce the continuity of species fluxes across the interface by evaluating the left-hand side of the PNM's molar balance equation (Eq. (3.17)):

$$\begin{aligned} & \int_{\Gamma_{\text{box},k}} \left[\sum_{\alpha} (x_{\alpha}^{\kappa} \varrho_{\text{mol}} \mathbf{v} + \mathbf{j}_{\text{diff,mol}}^{\kappa})_{\alpha} \cdot \mathbf{n} \right]^{\text{REV}} d\Gamma \\ &= - \sum_{i \in \Gamma_{\text{box},k}} \left[V_i \frac{\partial (\sum_{\alpha} (x_{\alpha}^{\kappa} \varrho_{\text{mol},\alpha} S_{\alpha})_i)}{\partial t} \right. \\ & \left. + \sum_{\alpha} \sum_j (x_{\alpha}^{\kappa} \varrho_{\text{mol},\alpha} Q_{\alpha})_{ij} + \sum_{\alpha} \sum_j (j_{\text{diff,mol},\alpha}^{\kappa, \text{PNM}} A_{\alpha})_{ij} \right]^{\text{PNM}}. \end{aligned} \quad (4.21)$$

Again, this is used as an internal Neumann flux for Ω^{REV} .

As for the pressure, we assume the continuity of mole fractions at the interface, bearing in mind the conceptual, scale-related issues discussed above:

$$[x_{\alpha}^{\kappa}]^{\text{PNM}} = [x_{\alpha}^{\kappa}]^{\text{REV}}. \quad (4.22)$$

Like before, the values of x_{α}^{κ} are linearly interpolated and used as internal Dirichlet condition for Ω^{PNM} :

$$[x_{\alpha}^{\kappa}]^{\text{REV}} = \tilde{x}_{\alpha}^{\kappa}(\mathbf{x}_i) = \sum_k \omega_k(\mathbf{x}_i) \hat{x}_{\alpha,k}^{\kappa}. \quad (4.23)$$

Energy balance The continuity of energy fluxes is enforced by evaluating the left-hand side of the PNM's energy balance equation (Eq. (3.22)) and using this as an internal Neumann flux for Ω^{REV} :

$$\begin{aligned}
& \int_{\Gamma_{\text{box},k}} \left[\left(\sum_{\alpha} (h \varrho \mathbf{v})_{\alpha} - \lambda_{\text{pm}} \nabla T \right) \cdot \mathbf{n} \right]^{\text{REV}} d\Gamma \\
&= - \sum_{i \in \Gamma_{\text{box},k}} \left[V_i \frac{\partial (\sum_{\alpha} (\varrho_{\alpha} u_{\alpha} S_{\alpha})_i)}{\partial t} + \sum_{\alpha} \sum_j (\varrho_{\alpha} h_{\alpha} Q_{\alpha})_{ij} \right. \\
&\quad + \sum_{\alpha} \sum_j \left(A_{\alpha,ij} \sum_{\kappa} \left(j_{\text{diff,mol},\alpha}^{\kappa, \text{PNM}} h_{\alpha}^{\kappa} \right)_{ij} \right) \\
&\quad \left. + \sum_{\alpha} \sum_j \frac{\lambda_{\alpha,i} + \lambda_{\alpha,j}}{2} \frac{T_i - T_j}{l_{ij}} A_{\alpha,ij} \right]^{\text{PNM}} .
\end{aligned} \tag{4.24}$$

For non-compositional systems, the molecular diffusive energy flux $j_{\text{diff,mol},\alpha}^{\kappa, \text{PNM}} h_{\alpha}^{\kappa}$ is zero. We assume the continuity of temperature at the interface:

$$[T]^{\text{PNM}} = [T]^{\text{REV}} . \tag{4.25}$$

Again, linear interpolation yields the internal Dirichlet temperature values at the location of the interface pore bodies:

$$[T]^{\text{REV}} = \tilde{T}(\mathbf{x}_i) = \sum_k \omega_k(\mathbf{x}_i) \hat{T}_k . \tag{4.26}$$

In addition to the conceptual weaknesses previously discussed for the continuity of pressures of different scales, we note a further potential inconsistency: While the REV-scale model incorporates energy fluxes and storage within both the fluid and solid phases (see Section 2.3 and Eq. (2.20)), only the fluid phases are considered for heat transport and storage in Ω^{PNM} (see Section 3.2). This could be addressed in future work by explicitly accounting for the solid matrix conceptually surrounding the void space in Ω^{PNM} [e.g., Surasani et al., 2008].

5 Implementation and software

This section describes the implementation of all sub-models discussed above and the software dependencies used in this work. A fully implicit backward Euler method is employed for all sub-models (if used alone without being coupled to another model) and for the coupled models. The *Newton-Raphson* scheme solves the potentially non-linear systems of equations. We follow a monolithic coupling approach, i.e., all discrete balance equations are assembled into one large linear system of equations and hence solved simultaneously which means that no coupling iterations are required and the scheme is inherently mass and energy conservative. Further aspects of the monolithic scheme are discussed elsewhere [Mosthaf, 2014] while the pattern of the global system matrix is shown in Eq. (5.1).

Software All sub-models are implemented in DuMu^x [Flemisch et al., 2011, Koch et al., 2020a, Heck et al., 2019], an open-source simulation toolbox for flow and transport in porous media based on DUNE, a modular C++ framework for grid-based numerical methods [Bastian et al., 2008b,a, 2019]. Apart from the DUNE core modules, we further rely on `dune-foamgrid` [Sander et al., 2017] for handling the one-dimensional pore-network grids and `dune-subgrid` [Gräser and Sander, 2009] for certain free-flow domains.

Due to the high degree of modularity of DuMu^x, which has been further increased in the latest version 3 [Koch et al., 2020a], large parts of core functionality code, such as assembly routines or the `fluidsystem` framework [Lauser, 2012] providing the physical fluid properties and constitutive laws, could be used with little or no modifications necessary.

The pore-network models presented in this thesis are implemented in a general and extensible way such that pre-existing porous-medium flow (REV-scale) models, such

as the `2p2c` or `mpnc` model, can be reused in the context of pore-network modeling by inheriting from the general physical properties (i.e., balance equations) and adapting the spatial discretization scheme to the network concept accordingly.

Model coupling Model coupling is realized using the recently developed `multi-domain` framework of `DuMux 3` [Koch et al., 2020a] and no further external dependencies are required. This framework is designed to facilitate the coupling of an arbitrary number of sub-models while keeping the modifications to the core modules as small as possible, i.e., maximize code reusability.

One central feature of the framework is a so-called *coupling manager* which exchanges data between the sub-models and identifies which degrees of freedom of the individual models are actually coupled with each other. Technically, the coupling between the sub-models is realized in terms of inner boundary conditions and source or sink terms which yield the relevant coupling quantities of the other domains.

A search algorithm based on an axis-aligned bounding box tree [e.g., Ericson, 2004] is executed once at the beginning of each model run in order to determine the intersections between the degrees of freedom of the individual sub-models at the respective coupling interface. This yields *coupling stencils* necessary to assemble the global Jacobian matrix incorporating the derivatives of all sub-models' residuals with respect to the coupled degrees of freedoms, as we follow a monolithic coupling approach where all balance equations of all sub-models are solved simultaneously, as described later on.

A further generalization of the coupling manager concept makes it possible to combine multiple two-domain coupling managers (e.g., the one used for coupling the free-flow model with the pore-network model and the one for coupling the pore-network model with the Darcy model) in a rather straightforward manner which makes the system open and flexible for further extension.

Solving the linear equation system The partial differential equation (PDE) system in residual form for n sub-domains is given by

$$\underbrace{\begin{bmatrix} \mathbf{J}_1 & \mathbf{C}_{12} & \dots & \mathbf{C}_{1n} \\ \mathbf{C}_{21} & \mathbf{J}_2 & & \\ \vdots & & \ddots & \\ \mathbf{C}_{n1} & & & \mathbf{J}_n \end{bmatrix}}_{\mathbf{J}_{\text{global}}} \underbrace{\begin{bmatrix} \Delta \mathbf{u}_1 \\ \Delta \mathbf{u}_2 \\ \vdots \\ \Delta \mathbf{u}_n \end{bmatrix}}_{\Delta \mathbf{u}_{\text{global}}} = \underbrace{\begin{bmatrix} \mathbf{r}_1 \\ \mathbf{r}_2 \\ \vdots \\ \mathbf{r}_n \end{bmatrix}}_{\mathbf{r}_{\text{global}}}. \quad (5.1)$$

$\mathbf{J}_i = \frac{\partial \mathbf{r}_i}{\partial \mathbf{u}_i}$ is the Jacobian matrix for sub-domain i and $\mathbf{C}_{ij} = \frac{\partial \mathbf{r}_i}{\partial \mathbf{u}_j}$ is the coupling block containing derivatives of residuals of domain i with respect to degrees of freedom of domain j . $\Delta \mathbf{u}_i$ is the shift of the solution vector of sub-domain i and \mathbf{r}_i is the respective residual vector. The saddle-point structure of the Jacobian of the free-flow model $\mathbf{J}_{\Omega^{\text{FF}}}$ [Benzi et al., 2005] and the poor condition number of $\mathbf{J}_{\text{global}}$ [Grüninger, 2017] renders the system inaccessible to standard Krylov-type iterative linear solvers [Saad, 2003]. We therefore employ UMFPACK [Davis, 2004], a direct linear solver, bearing in mind its unfavorable scaling behavior, both in CPU time and memory consumption, for larger systems [Grüninger, 2017]. Since the sub-matrices and sub-vectors of the above-mentioned discrete PDE system themselves constitute a block structure, more advanced and efficient solution strategies and preconditioners might be incorporated in future work [e.g., Kuchta et al., 2018].

Time step adaptivity The time step sizes for the backward Euler method are chosen heuristically based on the convergence rate of the Newton scheme:

$$\Delta t^{n+1} = \begin{cases} \Delta t^n \left(\frac{1}{1 + \frac{n_{\text{It}} - n_{\text{It,target}}}{n_{\text{It,target}}}} \right) & n_{\text{It,max}} > n_{\text{It}} > n_{\text{It,target}}, \\ \Delta t^n \left(1 + \frac{n_{\text{It,target}} - n_{\text{It}}}{1.2 n_{\text{It,target}}} \right) & n_{\text{It}} \leq n_{\text{It,target}}. \end{cases} \quad (5.2)$$

n_{It} is the number of Newton iterations required for the previous time step, $n_{\text{It,target}}$ is an input target value. If n_{It} exceeds a given $n_{\text{It,max}}$, the time step size is reduced by a given factor, e.g., 0.5.

6 Code verification

Numerical models need to be *verified* in order to make sure they reproduce the underlying mathematical model with sufficient accuracy. A verified model does not necessarily represent reality. Physical consistency is checked by model *validation*, e.g., by means of comparing the model results to experimental data [Oberkamp et al., 2004].

In this section, code verification is performed. In analogy to Fetzner [2018], grid convergence studies and comparisons with published numerical results are performed to assess the free-flow model. This apparent repetition is needed because the model used in this thesis has been re-implemented from scratch in the framework of DuMu^x 3 [Koch et al., 2020a]. Similarly, the pore-network model has been newly implemented and thus requires verification. In contrast to that, the REV-scale model used for the bulk domain Ω^{REV} has been tested and used extensively elsewhere [e.g., Flemisch et al., 2011].

6.1 Free-flow model

Grid convergence Grid convergence is tested by comparing the numerical results to a given analytical solution at different grid refinement levels m . We use the discrete L^2 -error norms for the pressure p and the two velocity components v_x and v_y :

$$e_p^m = \left(\sum_{C \in \mathcal{G}_m} |C| (p_C - p_C^{\text{ref}})^2 \right)^{\frac{1}{2}}, \quad (6.1)$$

$$e_{v_i}^m = \left(\sum_{C_i^* \in \mathcal{G}_{i,m}^*} |C_i^*| (v_{C_i^*} - v_{C_i^*}^{\text{ref}})^2 \right)^{\frac{1}{2}}, \quad i \in \{x, y\}. \quad (6.2)$$

p_C is the discrete pressure at the center of cell C with volume $|C|$, while p_C^{ref} is the value of the exact solution evaluated at this location. $v_{C_i^*}$ is the discrete velocity component value at the center of the staggered control volume C_i^* (the center of the corresponding primal grid face), $v_{C_i^*}^{\text{ref}}$ is the exact value at this position. \mathcal{G}_m and $\mathcal{G}_{i,m}^*$ are the primal and dual grids for the pressure and velocity unknowns after m uniform grid refinement steps.

The convergence rate is given by

$$cr = \frac{\log(e^m) - \log(e^{m-1})}{\log(0.5)}. \quad (6.3)$$

Stokes flow Donea and Huerta [2003] consider stationary Stokes flow on $\Omega = [0, 1 \text{ m}] \times [0, 1 \text{ m}]$ with $\nu = 1 \text{ m}^2 \text{ s}^{-1}$. The exact solution for \mathbf{v} and p is given by

$$v_x^{\text{ref}}(x, y) = x^2(1 - x)^2(2y - 6y^2 + 4y^3) \quad (6.4a)$$

$$v_y^{\text{ref}}(x, y) = -y^2(1 - y)^2(2x - 6x^2 + 4x^3) \quad (6.4b)$$

$$p^{\text{ref}}(x, y) = x(1 - x), \quad (6.4c)$$

and a source term for the momentum balance is prescribed:

$$f_x(x, y) = (12 - 24y)x^4 + (-24 + 48y)x^3 + (12 - 48y + 72y^2 - 48y^3)x^2 + (-2 + 24y - 72y^2 + 48y^3)x + 1 - 4y + 12y^2 - 8y^3 \quad (6.5a)$$

$$f_y(x, y) = (8 - 48y + 48y^2)x^3 + (-12 + 72y - 72y^2)x^2 + (4 - 24y + 48y^2 - 48y^3 + 24y^4)x - 12y^2 + 24y^3 - 12y^4. \quad (6.5b)$$

The stationary Stokes equations (Eq. (3.2) and Eq. (3.4)) are solved on a uniform Cartesian grid and Eq. (6.4a) and Eq. (6.4b) are applied as Dirichlet conditions for \mathbf{v} on all boundaries. The pressure at the lower left cell is fixed according to Eq. (6.4c). Table 6.1 reveals second-order convergence for all primary variables, which is expected for the staggered-grid scheme [Li and Sun, 2014].

Table 6.1 – Convergence test results for Stokes flow. L^2 errors and convergence rates for the test case of Donea and Huerta [2003].

m	cells	e_p	cr_p	e_{v_x}	cr_{v_x}	e_{v_y}	cr_{v_y}
0	8×8	1.37×10^{-3}		5.35×10^{-4}		5.35×10^{-4}	
1	16×16	4.12×10^{-4}	1.73	1.38×10^{-4}	1.96	1.38×10^{-4}	1.96
2	32×32	1.09×10^{-4}	1.92	3.47×10^{-5}	1.99	3.47×10^{-5}	1.99
3	64×64	2.77×10^{-5}	1.98	8.69×10^{-6}	2.00	8.69×10^{-6}	2.00
4	128×128	6.95×10^{-6}	1.99	2.17×10^{-6}	2.00	2.17×10^{-6}	2.00
5	256×256	1.74×10^{-6}	2.00	5.43×10^{-7}	2.00	5.43×10^{-7}	2.00
6	512×512	4.35×10^{-7}	2.00	1.36×10^{-7}	2.00	1.36×10^{-7}	2.00

Navier-Stokes flow In analogy to Kim and Moin [1985], we consider the following analytical solution of the stationary Navier-Stokes equations (Eq. (3.1) and Eq. (3.4)) on $\Omega = [0, 2\pi \text{ m}] \times [0, 2\pi \text{ m}]$ with $\nu = 1 \times 10^{-3} \text{ m}^2 \text{ s}^{-1}$,

$$v_x^{\text{ref}}(x, y) = -\cos(x) \sin(y) \quad (6.6a)$$

$$v_y^{\text{ref}}(x, y) = \sin(x) \cos(y) \quad (6.6b)$$

$$p^{\text{ref}}(x, y) = -0.25(\cos(2x) + \cos(2y)) , \quad (6.6c)$$

again setting a momentum-balance source term:

$$f_x(x, y) = -2\nu \cos(x) \sin(y) \quad (6.7a)$$

$$f_y(x, y) = 2\nu \cos(y) \sin(x) . \quad (6.7b)$$

As before, a regular Cartesian grid with Dirichlet values for \mathbf{v} on all boundaries is used and the lower left cell's pressure is set according to Eq. (6.6c). An upwind weight of 0.5 is set for the calculation of the advective momentum flux, i.e., the arithmetic mean of the upstream and downstream momentum value is used. Again, second-order convergence for \mathbf{v} and p is achieved (see Table 6.2).

Table 6.2 – Convergence test results for Navier-Stokes flow. L^2 errors and convergence rates for the test case of Kim and Moin [1985].

m	cells	e_p	cr_p	e_{v_x}	cr_{v_x}	e_{v_y}	cr_{v_y}
0	128×128	4.58×10^{-4}		2.68×10^{-4}		2.68×10^{-4}	
1	256×256	1.16×10^{-4}	1.98	6.76×10^{-5}	1.99	6.76×10^{-5}	1.99
2	512×512	2.87×10^{-5}	2.01	1.68×10^{-5}	2.01	1.68×10^{-5}	2.01
3	1024×1024	7.17×10^{-6}	2.00	4.18×10^{-6}	2.00	4.18×10^{-6}	2.00

Lid-driven cavity test case Flow in a cavity with $\Omega = [0, 1 \text{ m}] \times [0, 1 \text{ m}]$ is considered in this test case. On the walls of the cavity, $\mathbf{v} = 0$ is set while the lid at the top of the domain moves constantly at $v_x = 1 \text{ m/s}$. Two different flow regimes at $Re = 1$ ($\nu = 1 \text{ m}^2 \text{ s}^{-1}$) and $Re = 1000$ ($\nu = 1 \times 10^{-3} \text{ m}^2 \text{ s}^{-1}$) are simulated, where Re is defined with respect to the cavity's side length. A uniform Cartesian grid with 129×129 cells is used and like before, an upwind weight of 0.5 is set for the advective momentum fluxes. Fig. 6.1 shows an excellent agreement between the velocity profiles obtained by DuMu^x and results reported in literature [Jurjević, 1999, Ghia et al., 1982].

In conclusion, the free-flow code implemented in DuMu^x yields the expected grid-convergence rate of two and reproduces the popular lid-driven cavity test case exactly. We therefore consider it verified and continue with the assessment of the pore-network model in the next section.

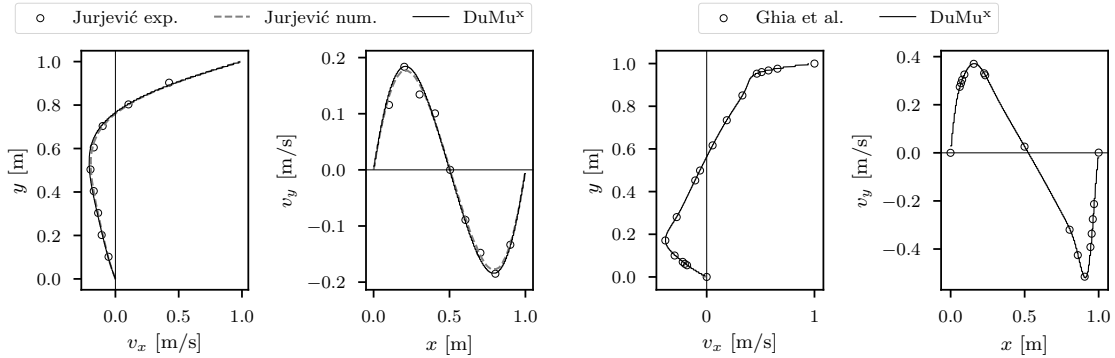


Figure 6.1 – Results for the lid-driven cavity test. Horizontal and vertical velocity profiles at $x = 0.5 \text{ m}$ and $y = 0.5 \text{ m}$ for $Re = 1$ (left) [Jurjević, 1999] and $Re = 1000$ (right) [Ghia et al., 1982]. exp: experimental data; num: numerical data.

6.2 Dynamic two-phase pore-network model

The dynamic two-phase pore-network model is verified by conducting a numerical drainage experiment on a randomly generated network and comparing the resulting capillary pressure-saturation curve to the solution of a quasi-static pore-network (Section 2.4.3) which has been implemented in DuMu^x as well.

The network was generated using the algorithm described by Raouf and Hassanizadeh [2009]. Starting from a fully connected cubic lattice of $10 \times 10 \times 10$ pores with 1×10^{-3} m side length, pore throat connections were deleted with a probability of 90% for all spatial directions. The pore body radii follow a log-normal distribution (4.5×10^{-5} m mean pore radius, 3×10^{-6} m standard deviation) and the throat radii were calculated according to Joekar-Niasar et al. [2008]. Figure 6.2 shows the resulting network where 207 out of 765 throats have already been invaded by the non-wetting phase.

Assuming cubic pore bodies, local pore-scale $p_c - S_w$ curves given by Eq. (2.35) are used. The pore throats feature square cross-sectional shapes and the single-phase throat conductance is given by Eq. (2.40) while Eq. (2.43) is used for the wetting layer conductance and Eq. (2.51) for the conductance of the bulk non-wetting phase. A fixed value for $\gamma = 0.0725 \text{ kg s}^{-2}$ is set while the `H20Air fluidsystem` implemented in DuMu^x is used with water as the wetting phase. Equation (2.30) is used to determine the throats' capillary entry pressure $p_{c,e}$ with $\theta_r = 0$.

Conceptually, the network's lateral sides are closed while the left side is connected to a non-wetting phase reservoir and the right side is connected to a wetting phase reservoir with given pressures $p_{n,inlet}$ and $p_{w,outlet}$. The non-wetting phase is prevented from leaving the domain on the right side. The invasion process is driven by a global capillary pressure difference,

$$p_{c,global} = p_{n,inlet} - p_{w,outlet} , \quad (6.8)$$

which is gradually increased as soon as capillary equilibrium is reached, i.e., the two phases have come to rest and $p_{c,global} = p_c$ at all pores connected to the non-wetting phase. These (and only these) equilibrium points are also modeled by the quasi-static pore-network model.

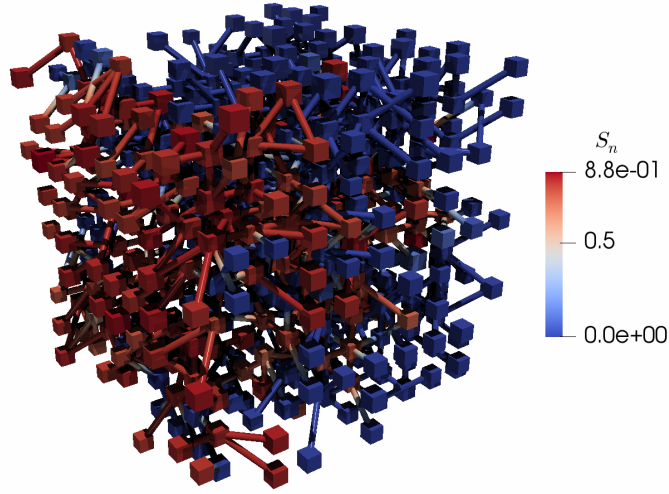


Figure 6.2 – Phase distribution on a randomly generated pore network. $\langle S_w \rangle \approx 0.74$. The throats actually feature square cross sections but ParaView [Ayachit, 2015] only provides a cylindrical *Tube* filter.

We calculate the averaged wetting-phase saturation,

$$\langle S_w \rangle = \frac{\sum_i (S_w V)_i}{\sum_i V_i}, \quad (6.9)$$

and the averaged capillary pressure,

$$\langle p_c \rangle = \frac{\sum_i (S_n p_n V)_i}{\sum_i (S_n V)_i} - \frac{\sum_i (S_w p_w V)_i}{\sum_i (S_w V)_i}, \quad (6.10)$$

which equals $p_{c,\text{global}}$ at the equilibrium points. Figure 6.3 shows the resulting capillary pressure-saturation curves for the dynamic and the quasi-static pore-network model, matching exactly at the equilibrium points.

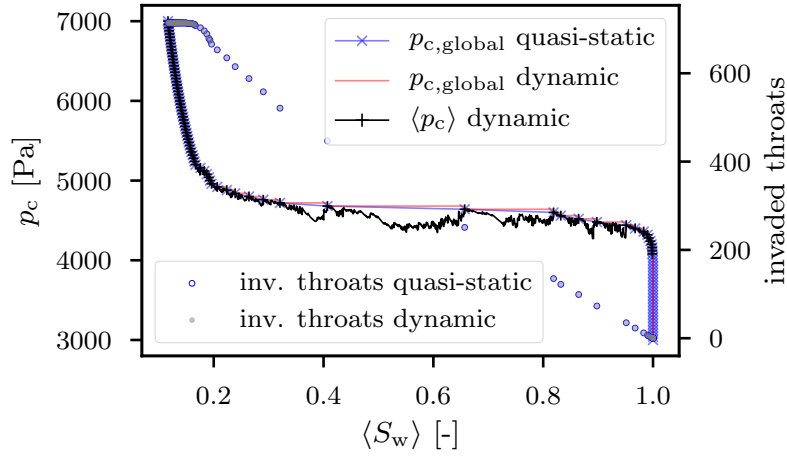


Figure 6.3 – Capillary pressure-saturation curves. Results for the quasi-static and the dynamic PNM with pore throat invasion restriction.

As observed by Joekar-Niasar et al. [2010a], the dynamic curve fluctuates between these points. Figure 6.3 additionally shows that the number of throats invaded by the non-wetting phase for each equilibrium point is exactly the same for both the quasi-static and the dynamic pore-network model. This indicates that the dynamic model precisely recovers the equilibrium states of the drainage process. We note that the dynamic model was adapted such that only throats with $p_{c,e} < p_{c,global}$ could be invaded by the non-wetting phase. This type of restriction was necessary for exactly reproducing the quasi-static results and can be found in similar form, e.g., in Joekar-Niasar et al. [2010a] who limited the minimal admissible wetting phase saturation in each pore body based on $p_{c,global}$.

For comparison, Fig. 6.4 shows the results of the dynamic pore-network model where the invasion restriction criterion was switched off. Still, a very close fit to the quasi-static results can be found, however, the equilibrium points at $\langle S_w \rangle \approx 0.65$ do not match exactly anymore.

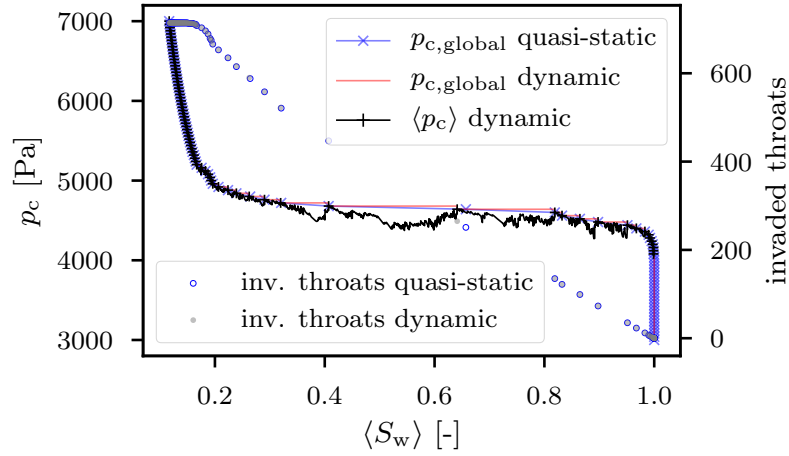


Figure 6.4 – Capillary pressure-saturation curves. Results for the quasi-static and the dynamic PNM without pore throat invasion restriction.

In summary, we consider the dynamic two-phase pore-network model implemented in DuMu^x verified as it exactly reproduces the results of a quasi-static model at the equilibrium points. Even when a rather restrictive, yet widely used, throat invasion criterion is not enforced, a very close fit to the reference solution can still be found. Having verified the essential parts of the code, the results of the coupled model will be presented in the next sections.

7 Results and Discussion I: single-phase flow

In the following two chapters, the coupled model is applied to a range of different applications and scenarios, focusing on the coupling between Ω^{FF} and Ω^{PNM} . Starting with stationary single-phase flow over highly regular porous media, the model complexity is gradually increased to compositional and non-isothermal two-phase flow in Ω^{PNM} . We also present an exemplary three-domain scenario featuring compositional single-phase flow in Ω^{FF} , Ω^{PNM} and Ω^{REV} . Chapter 7 is largely based on Weishaupt et al. [2019a,b]. Any notable differences between these papers and the thesis at hand are indicated by footnotes.

7.1 Recalculation of single-phase flow micromodel experiments¹

In this section, the coupled free-flow/pore-network model is used to recalculate microfluidic single-phase flow experiments presented by Terzis et al. [2019]. The purpose of these experiments was the investigation of free channel flow over a regular structured porous material at very low Reynolds numbers by means of micro-Particle Image Velocimetry (micro-PIV).

While fully supporting three-dimensional domains in principle, the current dependence on `UMFPack` as direct linear solver (see Chapter 5) limits the practical applicability of the free-flow solver implemented in `DuMux` to rather small or two-dimensional problem

¹Large parts of this section are taken and partly modified from [Weishaupt et al., 2019a] and [Weishaupt et al., 2019b].

setups, both in terms of CPU time and memory usage. Obviously, this also concerns the coupled free-flow/pore-network model which also makes use of said free-flow solver. Therefore, a two-fold model reduction strategy was followed: First, the 3D numerical model was simplified to a two-dimensional model where an additional wall friction term is introduced to mimic three-dimensional flow characteristics. Second, the porous part of the model domain was replaced by a pore-network model for which effective parameters had to be determined a priori.

As a first step, a three-dimensional simulation of the entire micromodel was performed using the open-source CFD tool OpenFOAM [Jasak, 2009] (version 1806). After a comparison with experimental data reported in [Terzis et al., 2019], the numerical data served as a reference solution for assessing the simplified reduced models.

The presence of creeping flow in the experiments make it sufficient to perform comparisons based on normalized values as long as $Re < 1$ is satisfied. This implies that different flow rates Q_1 and Q_2 applied at the inlet of the model result in the same velocity and pressure distributions, scaled linearly by a constant factor Q_1/Q_2 . Furthermore, preliminary simulations showed that applying fixed-pressure boundary conditions ($\frac{\partial \mathbf{v}}{\partial x} = 0$) at the inlet and the outlet of the free flow channel decreases the required start-up length for establishing a fully developed velocity profile, thus saving computational cost. Since no pressures were measured in the experiments, we assigned a somehow arbitrary pressure drop $\Delta p = 1 \times 10^{-3}$ Pa between the inlet and the outlet of the free flow channel for all numerical results presented here, which always yields $Re \ll 1$ based on both the free-flow channel height and the width of the pore throats.

A fixed fluid viscosity of $\mu = 1 \times 10^{-3}$ Pa s and density $\rho = 1 \times 10^3$ kg/m³ was used for all simulations, gravity was neglected.

7.1.1 Experimental setup

Here, we briefly describe the micromodel geometry which served as the computational domain for the numerical models. For details concerning the experimental setup and procedure, we refer to Terzis et al. [2019]. Figure 7.1 shows the layout of the polydimethylsiloxane (PDMS) micromodel which was used in the experiments.

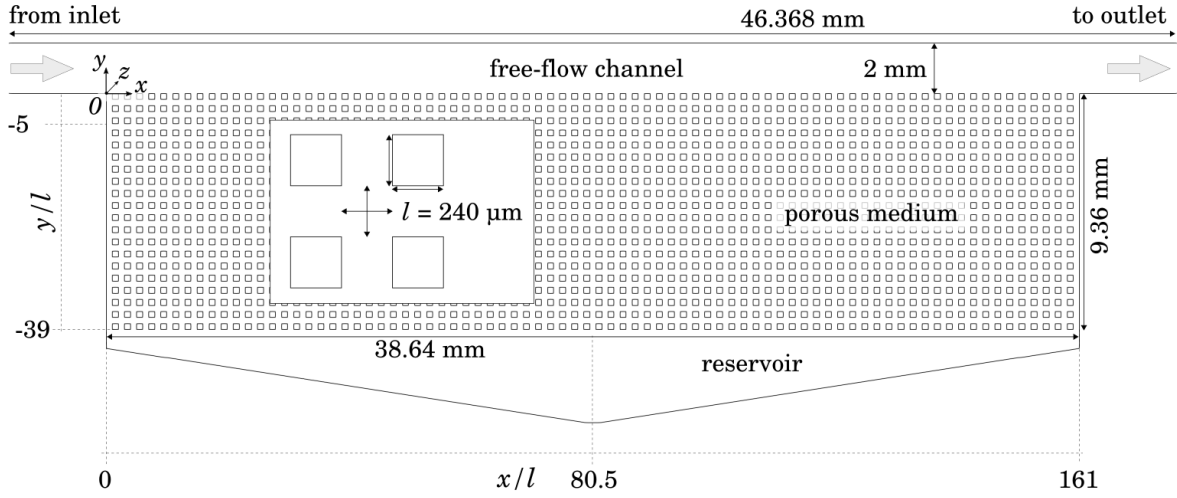


Figure 7.1 – Micromodel geometry. Schematic of the PDMS micromodel used in the micro-PIV experiments (redrawn from Terzis et al. [2019]) with dimensions, origin of coordinates and flow direction. The model has a height in z -direction of $h_{\Omega} = 200 \mu\text{m}$, the pillars are quadratic with $l = 240 \mu\text{m}$ and are evenly spaced throughout the porous domain. Taken from Weishaupt et al. [2019b] (license: CC BY 4.0).

It features three main regions: (1) the free-flow channel at the top, (2) the porous medium made of 80×20 evenly spaced quadratic pillars and (3) a triangular reservoir region which was included into the design to facilitate the complete saturation of the model with water through an auxiliary inlet (not shown) at the bottom. This inlet was closed during the experiments. For convenience, two dimensionless lengths x/l and y/l are introduced, where $l = 240 \times 10^{-6} \text{ m}$ is the width of the pores and throats in the porous region. The model has a uniform height of $h_{\Omega} = 200 \times 10^{-6} \text{ m}$ in z -direction. Note that the inlet and outlet parts of the actual micromodel are longer to ensure a fully developed flow profile on the left side of the porous medium. For the simulations, these parts of the channel have been shortened (and correspond to the dimensions given in the drawing) for efficiency reasons while fully developed flow was still achieved due to the choice of aforementioned pressure boundary conditions.

Working under fully saturated conditions, water doped with fluorescent particles was injected at the inlet on the left side of the model ($Re < 1$). Micro-PIV was used to obtain pore-scale velocity distributions in the porous medium and at the interface region between the free-flow channel and the porous medium. As the camera's field of view was restricted to 5 x 3 pillars in x - and y -direction, a series of measurements conducted under steady-state conditions at different locations of the micromodel was assembled for a full coverage of the model.

7.1.2 3D simulation results and comparison with micro-PIV experimental data

OpenFOAM was used to create a 3D reference solution for comparison with the simplified quasi-3D model. For this, the above-described micromodel geometry was meshed discretely using regular, axis-parallel cells. Having assured grid convergence, a mesh resolution was chosen such that each pore throat is discretized with 20 cells in all directions ($\Delta x = \Delta y = 1.2 \times 10^{-5}$ m, $\Delta z = 1.0 \times 10^{-5}$ m), resulting in a total number of around 62 million grid cells.

No-flow/no-slip boundaries were considered everywhere, except at the left and right end of the free flow channel, where fixed pressure values $p_{in} = 1 \times 10^{-3}$ Pa and $p_{out} = 0$ Pa were set. Solving the problem took around 5 hours on 30 cores (Intel Xeon CPU E5-2683 v4 @ 2.10GHz). Note that the chosen solver `icoFoam` (PISO algorithm) is implemented in a transient manner, solving Eq. (3.1) and Eq. (3.4). Therefore, the simulation was run until a steady state was reached. Solving one time step took around four minutes.

Figure 7.2a shows the resulting center-plane ($z = 100 \times 10^{-6}$ m) velocity field. As seen in the microfluidic experiments [Terzis et al., 2019], the flow enters the porous domain almost vertically on the left side of the porous medium, traverses it mainly parallel and re-enters the channel on the right side of the porous domain. A substantial fraction of flow passes through the triangular reservoir at the bottom of the model as this features less resistance than the narrow flow channels within the porous medium. The maximum resulting Reynolds number, both with respect to the free-flow channel width and the width of the pore throats, is always below 1×10^{-3} .

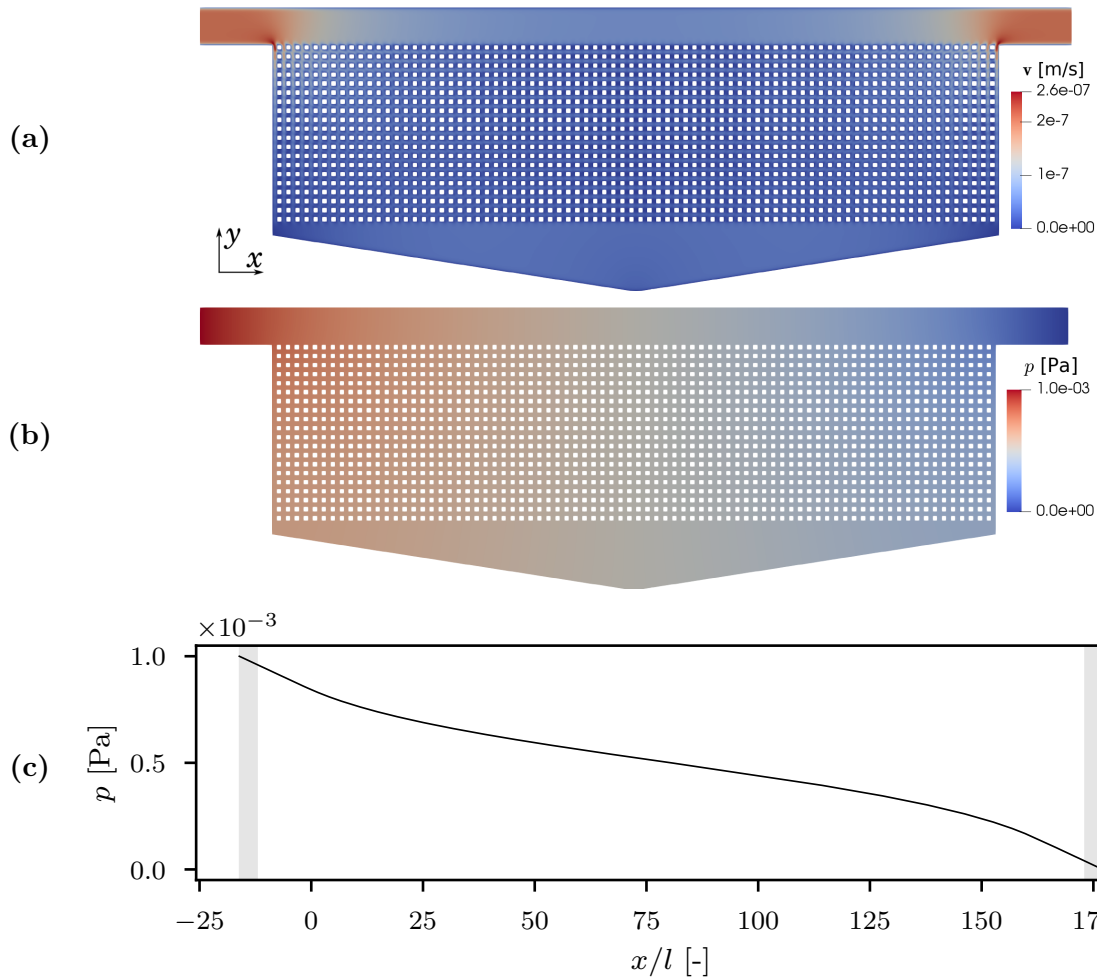


Figure 7.2 – 3D simulation results. Center-plane velocity (a) and pressure (b) field ($z = 100 \times 10^{-6}$ m) obtained by the 3D model (OpenFOAM). (c) shows the pressure curve along the free-flow channel’s central axis, the gray boxes indicate an almost linear pressure gradient. Note that `icoFoam` returns $p^* = p/\rho$, depicted here is p . Taken from Weishaupt et al. [2019b] (license: CC BY 4.0).

The corresponding pressure field of the entire domain is presented in Fig. 7.2b while Fig. 7.2c shows the pressure curve along the central axis of the free-flow channel. An approximately linear pressure gradient is found close to the inlet and the outlet (marked with gray boxes) as there is virtually no flow in y -direction.

We use this pressure gradient value to evaluate the analytical solution [White, 1991] for fully developed laminar flow in a rectangular duct:

$$v_{x,\text{an.}}(Y, Z) = -\frac{\partial p}{\partial x} \frac{4b^2}{\mu\pi^3} \sum_{i=1,3,\dots}^{\infty} (-1)^{(i-1)/2} \left[1 - \frac{\cosh(i\pi Z/b)}{\cosh(i\pi a/2b)} \right] \frac{\cos(i\pi Y/b)}{i^3}. \quad (7.1)$$

Here, $a \leq b$ are the side lengths of the duct with $a = 200 \times 10^{-6}$ m and $b = 2 \times 10^{-3}$ m. Y and Z are local coordinates such that $-a/2 \leq Z \leq a/2$ and $-b/2 \leq Y \leq b/2$ (cf. Fig. 7.7).

Using $i \in \{1, 3, \dots, 1000\}$, the analytical velocity profiles over the free-flow channel's width (at $z = 100 \times 10^{-6}$ m) and height (at $y = 1 \times 10^{-3}$ m) are essentially identical to the corresponding numerical values as shown in Fig. 7.3.

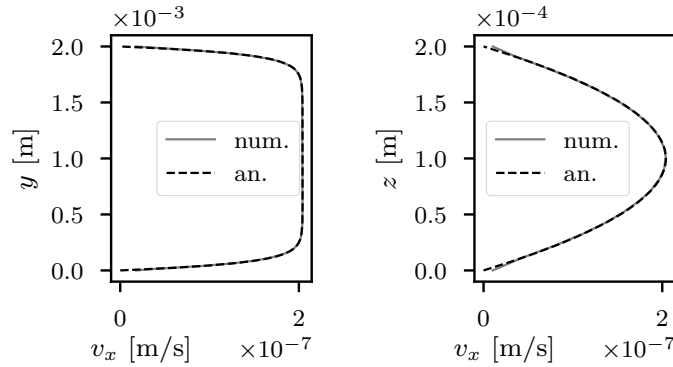


Figure 7.3 – Velocity profiles at the channel inlet. Stream-wise velocity profiles at the left inlet of the free-flow channel over the channel width (y , left) and the channel height (z , right) obtained by the 3D model (OpenFOAM). Both the numerical result and the analytical solution from Eq. (7.1) for the given pressure gradient are shown. Taken from Weishaupt et al. [2019b] (license: CC BY 4.0).

In analogy, we find that the integral volumetric flow through the channel inlet determined numerically,

$$Q_{\text{num.}} = \int_A (\mathbf{v} \cdot \mathbf{n}) dA = \bar{\mathbf{v}} A, \quad (7.2)$$

where \mathbf{n} is the unit vector normal to surface A over which the flux is evaluated, deviates by less than 0.3 % from the analytical solution

$$Q_{\text{an.}} = -\frac{\partial p}{\partial x} \frac{ab^3}{12\mu} \left[1 - \frac{192b}{\pi^5 a} \sum_{i=1,3,\dots}^{\infty} \frac{\tanh(i\pi a/2b)}{i^5} \right]. \quad (7.3)$$

The throats at $x/l \approx 80.5$ feature almost parallel flow along the x -axis where again a close to linear pressure gradient in x -direction can be found. At $(x/l = 79.5, y/l = 37.5)$, which is close to the lower interface towards the triangular region, the evaluated pressure gradient within the throat yields an analytic flow rate from which the numerical results deviate by less than 1 %. This and the above findings underline that the mesh resolution of the numerical model is sufficiently fine.

Figure 7.4 is a reproduction of Fig. 7a presented in Terzis et al. [2019], using the same experimental data and color scheme. In the right column, the results of the micro-PIV measurements are shown in terms of v_y and the velocity vector fields for four different locations A, B, C and D, as indicated in the schematic drawing on the top of the figure. The left column displays the corresponding simulation results (OpenFOAM) which show a very good agreement with the experimental data in a qualitative sense, reproducing the same distinct flow patterns at the various locations: in region A, a pronounced inflow from the free-flow channel into the porous structure can be observed which diminishes in streamwise direction. Region C basically shows a mirrored flow field as the fluid leaves the porous medium and re-enters the channel in a symmetrical fashion compared to A. Here, the vertical flow intensity increases again in streamwise direction. In region B, at the center of the porous domain, no net influx or outflux occurs. The fluid crosses the interface in a downwards motion on the right sides of the solid blocks (red spots) and returns to the free flow channel at left sides of the blocks (blue spots). Region D lies inside the porous domain and features mainly parallel flow in x -direction.

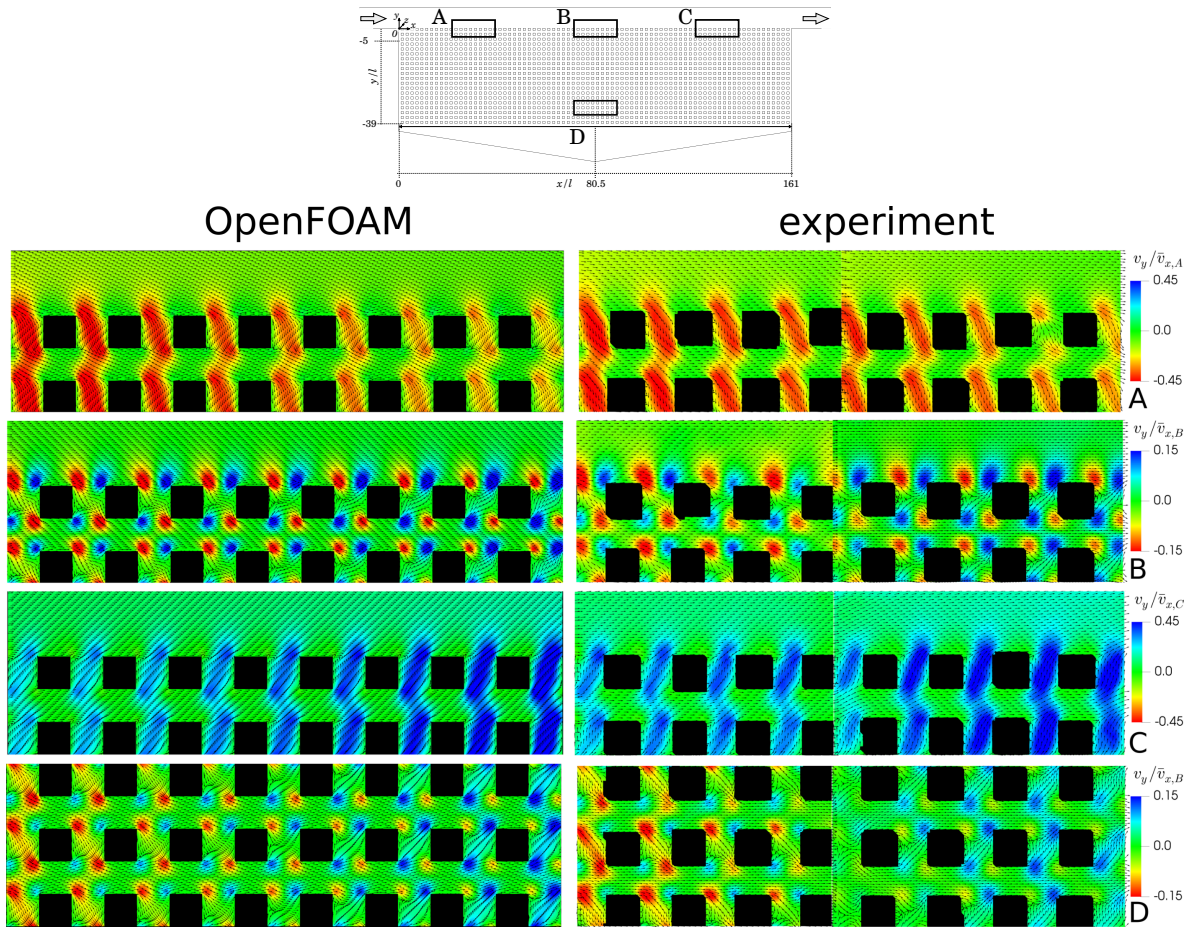


Figure 7.4 – Experimental and numerical flow fields. Comparison of flow fields obtained by numerical simulation with OpenFOAM (left column) and micro-PIV measurement results (right column, reproduced from the original data of Terzis et al. [2019]). Adapted from Weishaupt et al. [2019b] (license: CC BY 4.0).

In Fig. 7.5a, a more quantitative comparison is performed. Here, v_x is averaged in x -direction between $75 \leq x/l \leq 85$ at different locations of y . Both the experimental and numerical data are given and the graphs are normalized by the respective maximum values in the free-flow region. A very good fit can be found, both qualitatively and quantitatively. The local deviations can be explained by measurements uncertainties [Terzis et al., 2019] or small-scale structural differences between the actual micromodel geometry and the computational domain, such as surface roughness [Silva et al., 2008] which is not captured by the numerical model. While Fig. 7.5b shows that the pillars of the PDMS model are indeed not entirely smooth and that the corners are slightly rounded, the numerical model only considers perfectly smooth squares with sharp cor-

ners. This could also explain the local deviations of flow angles ϑ close to the interface between the free-flow channel and porous medium, as presented in Fig. 7.6. A detailed analysis of the impact of the pillars' rounded edges is beyond the scope of this work and should be addressed in future studies.

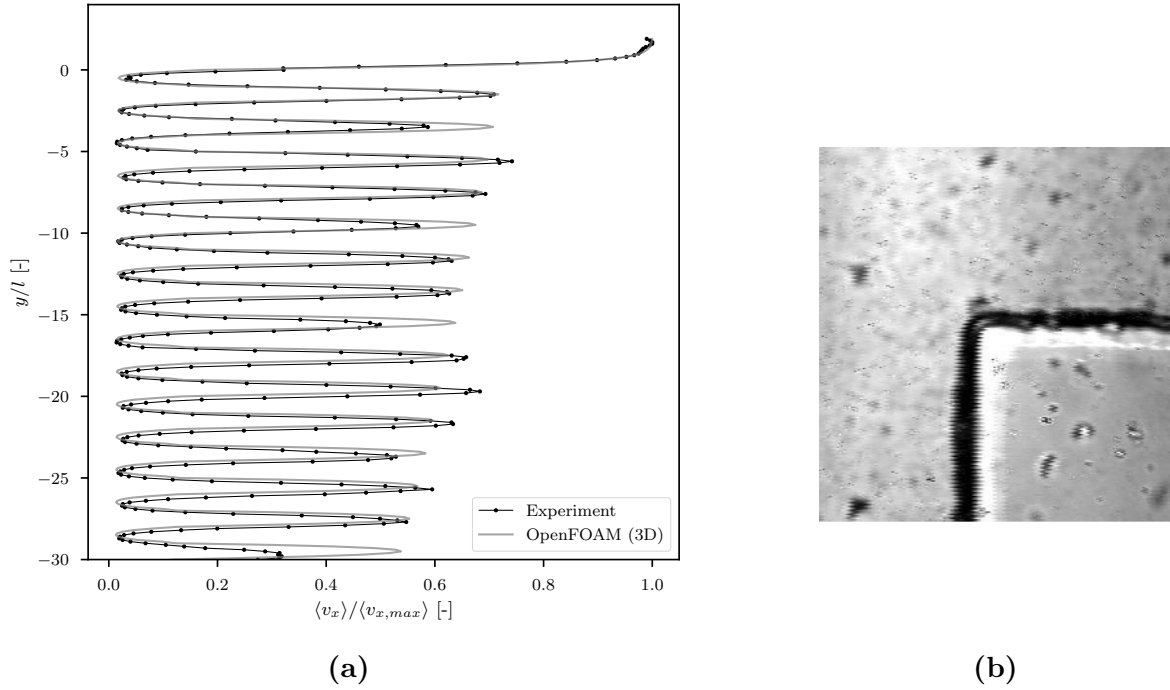


Figure 7.5 – Experimental and numerical velocity profiles. Left (a): Comparison of averaged velocity profiles ($75 \leq x/l \leq 85$) between simulation (OpenFOAM) and experiment. The original data of Terzis et al. [2019] were used. Right (b): camera image of a pillar within the porous domain. Adapted from Weishaupt et al. [2019b] (license: CC BY 4.0).

Figure 7.6 shows a symmetric characteristic of the flow angles due to the inflow into the porous medium and the outflow back into the free-flow channel. On the left, the velocity vectors feature a negative inclination as the flow enters the porous domain while the same angles with opposed sign can be found on the right side, where the flow returns to the free-flow channel. The local oscillations are caused by the same up- and downwards movement of the flow between the pillars as explained for region B in Fig. 7.4. The angles are greater for $y/l = 0.1$, which is closer to the interface, as the free flow senses a stronger influence of the porous medium compared to $y/l = 0.5$.

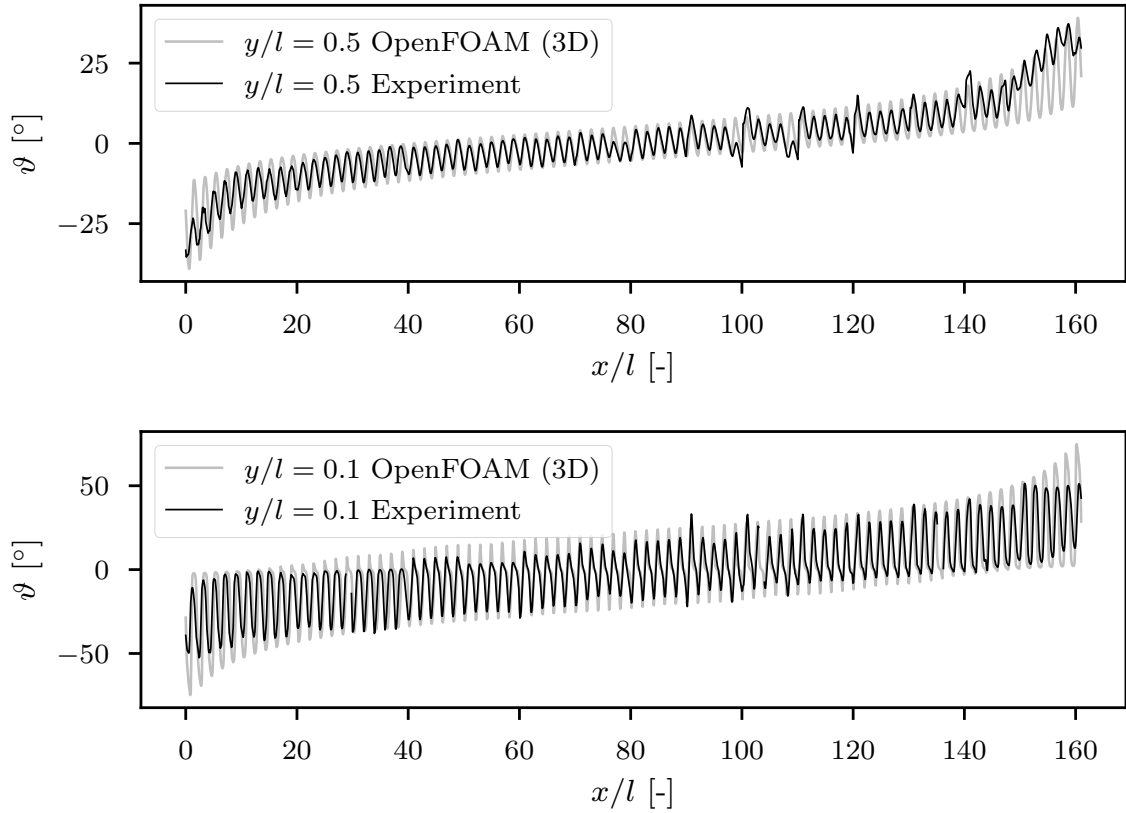


Figure 7.6 – Experimental and numerical flow angles. Comparison of the flow angles ϑ close to the interface between free flow and porous medium at $y/l = 0.5$ (top) and $y/l = 0.1$ (bottom) for the simulation and the experiment. The original data of Terzis et al. [2019] were used. Adapted from Weishaupt et al. [2019b] (license: CC BY 4.0).

In summary, the three-dimensional numerical model is able to reproduce the experimental data adequately. The obtained reference solution is thus suited for comparison with the reduced model’s results as described in the upcoming sections.

Prior to this, however, we first examine the expectable degree of accuracy when using a two-dimensional, quasi-3D model incorporating the wall friction term, as described in Section 3.1, when modeling three-dimensional domains.

7.1.3 Dimensional reduction by inclusion of a wall friction term

This section examines the applicability and limitations of using a wall friction term to account for three-dimensional flow characteristics on the example of a simple rectangular duct with different cross-sectional aspect ratios a/b as shown in Fig. 7.7.

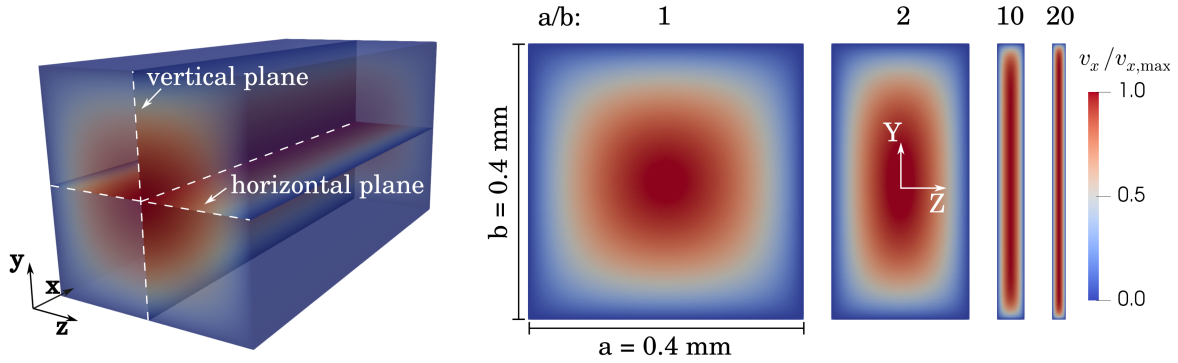


Figure 7.7 – Variation of channel aspect ratios. Channel-flow setup with various aspect ratios a/b . A pressure gradient is applied in x -direction. Y and Z are the local coordinates in Eq. (7.1).

The channel's length and height are fixed at 400×10^{-6} m. The setup was both modeled using a full three-dimensional description of the domain and the quasi-3D model, omitting the z -coordinate as described in Section 3.1. Fixed pressure boundary conditions at the inlet and the outlet ($\frac{\partial \mathbf{v}}{\partial x} = 0$) ensure a fully developed laminar flow throughout the whole domain with $p(x = 0) = 0.4$ Pa and $p(x = 400 \times 10^{-6} \text{ m}) = 0$ Pa. No-flow/no-slip conditions are set at the remaining boundaries.

The free-flow solver implemented in DuMu^x was used both for the quasi-3D and 3D simulations. This was feasible due to the small spatial extent of the computational domains. The grid featured 200 cells in both y - and z -direction (for the 3D model) while the presence of a fully developed flow profile made it possible to use only one cell in x -direction.

Figure 7.7 shows the resulting cross-sectional velocity profiles, normalized by the respective maximal velocity at the channel center. The narrower the channel, the more homogeneous the velocity field. This is also seen in the center column of Fig. 7.8 which shows the velocity profiles for the vertical center plane (see left part of Fig. 7.7) obtained from the 3D numerical simulations.

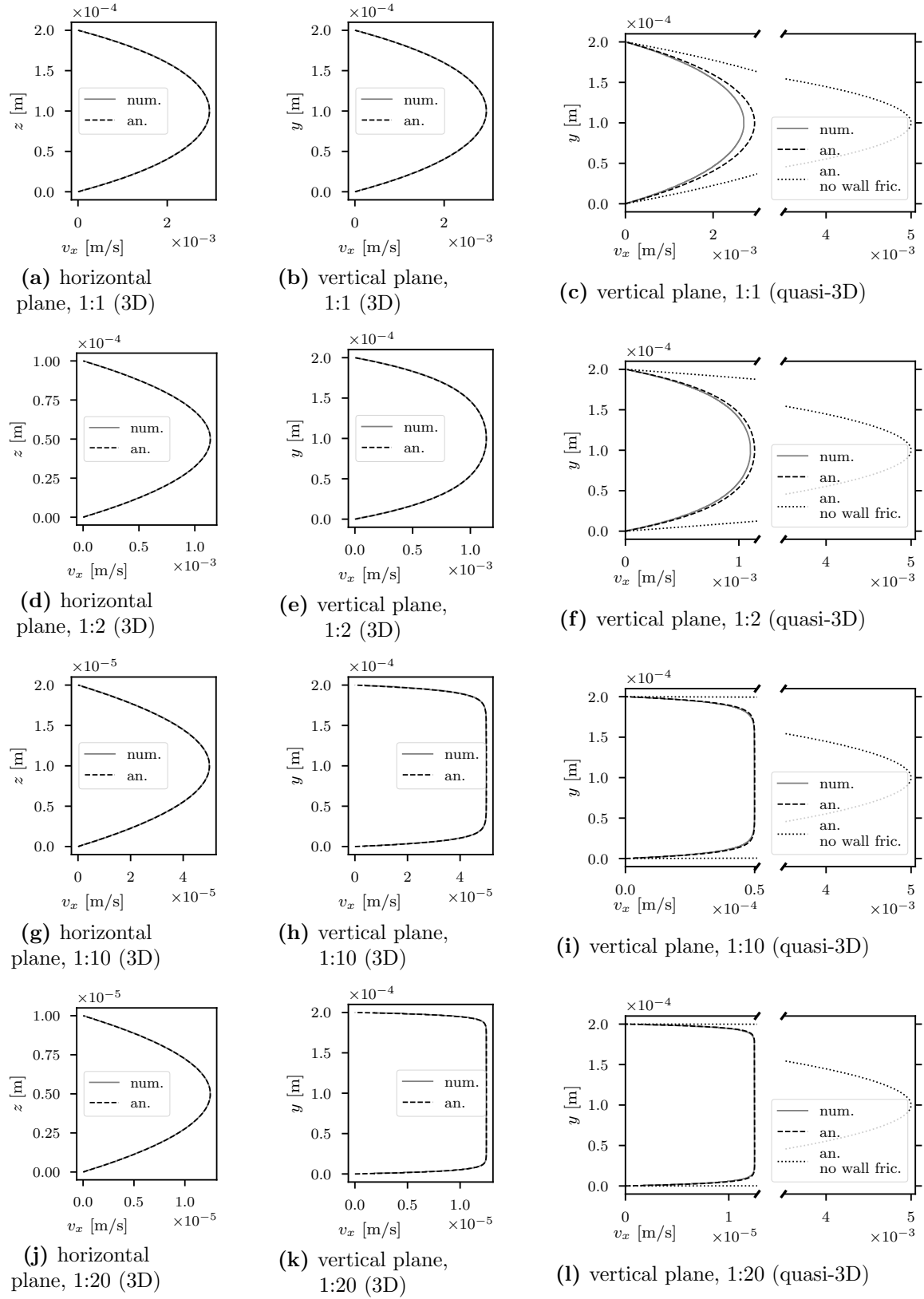


Figure 7.8 – Influence of aspect ratio. Velocity profiles for the 3D model and the quasi-3D model ($c = 8$, maximum center-plane velocity) and analytical solution (Eq. (7.1)).

In addition, the results of the analytical solution (Eq. (7.1)) are plotted in Fig. 7.8, revealing an exact fit with the corresponding 3D numerical results. While the profiles along the horizontal and the vertical plane are identical for $a/b = 1$ (see Figs. 7.8a and 7.8b), the curves over y (center column) become more and more compressed for increasing aspect ratios and finally exhibit an almost uniform velocity distribution over a large part of the channel. At the same time, the flow profiles over z (left column) become more and more parabolic, confirming the assumption made for Eq. (3.3).

The right column of Fig. 7.8 shows the velocity profiles along the vertical plane (y -axis) for the quasi-3D model, using a factor of $c = 8$ in Eq. (3.3) which yields the maximal center-plane velocity. The greater the aspect ratio, the smaller the deviation from the analytical solution. The case of $a/b = 1$ therefore corresponds to the worst-case scenario with a maximal velocity deviation of about 8%. For $a/b \geq 10$, the errors become negligible. For comparison, the velocity profiles for flow between two parallel plates, corresponding to neglecting the wall friction contribution for the given setup, are also presented in the right column of Fig. 7.8. Here, the results differ by more than two orders of magnitude which underlines the importance of correctly accounting for the wall drag forces.

It is also possible to consider the channel's height-averaged velocity instead of the maximal center-plane velocity by setting the corresponding factor in Eq. (3.3) to $c = 12$ instead of $c = 8$. Figure 7.9 shows the resulting velocity profiles of the 3D model (v_x averaged over h_Ω) and the quasi-3D model. The same trend as before can be observed: the narrower the channel, the better the approximation by including the wall friction term.

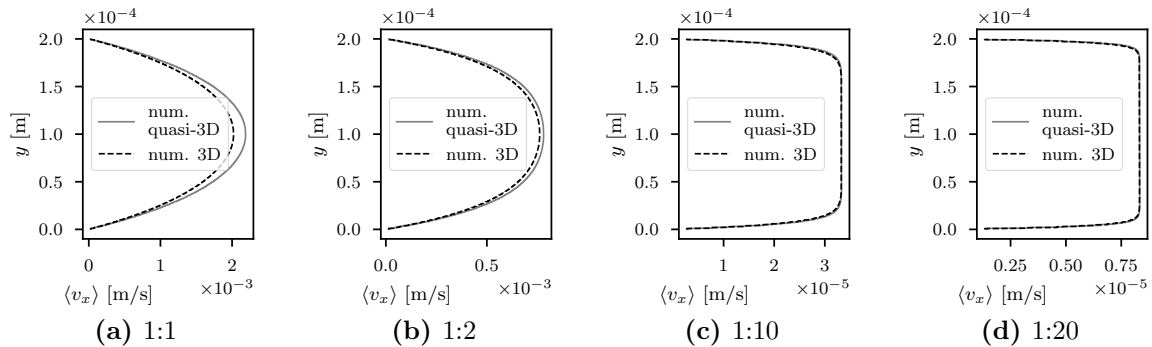


Figure 7.9 – Influence of aspect ratio. Height-averaged velocity profiles over y for the quasi-3D model ($c = 12$) and the 3D model.

In order to obtain a volume flow (in m^3/s) from the quasi-3D model, we assume a height-averaged velocity of

$$\bar{\mathbf{v}}_{2\text{D}} = \frac{2}{3}\mathbf{v}_{2\text{D}} \quad (7.4)$$

for $c = 8$ (maximum center-plane velocity). This leads to the approximation of the volumetric flow over a given line s which is extruded in the virtual z -direction by the domain's height h_Ω :

$$Q_{\text{num},2\text{D}} = \frac{2}{3}h_\Omega \int_s (\mathbf{v}_{2\text{D}} \cdot \mathbf{n}) ds . \quad (7.5)$$

Here, \mathbf{n} is a two-dimensional unit vector normal to s and $\mathbf{v}_{2\text{D}}$ is the two-dimensional velocity vector obtained by the quasi-3D model.

For $c = 12$, $\mathbf{v}_{2\text{D}}$ is already height-averaged, thus

$$Q_{\text{num},2\text{D}} = h_\Omega \int_s (\mathbf{v}_{2\text{D}} \cdot \mathbf{n}) ds . \quad (7.6)$$

Table 7.1 summarizes the volume flows for each aspect-ratio setup, considering the analytical solution (Eq. (7.3)), the 3D numerical model and both variants of the quasi-3D numerical model. The volume flow Q scales non-linearly with the aspect ratio a/b . The 3D numerical model results deviate by less than 1% from the analytical value. The accuracy slightly drops for larger values of a/b . This could be related to increasingly unfavorable grid cell aspect ratios which make the staggered-grid scheme's numerical evaluation of the velocity gradients less and less accurate.

In contrast to that, the quasi-3D results substantially gain accuracy with increasing values of a/b . Here, the assumption of having a parabolic flow profile in the neglected z -coordinate becomes more and more justified, as explained above. Considering the maximal flow velocities consistently underestimates the real volume flows while the opposite is true for considering the height-averaged velocities. Here, the flow is always overestimated but actually closer to the analytical solution. In summary, aspect ratios above 10 yield errors below 1% for both quasi-3D approaches while this error may rise to around 12% at worst for quadratic channel cross sections.

Table 7.1 – Flow rates and accuracy of the quasi-3D model. Results of comparing the volumetric flow rates for different models and aspect ratios. an.: analytical solution; num. 3D: numerical 3D model; num. q-3D (max.): numerical quasi-3D model considering the center-plane maximal velocities; num. q-3D (avg.) numerical quasi-3D model considering the height-averaged velocities.

a/b	Q [$\text{m}^3 \text{s}^{-1}$] / err. [%]			
	an.	num. 3D	num. q-3D (max.)	num. q-3D (avg.)
1	5.62×10^{-11}	5.62×10^{-11} / 0.01	4.96×10^{-11} / -11.83	6.10×10^{-11} / 8.53
2	1.14×10^{-11}	1.14×10^{-11} / 0.01	1.08×10^{-11} / -5.41	1.19×10^{-11} / 3.77
10	1.25×10^{-13}	1.25×10^{-13} / 0.03	1.24×10^{-13} / -0.80	1.26×10^{-13} / 0.59
20	1.61×10^{-14}	1.61×10^{-14} / 0.05	1.61×10^{-14} / -0.36	1.62×10^{-14} / 0.32
40	2.05×10^{-15}	2.05×10^{-15} / 0.08	2.05×10^{-15} / -0.13	2.05×10^{-15} / 0.22

Finally, we consider a problem setup more similar to the actual micromodel geometry shown in the previous section. Here, horizontal flow in a channel with $a/b = 2$ is deflected vertically towards a smaller channel with $a/b = 1$. The left part of Fig. 7.10 shows the result of the 3D simulation where $p = 1 \times 10^{-6}$ Pa was applied as a pressure boundary condition at the inlet on the left side of the domain and $p = 0$ Pa was set at the bottom outlet. Again, all other boundaries were considered as rigid walls. The domain's spatial extent is $0.5 \times 0.75 \times 0.25 \text{ mm}^3$. The right part of Fig. 7.10 depicts the difference between the quasi-3D model ($c = 8$) results and the 3D model results at the center plane. The error is largest in the vertical channel section with $a/b = 1$. The 3D numerical model yields an outflow of $2.84 \times 10^{-13} \text{ m}^3 \text{ s}^{-1}$ while the quasi-3D models' values are $2.53 \times 10^{-13} \text{ m}^3 \text{ s}^{-1}$ for the maximal velocity variant and $3.05 \times 10^{-13} \text{ m}^3 \text{ s}^{-1}$ for the average velocity variant. This corresponds to percentage errors of -10.91% and 7.12% , respectively, which goes in line with the previous finding for unidirectional flow (Table 7.1).

In summary, we may expect a consistent underestimation of the real velocities of up to 12% by the quasi-3D model considering maximal velocities. The other variant considering averaged velocities yields slightly better results while generally overestimating the velocities. For both variants, the error drops below 1% for $a/b \geq 10$. In the next section, the quasi-3D model is used to recalculate the micromodel experiments described previously.

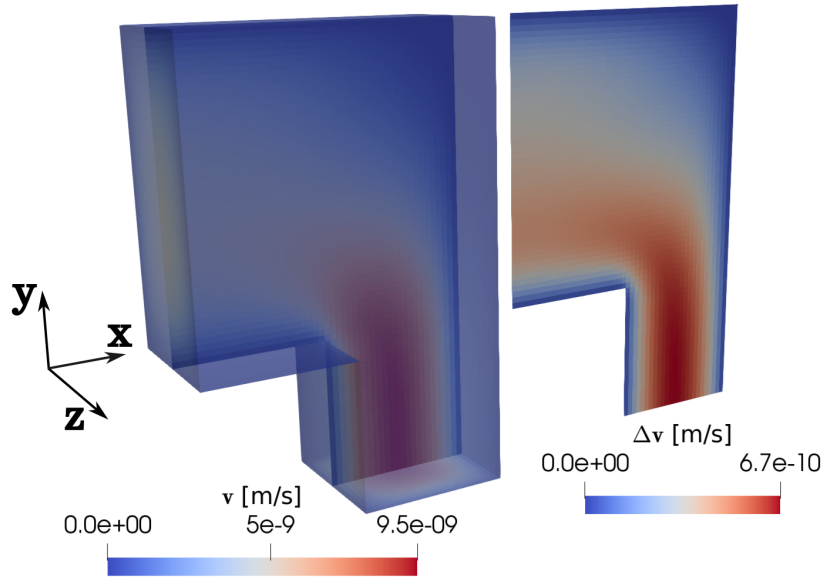


Figure 7.10 – Channel with a bend. Channel-flow setup with a bend and a change of aspect ratio from two to one. Left: 3D model. Right: center-plane velocity deviations of the quasi-3D model ($c = 8$).

7.1.4 Quasi-3D simulation results for the micromodel geometry

In order to assess the validity of the quasi-3D approach for the given micromodel geometry (see Fig. 7.1), the three-dimensional mesh used previously is flattened by neglecting the z -coordinate which reduces the number of grid cells by a factor of 20. The same boundary conditions as before are applied, i.e, a pressure gradient between the channel inlet and outlet is set. The stationary Stokes equations (Eq. (3.2)) in two dimensions (x and y) are considered, including the wall friction term \mathbf{f}_{drag} given by Eq. (3.3) with a factor of $c = 8$ in order to recover the central-plane maximal velocity. Solving the quasi-3D problem with DuMu^x on a single core of the same machine as for the 3D model took less than 11 minutes compared to five hours for the full 3D simulation. As mentioned earlier, the current implementation of the quasi-3D model is based on UMFPack as direct linear solver which does not support parallelization. The extension to preconditioned Krylov-type solvers is part of future work. Figure 7.11 shows the resulting velocity field which corresponds to the central z -plane of the three-dimensional model.

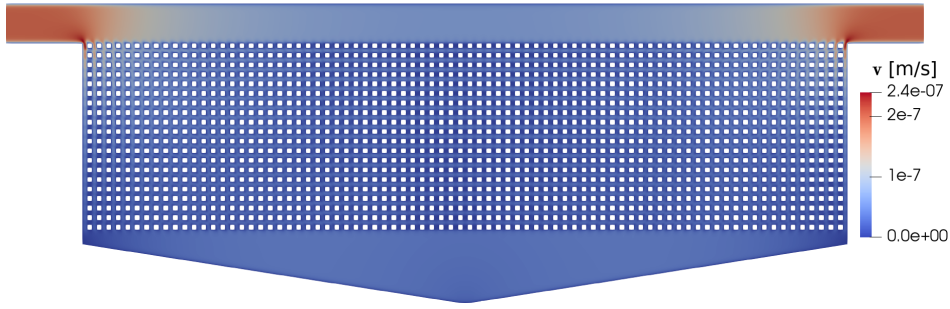


Figure 7.11 – Quasi-3D flow field. Two-dimensional velocity field (\mathbf{v}_{2D}) obtained by the quasi-3D model corresponding to the center plane ($z = 100 \times 10^{-6}$ m) of the 3D model. Taken from Weishaupt et al. [2019b] (license: CC BY 4.0).

The quasi-3D model captures the main features of the flow accurately when compared to Fig. 7.2a. For a quantitative comparison, Fig. 7.12 shows the difference

$$\Delta \mathbf{v}_{2D-3D} = \begin{pmatrix} u_{3D,x} - v_{2D,x} \\ u_{3D,y} - v_{2D,y} \end{pmatrix} \quad (7.7)$$

between the two velocity fields. Here, \mathbf{v}_{3D} corresponds to the three-dimensional reference solution discussed earlier while \mathbf{v}_{2D} is the velocity obtained by the quasi-3D model.

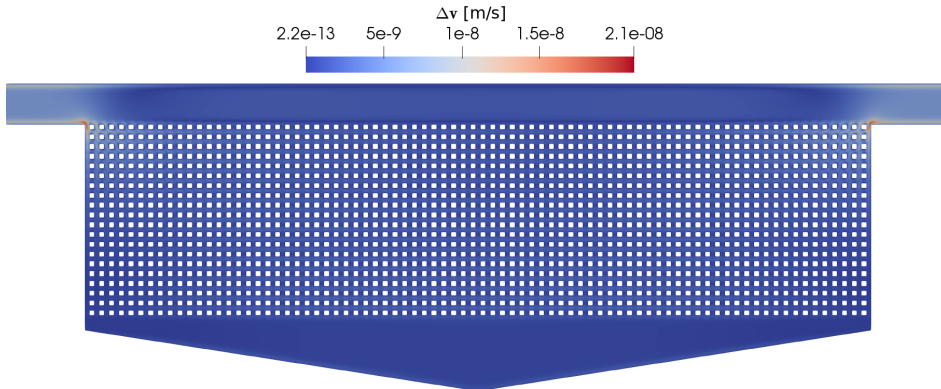


Figure 7.12 – Difference between the 3D and the quasi-3D velocity fields. $\Delta \mathbf{v}_{2D-3D}$ at the center plane ($z = 100 \times 10^{-6}$ m) of the 3D model. Taken from Weishaupt et al. [2019b] (license: CC BY 4.0).

Local deviations of up to 8% can be observed, especially at the leftmost and the rightmost vertical throat intersecting with the interface between free flow and porous

medium. This is probably due to the velocity gradients which are highest at these positions and the sudden change of flow direction. In addition, the aspect ratio between the model height h_Ω and the flow cross-section width changes from a value of $\frac{200\ \mu\text{m}}{2000\ \mu\text{m}} = 0.1$ in the channel to a less favorable value of $\frac{200\ \mu\text{m}}{240\ \mu\text{m}} = 0.83$ in the pore throats, which impairs the validity of Eq. (3.3), as shown in the previous section. The maximal error of around 8% is the same as for the single-tube case with an aspect ratio of 1 (see Fig. 7.8c). Globally, the errors are quite small which corresponds to the findings of Venturoli and Boek [2006] and Laleian et al. [2015].

We define a relative error as the Euclidean norm of the velocity differences normalized by the Euclidean norm of the reference velocities,

$$\text{relErr}(\Delta\mathbf{v}, \mathbf{v}_{\text{ref}}) = \frac{\|\Delta\mathbf{v}\|_2}{\|\mathbf{v}_{\text{ref}}\|_2} = \frac{(\sum_i (\Delta v_x^2 + \Delta v_y^2)_i)^{1/2}}{(\sum_i (v_{\text{ref},x}^2 + v_{\text{ref},y}^2)_i)^{1/2}}, \quad (7.8)$$

which takes a value of 3.28×10^{-2} for the quasi-3D solution compared to the 3D center-plane solution ($\Delta\mathbf{v} = \Delta\mathbf{v}_{2\text{D}-3\text{D}}$ and $\mathbf{v}_{\text{ref}} = \mathbf{v}_{3\text{D}}$). Analogously, the relative error for p is 3.7×10^{-3} .

Figure 7.13 depicts the profiles of p and v_x along the free-flow channel's central axis in the x -direction for both the 3D and the quasi-3D simulation. All values are normalized by the maximum values of the 3D simulation. The pressure curves are virtually identical and, as stated earlier, a linear pressure gradient can be found at the inlet and the outlet of the channel. At these regions, some differences with regard to v_x occur (2.6%) while there is a very close match between the solutions otherwise.

The profiles of v_x along the y -axis at the center of the micromodel ($x/l = 80.5$) are presented in Fig. 7.14a. Again, all values are normalized by the maximum velocity obtained by the 3D model. The three flow domains of the micromodel can be distinguished clearly: first, the free-flow channel at the top ($y/l > 0$), where there is a rather uniform flow profile, slightly skewed due to the interaction with the porous domain. The latter is seen at $-40 \leq y/l < 0$. Here, the velocity peaks between the solid blocks are distinctly visible while $v_x = 0$ at the locations of the blocks. There is also a gradual decrease of the peaks from top to bottom.

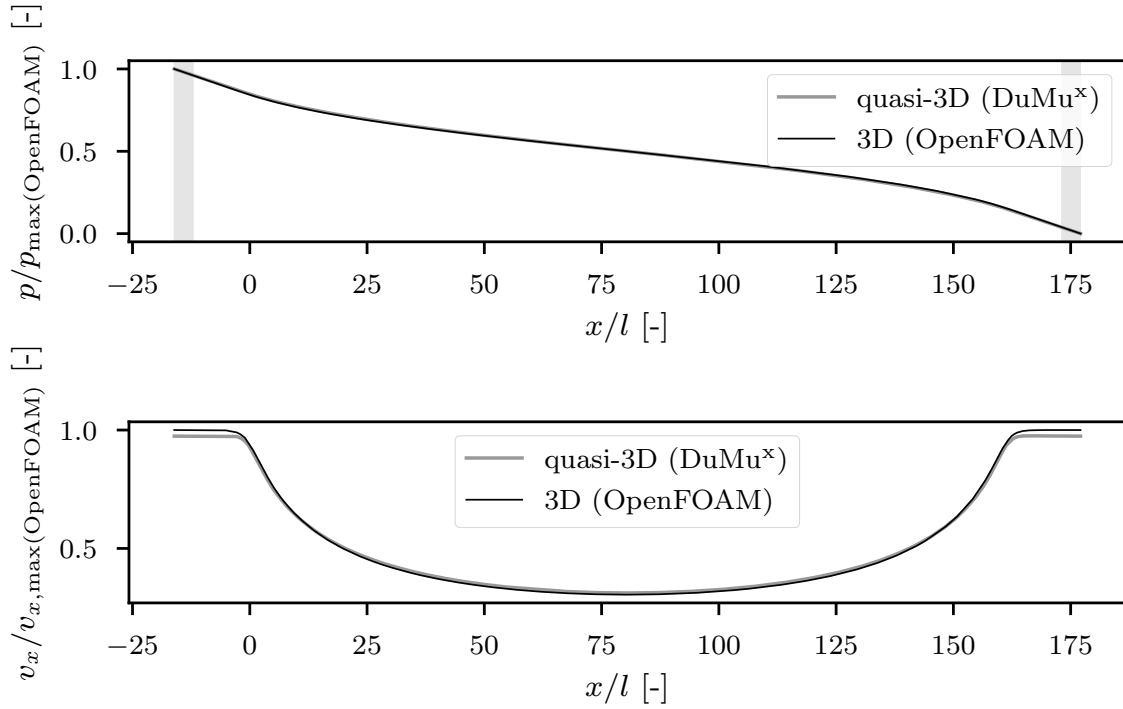


Figure 7.13 – Pressure and velocity in the channel. Profiles of p (top) and v_x (bottom) along the central axis of the free-flow channel ($y = 1 \times 10^{-3}$ m, $z = 100 \times 10^{-6}$ m) for both the 3D and the quasi-3D model. The gray boxes indicate an almost linear pressure gradient. All results are normalized by the maximum values of the 3D model. Adapted from Weishaupt et al. [2019b] (license: CC BY 4.0).

The velocity increases again in the triangular reservoir ($y/l < -40$) where it reaches around 60 % of the free-flow channel velocity. The solution of the quasi-3D model closely follows the reference solution. It slightly over-predicts v_x with a maximum deviation of 7.6 % in the lower part of the porous medium. As previously mentioned, the error within the pore throats is likely due to the less favorable aspect ratio of the geometry with respect to the accuracy of Eq. (3.3).

Focusing on the inlet part of the free-flow channel, we again evaluate the local linear pressure gradient and use this value to compute the corresponding analytical solution (Eq. (7.1)) for v_x over the channel width (see Fig. 7.14b, in analogy to Fig. 7.3). As for the 3D model, the analytical and numerical solutions are virtually identical.

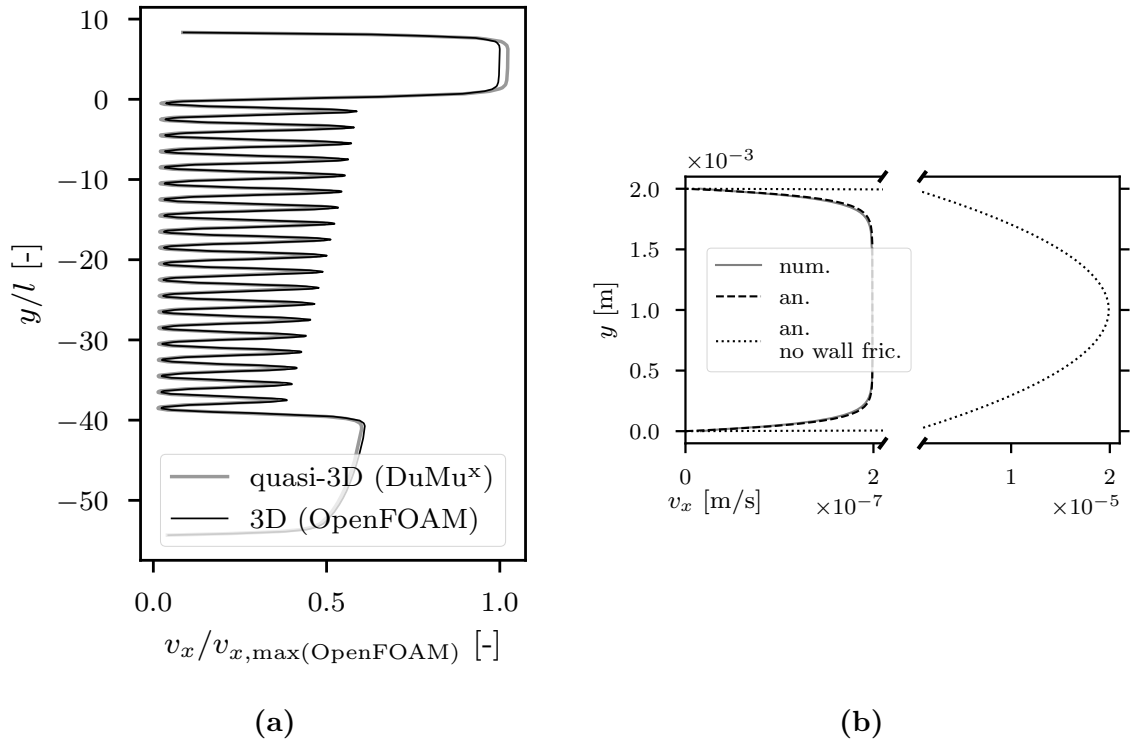


Figure 7.14 – Horizontal velocity profiles over height. Left (a): Velocity profiles v_x over y at $y/l = 80.5$ for the 3D and the quasi-3D model. Right (b): Velocity profile at the inlet of the free-flow channel and corresponding analytical solution (Eq. (7.1)). For comparison, also a parabolic flow profile, neglecting the friction of the top and bottom wall is shown. Adapted from Weishaupt et al. [2019b] (license: CC BY 4.0).

For comparison, Fig. 7.14b also shows the analytical solution when not including the wall friction term, which is just an ordinary parabolic profile where the maximum velocity is two orders of magnitude higher. This highlights the importance of including Eq. (3.3) for an accurate description of the flow field. The integral volumetric flow based on Eq. (7.5) deviates by less than 0.9% from the respective analytical value (Eq. (7.1)).

Figure 7.15 shows the evolution of the vertical velocities v_y along the interface for both the 3D and the quasi-3D model. As expected, there are peaks at the centers of the pore throats while v_y goes to zero at the solid blocks. The highest inflow into the porous domain, i.e., the most negative v_y , occurs at the very left throat. The amplitude of the velocity fluctuation then decreases until it reaches a minimum at the center of the interface ($x/l = 80.5$) after which it increases again in a symmetric manner. The

same behavior could be observed in the experiment [Terzis et al., 2019] and in the 3D simulations presented before. Due to model symmetry, $v_y = 0$ at $x/l = 80.5$. There is again a very good fit between the quasi-3D solution and the reference solution with the highest deviation at the leftmost and the rightmost throat (6.5%).

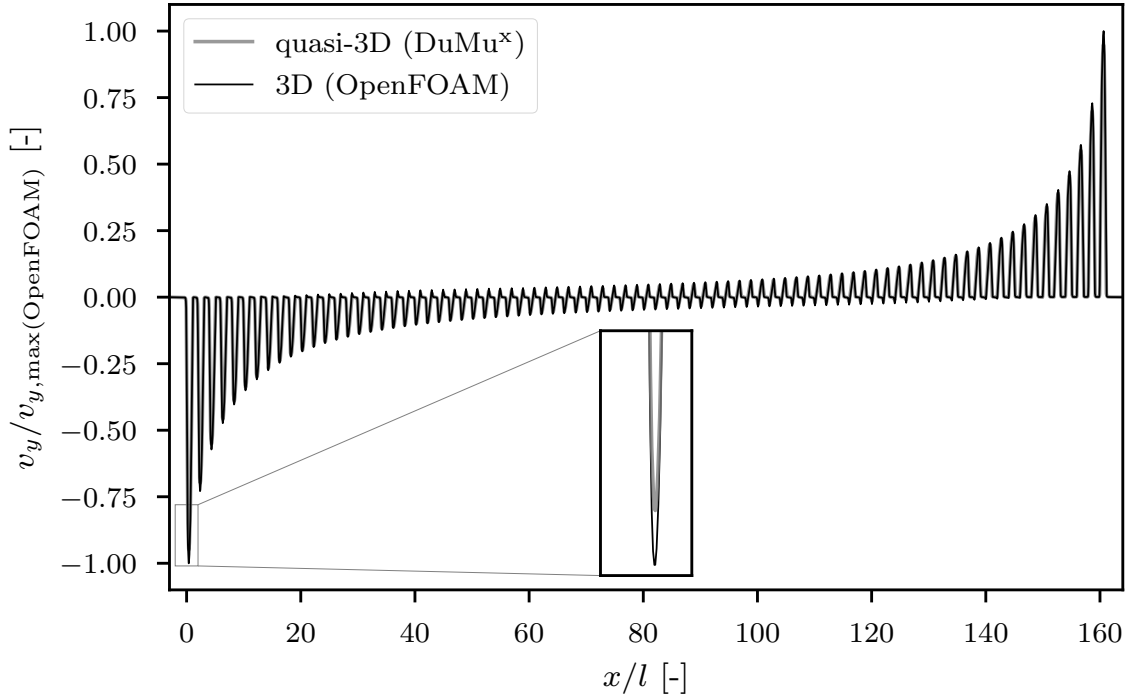


Figure 7.15 – Vertical velocity profiles over length. Normalized v_y at the interface in stream-wise direction ($y/l = 0$) for the 3D and the quasi-3D model. Adapted from Weishaupt et al. [2019b] (license: CC BY 4.0).

In conclusion, applying the quasi-3D model to the given micromodel geometry closely recovers the 3D reference solution both qualitatively and quantitatively, despite the unfavorable aspect ratio of 0.83 within the porous domain. The local errors observed are of the same order of magnitude as the ones found for the single-duct case shown in the section before. The quasi-3D model uses 20 times less grid cells and only 11 minutes of CPU time were needed in contrast to the 3D model which ran for over 4 hours. As a next step towards further model reduction, the necessary pore-network model parameters for the given geometry are evaluated in the following section.

7.1.5 Numerical determination of pore-network model parameters

This section discusses the numerical procedure for determining essential pore-network model parameters. First, the throat conductance g_{ij} for single-phase flow in the highly regular porous medium is evaluated since there is no closed analytical expression for this particular geometry. Second, the pore-scale slip coefficient β_{pore} is determined.

Throat conductance As explained in Section 2.4.2, the throat conductance factor g_{ij} can be determined analytically for rather simple geometries. Furthermore, the pressure drop within the pore bodies may often be neglected. This is not appropriate, however, for the porous structure of the microfluidic device where the pore bodies and throats feature the same spatial extent (see Fig. 7.1). Here, the pore bodies basically resemble cubes with open boundaries over which flow occurs. While analytical solutions for channel-type rectangular geometries (the throats) with only two open ends exist, e.g., Eq. (2.38), no such expression could be found for the open-boundary cubes.

Therefore, we performed numerical upscaling by discretely meshing a small part of the porous geometry and solving the stationary Stokes equations (Eq. (3.2)) on it. The results are given at the end of the paragraph. In addition, we conducted a brief parameter study to assess the validity and expectable accuracy of using a pore-network model to describe highly regular, rather technical porous media (see Fig. 7.16). The upscaling procedure is also explained there.

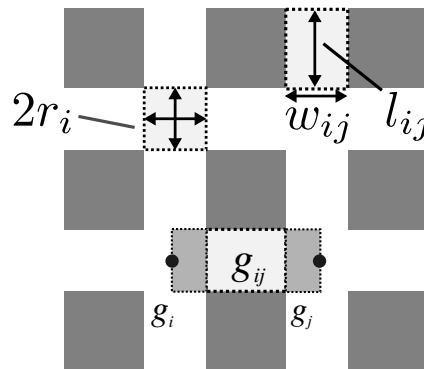


Figure 7.16 – Schematic depiction of the regular porous structure. Pore bodies are always quadratic ($w_{ij} = 2r_{ij} = 2r_i$) while the throat length l_{ij} might be greater than the width w_{ij} . Adapted from Weishaupt et al. [2019a] (license: CC BY 4.0).

Table 7.2 shows the three porous structures (A, B and C) with different pore body and pore throat dimensions considered for the study. Figure 7.16 illustrates that the width of the throats w_{ij} is always twice the inscribed radius r_i of the pore bodies. The throat lengths l_{ij} are different for each setup. Structure A has pore bodies and throats of the same size while B and C feature smaller pore bodies as well as longer and narrower pore throats. For sake of simplicity and in order to exclude any errors related to a quasi-3D description of the network, we consider a two-dimensional domain for this brief parameter study while the quasi-3D approach will be used for the upscaling of the actual micromodel geometry parameters, as explained later. We will therefore consider height-specific volume flow rates \tilde{Q}_{ij} (in $\text{m}^3/(\text{sm}) = \text{m}^2/\text{s}$) here but the method works exactly the same in 3D.

Table 7.2 – Variation of porous structures. Characteristic features of the three porous structures used for assessing the accuracy of the pore-network model. The number of degrees of freedom (n_{DOF}) refers to the reference solution (Stokes) where each throat is discretized with 40 grid cells per throat width. The pore-network model features 117 degrees of freedom for each structure. Adapted from Weishaupt et al. [2019a] (license: CC BY 4.0).

structure	w_{ij} [μm]	l_{ij} [μm]	n_{DOF} [-]	figure
A	250	250	1,260,720	
B	100	400	3,874,320	
C	50	450	8,230,320	

Figure 7.17 shows the setup used for the numerical upscaling process of the throat conductance. The positions for evaluating the relevant quantities are also shown in the figure. The domain is a cut-out of the actual porous structures A, B or C, featuring the same pore body and throat dimensions but only nine interior pore bodies.

A uniform grid (excluding the void parts of the structure) with 40 cells per throat width was used and fixed pressure boundary conditions with $\Delta p = 1 \times 10^{-3}$ Pa at the left and the right side of the domain were applied whereas no-flow/no-slip conditions were assigned elsewhere.

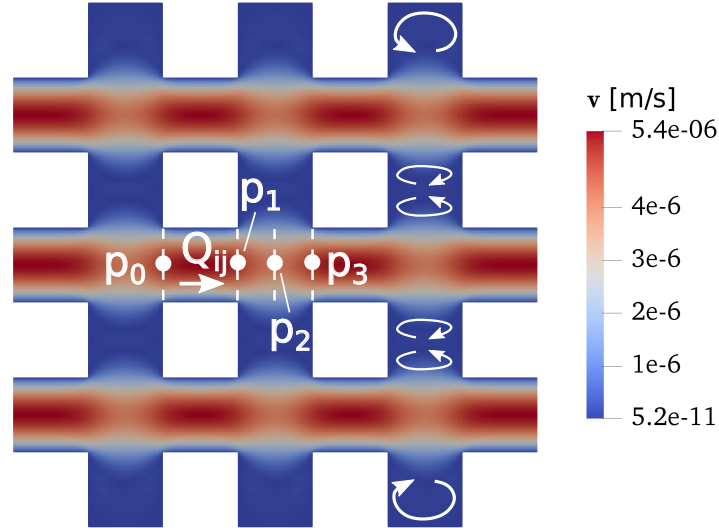


Figure 7.17 – Numerical determination of the conductance factors. $w_{ij} = l_{ij} = 250 \times 10^{-6}$ m. The throat conductance factor g_{ij} is evaluated using the pressures at p_0 and p_1 and the height-specific volumetric flow \tilde{Q}_{ij} . For the pore-body-half conductance factor g_i , p_1 and p_2 are considered (using p_2 and p_3 would yield the same result). The curved arrows indicate recirculation zones of different shapes at the domain's center and boundaries. Taken from Weishaupt et al. [2019a] (license: CC BY 4.0).

Though the porous structure itself is periodic, a computational domain including several pore bodies and throats was chosen in order to minimize potential internal and boundary-related influences and to obtain a conductance factor representative for interior pore bodies and throats. These influences can be seen, e.g., in the form of recirculation zones or *Moffat eddies* [Moffatt, 1964] of different shapes and sense of rotation as sketched in Fig. 7.17.

Equation (2.41) is used to determine the integral conductance value

$g_{ij}^* = (g_{ij}^{-1} + g_i^{-1} + g_j^{-1})^{-1}$ which accounts for the throat and the two pore body halves.

Relating the height-specific volume flow rate \tilde{Q}_{ij} through the pore throat highlighted in Fig. 7.17 with the measured pressure drop between the two points p_0 and p_1 yields a conductance factor for the throat after re-arranging Eq. (2.36):

$$g_{ij} = \tilde{Q}_{ij} (p_0 - p_1)^{-1}. \quad (7.9)$$

Similarly, the conductance factors for the pore body halves can be calculated:

$$g_i = g_j = \tilde{Q}_{ij}(p_1 - p_2)^{-1} = \tilde{Q}_{ij}(p_2 - p_3)^{-1} . \quad (7.10)$$

For the given structures, pore bodies at the boundaries are assumed to be volumeless and thus feature no resistance. Table 7.3 summarizes the results for A, B and C. Furthermore, the conductance values for the throats alone, as given by the analytical solution for two-dimensional flow between two parallel plates,

$$g_{ij} = \frac{w_{ij}^3}{12 \mu l_{ij}} , \quad (7.11)$$

are shown. The deviations between the analytical and the numerical values are less than 1%. The ratio between the plain pore throat conductance and the effective one, considering the pore bodies, is given by $\frac{g_{ij}}{g_{ij}^*}$ and can serve as an estimate of how much the volumetric flow rates might be overestimated when the pressure drop in the pore bodies is neglected and only the analytical solution for g_{ij} is used.

Table 7.3 – Upscaled results. Conductance factors for the throats g_{ij} (numerical and analytical values) and the pore body halves g_i for the three structures. Additionally, the effective conductance g_{ij}^* including the resistance of the throat and of the pores is given.

struct.	w_{ij}	l_{ij}	g_{ij} (num./an.)	g_i	g_{ij}^*	$\frac{g_{ij}}{g_{ij}^*}$
	[μm]					
A	250	250	$5.26 \times 10^{-6} / 5.21 \times 10^{-6}$	1.76×10^{-5}	3.30×10^{-6}	1.58
B	100	400	$2.09 \times 10^{-7} / 2.08 \times 10^{-7}$	2.83×10^{-6}	1.82×10^{-7}	1.14
C	50	450	$2.32 \times 10^{-8} / 2.31 \times 10^{-8}$	7.08×10^{-7}	2.18×10^{-11}	1.06

After evaluating the pore throat conductance factors on the reduced geometries presented in Fig. 7.17, we briefly assess the applicability of the pore-network model for the entire regular porous structures A, B and C, featuring 81 interior pore bodies in total.

For each structure, horizontal and diagonal flow is considered in order to estimate the error introduced by the pore-network model's inability to account for a deflection of the flow direction within certain pores and non-parallel flow within the throats.

Numerical reference solutions were created for all structures by solving the stationary Stokes equations (Eq. (3.2)) on a uniform grid with 40 cells per throat width (excluding the void parts of the structure). The boundary conditions for the reference solutions and the pore-network model were set according to Fig. 7.18. For horizontal flow, fixed pressures were applied at the left and the right boundary of the domain ($p_{\text{left}} = 1 \times 10^{-3}$ Pa, $p_{\text{right}} = 0$ Pa). For diagonal flow, a linear pressure gradient was set at the top of the domain ($p_{\text{top}} = 1 \times 10^{-3}$ Pa $(1 - \frac{x}{x_{\text{max}}})$) and again a fixed pressure of $p_{\text{right}} = 0$ Pa was assigned at the right border. No-flow/no-slip conditions were set at the remaining boundaries.

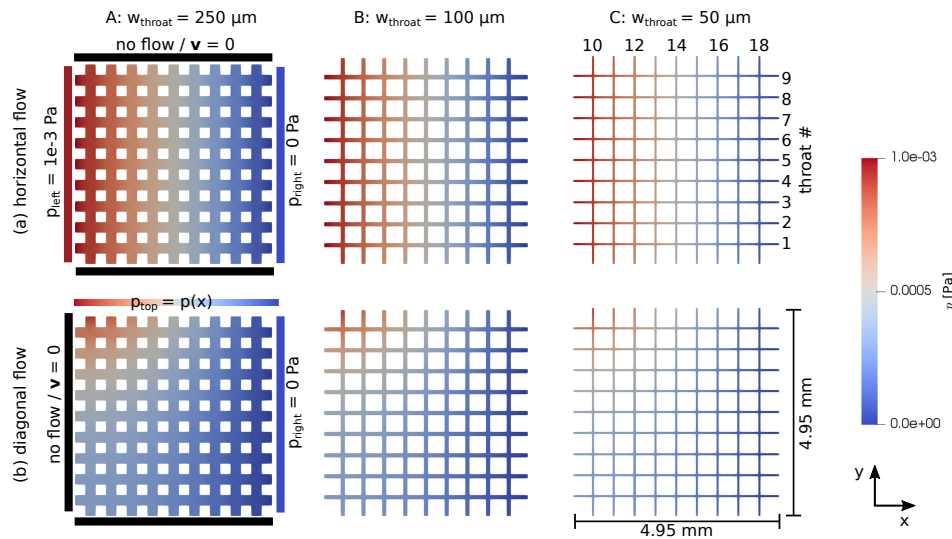


Figure 7.18 – Setups for assessing the PNM's accuracy. Boundary conditions and resulting pressure fields of the reference solutions for the different structures and flow configurations. Taken from Weishaupt et al. [2019a] (license: CC BY 4.0).

Figure 7.19 summarizes the height-specific volume flow rates per throat at the right boundary for the reference solution and the pore-network model. Note that the x -axis is logarithmic. The numbers on the y -axis correspond to the throats labeled at the top right part in Fig. 7.18. The results of the pore-network model neglecting the pore-body resistance clearly deviate from the corresponding 2D reference solutions, especially for the coarsest structure A. Including the pore-body resistance (PNM*) notably increases

the accuracy for the horizontal and the diagonal flow setup. This is also reflected in Table 7.4 where the errors with respect to the cumulative flow over all throats on the right side of the domain are given. For the coarsest structure A ($w_{ij} = 250 \mu\text{m}$), the actual outflow for the horizontal setup is overestimated by over 50% when neglecting the pore-body losses. This error decreases for the finer structure B ($w_{ij} = 100 \mu\text{m}$) to around 13% and is lowest for structure C ($w_{ij} = 50 \mu\text{m}$) with approximately 6%.

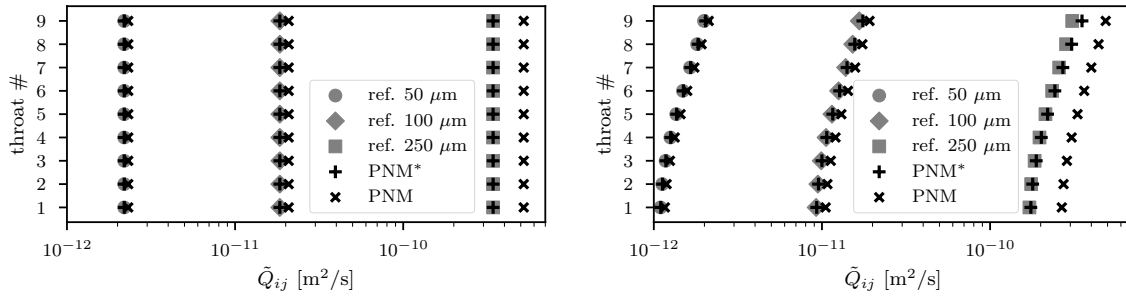


Figure 7.19 – Comparison of horizontal volume flow rates. Height-specific volume flow rates per throat on the right side of the domain for the reference solution (Stokes model) and the pore-network model for structures A-C. Left: horizontal flow; right: diagonal flow. The pore-network model PNM* considers pressure drops within the pore bodies while the other one does not. Adapted from Weishaupt et al. [2019a] (license: CC BY 4.0).

These deviations are very close to the estimated ones presented in Table 7.3. When including the pore-body resistance, the errors decrease to only 0.05% for structure A and even less for B and C. The coarser the structure, the greater the benefit of considering g_i . The same findings hold, in general, also for the diagonal flow setup (right side of Fig. 7.19). However, larger errors occur both locally at the upper throats and globally when considering the cumulative outflow even when considering the pore-body pressure losses. As seen in Table 7.4, the overestimation of the outflow grows to over 5% for structure A.

Table 7.4 – Accuracy of the pore-network model. Deviation of the pore-network model’s total outflow from the reference solution. In the first row (PNM), pressure drops within the pore bodies are neglected, yielding substantially higher errors.

structure	A		B		C	
	hor.	diag.	hor.	diag.	hor.	diag.
err. PNM	+52.14	+55.86	+12.89	+14.10	+5.66	+6.24
err. PNM*	+0.05	+5.47	+0.02	+2.01	+0.01	+0.98

Figure 7.20a shows the cumulative inflows through the top throats #10 -#18 (see upper right in Fig. 7.18).

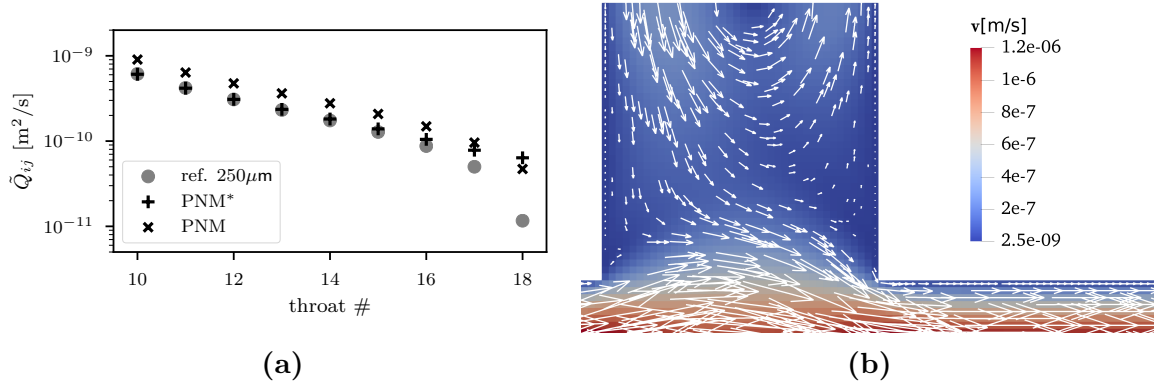


Figure 7.20 – Comparison of vertical volume flow rates. (a): height-specific volume flow rates per throat at the domain’s top for the reference solution (Stokes model) and the pore-network model for structure A. The pore-network model PNM* considers pressure drops within the pore bodies while the other one does not. (b): close-up of the velocity pattern at the upper rightmost throat #18. Adapted from Weishaupt et al. [2019a] (license: CC BY 4.0).

The pore-network model clearly fails to correctly predict the height-specific volume flow rates at the three rightmost throats #16 - #18 even when the pore-body resistance is considered (the result is even worse in the case of the last throat). The reason for this is seen in Fig. 7.20b which shows the velocity field of the reference solution at the rightmost throat #18. Here, pronounced recirculation can be identified at the top boundary, where some flow even leaves the domain. Here, the assumption of flow completely parallel to the throat’s walls is clearly violated, which is, however, a mandatory requirement for the pore-network model. This potential source of error should be kept in mind when applying the coupled model to rather coarse porous media. For the finer structures B and C, some recirculation can still be observed (not shown), however, of far smaller spatial extent and with less impact on the pore-network model’s accuracy.

Having a better understanding of the pore-network model’s reliability for regular structures, we finally present the throat conductance for the micromodel geometry of the actual experiment (Fig. 7.1). As this geometry features a rather unfavorable aspect ratio of 0.83 (see discussion in previous section), a three-dimensional reference model might yield more accurate upscaled conductance values compared to a quasi-3D one. We nevertheless made use of the latter for determining g_{ij}^* for sake of consistency with

the coupled model, where the free-flow part is also accounted for by the quasi-3D model. Following the same upscaling approach as before, values of $g_{ij} = 3.05 \times 10^{-10} \text{ m}^3/(\text{sPa})$ and $g_i = g_j = 8.47 \times 10^{-10} \text{ m}^3/(\text{sPa})$ were found for the PDMS micromodel.

Slip coefficient The second input parameter needed for the coupled model is the pore-scale slip coefficient β_{pore} (see Section 4.1). We approximate this value by solving a simplified, equivalent problem of free flow over a single pore throat intersecting with the lower boundary of the free-flow channel (see Table 7.5). We furthermore briefly investigate the accuracy of the slip-velocity approach.

As seen in Table 7.5, the setup consists of a quadratic free-flow channel with a side length of $1 \times 10^{-3} \text{ m}$ and a subjacent quadratic throat. Considering four different throat widths, a relation between β_{pore} and w_{ij} was found, applicable for a wider range of different porous geometries. Using the quasi-3D approach, a virtual height of $h_{\Omega} = 200 \text{ }\mu\text{m}$ was set for the free-flow channel and the throat for all cases. The geometry was meshed uniformly (40 cells per throat width) and the stationary Stokes model (Eq. (3.2)) was employed. A horizontal pressure drop of $\Delta p = 1 \times 10^{-9} \text{ Pa}$ was prescribed, while no-flow/no-slip conditions were set elsewhere. The slip velocities and the velocity gradients at the interface between throat and free flow (see dotted line at the bottom of Table 7.5) were then extracted, averaged and used to approximate the slip coefficient:

$$\beta_{\text{pore}} \approx \frac{\left\langle \frac{\partial v_x}{\partial y} + \frac{\partial v_y}{\partial x} \right\rangle}{\langle v_x \rangle}. \quad (7.12)$$

We neglected the horizontal velocity component in the throat's interior for geometrical reasons. The resulting factors are given in the last column of Table 7.5. They were used to recalculate the setups with the coupled model, i.e, replacing the small cavity by a single one-dimensional pore throat of the same width and length, for estimating the accuracy of the slip-velocity approach. The velocity fields of the quasi-3D (reference) model and of the coupled model are shown in the first and second column of Table 7.5, next to a comparison of the velocity profiles. The latter show virtually identical results for $w_{ij} = \{50, 100, 200\} \text{ }\mu\text{m}$ while the coupled models slightly underestimates the slip velocity at the bottom of the channel for $w_{ij} = 400 \text{ }\mu\text{m}$. The smaller the throat width, the better the fit.

Table 7.5 – Setups for the numerical determination of β_{pore} . Throat widths of $50\ \mu\text{m}$, $100\ \mu\text{m}$, $200\ \mu\text{m}$ and $400\ \mu\text{m}$ are considered, as indicated by the white numbers. The throats are quadratic ($w_{ij} = l_{ij}$), as well as the free-flow channel above them which features side lengths of $1 \times 10^{-3}\ \text{m}$. Depicted are the reference solutions (left), the solutions of the coupled model, and a plot comparing the velocity profiles of the two models along the vertical white line. On the right, the values of β_{pore} are given. The green boxes symbolize the virtual extent of the one-dimensional throats. The quasi-3D approach was used for the reference and for the coupled model. Adapted from Weishaupt et al. [2019b] (license: CC BY 4.0).

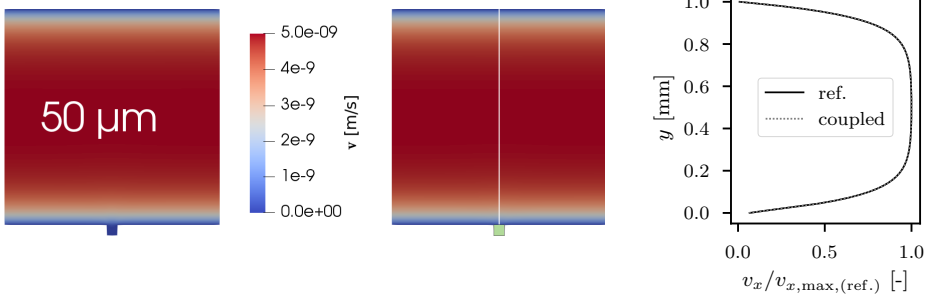
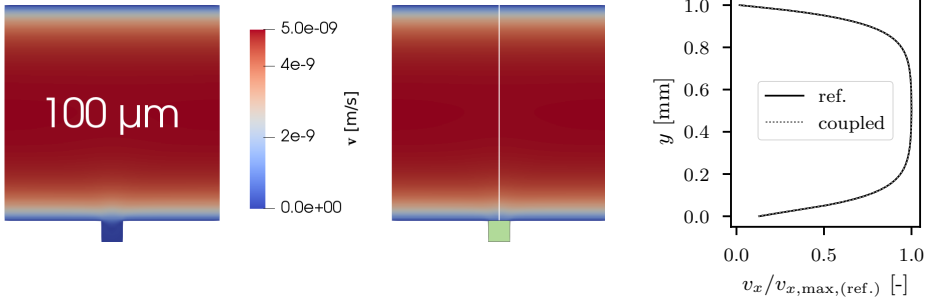
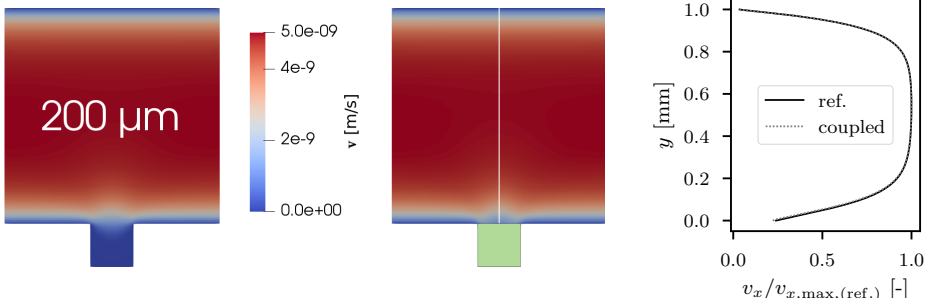
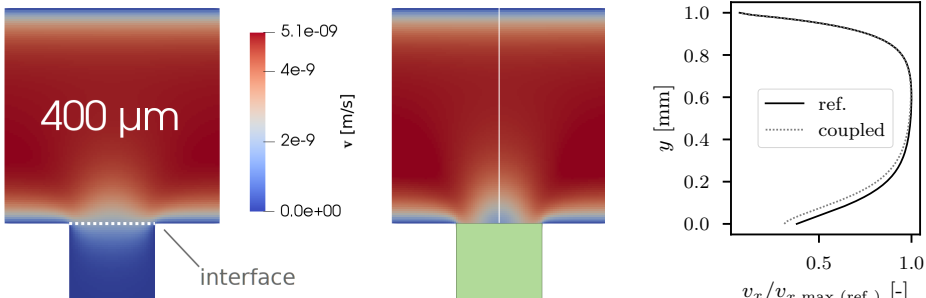
setup (reference / coupled model)	v_x over y	$\beta_{\text{pore}} [1/\text{m}]$
	176416	
	84550	
	39924	
	19087	

Figure 7.21 shows the different slip coefficients over w_{ij} . For sake of completeness, also values for purely two-dimensional setups neglecting the flow resistance of the channel's bottom and top wall (z -coordinate) are given.

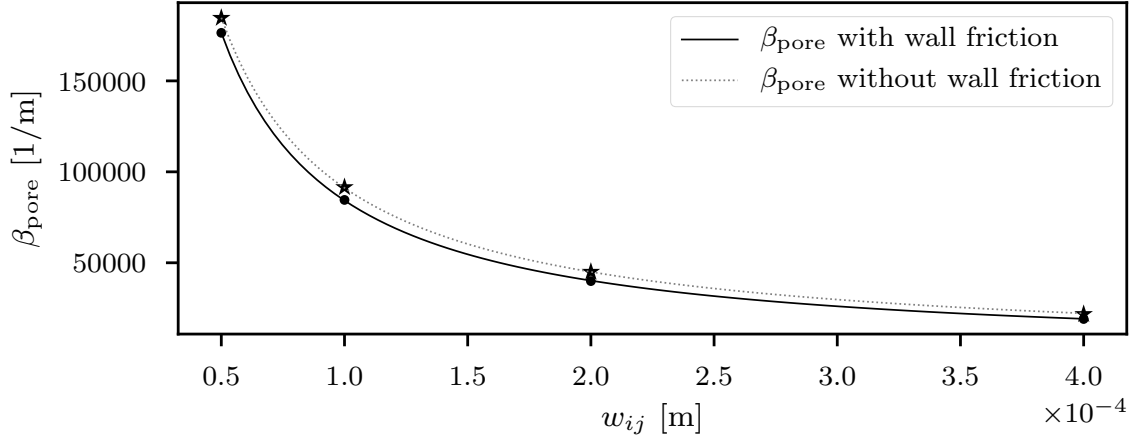


Figure 7.21 – Influence of the throat width on β_{pore} . Plot of β_{pore} over w_{ij} for a case considering wall friction ($h_{\Omega} = 200 \mu\text{m}$) and a case neglecting this influence. Adapted from Weishaupt et al. [2019b] (license: CC BY 4.0).

Using a power-law fit ($R^2 = 0.999$), a functional relation between β_{pore} and w_{ij} was found,

$$\beta_{\text{pore}}(w_{ij}) \approx aw_{ij}^b, \quad (7.13)$$

with the empirical constants $a = 4.531 \text{ m}^{0.067}$, $b = -1.067$ for the case with wall friction and $a = 7.68 \text{ m}^{0.019}$, $b = -1.019$ without wall friction. β_{pore} may be nondimensionalized by multiplication with w_{ij} which yields almost constant values of $\beta_{\text{pore}}^* = \{8.82, 8.45, 7.98, 7.63\}$ and $\beta_{\text{pore}}^* = \{9.23, 9.15, 9.00, 8.70\}$ (with and without wall friction) for the given widths w_{ij} . If the aspect ratio between throat and free-flow channel is kept constant for different values of w_{ij} (i.e., scaling both domains uniformly), β_{pore}^* will actually become a true constant for the case without wall friction. Interestingly, this does not hold if wall friction is considered.

The validity of the novel approach for incorporating the slip velocity over pore throats at the interface was further assessed. Figure 7.22 shows a close-up of the interface region

for $w_{ij} = 100 \mu\text{m}$. The yellow velocity vectors correspond to the solution of the reference model (quasi-3D), the purple vectors to the solution of the coupled model including the throat slip coefficient. For comparison, also black velocity vectors corresponding to the solution of the coupled model without considering a slip velocity at the interface ($v_x = 0$) are shown. Note that the vectors of the coupled models are only given in the free-flow channel because the cavity (below the white line) is modeled as a one-dimensional throat where only an averaged vertical velocity is defined. There is an excellent fit between the reference solution and the coupled model including the slip term: the corresponding velocity vectors both feature very similar magnitudes and orientations. This is in contrast to the coupled model employing a no-slip condition at the interface. Here, the black velocity vectors clearly deviate from the reference solution, especially at the very left and the very right part of the interface. The greater the distance to the interface, the smaller the deviations. The relative error for the velocities (compared to the reference solution, as defined by Eq. (7.8)) reduces by a factor of 9 from 5.26×10^{-3} to 5.83×10^{-4} when including the slip above the throats. For the pressure, this error drops by a factor of 3.72 from 1.85×10^{-3} to 4.98×10^{-4} .

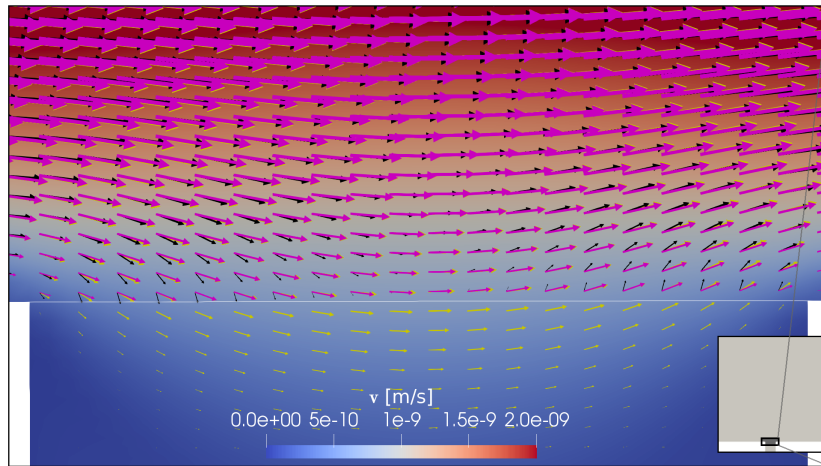


Figure 7.22 – Near-interface flow field. Close-up of the interface region (see gray inlay) for a vertical throat with $w_{ij} = 100 \mu\text{m}$. The yellow, purple and black velocity vectors correspond to the reference (quasi-3D) model, the coupled model including the slip term and the coupled model with a no-slip condition at the interface. Taken from Weishaupt et al. [2019b] (license: CC BY 4.0).

Figure 7.23 shows a modified situation where the pore throat is inclined by an angle of 45° and features an inflow of $1.33 \times 10^{-17} \text{m}^3/\text{s}$ from its bottom. For this case, the differences between the coupled models including or not including the slip term are

smaller than before. Both deviate from the reference solution at the left half of the image, close to the interface. The pronounced upward flow at the throat's left edge is not captured by the coupled models. Nevertheless, including the slip term slightly improves the global fit with the reference solution. The relative error for the velocity given by Eq. (7.8) reduces by a factor of 1.3 from 1.07×10^{-2} to 8.14×10^{-3} after including the slip term (compared to a factor of 9 for the orthogonal throat). The error for the pressure decreases from 4.78×10^{-3} to 3.23×10^{-3} which corresponds to a factor of 1.48 compared to 3.72 for the orthogonal throat.

Note that we still used β_{pore} from the case of the orthogonal throat without inflow from the bottom since the idea of the novel approach is to provide an approximation of the slip velocity with reasonable accuracy under a minimum of complexity and computational cost. Hence, evaluating β_{pore} on a multitude of different geometries and flow configurations is not intended here. This could be addressed in future work.

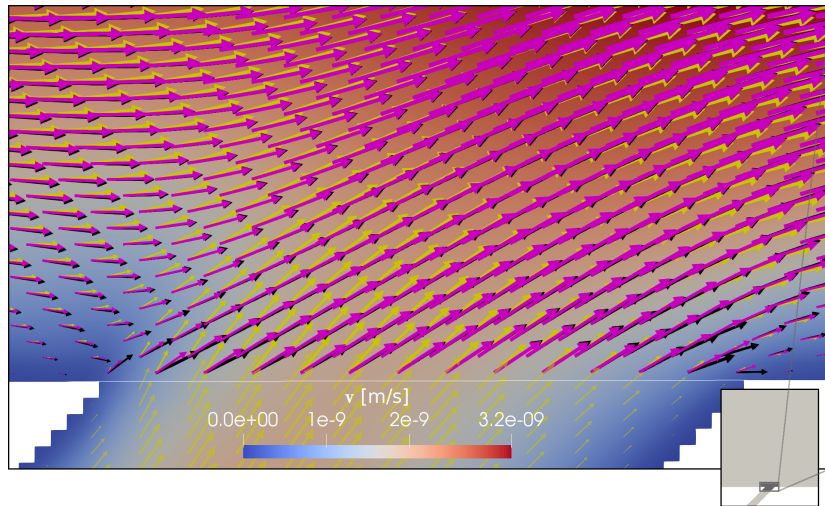


Figure 7.23 – Near-interface flow field. Close-up of the interface region (see gray inlay) for a throat inclined by 45° with $w_{ij} = 100 \mu\text{m}$. There is an inflow from the bottom of the throat and flow from left to right in the free-flow channel. The yellow, purple and black velocity vectors correspond to the reference (quasi-3D) model, the coupled model including the slip term and the coupled model with a no-slip condition at the interface. Taken from Weishaupt et al. [2019b] (license: CC BY 4.0).

Only for sake of a detailed analysis, we re-evaluated β_{pore} for the inclined flow setup, yielding a new value of 28001 (compared to 84550). However, this barely affected the results of the coupled model, which is why they are not shown here. Considering the

slip velocity has thus a negligible effect compared to the throat's horizontal velocity contribution $[\mathbf{v}]^{\text{PNM}} \cdot \mathbf{t}_k$ which dominates the coupling condition Eq. (4.10) in this case.

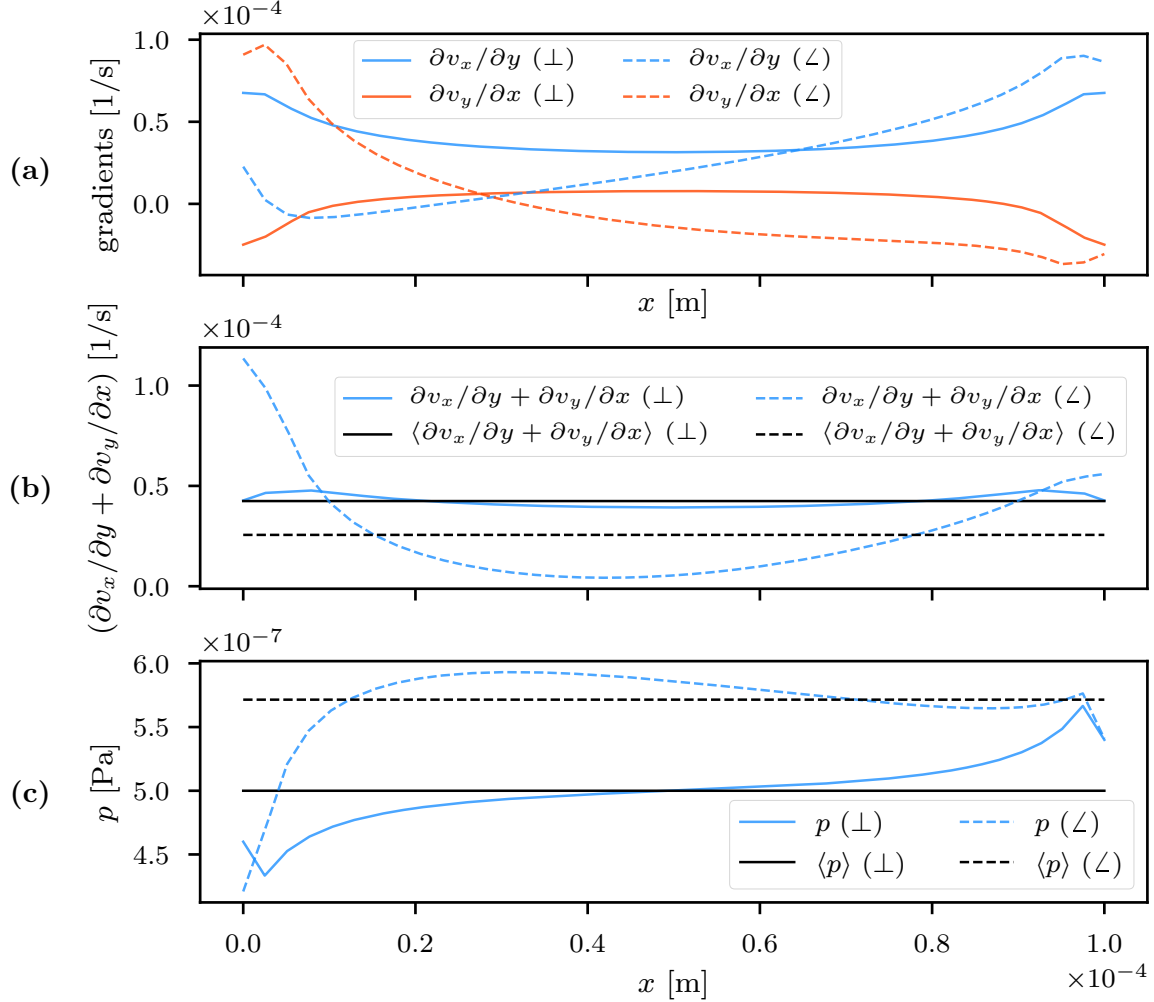


Figure 7.24 – Shear rates and pressure distribution at the interface. Comparison of the velocity gradient (a), shear rate (b), and pressure (c) at the interface for the orthogonal setup (\perp , Fig. 7.22) and the setup featuring a throat inclined by 45° with inflow from the bottom (\angle , Fig. 7.23). Mean values (with respect to the interface) are given by $\langle \cdot \rangle$.

Figure 7.24 shows the velocity gradients $\partial v_x / \partial y$ and $\partial v_y / \partial x$ as well as the shear rate $(\partial v_x / \partial y + \partial v_y / \partial x)$ and the pressure distribution p along the interface for the orthogonal and the inclined throat, in addition to the respective averaged values used in Eq. (7.12). While the curves for the orthogonal throat appear to be entirely symmetrical with rather small local deviations from the averaged value, the situation is quite different for the

inclined throat with bottom inflow. Here, the highest shear rates in Fig. 7.24b occur at the left edge of the throat and the curve is not symmetrical anymore. The averaged value therefore seems less adequate for describing the shear behavior in an integral way. In addition, the pressure distribution (Fig. 7.24c) is quite non-uniform for the case of bottom inflow which conflicts with our coupling condition for the normal momentum exchange (Eq. (4.4)), assigning a single and constant value of p at Γ_i .

We repeated the evaluation of β_{pore} under the consideration of the horizontal velocity within the throat's interior as given by the reference solution. This velocity, however, was actually slightly higher than the free-flow slip velocity at the interface, thus leading to negative values of β_{pore} and non-physical results in the coupled model.

In summary, both parameters for the coupled model, the effective throat conductance factor g_{ij}^* and the throat slip coefficient β_{pore} , have been determined numerically. A power-law functional relation between β_{pore} and w_{ij} was found. For a throat with no inclination, the coupled model including the slip velocity at the interface could accurately reproduce the reference solution for $w_{ij} < 400 \mu\text{m}$, which is a clear improvement compared to assuming a no-slip condition at the interface. Modifying the setup by considering an inclined throat with bottom inflow shows the limitations of the new approach. Nevertheless, the coupled model still benefits slightly from accounting for the slip velocities. Considerable deviations only occur directly at the interface and diminish with increasing distance. The micromodel geometry under consideration here (see Fig. 7.1) only features orthogonal throats at the interface, therefore the approach is suitable for increasing the coupled model's accuracy in a simple and efficient manner. In future work, this concept could be generalized for various types of geometries and flow configurations.

The pore-network model parameters evaluated here are needed in the next section where the microfluidic experiment is recalculated using the coupled free-flow/pore-network model.

7.1.6 Application of the coupled model on the micromodel geometry

In this section, we present the results of the hybrid-dimensional, coupled model applied to the PDMS micromodel experiment. For sake of comparability, the previously shown results (Section 7.1.4) of the quasi-3D model (which is also a component of the coupled model) will serve as reference solutions here. While the free-flow channel and the triangular reservoir are still discretely meshed and resolved in the same way as before, the porous domain is now substituted by an equivalent pore-network model. The input parameters are based on the numerical upscaling procedure described in the previous section, i.e., $w_{ij} = l_{ij} = 240 \mu\text{m}$, $g_{ij} = 3.05 \times 10^{-10} \text{ m}^3/(\text{sPa})$, $g_i = g_j = 8.47 \times 10^{-10} \text{ m}^3/(\text{sPa})$ and $\beta_{\text{pore}} = 33\,000 \text{ m}^{-1}$. The same boundary conditions as in Section 7.1.4 were chosen while all pore bodies on the boundaries, except those at the coupling interface Γ^{FF} , featured no-flow conditions. Running the coupled model on a single core of the same machine as before took less than 5 minutes which is only 43% of the CPU time required by the quasi-3D model. This is caused by the reduction of the number of degrees of freedom from 9 412 010 to 3 737 351 due to the use of the pore-network model in the porous domain. Figure 7.25 presents the corresponding velocity and pressure fields for the coupled model. Note that the pore throats show averaged velocities based on Eq. (3.9) which are by implication smaller than the peak free-flow velocities at the associated interface.

In Fig. 7.26, the central throat intersecting with the interface at $y/l = 0$, $x/l = 80.5$ is magnified. The velocity vectors of the quasi-3D reference solution are given in yellow, those of the coupled model with slip are shown in purple while those of the coupled model assuming a no-slip condition at the throat openings are marked black. The main-channel flow slightly dips into the throat cavity on the left and re-enters the main channel on the right. There is no net mass flux across the interface. This flow behavior is generally reflected by all three models. However, there is a significantly higher agreement between the reference solution's vectors and the one of the coupled model with slip, both in magnitude and orientation. The vectors' y -component of both coupled models is essentially determined by the coupling condition for the conservation of momentum in normal direction (Eq. (4.4)) and thus more or less identical. The black vectors, however, which correspond to the coupled model assigning a no-slip condition at the throats, feature drastically decreased x -components.

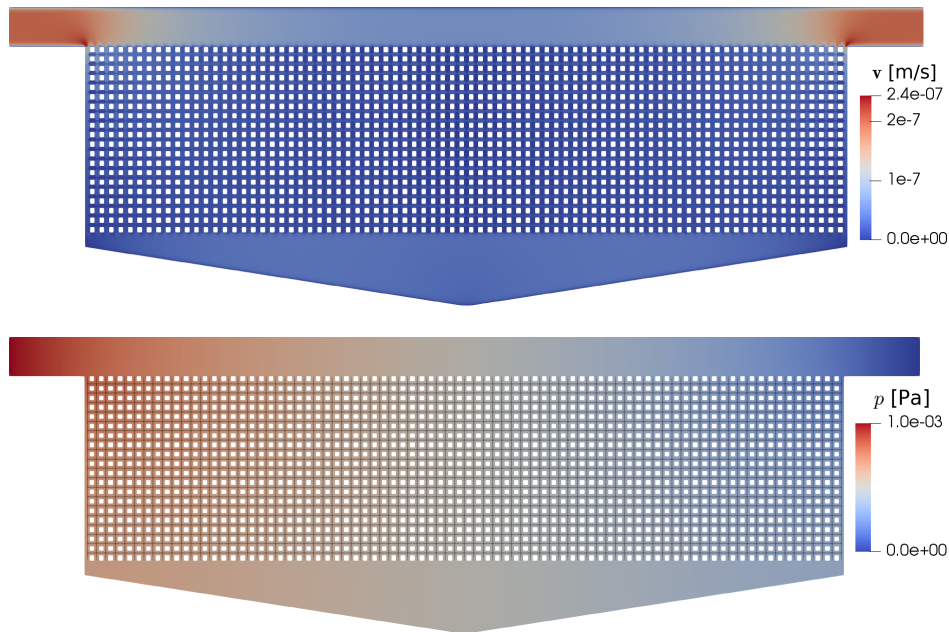


Figure 7.25 – Pressure and velocity fields of the coupled model. Two-dimensional velocity field (\mathbf{v}_{2D} , top) and pressure field (bottom) obtained by the coupled model (including the slip term) corresponding to the center plane ($z = 100 \times 10^{-6}$ m) of the 3D model. The one-dimensional throat elements of the pore-network model have been extruded for visualization purposes using ParaView’s [Ayachit, 2015] *Tube* filter. The pore throats show an averaged velocity based on Eq. (3.9). Taken from Weishaupt et al. [2019b] (license: CC BY 4.0).



Figure 7.26 – Near-interface flow field. Close-up of the interface region at the central throat ($x/l = 80.5, y/l = 0$). The yellow, purple and black velocity vectors correspond to the reference (quasi-3D) model, the coupled model including the slip term and the coupled model with a no-slip condition at the interface. Taken from Weishaupt et al. [2019b] (license: CC BY 4.0).

The same pattern can be observed in Fig. 7.27 which shows a close-up of the two leftmost throats at the interface. Here, we see a pronounced downward flow from the free-flow channel into the porous domain. Again there is a much better match with the

reference solution if the slip velocity is taken into account. Using Eq. (7.8) to calculate the relative error, based on the velocities in the free-flow channel and the triangular region, yields values of 9.49×10^{-3} for the coupled model including the slip term and 1.76×10^{-2} for the coupled model without the slip term, both with respect to the quasi-3D model simulation results as discussed before. In analogy, the relative error values for the pressure are 3.72×10^{-4} and 4.52×10^{-4} .

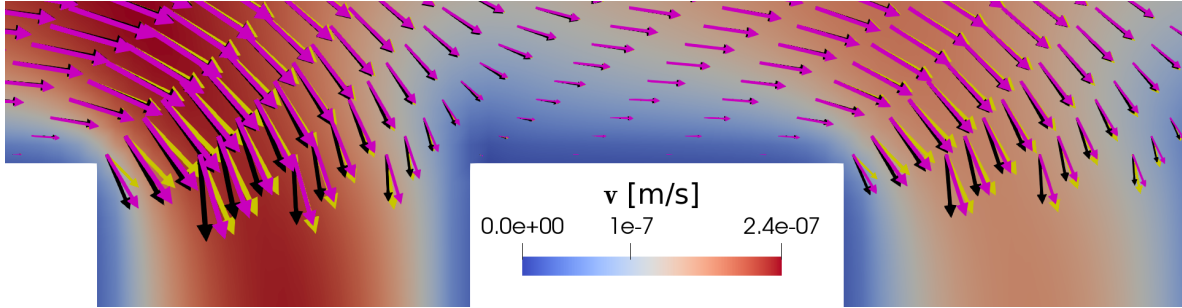


Figure 7.27 – Near-interface flow field. Close-up of the interface region at the two leftmost throats ($0 \leq x/l \leq 3, y/l = 0$). The yellow, purple and black velocity vectors correspond to the reference (quasi-3D) model, the coupled model including the slip term and the coupled model with a no-slip condition at the interface. Taken from Weishaupt et al. [2019b] (license: CC BY 4.0).

In Fig. 7.28, the vertical velocities v_y over the interface length are presented for the reference model and the coupled model including the slip term. Neglecting the slip term does not noticeably change the results, and thus the corresponding curve is not shown here. The solution of the coupled model qualitatively follows the one of the quasi-3D model, while generally over-predicting the velocity peaks, especially at the center of the model where discrepancies of up to 80% can be found. Large mismatches only occur near the edges of the throat openings. This can be explained by the symmetric downwards and upwards flows as previously discussed for Fig. 7.26, which is also reflected in the zoom-in shown in Fig. 7.28. As the over- and undershoots tend to cancel out at each throat, the global mass transfer over the interface does not suffer noticeably which is underlined by Fig. 7.29.

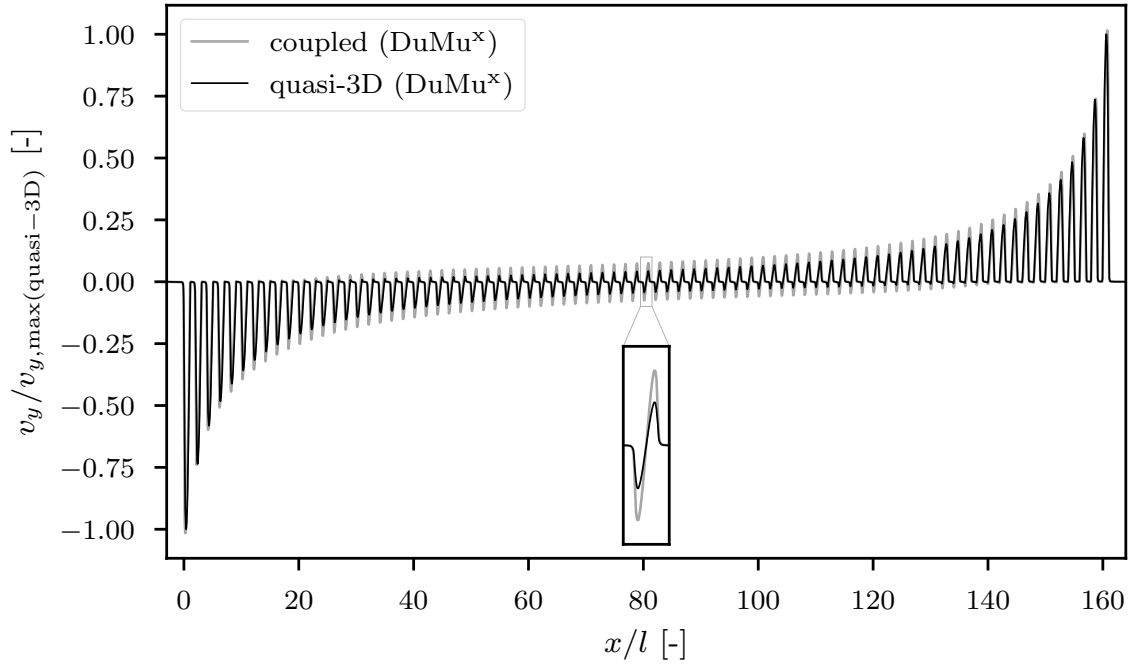


Figure 7.28 – Profiles of vertical velocity. Normalized v_y at the interface in stream-wise direction ($y/l = 0$) for the quasi-3D and the coupled model including the slip term. Taken from Weishaupt et al. [2019b] (license: CC BY 4.0).

Here, the total volumetric flow through each throat at the interface is shown, as evaluated by Eqs. (7.2) and (7.5). The throats are labeled with #1 to #81 from left to right. The values of the coupled models are almost identical to the ones of the quasi-3D reference solution, regardless whether slip is considered or not which means that the vertical mass exchange between free flow and porous medium is not significantly influenced by the slip velocity above the throats.

For comparison, also the throat volume flow rates of the 3D simulation conducted with OpenFOAM are shown in Fig. 7.29. The latter are in close accordance with the values for the quasi-3D and the coupled models implemented in DuMu^x. The deviations are largest at the very left and the very right throats which goes in line with the findings discussed previously for Fig. 7.11.

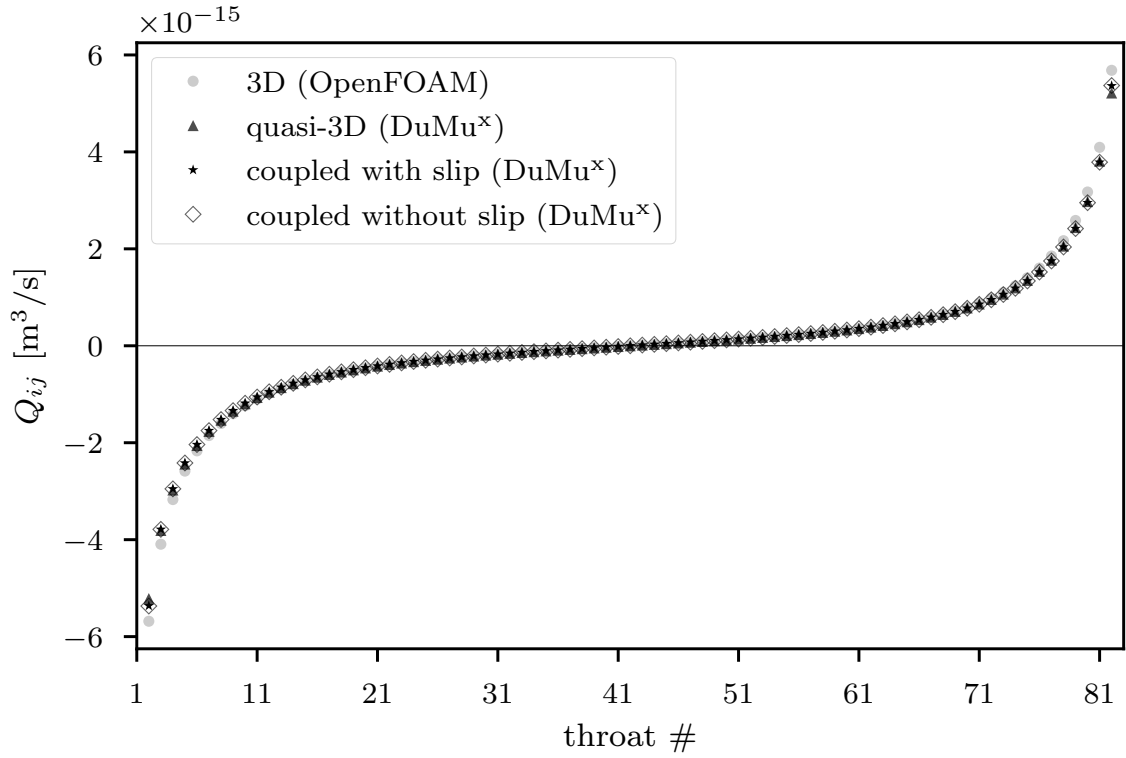


Figure 7.29 – Pore-local volume flow rates. Discrete volumetric flow rates at all throats intersecting with the interface for all numerical models. Adapted from Weishaupt et al. [2019b] (license: CC BY 4.0).

Finally, Fig. 7.30 sheds some light onto the flow conditions within the porous medium at the vertical center line of the micromodel. Depicted are the normalized horizontal velocities at $x/l = 80.5$, which is the exact center of the porous medium, and the integral volume flow rates Q at the throats directly left to the center line at $x/l = 79.5$, evaluated by Eqs. (2.36), (7.2) and (7.5) and likewise normalized. As the pore-network model only yields averaged velocities within the pore throats, v_x is only drawn in the free-flow channel and in the triangular region, where it matches almost perfectly with the solution of the quasi-3D model. Both models also give rise to very similar integral volume flow rates within the throats, which deviate by around 6% from the values of the 3D simulation. This can be explained by the aforementioned unfavorable aspect ratio of 0.83 in the pore throats which impairs the accuracy of Eqs. (3.3) and (7.5) used for the quasi-3D model from which subsequently also the throat conductances were derived by numerical upscaling, as described in Section 7.1.5.

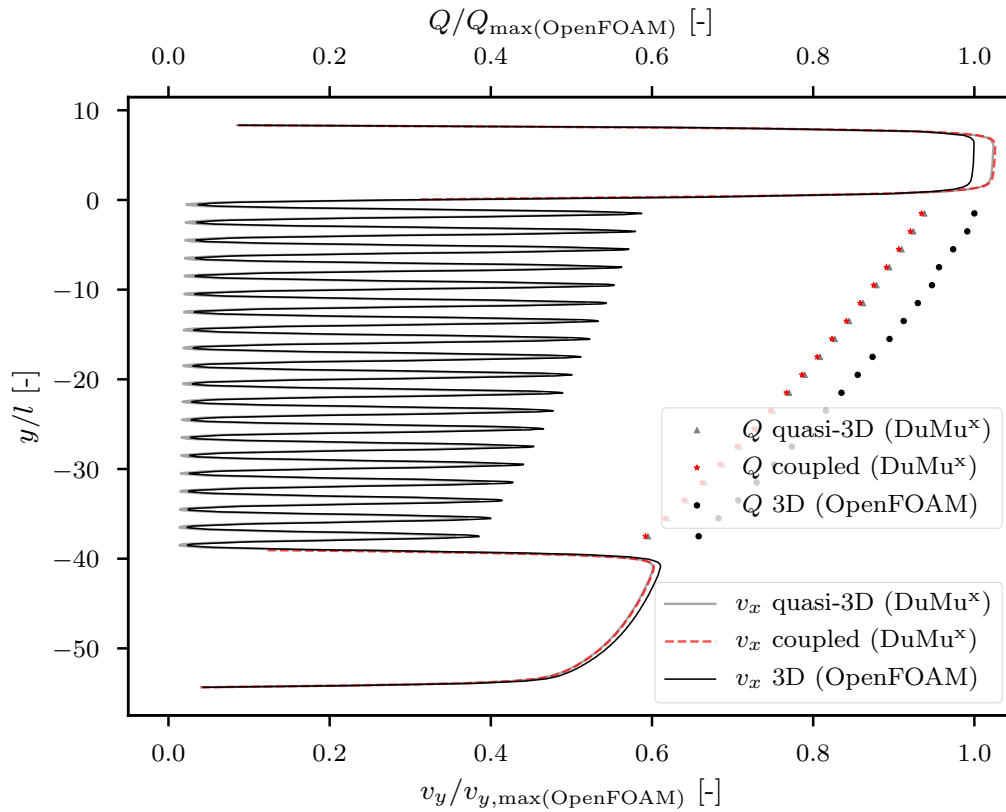


Figure 7.30 – Horizontal velocity profiles and volumetric flow rates over height. Velocity profiles v_x over y at $x/l = 80.5$ and discrete volumetric flow rates at $x/l = 79.5$ for all numerical models, normalized by the maximum values of OpenFOAM. The coupled model only features continuous velocities in the free-flow channel and the triangular region. Adapted from Weishaupt et al. [2019b] (license: CC BY 4.0).

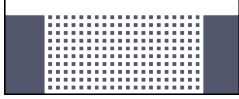
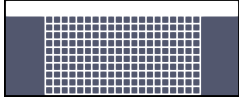
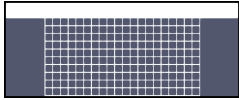
In summary, we have shown that the coupled, hybrid-dimensional model is able to reproduce the reference quasi-3D results both qualitatively and quantitatively. Pronounced velocity deviations occur very locally at the edges of the throat openings which, however, does not considerably impair the mass exchange across the interface between free flow and porous medium. Including a mechanism for slip velocities above the throats noticeably improves the results of the coupled model and comes with no additional run-time cost. The coupled model yields a speedup of 2.3 compared to the quasi-3D model.

The next section further examines the coupled free-flow/pore-network model by varying the regular porous geometry. Properties such as convergence behavior and CPU-times are discussed.

7.1.7 Further studies on structured porous geometries

This section assesses the coupled model’s accuracy, convergence behavior and efficiency in more detail. For this purpose, the micromodel geometry introduced before was slightly simplified by reducing the number of pores and by removing the triangular channel at the bottom of the domain. The setup was considered two-dimensional for sake of simplicity, which means that the wall friction term does not need to be considered here. However, we still took into account the slip velocities at the pore throats at the interface. The regular porous geometry was systematically varied in analogy to the structures examined in the course of the numerical upscaling procedure described in Section 7.1.5, i.e., throat widths of 50 μm , 100 μm and 250 μm were considered. Table 7.6 summarizes the three different geometries of the porous part. We used the conductance factors previously determined in Section 7.1.5.

Table 7.6 – Setup overview. Characteristic features and conductance factors of the three setups. As all interior pore bodies are identical, $g_i = g_j$. Adapted from Weishaupt et al. [2019a] (license: CC BY 4.0).

setup	w_{ij} [μm]	l_{ij} [μm]	g_{ij} [$\text{m}^2/(\text{sPa})$]	g_i [$\text{m}^2/(\text{sPa})$]	figure
A	250	250	5.26×10^{-6}	1.76×10^{-5}	
B	100	400	2.09×10^{-7}	2.83×10^{-6}	
C	50	450	2.32×10^{-8}	7.08×10^{-7}	

Two different laminar free-flow regimes were investigated: one with very low Reynolds numbers in the free-flow channel ($Re_{\max} \ll 1$) where the stationary Stokes equations (Eq. (3.2)) were solved, and one with $Re_{\max} \approx 400$. Here, inertial forces were not negligible anymore and the Navier-Stokes equations (Eq. (3.1), excluding the storage term) were considered. As before, numerical reference solutions were created for each structure by solving the two-dimensional stationary (Navier-)Stokes equations on the

entire domain. In order to ensure grid convergence, the reference solutions were uniformly refined several times until each throat was discretized with 20 cells per width. The same procedure was performed for the coupled model such that the grid in the free-flow region was identical to the one of the corresponding reference solution for each refinement step. In all coupled simulations, the slip term for the given throat width according to Fig. 7.21 was considered.

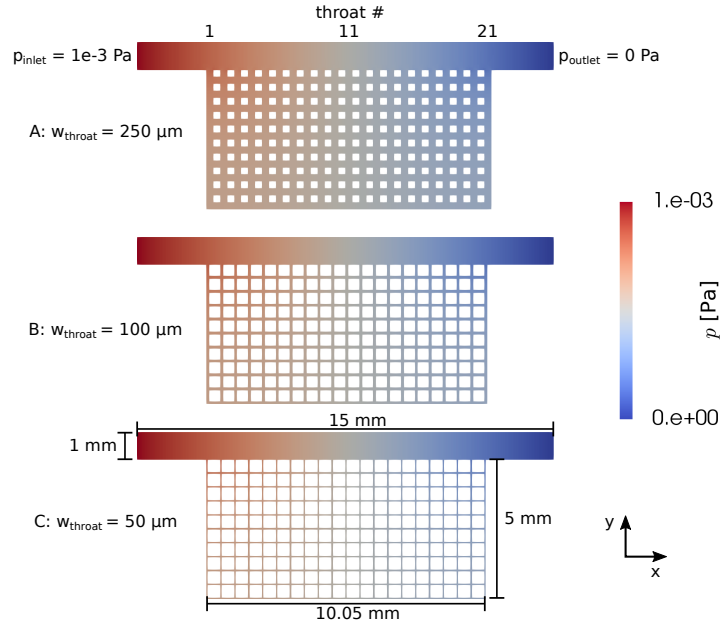


Figure 7.31 – Setup overview. Boundary conditions and geometrical details for three setups with regular porous structures. The vertical throats at the interface are numbered from #1 to #21. Taken from Weishaupt et al. [2019a] (license: CC BY 4.0).

For the low- Re case, fixed pressures were assigned at the inlet and the outlet of the structure ($p_{inlet} = 1 \times 10^{-3}$ Pa, $p_{outlet} = 0$ Pa), all remaining boundaries were closed with a no-flow/no-slip condition. The top-most throats at the interface between the two flow domains are numbered from #1 to #21 (see upper part of Fig. 7.31). The chosen boundary conditions yielded a maximal horizontal flow velocity in the free-flow channel of 9×10^{-6} m/s for setup A and values of 8.4×10^{-6} m/s and 8.3×10^{-6} m/s for B and C, respectively. This means that the maximal Reynolds number Re_{max} was always below 0.01. For all setups A-C, no recirculations (see Fig. 7.20b) within the pore bodies or pore throats could be observed.

Figure 7.32 depicts a comparison between the solutions of the reference model and the coupled one for setup A ($w_{ij} = 250$ μ m). The general flow pattern equals the one of the

experimental setup described before in Section 7.1.6: guided by the pressure gradient within the channel, the liquid enters the porous medium on the left side (throat #1), traverses it mainly parallel to the channel, and re-enters the latter on the right side of the structure (throat #21).

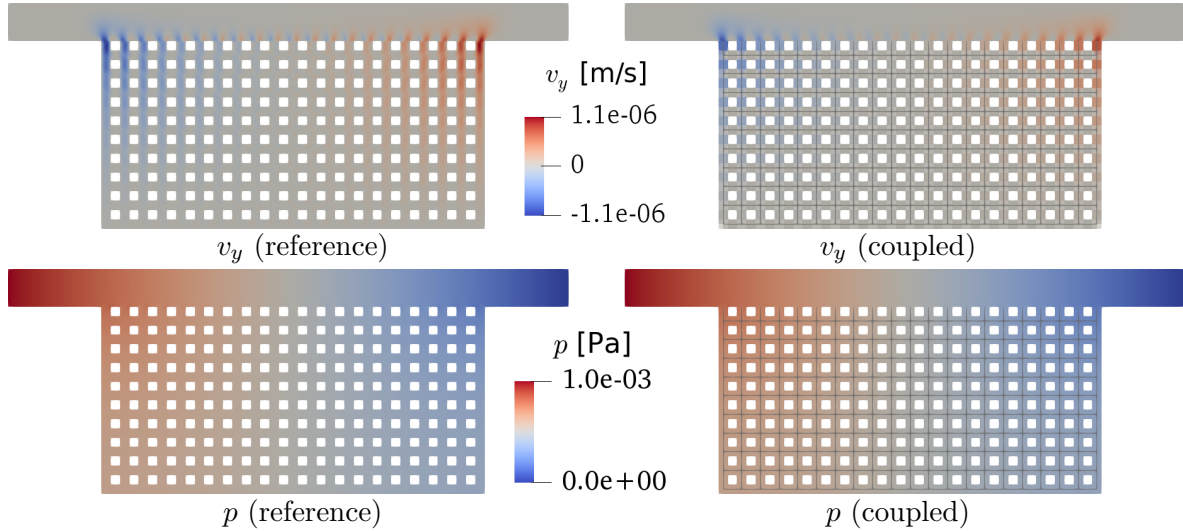


Figure 7.32 – Pressure and velocity fields. Velocity (y -component) and pressure fields for the reference and the coupled model ($w_{ij} = 250 \mu\text{m}$, $Re_{\text{max}} = 0.009$). ParaView’s [Ayachit, 2015] *Tube* and *Glyph* filters have been used on the pore-network model to extrude the one-dimensional elements. The figures correspond to the finest grids, respectively. Adapted from Weishaupt et al. [2019a] (license: CC BY 4.0).

The pressure fields are virtually identical and also the fields of v_y match very closely, keeping in mind that the velocities within the throats of the pore-network model are averaged ones, based on the throat’s volumetric flow rate. The inclination of the flow, especially at throats #1 and #21 (leftmost and rightmost throat) cannot be recovered by the coupled model if the throat slip velocity described in Section 7.1.5 is not taken into account (not shown here²).

Grid convergence was ensured by considering different grid refinement steps for both the reference model and the coupled model (see Table 7.7). Figure 7.33 shows that the corresponding height-specific volume flow rates of each throat #1 to #21 at the interface between the two domains converge against the finest reference solution for all setups. The latter was discretized with 20 cells per throat width. Furthermore, the

²Fig. 7.32 differs in this aspect from the corresponding figure in Weishaupt et al. [2019a] where the throat slip had not been included.

coupled model's solutions match very well with the finest reference solution, even when only one free-flow cell per throat width was used.

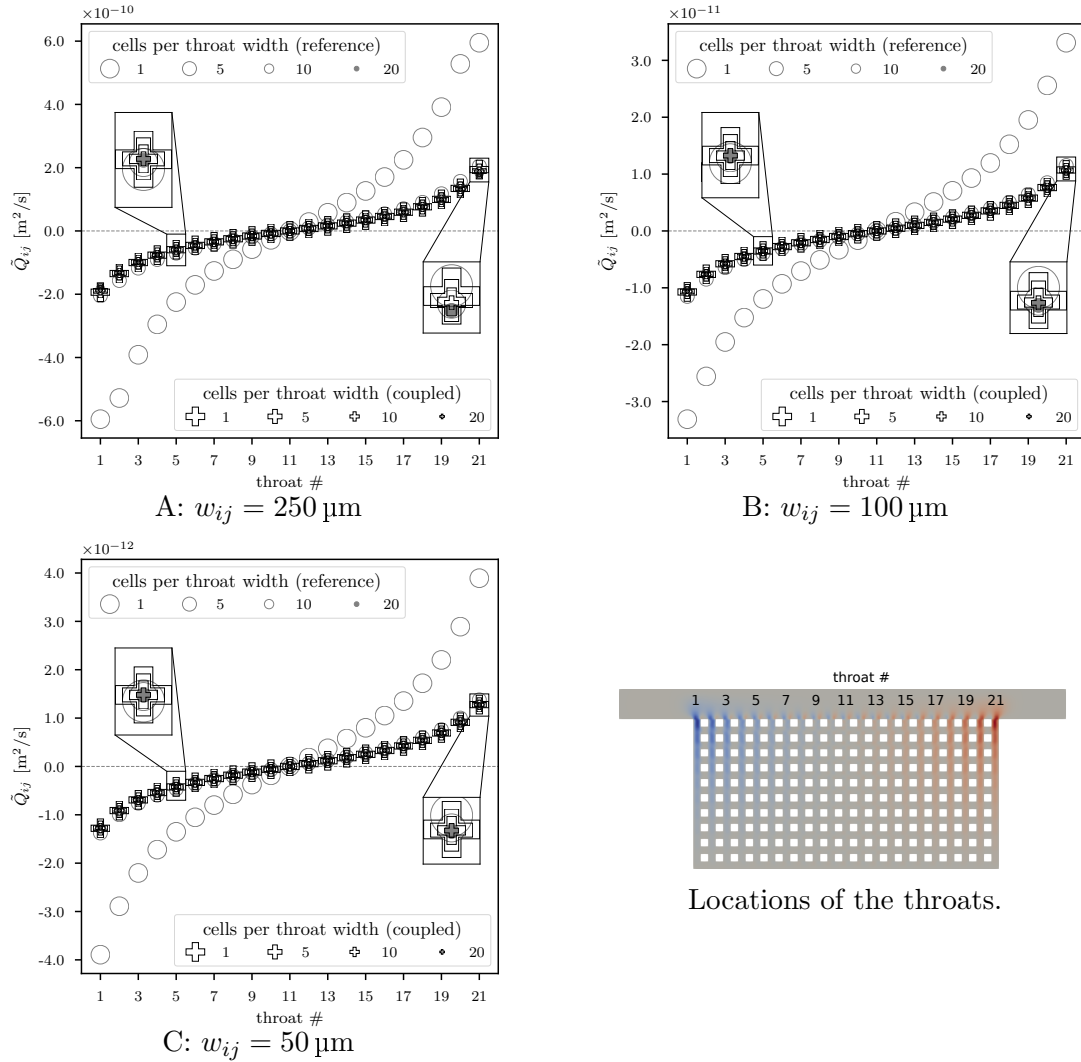


Figure 7.33 – Pore-local volume flow rates. Height-specific volume flow rates per throat at the interface (low- Re case) for the reference and the coupled model. Adapted from Weishaupt et al. [2019a] (license: CC BY 4.0).

The higher the flow rate per throat, the greater the deviation between the reference solutions and the results of the coupled model. Summing up the absolute values of all throat volume flows across the interface between free flow and porous medium yields an average error of less than 1% for all setups (with respect to the most refined solutions with 20 cells per throat width).

In order to investigate the influence of higher Reynolds numbers in the free-flow channel, the numerical simulations described above were repeated with modified boundary conditions ($p_{inlet} = 50 \text{ Pa}$, $p_{outlet} = 0 \text{ Pa}$) yielding $Re_{max} = 430$ for setup A and $Re_{max} = 420$ for B and C. As we still expected creeping flow in the porous structure ($Re \ll 1$), again the same pore-network model as above (neglecting any inertia terms) was used for the coupled model. A close qualitative fit between the reference and the coupled solution can again be found in Fig. 7.34, which also shows that the velocity and the pressure fields have lost their symmetrical nature for the coarsest structure A due to inertial forces.

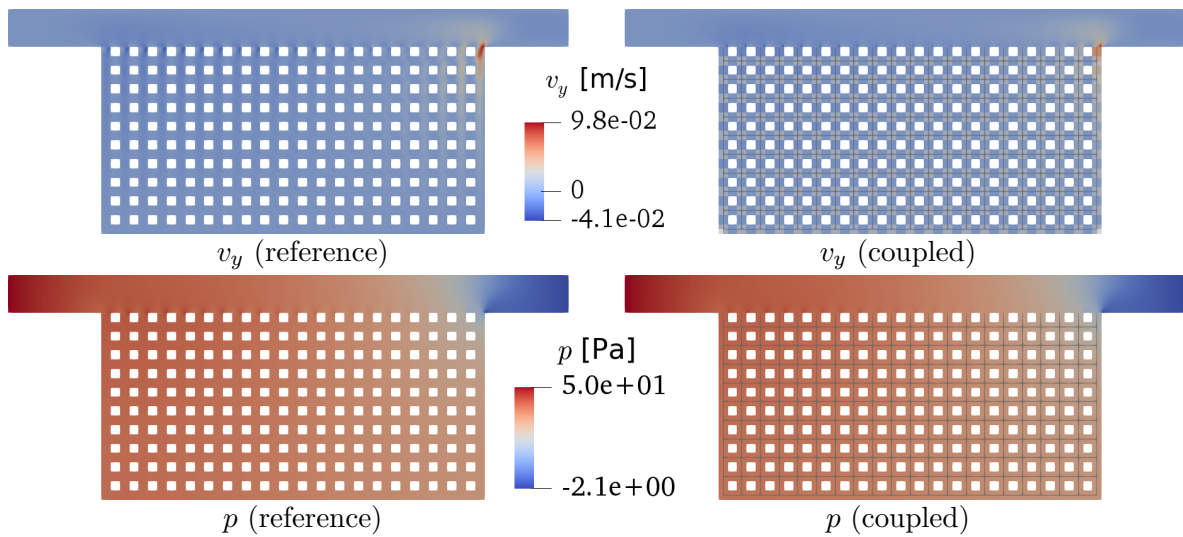


Figure 7.34 – Pressure and velocity fields. Velocity (y -component) and pressure fields for the reference and the coupled model ($w_{ij} = 250 \mu\text{m}$, $Re_{max} = 420$). ParaView’s [Ayachit, 2015] *Tube* and *Glyph* filters have been used on the pore-network model to extrude the one-dimensional elements. The figures correspond to the finest grids, respectively. Adapted from Weishaupt et al. [2019a] (license: CC BY 4.0).

This is also reflected by Fig. 7.35, where the height-specific volume flow rates per throat at the interface are plotted for the high- Re cases. While the flow enters the porous structure quite uniformly over several throats on the left-hand side, the outflow is more or less restricted to the right-most throat. This changes for B and C, where the velocity field is again rather symmetrical. As before, no zones of recirculation were found. Only for the coarsest structure A, some notable deviations (strongest at throat #21) can be observed for the coupled model that uses only one cell per throat width, which is apparently not enough to capture the actual flow behavior. As for the low- Re case,

the cumulative error with respect to the finest refinement steps is below 1% for B and C, while this error is slightly increased to around 2% for A. As before, grid refinement has a rather large impact on the reference solution whereas the solution of the coupled model is less affected (except for the one case discussed above).

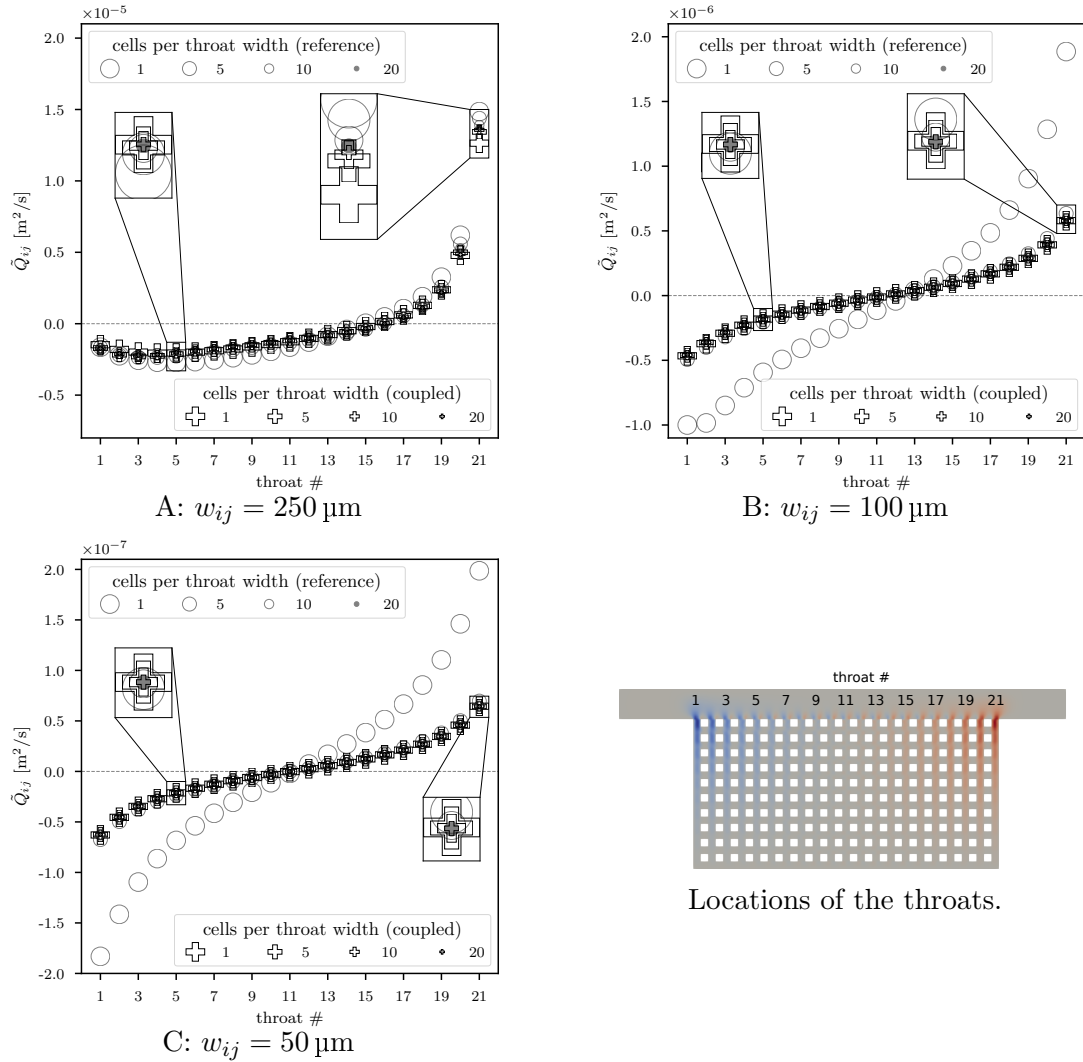


Figure 7.35 – Pore-local volume flow rates. Height-specific volume flow rates per throat at the interface (high- Re case) for the reference and the coupled model. Adapted from Weishaupt et al. [2019a] (license: CC BY 4.0).

Contrary to the assumption made above (creeping flow in the pore throats), the maximal Reynolds number in the porous domain is $Re_{\max, \text{PM}} = 27.5$ for the throat width of $w_{ij} = 250 \mu\text{m}$. This seems to have, however, no strong influence on the accuracy of the coupled solution. For setup B and C, $Re_{\max, \text{PM}}$ is still below one.

Table 7.7³ provides an overview of the CPU times required for all setups and refinement steps, for both the reference and the coupled model. The same computer as in Section 7.1.6 was used and care was taken that only one simulation run at a time was performed such that no mutual interference of the processes (which could be observed on preliminary runs) distorted the simulation times. Nevertheless, this should be seen rather as an estimate than an exact comparison.

Table 7.7 – Simulation statistics. Number of degrees of freedom (n_{DOF}) for the individual refinement steps and corresponding CPU times for the low- Re and the high- Re case for flow over regular structures. The refinement steps correspond to 1, 5, 10 and 20 cells per throat width. n_{DOF} is given both for the free-flow channel alone (FF) and as total value (total) including also the porous domain. The pore-network model always features 231 degrees of freedom. % FF is the percentage of DOFs within the free-flow domain.

setup	ref.	n_{DOF} [-]				CPU time [s]				speedup [-]	
		tot.		% FF		low Re		high Re		low Re	low Re
		ref.	coupl.	ref.	coupl.	ref.	coupl.	ref.	coupl.		
A	0	3,064	1,015	25.59	77.24	0.09	0.03	0.35	0.10	3.49	3.71
	1	66,920	18,551	27.38	98.75	2.80	0.72	8.63	2.50	3.90	3.45
	2	262,840	72,871	27.64	99.68	12.55	3.09	38.03	10.91	4.06	3.49
	3	1,041,680	289,511	27.77	99.92	55.99	13.59	169.51	42.19	4.12	4.02
B	0	11,860	4,891	39.29	95.28	0.35	0.16	1.44	0.50	2.19	2.88
	1	260,300	113,531	43.53	99.80	10.76	4.90	27.71	15.49	2.19	1.79
	2	1,023,100	451,831	44.14	99.95	49.57	22.32	127.33	69.46	2.22	1.83
	3	4,056,200	1,803,431	44.46	99.99	231.28	109.71	591.11	281.60	2.11	2.10
C	0	33,720	18,551	54.33	98.75	1.07	0.66	2.89	3.11	1.60	0.93
	1	762,600	451,831	59.22	99.95	35.66	22.58	90.55	70.44	1.58	1.29
	2	3,010,200	1,803,431	59.90	99.99	166.74	112.24	425.57	341.15	1.49	1.25
	3	11,960,400	7,206,631	60.25	99.99	858.88	570.42	2161.61	1450.95	1.51	1.49

The coupled model is always faster than the reference one. Considering the last refinement step, the CPU time for setup A is reduced by a factor of four. This speedup decreases to values of around 2 and 1.5 for setups B and C, respectively. This can be explained by the proportionally higher numbers of degrees of freedom (DOF) in the free-flow domain which still need to be accounted for by the coupled model. For structure A, more than 60% of the DOFS are spent to discretize the porous medium and

³The values here deviate slightly from the ones presented in Weishaupt et al. [2019a]. In this paper, 11 and 21 instead of 10 and 20 cells per throat width were used, increasing the total number of DOFs. Furthermore, we manually optimized a setting regarding the numerical differentiation for assembling the Jacobian in the present work.

therefore employing the pore-network model, which only features 231 DOFs, yields a massive reduction of the total number of DOFs and thus CPU time. This effect decreases for setups B and C where the main computational effort is spent on the solution of the free-flow domain which also holds for the coupled model, using the same number of DOFs in this region.

This issue could be addressed by using less DOFs in the free-flow channel by means of local grid refinement [e.g., Vittoz et al., 2017, Lipp and Helmig, 2020].

Table 7.8⁴ summarizes the number of Newton iterations required for solving the non-linear high- Re cases for the reference and the coupled model. For the finest refinement steps, those values are identical for both models, while generally, the coupled model needed at least one more iteration to converge. The convergence behavior was highly sensitive to the choice of an ε parameter used for the numerical differentiation of the balance equations' residuals. This is an essential part of assembling the global Jacobian matrix (see Eq. (5.1)) and some manual, grid-dependent optimization of ε was performed here. Further investigation and optimization is needed e.g., by considering automated differentiation [e.g., Griewank and Walther, 2008].

Table 7.8 – Simulation statistics. Number of Newton iterations (n_{It}) for the high- Re cases with different refinement steps (1, 5, 10 and 20 cells per throat width).

setup	n_{It} [-]					
	A		B		C	
	ref.	coupl.	ref.	coupl.	ref.	coupl.
refinement						
0	7	7	7	6	5	9
1	6	7	5	6	5	6
2	6	7	5	6	5	6
3	6	6	5	5	5	5

We conclude that the coupled model provides accurate results for both creeping and inertia-affected flow in the channel for all three tested regular geometries, provided that

⁴The values here deviate slightly from the ones presented in Weishaupt et al. [2019a]. We manually optimized a setting regarding the numerical differentiation for assembling the Jacobian in the present work.

the pore-body flow resistance is properly accounted for. Having assessed the model accuracy under steady single-phase flow conditions and highly regular porous structures, the next section presents a numerical example of transient component transport through a more natural, randomly generated porous medium.

7.2 Compositional single-phase flow over a random network ⁵

This section considers free flow over a highly irregular, randomly generated porous medium. Instead of stationary single-phase flow, we now solve a time-dependent problem where a tracer component is injected at the bottom of the network domain. It gets transported towards the free-flow channel through which it eventually leaves the system. Due to the complex geometry of this structure, no reference solution is provided. Here, we rather aim at demonstrating an outlook to further possible applications of the coupled model than providing results for a specific porous medium or application. The setup resembles a microfluidic model with a random porous structure [e.g., Karadimitriou et al., 2017] adjacent to a free-flow channel.

The random pore network with 347 pores and 500 throats (see Fig. 7.36) was created using Voronoi tessellation [e.g., Gostick, 2013] and the pore body radii were drawn from a spatially-uncorrelated truncated log-normal distribution (mean 100 μm , minimum 50 μm , maximum 300 μm , standard deviation 100 μm).

The size of the channel is 15 mm x 1 mm x 0.2 mm while the porous structure has a spatial extent of 10 mm x 5 mm x 0.2 mm. As in Section 7.1, the model geometry is two-dimensional but features a constant height of $h_\Omega = 0.2$ mm in both the free-flow channel and the porous domain⁶. We again employed the quasi-3D model in the free-flow channel and considered throats with rectangular cross sections. The latter have a uniform height $h_{ij} = h_\Omega = 0.2$ mm but varying widths w_{ij} , based on the adjacent pore bodies' inscribed radii as suggested by Joekar-Niasar et al. [2008].

⁵This section is based on Weishaupt et al. [2019a].

⁶This is in contrast to Weishaupt et al. [2019a] where only a two-dimensional domain without the influence of any wall friction was considered. Furthermore, the slip velocities above the pore throats were added here. The results are therefore slightly different.

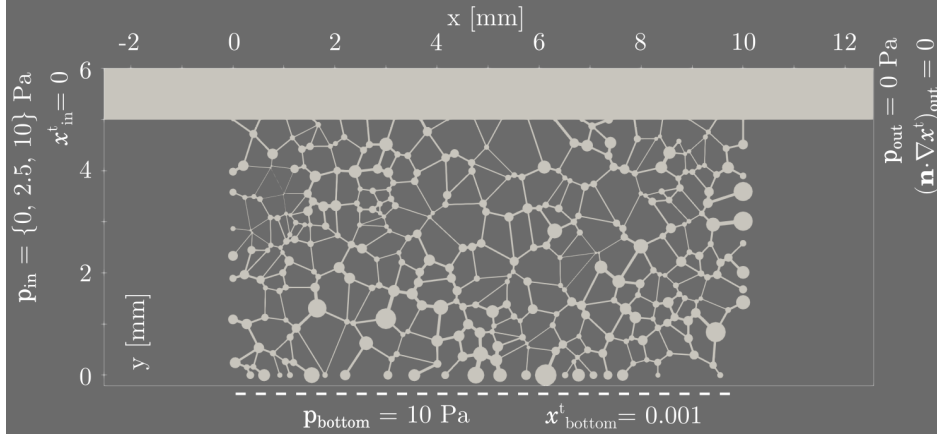


Figure 7.36 – Setup for compositional flow. Setup and boundary conditions for the compositional flow example. The entire domain has a constant and uniform height of $h_\Omega = 0.2$ mm. Adapted from Weishaupt et al. [2019a] (license: CC BY 4.0).

The pressure drop within the pore bodies was neglected because the network features rather large pore bodies and long and narrow pore throats. The conductance factor of the rectangular pore throats is given by

$$g_{ij} = \frac{h_{ij}^3 w_{ij}}{12 \mu l_{ij}} \left(1 - 0.63 \frac{h_{ij}}{w_{ij}} \right), \quad (7.14)$$

approximating Eq. (7.3) [Bruus, 2008]. Here, w_{ij} is the throat width and h_{ij} the respective height with $w_{ij} > h_{ij}$. The throat length is given by

$$l_{ij} = \|\mathbf{x}_i - \mathbf{x}_j\| - r_i - r_j, \quad (7.15)$$

where \mathbf{x}_i and \mathbf{x}_j are the adjacent pore body centers and r_i and r_j are the respective inscribed radii. No volume is assigned to the throats while the pore bodies are cylindrical with $V_i = \pi r_i^2 h_i$, where $h_i = h_{ij} = 0.2$ mm is the height of the pore body.

We solved the transient Navier-Stokes equations with two mole balance equations in the free-flow domain and two mole balance equations within the pore network (Eqs. (3.1), (3.5) and (3.12)). The channel was discretized with 50 uniform cells in y -direction and 1261 cells in x -direction, with Δx such that always five cells were aligned with the projected throat width at the interface, as explained in Chapter 4. Figure 7.36 illustrates the chosen boundary conditions. At the channel outlet on the right, a fixed pressure of $p_{\text{out}} = 0$ Pa in combination with an outflow condition $(\mathbf{n} \cdot \nabla x^t)_{\text{out}} = 0$ for

the transported component was assigned. At the channel inlet, a fixed mole fraction of $x_{\text{in}}^t = 0$ and a fixed pressure p_{in} were set. We considered three different flow velocities within the channel by varying the pressure value at the inlet (0 Pa, 2.5 Pa, 10 Pa). For the pore-network model, no-flow conditions held for the pores on the left and right side. At the bottom, a fixed pressure of $p_{\text{bottom}} = 10$ Pa and a fixed mole fraction of $x_{\text{bottom}}^t = 1 \times 10^{-3}$ were assigned. We used constant values of $\varrho = 1 \times 10^3$ kg/m³, $\mu = 1 \times 10^{-3}$ Pas and a diffusion coefficient of $D = 1 \times 10^{-9}$ m²/s.

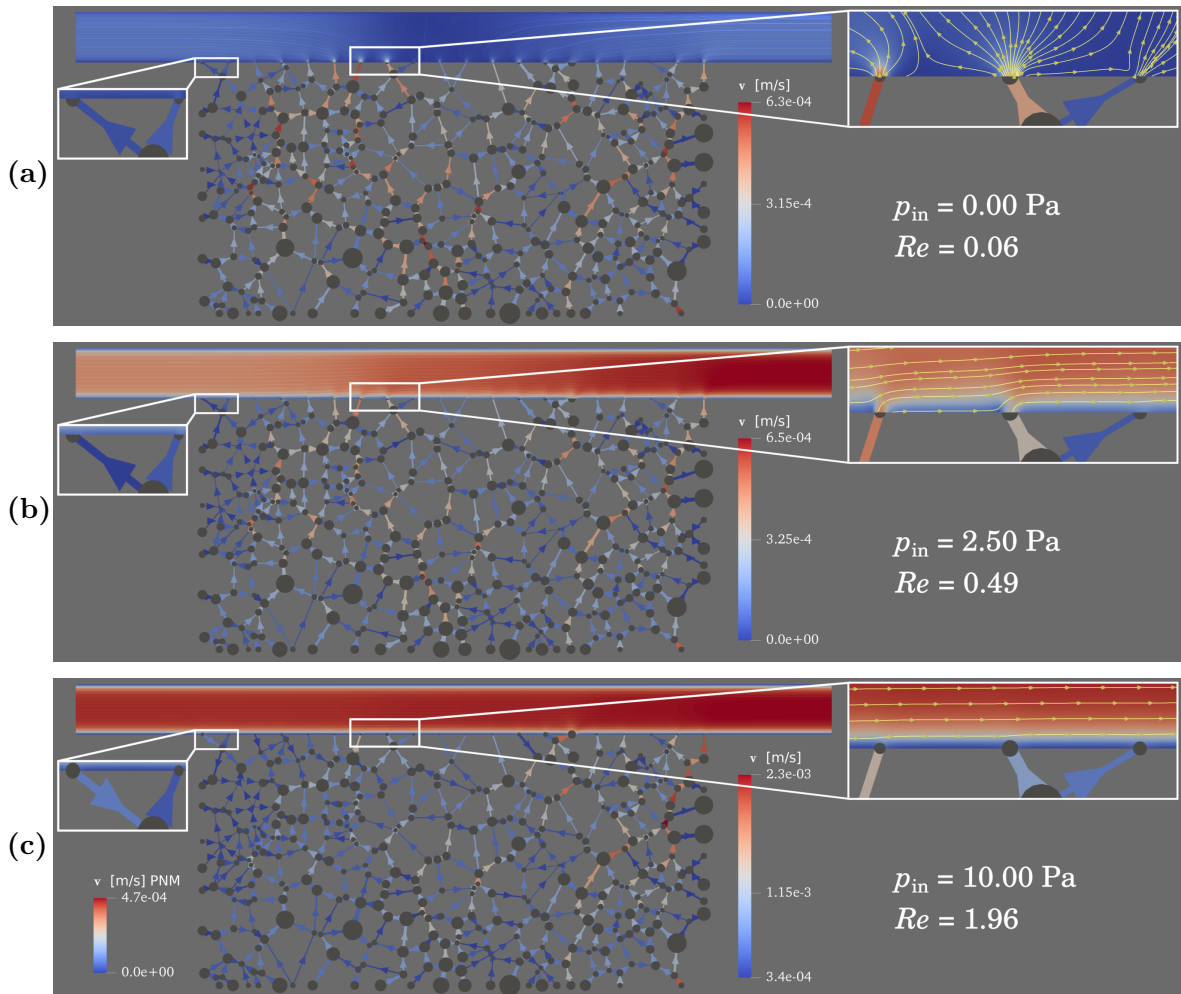


Figure 7.37 – Velocity fields. Velocity fields within both domains and close-ups for the three different scenarios. Re is based on the averaged velocity within the channel. Note the different color scale for the network in the third scenario (bottom). Adapted from Weishaupt et al. [2019a] (license: CC BY 4.0).

Figure 7.37 shows the velocity fields in both domains for all scenarios. Two close-ups emphasize local details. Applying an inlet pressure of $p_{\text{in}} = 0$ Pa (Fig. 7.37a) resulted in an average Reynolds number of $Re = 0.06$ in the channel. The highest velocities occur locally in the pore throats and some preferential flow paths can be clearly distinguished. The liquid leaves the channel more or less symmetrically through both ends. At the locations of the magnified center pore throats, the influence of the porous domain on the free-flow velocity pattern is clearly visible. Here, the streamlines at the interface follow the inclination of the pore throats which illustrates the advantage of the coupled hybrid model over REV-scale approaches that would not be able to capture these kinds of small-scale features. The channel in the second scenario (Fig. 7.37b), where $p_{\text{in}} = 2.5$ Pa was set, features an average Reynolds number of $Re = 0.49$. There is a distinct flow from left to right and the local influence of the pore-network on the free-flow pattern is strongly reduced. The flow velocity in the channel increases in x -direction due to the influx from the porous domain. Preferential flow paths in pore network are still visible, however, the velocities are smaller than in the previous scenario due to the higher pressures in the free-flow channel that globally govern the flow behavior in the porous part with respect to the Dirichlet pressure boundary condition at the bottom of the domain. In the last scenario with $p_{\text{in}} = 10$ Pa and $Re = 1.96$, the velocity field in the channel is virtually unaffected by the porous domain. As the flow velocities in the free-flow channel and the pore network differ by orders of magnitude, separate color scales have been used for this scenario in Fig. 7.37c. As opposed to the first two scenarios, fluid actually enters the pore network at the leftmost throat on the interface which can be seen in the close-ups on the left side of the figures.

Next, we focus on the transport characteristics for the different scenarios. Figure 7.38 shows the distribution of the component mole fraction x^t for each scenario at two given times t_1 and t_2 . For sake of comparability, these times were chosen such that the averaged component mole fraction (weighted by the pore body volume V_i),

$$\langle x^t \rangle = \frac{\sum_i (V x^t)_i}{\sum_i V_i}, \quad (7.16)$$

is approximately 5×10^{-4} for t_1 and 9×10^{-4} for t_2 .

Though the same values for the pressure $p_{\text{bottom}} = 10$ Pa and the mole fraction $x_{\text{bottom}}^t = 1 \times 10^{-3}$ were set at all pores at the bottom of the network, a heterogeneous spreading

behavior of the component could be observed for all scenarios. Due to the velocity field discussed before and the given network structure featuring pores of varying storage capacity, the component reached the free-flow channel through the throats located at the center of the channel first for all three scenarios. Regions of increased transport (e.g., at the center of the network) and stagnant zones with dead-end pores (left and right boundary of the network) can be clearly distinguished. The first scenario reached $t_1 = t(\langle x^t \rangle \approx 5 \times 10^{-4})$ after approximately 14 s (Fig. 7.38a) while the second and third required 20 s (Fig. 7.38c) and 30 s (Fig. 7.38e) for this, respectively. Driven by the velocity field within the pore network, the component leaves the system in the first scenario through both the inlet on the left and the outlet on the right, while in the second case, everything is transported to the right. The same is true for the third scenario. Due to the high velocities, x^t is very small in the free-flow channel as the component gets immediately transported away once it reaches the interface.

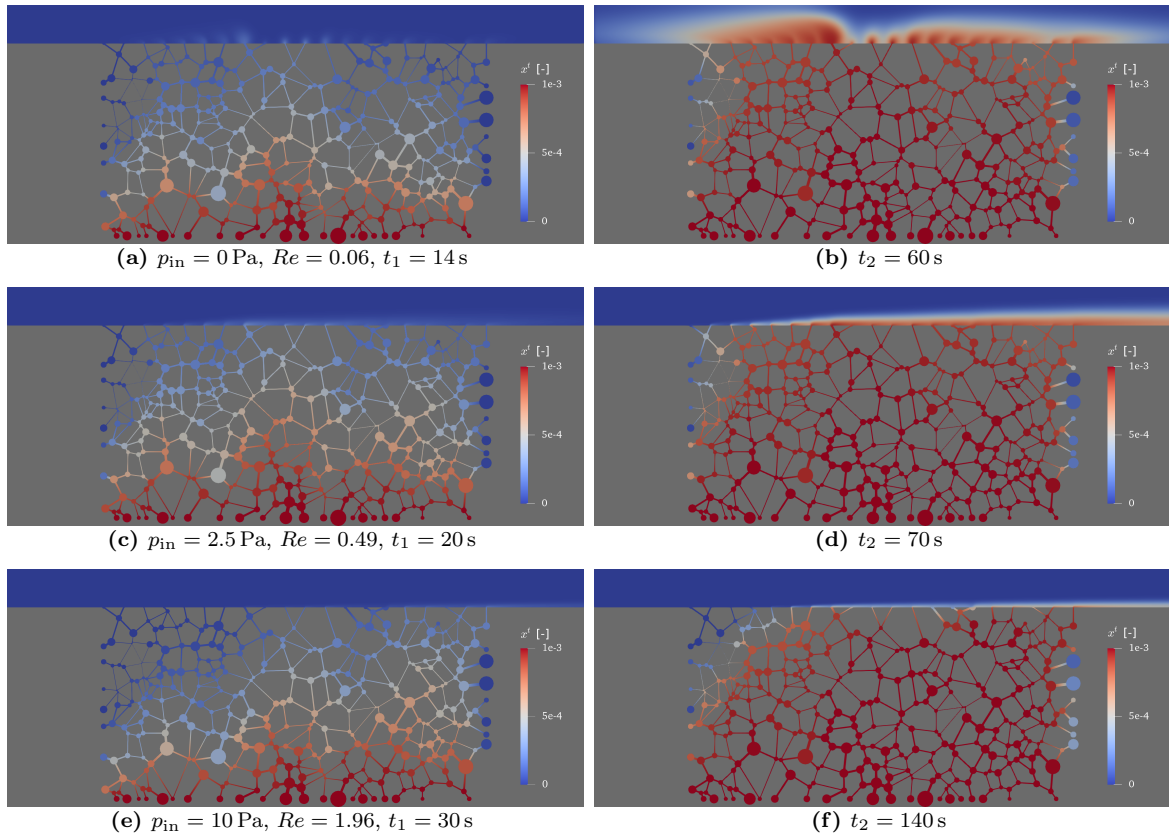


Figure 7.38 – Concentration fields. Distribution of the transported component mole fraction x^t within the porous and the free-flow domain for the three different scenarios at different times. Adapted from Weishaupt et al. [2019a] (license: CC BY 4.0).

At time t_2 (right side of Fig. 7.38), the pore bodies have almost reached their maximum mole fraction of $x^t = 1 \times 10^{-3}$. 50 s were required for the first scenario (Fig. 7.38b) to reach this state, while this time increased to 70 s (Fig. 7.38d) and 140 s (Fig. 7.38f) for the second and third scenario, respectively. While the concentration field within the porous domain was very similar for the first and the second case, substantial differences can be observed in the free-flow domain.

In the first scenario, the distribution of x^t in the channel is largely defined by extensive plumes above the pore throats intersecting with the interface. Each pore throat creates a distinct plume which reaches up to the upper wall of the channel - again a pore-scale feature that cannot be reproduced using REV-scale models. In the second scenario, the contribution of each pore throat is still clearly visible. However, the faster and unilaterally directed flow field in the channel gives rise to the formation of a concentration boundary layer at the interface which occupies approximately half of the channel's height. Focusing on the large dead-end pore bodies at the right boundary of the network, we can observe that their mole fraction has slightly increased compared to the previous time t_1 which is due to diffusion. The most prominent feature of the concentration field within the network of the third scenario can be observed in the top left corner. Here, almost no concentration has reached the pore bodies. This is caused by the fluid entering the leftmost throat and thereby repelling the fluxes within the pore network. This shifts the entire concentration field within the network towards the right. As in the second scenario, a concentration boundary layer evolves in the free-flow channel, however, of significantly smaller thickness which is caused by the higher velocities in the channel.

In summary, this section showed a clear example of the interaction between free flow and the porous medium which is caused by pore scale features. The topology of the network and the distribution of pore body radii yields stagnant zones and pronounced flow. The pore throats at the interface discretely influence the free-flow pattern and concentration fields. In return, the free flow also affects the flow and transport behavior within the network. The example therefore includes a sub-scale complexity that can trigger non-Fickian transport behavior like asymmetric breakthrough curves which can be observed experimentally but not reproduced numerically using classical REV-scale models that neglect said pore-scale characteristics [Bijeljic et al., 2013, Most et al., 2016]. The complexity even increases when two-phase flow is considered where geometry-dependent capillarity effects may govern the system. As it has been shown in recent experimental

[Karadimitriou et al., 2017, 2016] and computational studies [Aziz et al., 2018], the two-phase flow configuration creates different flow paths at different saturations as well as diffusion-controlled and advection-controlled regions which lead to a non-Fickian behavior in transport. This is addressed in Chapter 8 dealing with evaporation from a pore network. In the next and last section of this chapter, a numerical example comprising three model domains is presented.

7.3 A three-domain example

This section features a numerical example comprising three sub-domains. We revisit the setup presented in Section 7.2, i.e., compositional single-phase flow over a randomly generated network, and add a bulk porous medium region Ω^{REV} at the lower domain boundary of Ω^{PNM} (Fig. 7.39a). The bulk domain has the same spatial extent as Ω^{PNM} (10 mm x 5 mm) and features the same constant height of $h_{\Omega} = 0.2$ mm, which is incorporated in terms of an extrusion factor, since Ω^{REV} is, like Ω^{FF} , a two-dimensional computational domain. Like before, we employ the quasi-3D approach for Ω^{FF} . Using numerical upscaling on Ω^{PNM} , we determined the material parameters $K_{xx} = 9.07 \times 10^{-12} \text{ m}^2$, $K_{yy} = 1.01 \times 10^{-11} \text{ m}^2$ and $\Phi = 1.32 \times 10^{-1}$ for Ω^{REV} . The latter is discretized with 5×5 grid cells.

As in Section 7.2, the lateral sides of the porous medium are closed which means that Neumann no-flow conditions hold on the left and the right boundary of both Ω^{PNM} and Ω^{REV} . A fixed pressure boundary condition is set at the bottom of Ω^{REV} . Since the (combined) porous medium has effectively doubled its vertical extent compared to Section 7.2, we also double the pressure boundary value by setting $p_{\text{bottom}} = 20$ Pa in order to establish a comparable pressure gradient in the porous medium. All remaining initial and boundary conditions are chosen as in Section 7.2, where the inlet pressure of Ω^{FF} was varied between 0 and 10 Pa in order to examine the influence of different free-flow velocities.

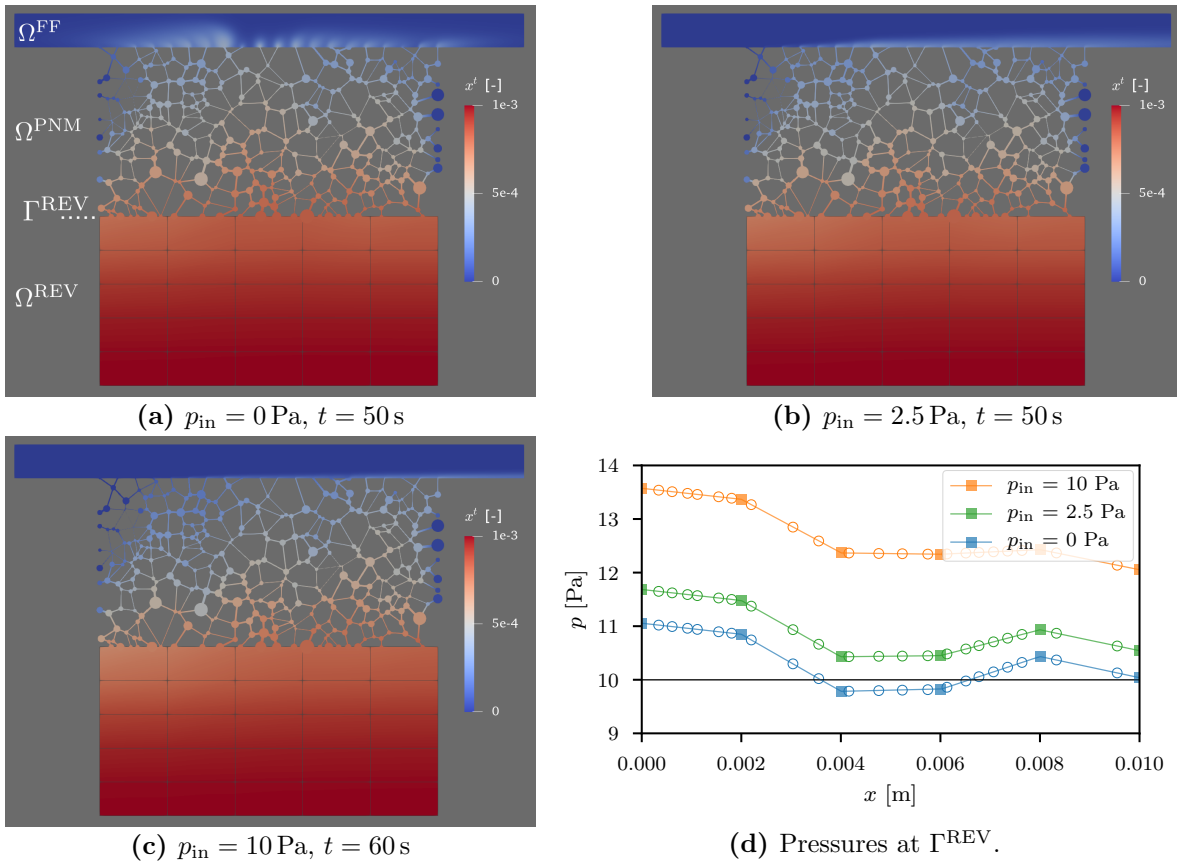


Figure 7.39 – Concentration fields and interface pressures for a three-domain setup. The averaged mole fraction (Eq. (7.16)) in Ω^{PNM} is around 5×10^{-4} for all cases. Squares in (d) indicate the discrete nodal values of Ω^{REV} on Γ^{REV} while the respective pore-body pressures are marked with circles.

Figures 7.39a to 7.39c show the resulting concentration fields in all three sub-domains for the different inlet pressures in Ω^{FF} . The results in Ω^{FF} and Ω^{PNM} are very similar to the ones presented in Fig. 7.38, where only those two sub-domains had been considered. Obviously, the tracer takes longer to saturate the network since it first has to traverse the bulk porous domain before reaching Ω^{PNM} . Preferential flow paths in the network lead to a slightly non-uniform spreading behavior of the tracer in Ω^{REV} , which can be seen at the interface Γ^{REV} . Here, x^{tracer} is marginally lower on the left side, as best seen in Fig. 7.39c where additionally the increased pressure on the left side of Ω^{FF} repels the tracer as explained in Section 7.2.

Figure 7.39d shows the pressure distribution along Γ^{REV} for both Ω^{PNM} and Ω^{REV} . The square markers indicate the discrete pressure values at the interface nodes of the

bulk model's grid, which are linearly interpolated in between using the Box method's ansatz functions (Section 4.2). As imposed by the coupling conditions, the pressure values of the pores intersecting with the interface are identical to the interpolated bulk model values. In contrast to the uniform bottom pressure value of 10 Pa set for the two-domain example in Section 7.2 (see black line in Fig. 7.39d), the pressure varies along Γ^{REV} which is caused by the aforementioned preferential flow paths in Ω^{PNM} and the pressure gradient imposed in the free-flow channel. The higher p_{in} , the higher the pressure level at Γ^{REV} . The admittedly small deviations from the uniform boundary value may be irrelevant for the given setups but there could be other situations where this has a bigger impact. Adding a bulk porous medium relaxes the constraints on the boundaries of Ω^{PNM} and permits the system to find its own equilibrium state, provided the coupling conditions formulated on Γ^{REV} are physically meaningful (cf. Section 4.2). We leave this discussion open for further research. The example presented here should be seen merely as a proof of concept for the three-domain coupled model.

8 Results and Discussion II: evaporation studies

This chapter highlights the non-isothermal two-phase, two-component capabilities of the newly developed coupled model on the example of evaporation of water from a porous medium adjacent to an air atmosphere which can be either at rest or moving.

The Navier-Stokes equations for non-isothermal compositional flow (Eqs. (3.1), (3.5) and (3.7)) are solved in Ω^{FF} , while the compositional, non-isothermal pore-network model (Eqs. (3.15), (3.17) and (3.22)) accounts for Ω^{PNM} . Gravity is neglected in both domains. We consider both the PVS and the NCP model (see Sections 3.2.2 and 3.2.3) for Ω^{PNM} , i.e., we compare a model using a primary variable switch with a model solving for an additional non-linear constraint (Eq. (3.20)). Furthermore, the influence of neglecting changes in temperature during the evaporation process is examined by setting a fixed temperature and not solving for energy balances (isothermal models).

We consider a miscible system of two phases and two components within Ω^{PNM} . Water is the main component of the liquid wetting phase w , while the pseudocomponent air constitutes the main part of the non-wetting gaseous phase n . All required constitutive relations and physical properties are implemented in the `H2OAir fluidsysteM` of DuMu^x [Flemisch et al., 2011, Lauser, 2012], using data provided by the industry standard IAPWS [Wagner and Pruß, 2002] and Reid et al. [1987]. This means that the phase densities, viscosities, enthalpies, etc., are solution dependent with respect to pressure, temperature and phase composition. Only the gas phase exists in Ω^{FF} , thus $\alpha_{\alpha_{\text{FF}}} = n$. The solid matrix of the porous medium is assumed to be perfectly insulating and thus no heat exchange between the fluids in the network and the solid matrix (which is not modeled anyway) takes place. This process needs to be addressed in future work [e.g., Surasani et al., 2008].

Different configurations and setups are considered for our numerical simulations: A pore network with 19×10 pores in x and y direction (Ω^{PNM}) is placed under a region of free flow Ω^{FF} with a spatial extent of $1.5 \times 10^{-2} \text{ m} \times 0.5 \times 10^{-2} \text{ m} \times 4 \times 10^{-4} \text{ m}$. All sides of Ω^{PNM} are closed and no-flow conditions for mass and energy apply. The domain size of Ω^{PNM} is $1.04 \times 10^{-2} \text{ m} \times 5.2 \times 10^{-3} \text{ m} \times 4 \times 10^{-4} \text{ m}$.

As in the previous chapter, we follow a quasi-3D approach in Ω^{FF} and consider Eq. (4.9) at the coupling interfaces. The free-flow domain's uniform height of $h_{\Omega} = 4 \times 10^{-4} \text{ m}$ coincides with the cubic pore bodies' side lengths. Both square-shaped and circular throat cross sections are investigated, as described later on. The free-flow domain is discretized with 30 cells in y -direction and 133 cells in x -direction such that three grid cells coincide with one pore body at the interface.

We compare two different initial conditions for Ω^{PNM} : the network is either fully water-saturated ($S_{\text{w,init}} = 1$, $x_{\text{w,init}}^{\text{air}} = 1 \times 10^{-5}$) or features already two phases with $S_{\text{w,init}} = 0.99$, which is in line with, e.g., Mosthaf et al. [2011] or Fetzer [2018] who also always started from a partly saturated porous medium. We will later show that this choice is numerically favorable. The initial saturation of all pores at the coupling interface Γ^{FF} is 0.99 for both cases such that there is already some air in the pore bodies which is required conceptually for the coupling conditions described in Chapter 4. $p_{\text{n,init}} = 1 \times 10^5 \text{ Pa}$ and $T_{\text{init}} = 293.15 \text{ K}$ are chosen as initial conditions for the pressure and the temperature.

Different flow configurations in Ω^{FF} are examined by varying the boundary conditions on the lateral sides and the top: By applying no-flow/no-slip conditions for mass and energy to the lateral sides of the domain and fixing p , T and the water vapor mole fraction x^{water} at the top, we consider evaporation from Ω^{PNM} into an air atmosphere at rest (Fig. 8.1a). On the other hand, gas flow is induced by fixing p on the left and the right side of Ω^{FF} while the top of the domain features a no-flow/no-slip boundary condition for mass and energy (Fig. 8.1b). An outflow condition for mass and energy holds at the right boundary.

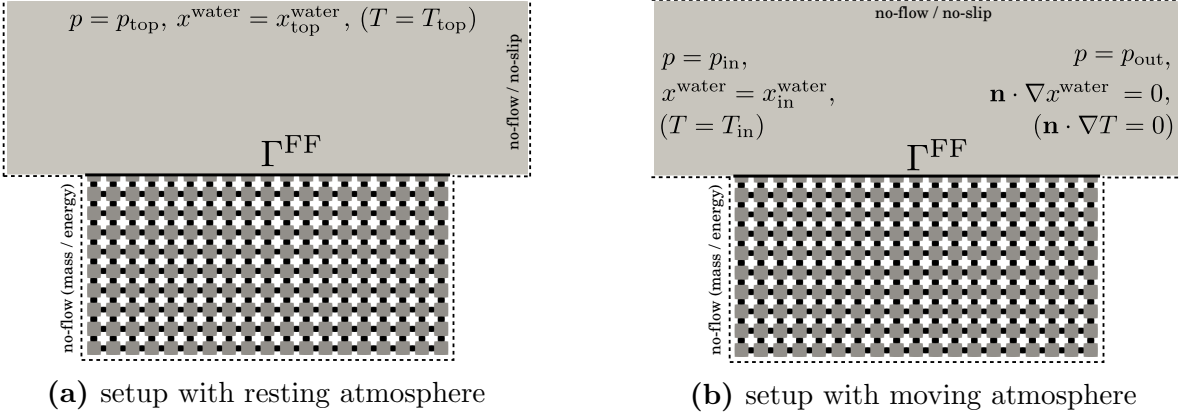


Figure 8.1 – Setups for evaporation studies. Schematic setups for the evaporation examples with and without air flow.

For Ω^{FF} , we chose initial and boundary values of $\mathbf{v}_{\text{init}} = 0$, $p_{\text{init}} = p_{\text{top}} = p_{\text{out}} = 1 \times 10^5 \text{ Pa}$, $x_{\text{init}}^{\text{water}} = x_{\text{top}}^{\text{water}} = x_{\text{in}}^{\text{water}} = 4.7 \times 10^{-3}$ (corresponding to a relative humidity of 0.2) and $T_{\text{init}} = T_{\text{top}} = T_{\text{in}} = 293.15 \text{ K}$ for all models. The setup with flowing air features $p_{\text{in}} = p_{\text{out}} + 1 \text{ Pa}$, yielding a maximum velocity of around $5.1 \times 10^{-2} \text{ m/s}$ and $Re \approx 17$ in Ω^{FF} .

We used the same pore-network constitutive laws as described in Section 6.2, i.e., Eq. (2.35) for the local $p_c - S_w$ curves and Eq. (2.30) to get the throats' capillary entry pressure $p_{c,e}$ with $\theta_r = 0$ and $\gamma = 0.0725 \text{ kg s}^{-2}$. Equation (2.40) accounts for the single-phase throat conductance while Eq. (2.43) determines the wetting layer conductance and Eq. (2.51) the conductance of the bulk non-wetting phase. The pressure drop within pore bodies is neglected. Variations of θ_r , γ and hence $p_c(S_w)$ and $p_{c,e}$ due to changes of pressure, temperature or phase composition are not considered.

The following subsections focus on various parameters that might affect the evaporation behavior both locally and globally. We consider the evaporation rate (in mm d^{-1})

$$\dot{e} = \frac{\dot{m}^{\text{water}}}{\varrho_w |\Gamma|} \frac{1000 \text{ mm}}{\text{m}} \frac{86400 \text{ s}}{\text{d}} \quad (8.1)$$

as a global measure for the evaporation process. \dot{m}^{water} (in kg s^{-1}) is the total mass transfer rate of water from Ω^{PNM} to Ω^{FF} . ϱ_w is the density of the wetting phase which we (though solution dependent as described above) approximate here with 1000 kg/m^3 . $|\Gamma|$ is the total interfacial area between the porous medium and the free-flow region,

including the areas of the coupled pore bodies and the areas of the solid grains in between them.

The specific evaporation rate (in mm d^{-1}) of an individual pore i at the interface Γ_i serves as a local measure:

$$\dot{e}_i = \frac{\dot{m}_i^{\text{water}}}{\rho_w |\Gamma_i|} \frac{1000 \text{ mm}}{\text{m}} \frac{86\,400 \text{ s}}{\text{d}}. \quad (8.2)$$

Here, \dot{m}_i^{water} (in kg s^{-1}) is the pore-local mass flux of water vapor across Γ_i .

8.1 Model comparison for a stagnant atmosphere and a homogeneous network with square-shaped throats

This section discusses the evaporation process for a setup with a resting air atmosphere above a perfectly uniform porous medium (see Fig. 8.1a). All pores are cubic and feature an inscribed radius of $r_i = 2 \times 10^{-4} \text{ m}$ while the inscribed radius of the rectangular throats is determined according to Joekar-Niasar et al. [2008], yielding $r_{ij} = 1.359 \times 10^{-4} \text{ m}$. We compare the physical and numerical model behavior of the different pore-network model concepts for compositional two-phase flow presented in Section 3.2.3: we analyze the influence of neglecting or considering the energy balance (isothermal vs. non-isothermal) and compare the primary variable switch approach (PVS) with the NCP model solving for an additional non-linear constraint. This results in four different model combinations in total. All simulations were run until the average wetting-phase saturation $\langle S_w \rangle = \frac{\sum_i (V S_w)_i}{\sum_i V_i}$ in Ω^{PNM} approached zero, i.e., the pore network dried out.

Physical process description Figure 8.2 shows the temporal development of the evaporation process for an initial water saturation of 1.0 in Ω^{PNM} , using the NCP model. The left column displays the isothermal results (i.e., no energy balance was considered), the right column shows the results of the non-isothermal model.

Initially, the water saturation S_w of the pores adjacent to the free-flow interface decreases while at the same time, the water vapor mole fraction x^{water} in Ω^{FF} strongly increases at the interface. As soon as S_w and thus p_c reach a critical value, the entry capillary pressure $p_{c,e}$ of the throats at the interface can no longer prevent the intrusion of air into Ω^{PNM} and the throats at the interface get invaded by the non-wetting phase. After some time, all throats at the interface are invaded and the drying front moves further downwards into the porous medium until every throat is invaded and the medium dries out eventually.

Figure 8.2 reveals slightly different invasion patterns for the non-isothermal and the isothermal model which is probably due to the highly non-linear nature of the drying process that is furthermore marked by discrete, step-wise perturbations of the system when a throat gets invaded. We found a high sensitivity related to the time step size and other numerical properties, e.g., the allowed Newton convergence tolerance, such that no exact one-to-one correspondence between the models was found for the chosen settings.

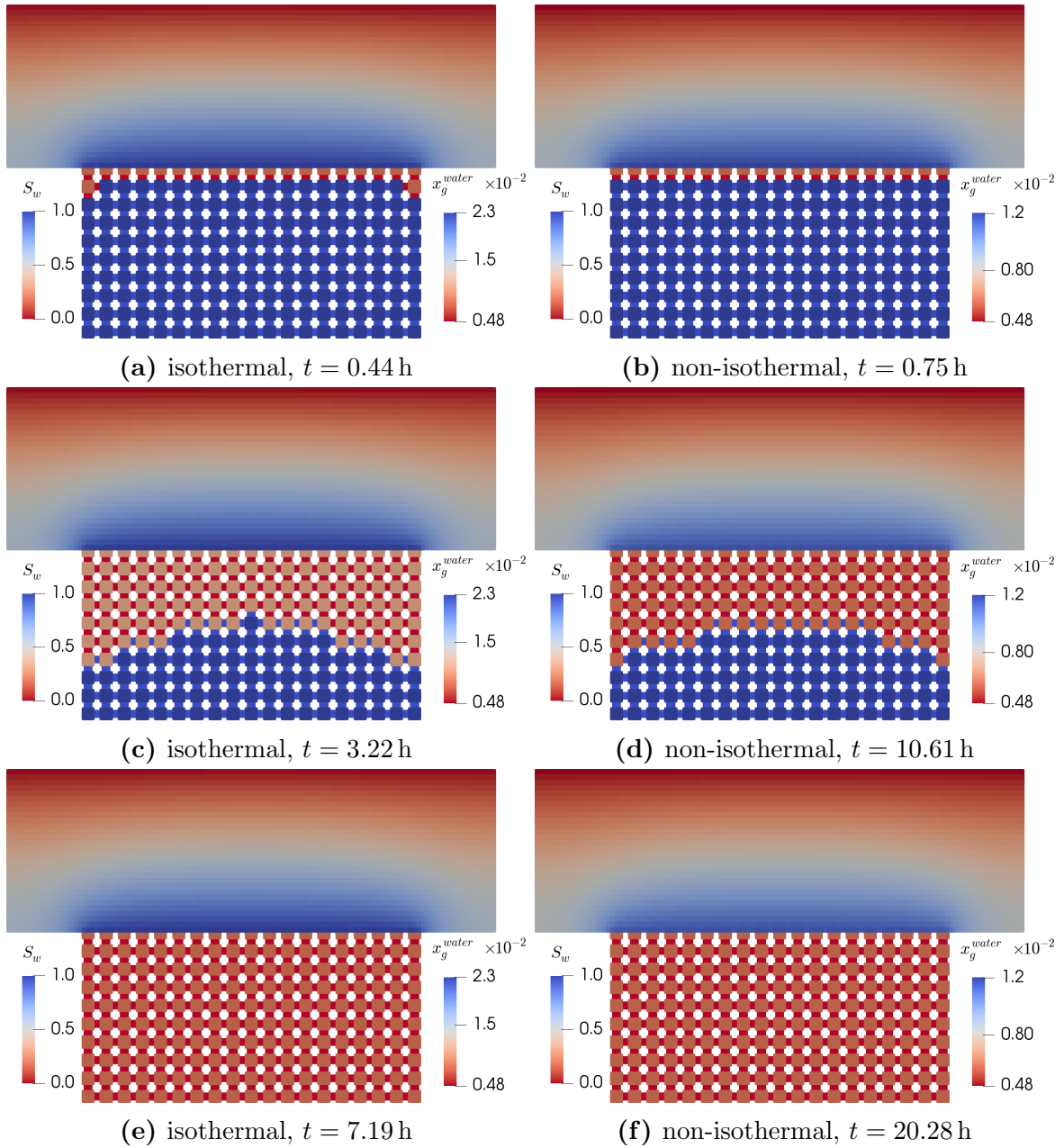


Figure 8.2 – Vapor concentration fields and saturation distribution. Temporal evolution of an evaporation process with resting air atmosphere. The initial water saturation in the porous domain was 1.0. Left column: isothermal NCP model; right column: non-isothermal NCP model. Blue pore throats are fully occupied by the wetting phase (liquid water) while red throats are invaded by the gaseous non-wetting phase. The wetting phase saturation S_w is given for Ω^{PNM} and the water vapor mole fraction x^{water} is shown for Ω^{FF} .

Strictly limiting the allowed time step size lowered the discrepancy but was infeasible for longer simulation runs. This situation is comparable to the numerical issues encountered when simulating density-driven flow in porous media, where fingers of denser fluids are formed due to numerical imperfections and the results strongly depend on the chosen mesh and time step size [Diersch and Kolditz, 2002, Johannsen et al., 2006]. We therefore accept local saturation and invasion differences when comparing different model results and attribute them to numerical origin. As shown later in Fig. 8.4, the local deviations do not influence the global system behavior, i.e., the total evaporation rate.

The overall drying rate of the non-isothermal model is much lower compared to the one of the isothermal model. Only around seven hours are needed until all throats are invaded for the latter, while this time increases to more than twenty hours when considering the energy balance.

The evaporative cooling effect (see Section 2.3.3, [e.g., Mosthaf et al., 2014]) lowers the vapor saturation pressure and thus the vapor mole fraction at the interface pores. This in turn leads to a decreased evaporative flux across the interface. Fig. 8.3 shows this effect on the example of the leftmost pore body at the interface for the NCP models. The pore-local evaporation rates for the isothermal and the non-isothermal model are plotted on the upper graph. The thin vertical lines correspond to peaks associated with throat invasion processes. The thicker curves have been smoothed using a moving median filter for ease of presentation. The lower graph shows the local water vapor concentrations of the pore body and the corresponding average value of the adjacent free-flow grid cells (cf. Fig. 4.3), as well as the corresponding temperatures for the non-isothermal model. We observe a very steep decrease of \dot{e}_i immediately after the evaporation process has started for both models. This is due to the virtually instantaneous equalization of x^{water} from both sides of the interface, as seen in the lower graph. The isothermal model only takes seconds to reach an equilibrium state after which the mole fraction difference across the interface and hence the evaporation rate remains constant. This is in contrast to the non-isothermal model, where x^{water} continues to fall for around an hour until reaching a steady-state value which is less than half of the isothermal model one's. A substantial decrease of temperature by over 10 K goes along with this, which actually causes the drop of x^{water} in Ω^{PNM} . Altering the top boundary condition to a higher value of x^{water} (not shown here) decreases the temperature drop as the evaporation process occurs slower.

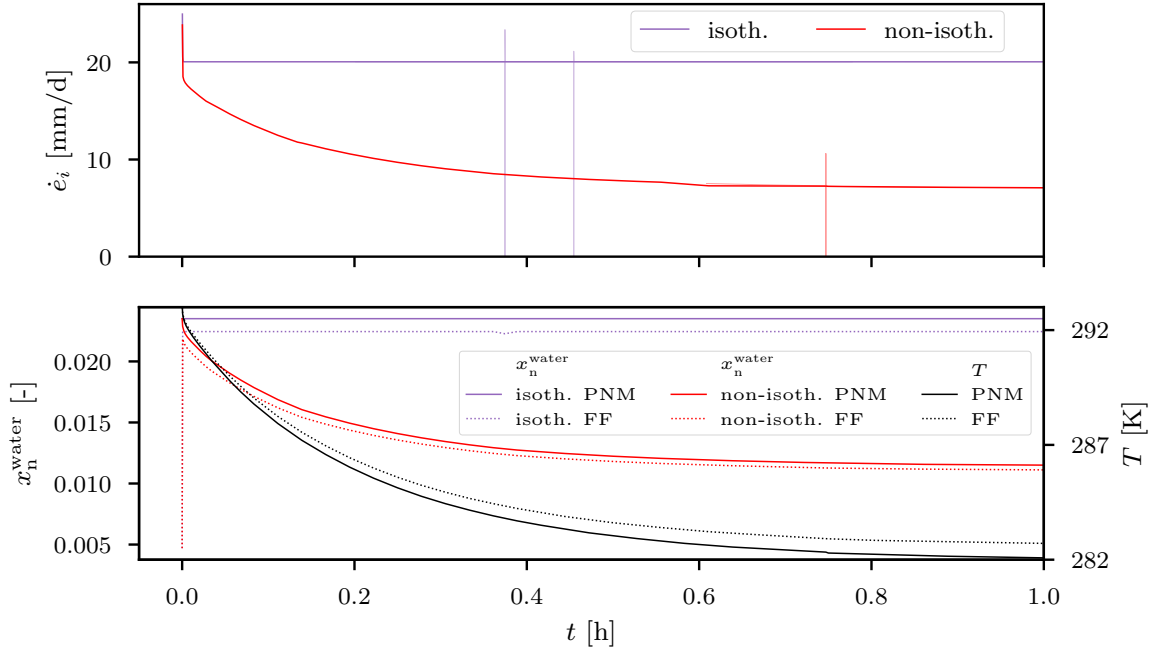


Figure 8.3 – Pore-local evaporation rates and interface quantities. Local evaporation rates (top), water vapor mole fractions and temperatures at the leftmost pore of the interface and the corresponding free-flow values for the isothermal and the non-isothermal NCP model. The temperature for the isothermal model is not plotted as it remains constant at $T = 293.15$ K.

Figure 8.4 shows the global evaporation rates for all four model options. As already seen in Fig. 8.2, the medium dries out more than twice as fast in case the energy balance is not considered. As for the local rates (Fig. 8.3), peaks and oscillations can be seen for the global rates, caused by local throat invasion processes which engender small pressure fluctuations throughout the whole network. Again, the thick curves have been smoothed using a moving median filter while the thin curves still show the oscillatory behavior of the system. Like the local evaporation rates presented in Fig. 8.3, the global rates drop rapidly at the beginning and remain virtually constant afterwards for the isothermal models. The rates of the non-isothermal models continue to fall and reach a much lower equilibrium state which is due to the previously mentioned drop of temperature. This corresponds to stage-I evaporation (cf. Section 2.3.3 and Fig. 2.5), including both a falling and a constant phase, which can also be observed on the REV scale [e.g., Mosthaf et al., 2014].

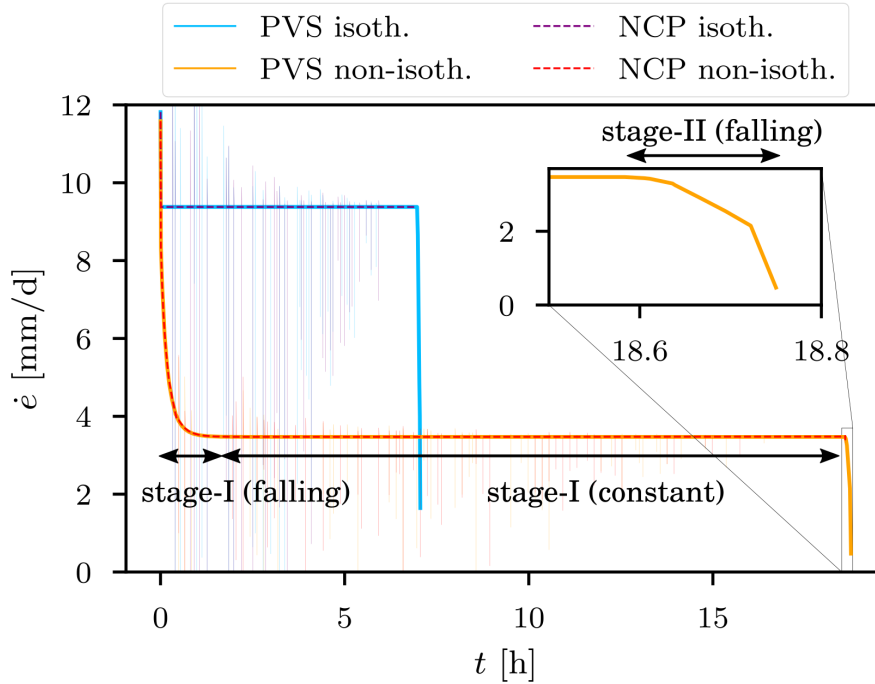


Figure 8.4 – Global evaporation rates. Evaporation rates for the isothermal and the non-isothermal models starting from $S_w = 0.99$. The air atmosphere is stagnant. The different stages of evaporation are marked for the non-isothermal models.

A sharp drop of \dot{e} marks the transition to stage-II evaporation, as highlighted by the close-up in Fig. 8.3. Starting from the interface, the pores fall completely dry which considerably slows down the evaporation process since water vapor now has to diffuse from deeper regions of the pore network towards the interface. This phase is very short because of the almost uniform and very low water saturation (around 0.003 for the non-isothermal case) within the network shortly before stage-II is reached: due to the absence of gravity, the presence of wetting-layer flow in the throat corners and the uniform pore-network geometry, the water saturation is distributed almost homogeneously throughout the network as soon as all pore throats are invaded by the gas phase (which happens before a pore dries out).

Figure 8.4 shows the results for an initial water saturation of 0.99. Setting this value to 1.0 essentially leads to the same results for the NCP models while the PVS models were not able to finish the simulation run within the given time. Very poor Newton convergence resulted in automatically decreased, unfeasible small time step sizes (see Chapter 5) such that the simulation had to be stopped manually.

Numerical model behavior Having discussed the physical aspects of the evaporation process, we now center our attention to the numerical behavior of the different models.

Figure 8.5 sheds light on the numerical model performance ($S_{w,init} = 0.99$) by comparing the temporal development of the four models' cumulative values of CPU time, time step sizes, number of Newton iterations and cumulative number of wasted Newton iterations in case of rejected time steps. Furthermore, the change of total water mass within Ω^{PNM} is given in Fig. 8.5a, where a linear decrease is found, as expected from the essentially constant global evaporation rates at later times (see Fig. 8.4). The PVS and the NCP models yield the same temporal evolution of the water mass, i.e., they are physically consistent.

However, the numerical performance differs significantly for the two approaches. While the non-isothermal PVS model runs for over 18 h, the NCP counterpart finishes in less than 9 h (Fig. 8.5b). This is explained by the consistently higher time step sizes Δt which remain close to the maximum allowed value of 100 s for the NCP model over large parts of the simulation run, whereas severe breakdowns and fluctuations slow down the PVS model (Fig. 8.5c), caused by the frequent triggering of the primary variables switch [Lauser et al., 2011]. This is seemingly paradox because the simulation is already started with two phases present and hence there should be no switching until the very end of the process when the network completely dries out. The switch, however, is triggered during the Newton iterations where the primary variables are not necessarily in a physically meaningful state.

Applying an appropriate *Newton chopping* strategy limits the shift of the solution between two consecutive Newton iterations to predefined bounds and improves the model's robustness. However, this is only effective to a certain degree. It is worth mentioning that also the NCP models benefit greatly from applying a Newton chop scheme. As mentioned in Section 3.2.3, it was also necessary to add a primary variable switch to the NCP model in order to simulate a complete drying of the network. This bears potential for further investigation and optimization in future work.

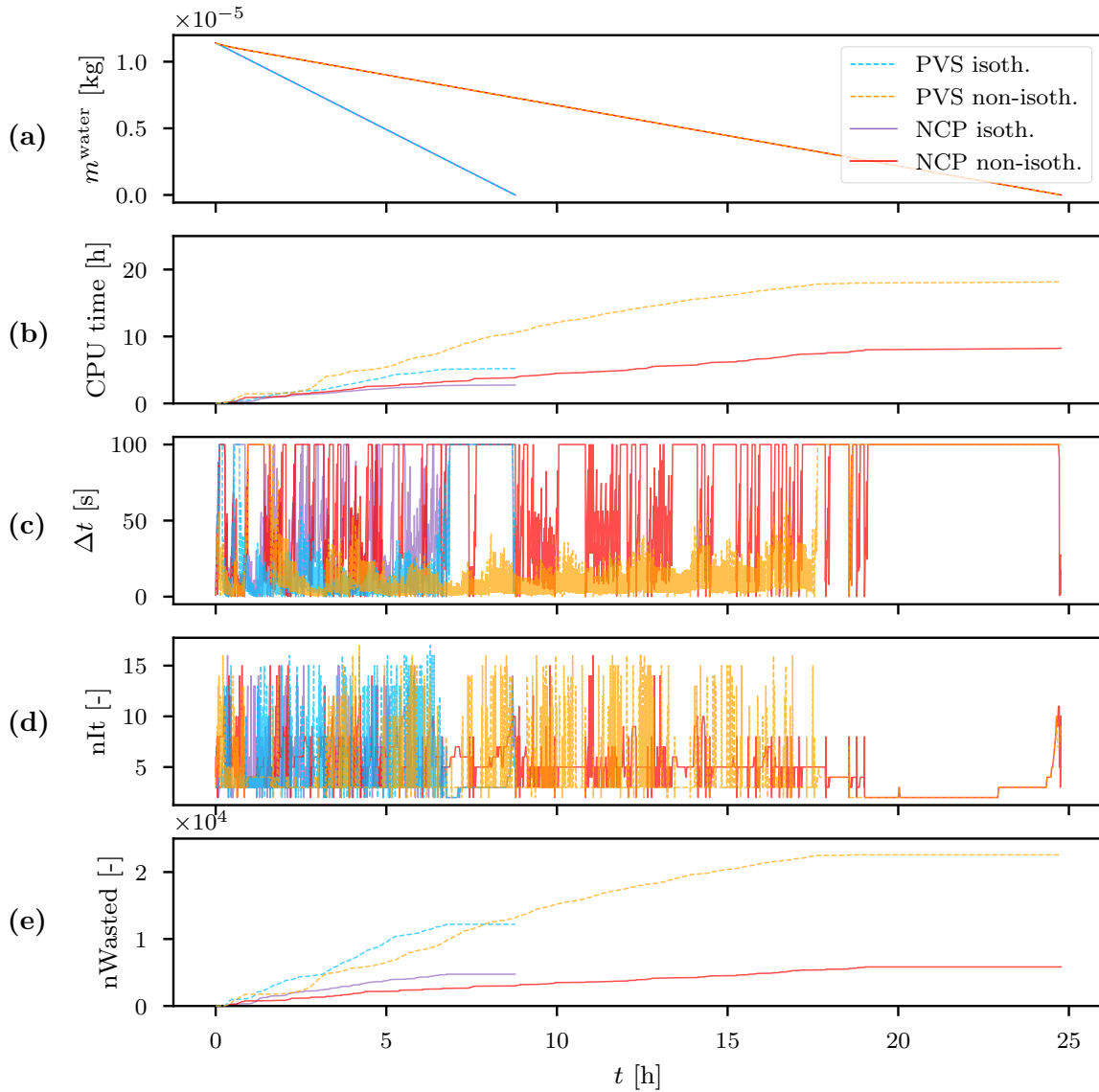


Figure 8.5 – Simulation statistics over time. Temporal evolution of the total water mass within Ω^{PNM} , the cumulative CPU time, the time step size, the number of Newton iterations and the number of wasted Newton iterations for an initial saturation of 0.99 and a resting atmosphere. Only the NCP models were able to finish the simulation.

Generally, the NCP models run much smoother as seen by the continuously lower number of Newton iterations per time step, which only increase noticeably in case of throat invasion events (Fig. 8.5d). Furthermore, the number of wasted Newton iterations, i.e., iterations that did not result in a successful time step, is tremendously decreased for the NCP models, underlining their superior numerical stability (Fig. 8.5e).

For both non-isothermal models (NCP and PVS), virtually all time steps are successful after around 20 h (as indicated by the flat curve in Fig. 8.5e), corresponding to the complete invasion of the entire network. After this point, the numerical complexity of the problem is greatly reduced as no further throat invasion processes take place. The same findings apply for the isothermal models which obviously require less CPU time as the evaporation process is significantly faster.

Table 8.1 – Simulation statistics. Statistics for the PVS and the NCP models and an initial saturation of 0.99. Δt is the time step size, n_{wasted} is the number of wasted Newton iterations and n_{It} is the number of Newton iterations per time step, for which only the successful time steps are considered.

model	tot. CPU time [h]			avg. Δt [s]		tot. n_{wasted}		avg. n_{It}	
	PVS	NCP	speedup	PVS	NCP	PVS	NCP	PVS	NCP
isoth.	5.21	2.74	1.90	5.72	10.75	12198	4746	3.40	3.86
non-isoth.	18.14	8.26	2.20	8.63	21.69	22570	5831	3.29	3.86

Table 8.1 shows that the NCP models are around two times faster than the PVS models which correlates with the increased average time step size. Furthermore, the number of wasted Newton iterations, resulting from unsuccessful time steps which had to be repeated with a smaller Δt , is greatly reduced for the NCP models, highlighting their numerical stability. This more than compensates for the slightly increased average number of Newton iterations per successful time step.

Setting an initial water saturation of 0.99 in Ω^{PNM} is numerically beneficial, especially for the PVS models, as shown by Fig. 8.6, where $S_{\text{w,init}} = 1.0$ was chosen. The simulation runs of the PVS models had to be aborted manually after around one day of CPU time due to an excessive decrease of Δt resulting from failing Newton convergence. The inevitable switch of primary variables (essentially for each pore in contact with the gas phase) eventually brought the PVS models to their proverbial knees, while the NCP models performed comparably well, as also shown in Table 8.2. The required CPU time was increased by 4 % for the isothermal and by 30 % for the non-isothermal NCP model. The reason for this decrease of efficiency could not be fully identified. It might be related to the non-linearity of Eq. (3.20). Further investigation on this is required in future work, e.g., applying different means of regularization or by adapting Eq. (3.21) which is not continuously differentiable [e.g., Bui and Elman, 2020].

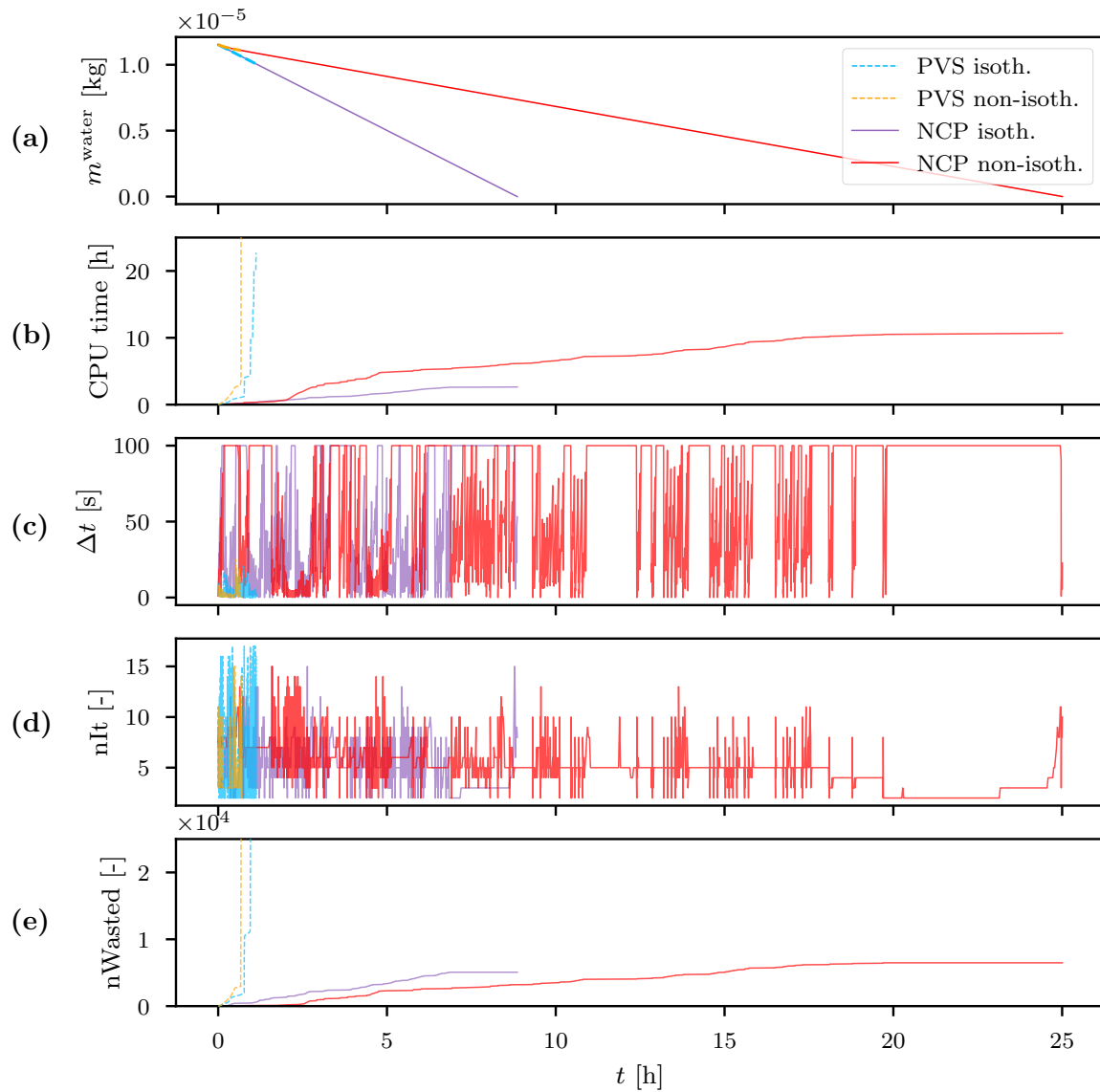


Figure 8.6 – Simulation statistics over time. Temporal evolution of the total water mass within Ω^{PNM} , the cumulative CPU time, the time step size, the number of Newton iterations and the number of wasted Newton iterations for an initial saturation of 1.0 and a resting atmosphere.

Table 8.2 – Simulation statistics. Statistics for an initial saturation of 0.99 and 1.0 for the NCP models. Δt is the time step size, n_{wasted} is the number of wasted Newton iterations and n_{It} is the number of Newton iterations per time step, for which only the successful time steps are considered.

	tot. CPU time [h]		avg. Δt [s]		tot. n_{wasted}		avg. n_{It}	
	1.0	0.99	1.0	0.99	1.0	0.99	1.0	0.99
$S_{\text{w,init}}$								
isoth.	2.64	2.74	9.79	10.75	5070	4746	4.18	3.86
non-isoth.	10.70	8.26	17.41	21.69	6481	5831	4.60	3.86

Summary This section focused on the evaporation of water from a regular pore network with rectangular throats into a stagnant air atmosphere. Four different model concepts for Ω^{PNM} were compared: the primary variable switch approach (PVS) and the non-linear complementarity problem (NCP) method, each either under isothermal or non-isothermal conditions.

The first part of this section discussed the temporal development of the evaporation process under physical considerations. The evaporative flux across the coupling interface induced a significant temperature drop for the non-isothermal models. This in turn lead to a considerable decrease of the initial evaporation rate, caused by the reduction of the temperature-dependent water vapor pressure. It took around 7 h to invade all pore throats with air for the isothermal models while this time increased to over 20 h for the non-isothermal models due to the reduced evaporative flux. Small local deviations with respect to the invasion patterns of the PVS and the NCP models were found, which, however, did not affect the overall evaporation rate over time.

The numerical characteristics of the different model types differed significantly, as shown in the second part of this section. The NCP models were twice as fast as the PVS models. The latter failed to simulate an evaporation process starting from a completely saturated medium, owing to the frequent triggering of the primary variable switch. This highlights the NCP models' superior numerical stability.

We will only consider the non-isothermal NCP model for the upcoming sections where we focus on the influence of different setup parameters, starting with a non-uniform, random pore-size distribution in Ω^{PNM} .

8.2 Influence of network heterogeneity

In the following, the inscribed pore body radii r_i follow a log-normal distribution (mean 2×10^{-4} m, standard deviation 1×10^{-5} m) while all other parameters are exactly the same as before (stagnant atmosphere, rectangular throats). We use the non-isothermal NCP model and an initial water saturation of one. Since the pore throat radii correlate with the adjacent pore body radii, the capillary entry pressures and the pore throat conductivities are non-uniform, too (see Fig. 8.7).

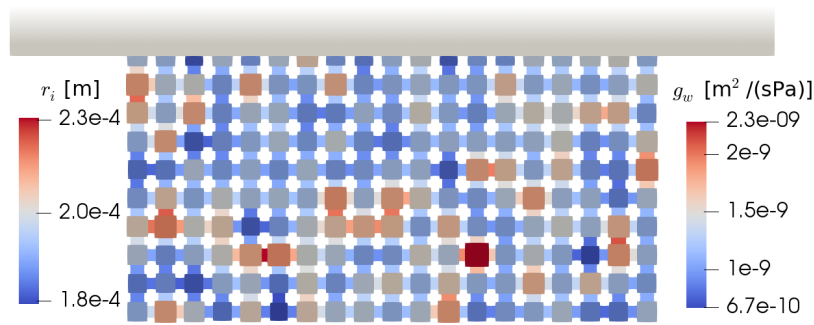


Figure 8.7 – Network with randomly distributed pore body radii. The corresponding throat wetting-phase conductance for single-phase flow varies by over one order of magnitude.

Physical process description The temporal evolution of the evaporation process presented in Fig. 8.8 differs significantly from the one shown for a uniform network in Fig. 8.2. The throats featuring the lowest $p_{c,e}$ are invaded first, generating an unsymmetrical invasion pattern with clearly distinguishable patches of completely wet and partly saturated pores. As mentioned earlier, $p_{c,e}$ is not solution-dependent. For future work, it would be interesting to include the influence of T on γ and assess to which extent this influences the invasion process.

Despite the fundamental differences in invasion patterns, the random network yields virtually the same global evaporation rate over time compared to the uniform pore network, as shown in Fig. 8.9. Since all pore bodies remain at least partly saturated due to the presence of wetting layers in the throats' corners during stage-I (cf. Section 8.3), the evaporation rate does not depend on the network geometry but only on the atmospheric demand [e.g., Or et al., 2013].

Oscillations of the evaporation rate (shown by the thin red lines in Fig. 8.9) associated with throat invasion processes occur much more frequently and with larger magnitude for the random network. In the uniform network, basically all throats of a horizontal row are invaded simultaneously (see Fig. 8.2), which more or less results in a single spike of the evaporation rate. This is not the case for the random network where throat invasions occur rather continuously over time, as given by the broad range of the throats' entry capillary pressures.

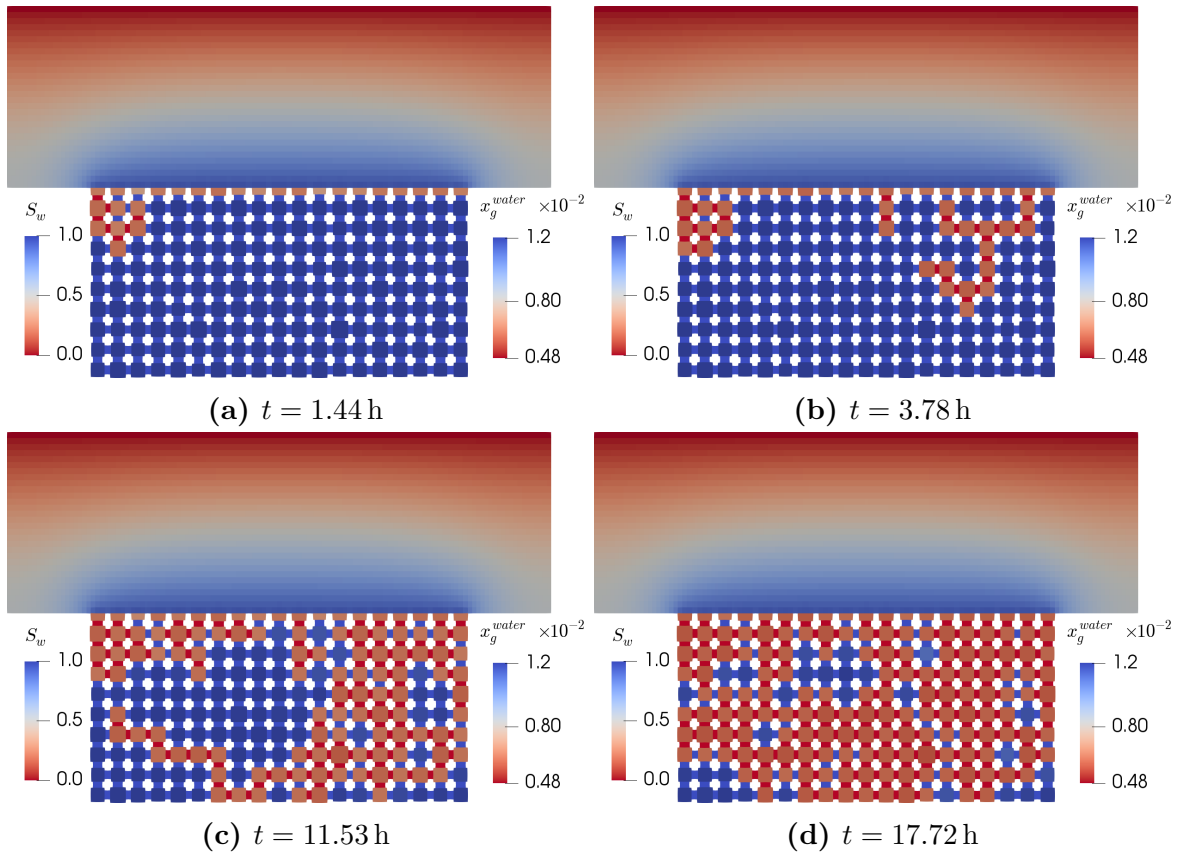


Figure 8.8 – Vapor concentration fields and saturation distribution. Temporal evolution of an evaporation process with resting air atmosphere and a non-uniform network. Blue pore throats are fully occupied by the wetting phase (liquid water) while red throats are invaded by the gaseous non-wetting phase. The wetting-phase saturation S_w is given for Ω^{PNM} and the water vapor mole fraction x^{water} is shown for Ω^{FF} .

Numerical model behavior Considering a random network strongly increases the numerical complexity as shown by Fig. 8.10. The CPU time raised from 10.7 h for the uniform network to 50.05 h for the random network (Fig. 8.10b). While for the former,

the time step size Δt could be maintained at its maximum allowed value of 100 s over large parts of the simulation run (Fig. 8.10c), this was only possible for the random network after all throats had been invaded. This directly results from the comparatively poor Newton convergence behavior (Fig. 8.10d) and the high number of wasted Newton iterations (Fig. 8.10e).

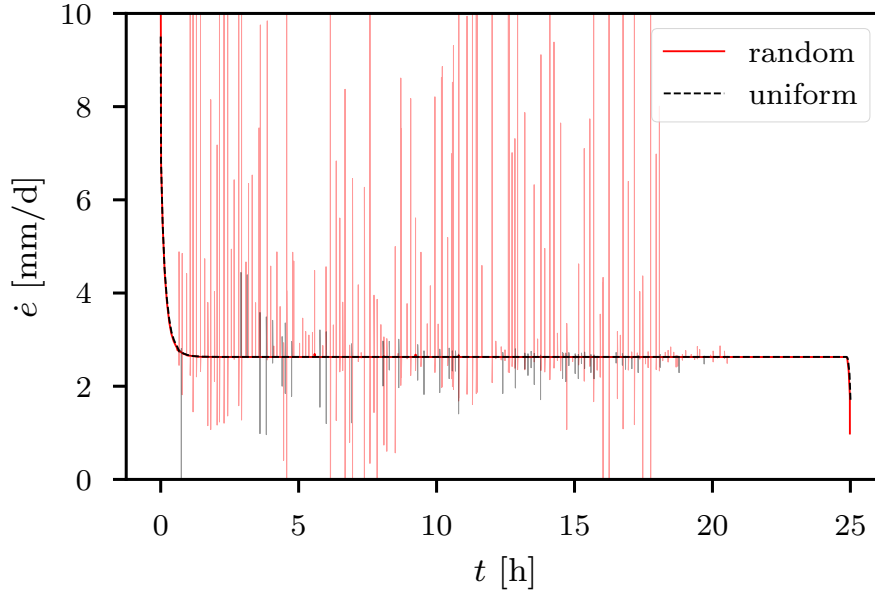


Figure 8.9 – Global evaporation rates. Global evaporation rate for the random network and the corresponding curve for the uniform network discussed in the previous section.

A possible explanation for this is presented in Fig. 8.11 which shows the throat-local flow rates of the wetting phase at different times. Figs. 8.11a and 8.11c depict relatively stable configurations where the highest flow rates occur at the interface between Ω^{FF} and Ω^{PNM} . The figures also show that only partly saturated pores connected to the air phase are able to distribute water in multiple directions (i.e., permit a local divergence of the wetting-phase flow field) because here, the intruding air phase can compensate for the loss of water volume. Returning to the issue of poor Newton convergence, Figs. 8.11b and 8.11d are temporal snapshots close to throat invasion events. Here, the maximum flows do not occur at the domain interface, but locally, close to the invaded throat. These events can trigger a complete temporary inversion of the flow field within Ω^{PNM} , with local flow rates seven orders of magnitude higher compared to the stable situations, as seen by comparing the color bars of Figs. 8.11a and 8.11b.

The physical accuracy of this remains to be assessed, e.g., by means of experiments. Nevertheless, this numerically challenging behavior may explain the Newton convergence issues discussed above.

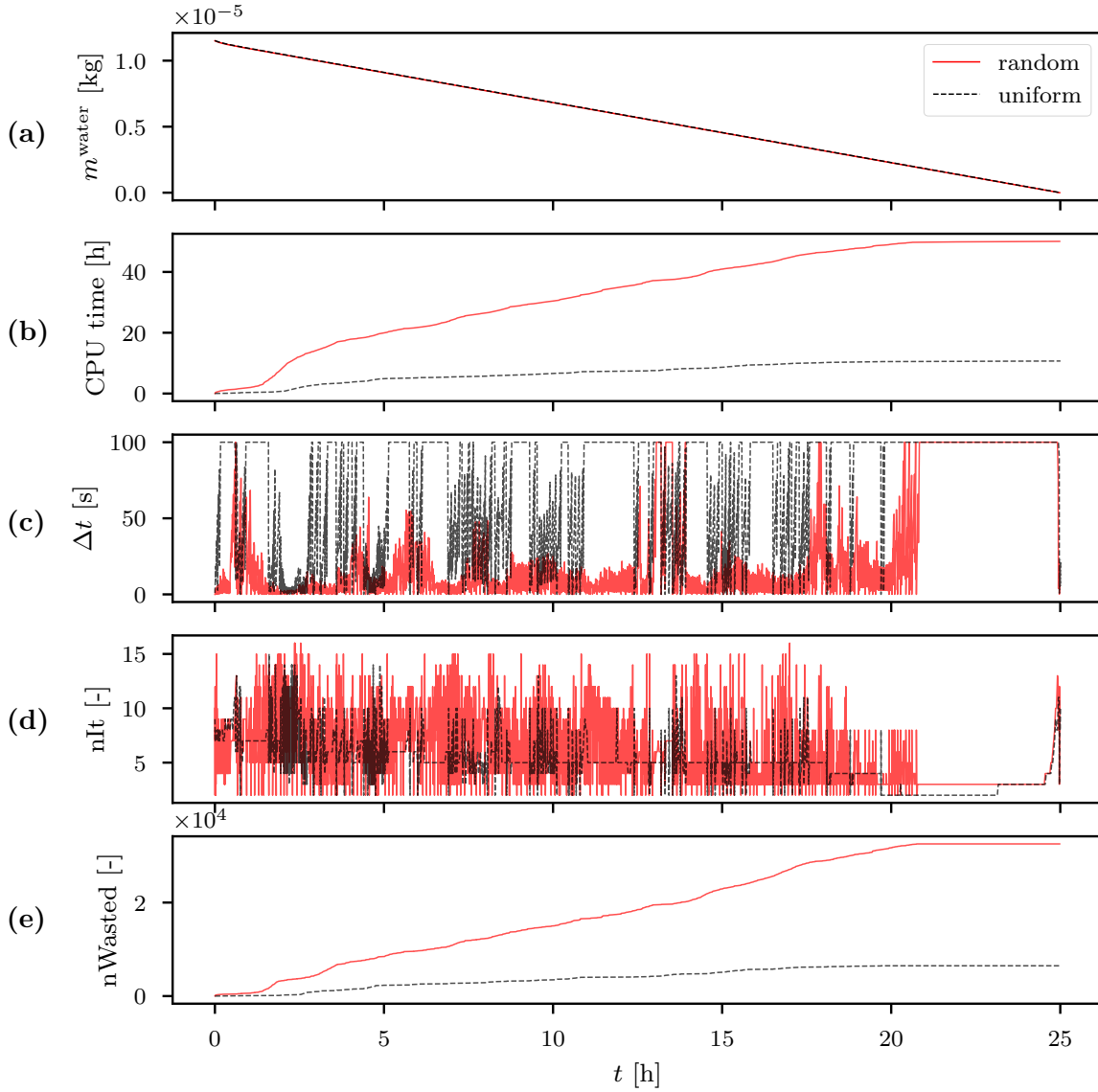


Figure 8.10 – Simulation statistics over time. Temporal evolution of the total water mass within Ω^{PNM} , the cumulative CPU time, the time step size, the number of Newton iterations and the number of wasted Newton iterations for the random and the uniform pore network (square throats, $S_{w,\text{init}} = 1.0$, resting atmosphere).

Table 8.3 summarizes the data related to model convergence behavior.

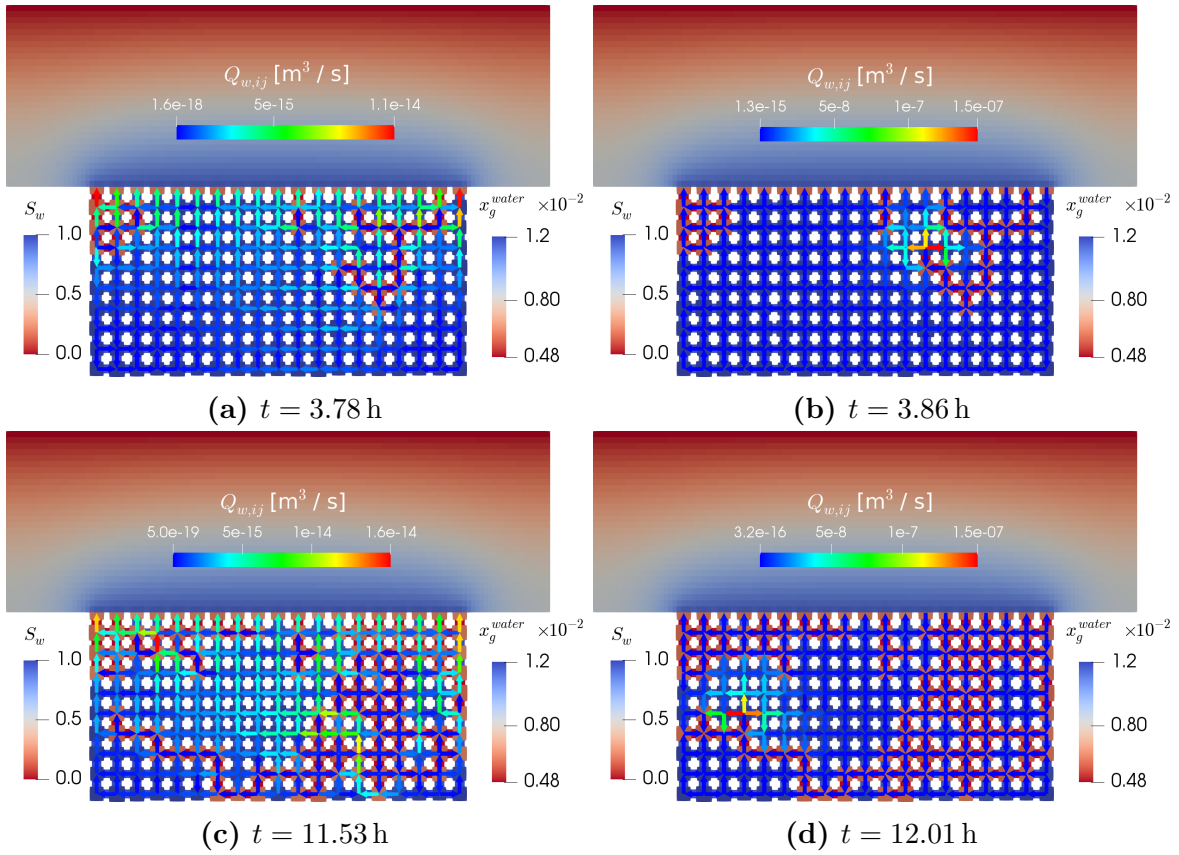


Figure 8.11 – Wetting-phase flow field in Ω^{PNM} . Temporal evolution of the wetting-phase flow field in Ω^{PNM} . (b) and (d) correspond to throat invasion events.

Table 8.3 – Simulation statistics. Statistics for a random and a uniform network. Δt is the time step size, n_{wasted} is the number of wasted Newton iterations and n_{It} is the number of Newton iterations per time step, for which only the successful time steps are considered.

network	tot. CPU time [h]		avg. Δt [s]		tot. n_{wasted}		avg. n_{It}	
	uni.	rand.	uni.	rand.	uni.	rand.	uni.	rand.
	10.70	50.05	17.41	3.81	6481	32544	4.60	4.97

Summary Including network heterogeneity leads to a different invasion pattern compared to a uniform network while the global evaporation rate remains unaffected. More than four times of CPU time is required due to poor Newton convergence possibly related to a highly fluctuating flow field within Ω^{PNM} in case of invasion events. In the next section, we will return to a uniform network where the throat cross-sectional shape is changed from a rectangular to a circular geometry.

8.3 Influence of the throat cross-sectional shape

The previous sections investigated a pore network with square throat cross-sectional shapes, i.e., the wetting phase was continuously connected due to wetting-layer corner flow [Chauvet et al., 2009]. Here, we break this continuity by employing circular throat cross sections devoid of corners and thus wetting layers (see Section 2.3.2). Again, a stagnant air atmosphere is considered and the same initial ($S_{w,init} = 1.0$) and boundary conditions as in the previous sections were applied. Except for the throat cross-sectional shapes, the properties of Ω^{PNM} are exactly as in Section 8.1, i.e., a uniform network of cubic pore bodies and circular throats is considered. The non-isothermal NCP model is used.

Physical process description Figure 8.12 compares the resulting temporal evolution of the global evaporation rate with the corresponding curve of Section 8.1, employing square-shaped throat cross sections. The time for a complete invasion of all throats is significantly increased to almost 33 h for the circular pore throats. This is due to the overall reduction of the global evaporation rate. The falling stage-I period is virtually identical for both the square and the circular throats. Here, liquid water is present at the domain interface in both cases and the same reduction of \dot{e} due to falling temperatures, as explained in Section 8.1, takes places. While the square cross-sections provide a pathway for liquid water in their corners throughout almost the whole simulation run (and hence maintain a constant stage-II period), the connection of the wetting phase at the surface to deeper regions of the network gets abruptly severed once the air phase invades a circular throat. Due to the lack of corners, no water films can reside in the circular throats which reduces the water mass transfer to a slow diffusion process.

Each of the nine clearly distinguishable plateau steps in Fig. 8.12 effectively corresponds to a sort of constant stage-II period where the distance of the water table from the surface determines the diffusion length and hence the evaporation rate [Shokri and Or, 2011]. The combination all nine steps can be seen as a falling stage-II period. Since the network is uniform, essentially all throats at a certain depth are invaded simultaneously (ignoring the previously mentioned numerical inaccuracies) which explains the discrete, step-shaped form of the curve. As seen from the inset pictures in Fig. 8.12, the number

of invaded throat rows matches with the number of discrete steps on the evaporation curve.

For example, five horizontal rows of throats are invaded at the central image ($t = 12.9$ h) which corresponds to five steps on the curve when counted from the left side.

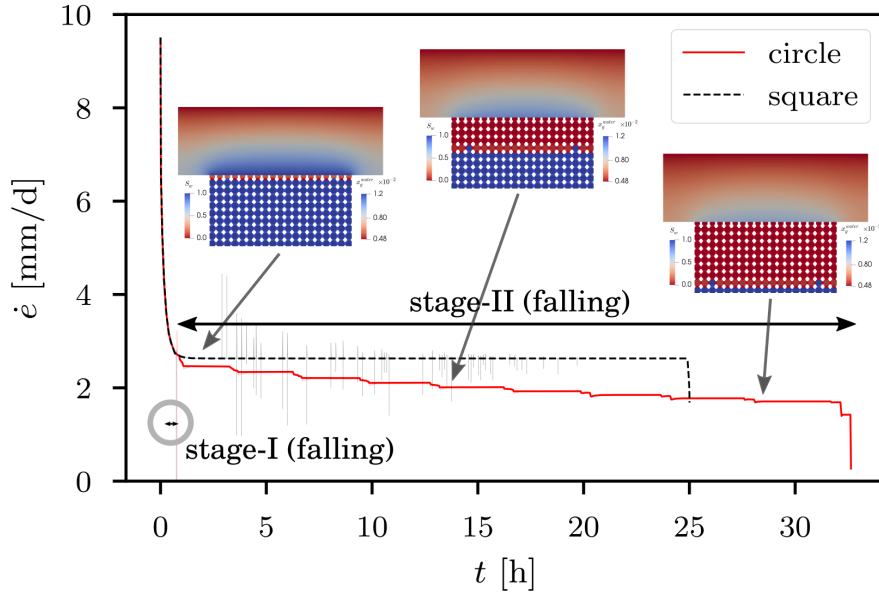


Figure 8.12 – Global evaporation rates. Comparison of evaporation rates for square and circular throat cross sections (non-isothermal NCP model). The air atmosphere is stagnant, $S_{w,init} = 1.0$. The different stages of evaporation are marked for the circular throats. The inset images correspond to 0.8 h, 12.9 h and 27.8 h.

As discussed in Section 8.1 and shown by the inset images in Fig. 8.12, the evaporation front does not move perfectly uniformly due to small numerical perturbations. Figure 8.13 shows the situation in closer detail. At $t = 0.89$ h (Fig. 8.13a), the complete first row of throats at the interface is invaded, except for the third throat from the left. We exploit this situation for elaborating on a pore-scale evaporation mechanism described by Shahræeni et al. [2012] and Or et al. [2013], who showed that the pore-local evaporation rate increases if the neighboring pores fall dry. As long as all pores at the surface still hold some liquid water (Fig. 8.13a), the diffusive fluxes are essentially oriented normally to surface, rendering the process one-dimensional, as shown by the pink arrows which are scaled and oriented by the gradient of x_n^{water} in Ω^{FF} .

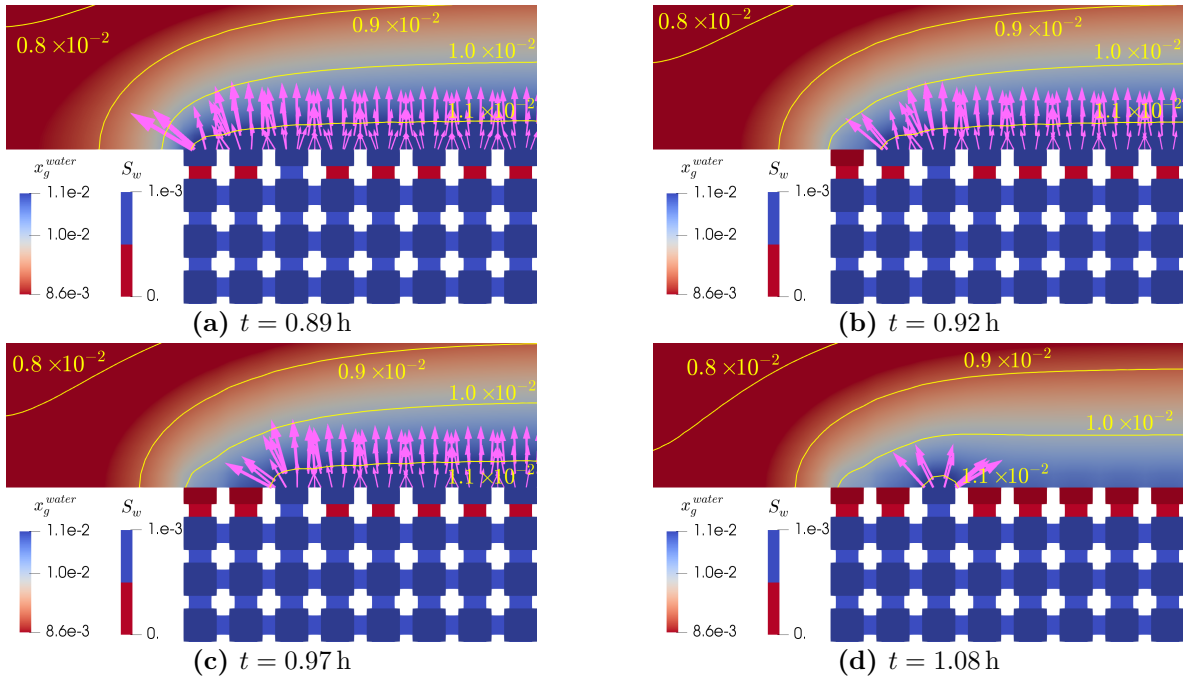


Figure 8.13 – Diffusion at the interface. Temporal evolution of the diffusive fluxes at the interface (pink arrows, scaled and oriented by the gradient of x_n^{water} in Ω^{FF}). Isolines of x_n^{water} are marked in yellow. Red colors in Ω^{FF} indicate invaded throats and fully dried-out pores.

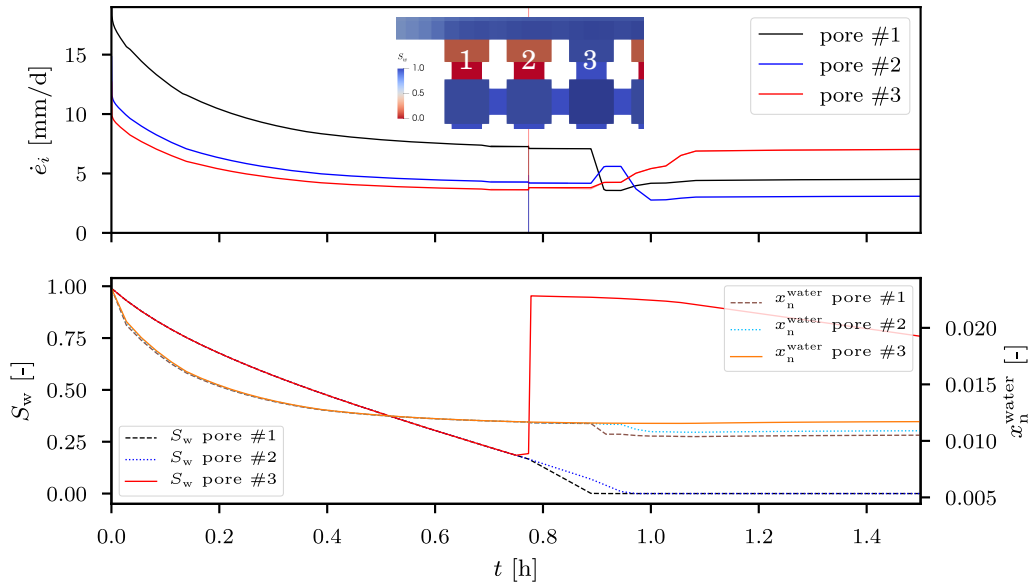


Figure 8.14 – Pore-local evaporation rates. Local evaporation rates for the three leftmost pores (upper figure) and temporal development of S_w and x_n^{water} (lower figure). Throat #3 is not invaded while the other ones are.

Only the leftmost pore exhibits some lateral diffusion because of the vapor concentration gradient at the edge of the interface. This noticeably increases the pore's local evaporation rate, as indicated in the upper part of Fig. 8.14. Here, the local evaporation rates show the same initial falling characteristics described for Fig. 8.3 as the system strives for equilibrium. In contrast to the other throats, throat #3 does not get invaded by the air phase at $t = 0.8$ h, as shown by the inset image. Quite the opposite is true: the high capillary pressure due to the pores' preceding de-saturation (see lower figure) leads to a refilling of pore body #3 as soon as the other pore bodies get disconnected from the bulk wetting phase within the network during the invasion event, indicated by the jump in saturation in the lower figure. Shortly after the invasion event, at 0.92 h, pore #1 dries out, i.e., its saturation goes to zero, as also visible in Fig. 8.13b.

This temporally increases the evaporation rate of the directly neighboring pore #2 until the latter also dries out at $t = 0.97$ h (Fig. 8.13c). Eventually, all pores neighboring to pore #3 fall dry, yielding a fully two-dimensional diffusion behavior at this position, which increases the local evaporation rate considerably by 80 %, as seen in the lower part of Fig. 8.14. The latter also reveals that the water vapor mole fraction drops for pore bodies #1 and #2 after the wetting phase has vanished while it remains constant at its thermodynamic equilibrium value for pore #3 where the wetting phase is still present.

Numerical model behavior Using circular throats instead of rectangular ones increases the model's numerical stability, as shown in Table 8.4. The CPU time reduces by 28.5 % while less than half of the Newton iterations are wasted. This goes in line with the visible appearance of the evaporation rate's curve in Fig. 8.12, where substantially fewer fluctuations occur compared to the curve for rectangular throats. For the latter, invasion events always induce rather profound pressure and flux oscillations throughout the whole system. Due to the possible coexistence of the wetting and the non-wetting phase in a throat, potential counter-current flows might cause numerical difficulties. This is not the case for circular throats where the wetting-phase pressure coupling between pore bodies connected by an invaded throat is eliminated.

Table 8.4 – Simulation statistics. Statistics for circular and square-shaped throats (non-isothermal NCP models, $S_{w,init} = 1.0$). Δt is the time step size, n_{wasted} is the number of wasted Newton iterations and n_{It} is the number of Newton iterations per time step, for which only the successful time steps are considered.

shape	tot. CPU time [h]		avg. Δt [s]		tot. n_{wasted}		avg. n_{It}	
	□	○	□	○	□	○	□	○
non-isoth.	10.70	7.65	17.41	36.07	6481	3012	4.60	5.56

Summary This section showed that switching from square to circular throat cross-sectional shapes decelerates the evaporation process by around 30 % for the given setup which is due to the absence of wetting layers in the pore throats which would otherwise keep the water phase continuously connected throughout the network. As soon as the first throats are invaded, the evaporation process is limited by diffusion and hence the distance between the water table and the porous medium surface. A pore’s local evaporation rate at the surface strongly increases if the neighboring pores fall dry because the previously one-dimensional diffusion process becomes two-dimensional. Using circular throats increases the numerical stability for the given setup.

In the last section concerned with evaporation, we will return to employing square-shaped throats whereas the atmosphere above Ω^{PNM} will no longer be stagnant.

8.4 Evaporation into a moving atmosphere from a homogeneous network with square-shaped throats

In this section, the network is again identical to the one used in Section 8.1, i.e., uniform with rectangular throats. The focus here lies on inducing an air flow above the porous medium ($Re \approx 17$ in Ω^{FF}), as presented in Fig. 8.1b. We use the non-isothermal NCP model and start from an initial water saturation of one.

Physical process description Fig. 8.16 shows the temporal development of the evaporation process and indicates the formation of a vapor boundary layer above the interface

between Ω^{PNM} and Ω^{FF} . As seen in Fig. 8.15d, this boundary layer shrinks and ultimately vanishes as the medium dries out completely, beginning from the upstream (left) region of the interface.

The invasion of the air phase into the network starts on the left side of the interface (see Fig. 8.15b), where the air humidity in Ω^{FF} is lowest and the largest pore-local evaporation rates occur, as seen in Fig. 8.17d. The air phase spreads vertically in Ω^{PNM} until it reaches the network's bottom and continues to invade throats in a rightward direction. It temporally encloses a patch of completely saturated pores, as shown in Fig. 8.15c, before the network eventually dries out.

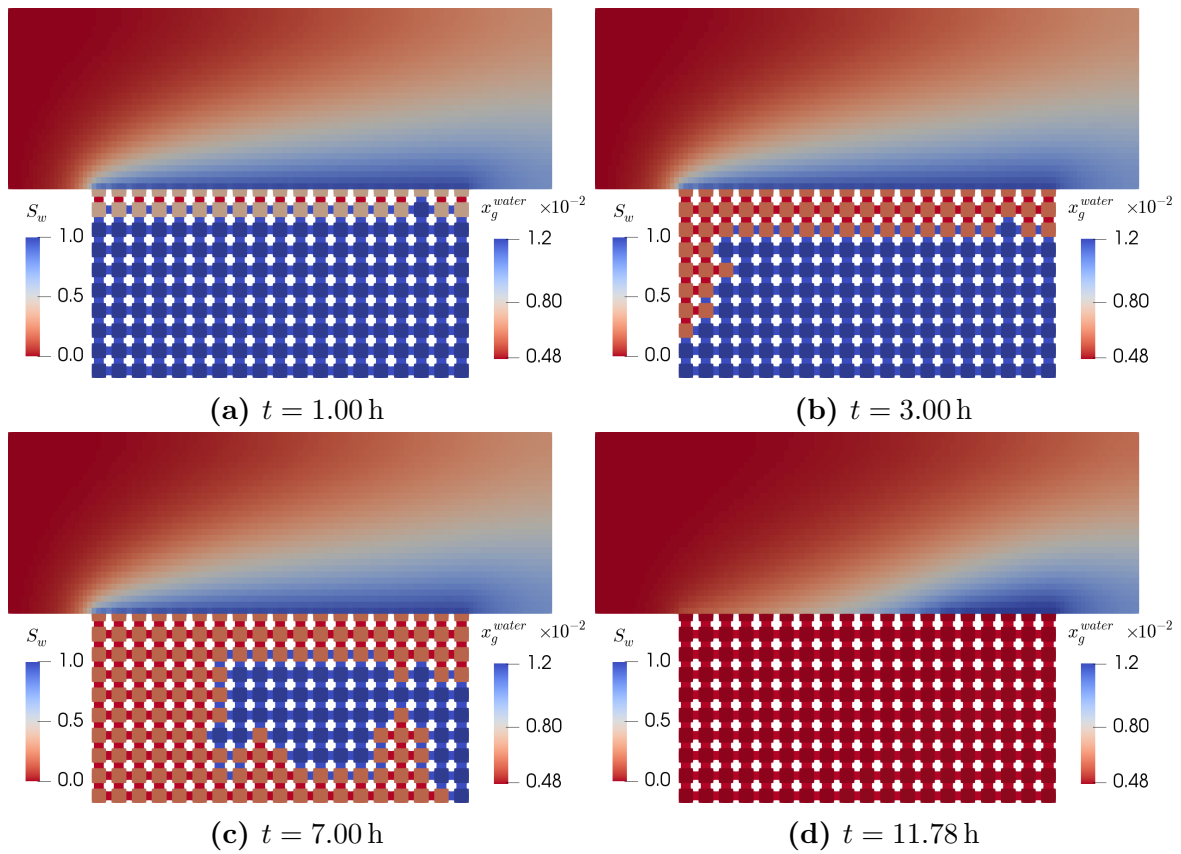


Figure 8.15 – Vapor concentration fields and saturation distribution. Temporal evolution of an evaporation process with air flow above the network. Blue pore throats are fully occupied by the wetting phase (liquid water) while red throats are invaded by the gaseous non-wetting phase. The wetting phase saturation S_w is given for Ω^{PNM} and the water vapor mole fraction x^{water} is shown for Ω^{FF} .

The global evaporation rate shown in Fig. 8.16 is strongly increased due to the continuous supply of warm, dry air in Ω^{FF} , resulting in only around 14h needed to completely dry the medium compared to 25h for the resting atmosphere case. The temporal development of the evaporation rate may seem unexpected at first glance: after the initial, previously discussed fall of the curve due to temperature equilibration and a short constant phase, the evaporation rate actually increases again over time. This is in strong contrast to the findings presented in Section 8.1, where a constant stage-II evaporation [e.g., Or et al., 2013] could be observed, as shown by the black curve in Fig. 8.16.

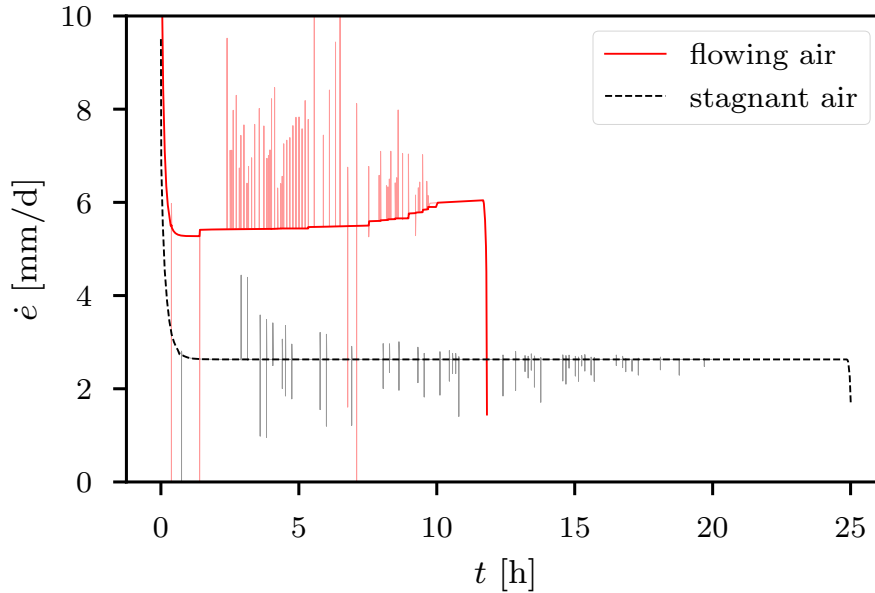


Figure 8.16 – Global evaporation rates. Comparison of evaporation rates for a moving and a resting gas atmosphere. $S_{w,\text{init}} = 1.0$.

Figure 8.17 explains this behavior by showing the local flow rates of the gas phase $Q_{n,ij}$ within the network's throats as well as the pore-local evaporation rates at the interface for different times. As seen in Fig. 8.15a, only the vertical throats at the interface are invaded at $t = 1$ h which corresponds to the expected distribution of local evaporation rates along the interface shown by the blue curve in Fig. 8.17d: Evaporation is strongest at the leftmost pore, where the air in Ω^{FF} is driest, and continues to decrease along the interface as the air gets more and more saturated with water vapor. The situation changes, however, as soon as the first row of horizontal throats next to the interface

gets invaded (see Fig. 8.17a) which establishes a flow path for the air phase. The arrows indicate that air now enters the network at the leftmost throat #1, flows parallel to the interface and exits the network again at the rightmost throat #19. This strongly increases the evaporative flux at throat #19, shown by the yellow curve in Fig. 8.17d. The flow of air pushes the water vapor out of Ω^{PNM} , and hence the evaporation process is no longer only diffusion-driven but dominated by advection. This becomes even more clear as the air phase continuous to invade more and more throats, creating new pathways for advective gas flow in the network, as shown by Fig. 8.17b and the green line in Fig. 8.17d.

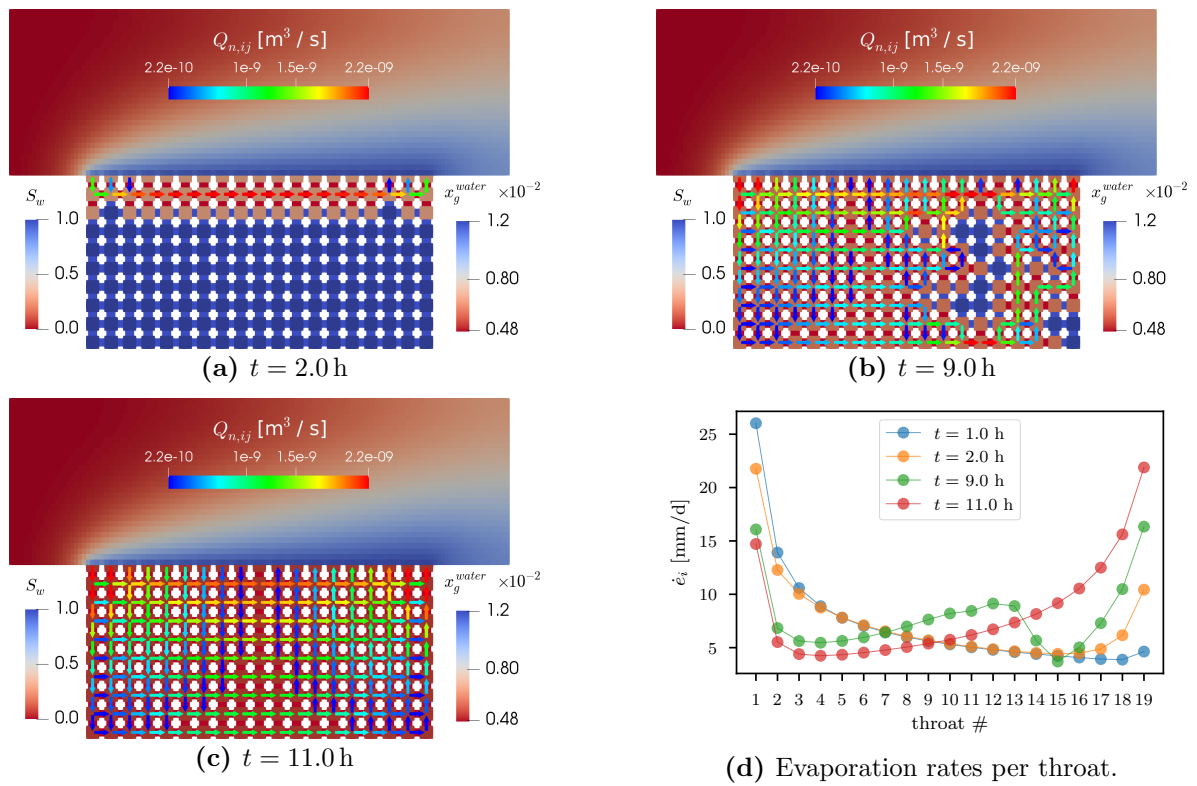


Figure 8.17 – Non-wetting phase flow in Ω^{PNM} . Internal gas phase flows in Ω^{PNM} and pore-local evaporation rates at different times. The pores at the interface are numbered from 1 to 19 (from left to right). The lines connecting the dots in (d) are for ease of visualization and have no physical meaning.

The latter exhibits a drop at pores #14 to #17 due to the locally decreased outflow of gas which is caused by the given saturation distribution in the network. When all throats are invaded by the gas phase (see Fig. 8.17c), the flow field in Ω^{PNM} essentially resembles the one described for single-phase flow in Section 7.1. The air enters the

network along the left half of the interface and leaves Ω^{PNM} symmetrically across the right half of the interface, which explains the strongly elevated vapor fluxes on this side, as shown by the red curve in Fig. 8.17d. Diffusion-driven evaporation still takes place due to the presence of liquid water at the interface. At the left half of the interface, diffusion and advection are actually two competing mechanisms as the vapor concentration gradient yields a diffusive flux towards Ω^{FF} , reversely to the inbound advective flow. The red and green curves in Fig. 8.17d also show this reduction in evaporation rates for pores #1 to #10.

Numerical model behavior Adding air flow in Ω^{FF} noticeably increases the computational demand, as shown by Table 8.5. Compared to the equivalent case with a resting atmosphere, the total CPU time is increased by over 37% due to an overall decrease of time step sizes caused by deteriorated Newton convergence behavior. The increased physical complexity is reflected by an increase of wasted Newton iterations by around 60%.

Table 8.5 – Simulation statistics. Statistics for a moving atmosphere ($S_{w,\text{init}} = 1.0$). Δt is the time step size, n_{wasted} is the number of wasted Newton iterations and n_{It} is the number of Newton iterations per time step, for which only the successful time steps are considered.

Ω^{FF}	tot. CPU time [h]		avg. Δt [s]		tot. n_{wasted}		avg. n_{It}	
	still	flow	still	flow	still	flow	still	flow
non-isoth.	10.70	14.71	17.41	6.29	6481	10330	4.60	4.47

Summary A flowing gas atmosphere in Ω^{FF} leads to the formation of a water vapor boundary layer above the interface. Evaporation happens significantly faster compared to a setup with a resting atmosphere. The invasion of the gas phase into the network occurs non-uniformly, creating pathways for advective gas flux in Ω^{PNM} . This leads to a rather atypical (cf. Section 2.3.3) behavior of the evaporation rate over time. While the presence of liquid water technically still qualifies the process as stage-II evaporation, the evaporation rate actually increases over time due to advective water vapor transport out of Ω^{PNM} . Evaporation is no longer only diffusion-controlled but governed by advection, too. The computational complexity increases for flow in Ω^{FF} .

9 Summary and Outlook

9.1 Summary

This work investigated model concepts for systems of coupled free flow over a porous medium, where classical REV-scale approaches may fail to capture relevant sub-scale features and processes due to the averaging of the porous medium. We aimed at a pore-scale description of the interface region between the two flow domains using the pore-network modeling approach, which discretely resolves the porous domain in a simplified sense and thus comes with an acceptable degree of computational cost. Conceptually, the sharp and simple interface separating the region of free-flow Ω^{FF} and the bulk porous medium Ω^{REV} presented in a number of previous works [e.g., Layton et al., 2002, Mosthaf et al., 2011, Baber et al., 2016, Fetzer, 2018] was replaced by a pore-network model interface region Ω^{PNM} . A dynamic two-phase pore-network model allowed simulating systems beyond their capillary equilibrium state. Laminar flow was considered in all domains.

Model Chapter 2 outlined the basics of modeling porous media systems with a special focus on pore-network modeling, which is the centerpiece of our proposed coupled model concept. Chapter 3 then explained the mathematical and numerical model concepts employed in the individual sub-domains, including the discussion of the necessary coupling conditions. A fully coupled, fully implicit and monolithic approach was followed which yields a single system of equations that is solved simultaneously. Hence, no coupling iterations are needed and the scheme inherently conserves the fluxes of mass, momentum and energy across the coupling interfaces. Model concepts of varying physical complexity were presented, ranging from single-phase flow to non-isothermal, compositional two-phase flow in the porous medium.

A rather natural set of conditions for coupling Ω^{FF} and Ω^{PNM} was derived with a special focus on describing pore-scale slip velocities at the pore bodies intersecting with the interface. Coupling conditions for Ω^{PNM} and Ω^{REV} are presented and briefly discussed with respect to potential inconsistencies arising from the combination of different model concepts.

A staggered-grid scheme was used for the free-flow domain while the Box method was employed for both Ω^{PNM} and Ω^{REV} . The coupled models were implemented in the open-source simulation toolbox DuMu^x.

Results The free-flow model and the dynamic two-phase pore-network model were verified separately in Chapter 6. Numerical results were presented in Chapters 7 and 8. Including a wall friction term in the (Navier-)Stokes equations [Flekkøy et al., 1995] facilitated the simulation of relatively thin three-dimensional free-flow channels in 2D, thus reducing the computational cost. The larger the aspect ratio between channel width and depth, the better the approximation. A maximum error of around 10% was found for rectangular channels.

After this, single-phase flow micromodel experiments conducted by Terzis et al. [2019] were recalculated using a coupled model comprising Ω^{FF} and Ω^{PNM} , corresponding to the micromodel's free-flow channel and a subjacent porous structure. Essential pore-network model parameters were determined numerically beforehand. Highly resolved numerical three-dimensional reference solutions for the complete micromodel were obtained by using the CFD tool OpenFOAM. A close match between experimental results, the fine-scale simulation data and results of the coupled model could be found. A further numerical study showed that the smaller the pores in the porous domain, the better the approximation by the pore-network model.

A numerical example of compositional free flow over a randomly generated pore network showed the interaction between the two model domains. Concentration boundary layers above the domain interface evolved with a thickness depending on the Reynolds number within Ω^{FF} . Preferential flow paths were found in Ω^{PNM} .

Simulating evaporation from a pore network featured the most complex physics in this work. Here, different model concepts for the description of non-isothermal two-phase, two-component flow in the pore-network were investigated. A primary variable switch

(PVS) approach, used also in [e.g., Mosthaf et al., 2011], was compared with a non-linear complementarity problem (NCP) method [Lauser et al., 2011]. For the latter, it was also necessary to add a simple primary variable switching technique in order to simulate a complete drying of the porous medium. After this modification, the NCP model was around two times faster and, in general, numerically more robust compared to the PVS model which failed to simulate an evaporation process from an initially fully water-saturated network. Apart from this, both models yielded the same physical results which are in accordance with theory, i.e., different stages of evaporation could be observed [e.g., Or et al., 2013]. Using the NCP model, different modifications of the problem setup were investigated: adding random network heterogeneity did not change the global system behavior, i.e., evaporation rate, but strongly impaired the invasion pattern of the air phase into the network. Strong local oscillations in flow rates and pressure due to throat invasion processes made this case numerically more challenging compared to a uniform network. Replacing the rectangular throats with such of circular cross sections decreased the evaporation rate, as liquid water film flow in the corners of the throats towards the porous medium surface was no longer possible and evaporation was soon diffusion limited. Compensation effects could be observed in terms of locally increased evaporation rates for pores surrounded by dry neighbor pores [Shahraeeni et al., 2012, Or et al., 2013]. Considering air flow instead of a resting gas atmosphere strongly changed the evaporation behavior: on the one hand, the process was faster due to the constant resupply of warm, dry air. On the other hand, the intrinsically diffusion-controlled evaporation process was strongly affected by advection as soon as the gas phase could establish flow paths within Ω^{PNM} , leading to a rather unexpected temporal rise of the evaporation rate.

Finally, a numerical example for a model comprising three sub-domains, i.e., including the bulk porous medium Ω^{REV} , was presented. Adding this domain may help to achieve better boundary conditions for Ω^{PNM} , however, the coupling conditions involved here need revision in future work.

9.2 Outlook

Potential applications for the coupled model The model concepts presented in this work can help to deepen the understanding of pore-scale processes at the interface between porous medium and free flow. Applicable to a range of different environmental or technical applications, the coupled model may also serve as a tool to obtain averaged quantities for upscaled models in a comparatively efficient manner. Thoroughly optimizing the coupled model may even permit its use in the context of machine learning [e.g., Sotgiu et al., 2018] for finding pore-scale-driven interface closures, where fast yet reasonably accurate models are beneficial for training the algorithm.

Further work is required for improving the model both in terms of conceptual and numerical aspects.

Free-flow model The free-flow model could be made more efficient by introducing local adaptive grid refinement close to the intersecting pores at the interface while employing a generally coarser grid in the remaining parts of the domain [e.g., Manhart, 2004, Vittoz et al., 2017, Lipp and Helmig, 2020]. Furthermore, the model should be made more flexible in terms of handling arbitrary domain geometries, including non-uniform interface topologies [Fetzer, 2018], by supporting unstructured, non-Cartesian meshes [e.g., Jofre et al., 2013, Eymard et al., 2014]. Finally, the physical complexity could be increased by adding turbulence models [Fetzer, 2018] which may require the application of higher-order schemes [e.g., Sweby, 1984, Vescovini, 2018].

Pore-network model Advective transport in the pore-network model could be described more accurately by considering streamline methods [Mehmani and Balhoff, 2014] which reduce numerical diffusion [Ostrom et al., 2016] or by adding pore-scale dispersion concepts [e.g., Raouf and Hassanizadeh, 2013] to improve the physical description of the transport process. Non-linear flux terms based on the Forchheimer equation could be included for modeling higher flow velocities [e.g., Balhoff and Wheeler, 2009, Veyskarami et al., 2017].

Geochemical processes such as dissolution or precipitation of solids could be added to the pore-network model [e.g., Raouf et al., 2012, Nogues et al., 2013], as well as bacterial

growth [e.g., Hommel et al., 2013]. Salt precipitation [e.g., Jambhekar et al., 2016] and its potential impact on evaporation [e.g., Shokri-Kuehni et al., 2017] could be included.

The fully implicit two-phase approach should be further improved in terms of robustness and efficiency. In this work, only wetting materials were considered. This should be extended to hydrophobicity, especially in the context of fuel-cell modeling [e.g., Gostick, 2013, Baber et al., 2016].

Energy storage and transport in the solid matrix which conceptually surrounds the network should be considered [e.g., Surasani et al., 2008, 2010]. First results of using a dual network approach [Aghighi and Gostick, 2017, Khan et al., 2019] are promising and highlight local thermal non-equilibrium effects between the solid and the liquid phase [Jürß, 2019]. Here, the solid grains also constitute a network and exchange heat with the fluids in the pores. An alternative approach is based on the work of Koch et al. [2018, 2020c,b] and involves embedding the pore network into a higher dimensional REV-type domain on which the heat equation is solved. Energy exchange between the models is then realized by appropriate coupling source terms. Here, a prototype implementation showed promising results in terms of a qualitative resemblance with tentative and preliminary micromodel experiments.

Model coupling and numerical solution strategies As mentioned in Section 4.2, the conditions for coupling Ω^{PNM} with Ω^{REV} should be revised and further investigated in order to account for the different scales of the models involved. A possible idea would be the inversion of the coupling scheme proposed in this work: the pore-network quantities such as pressure at the interface could be averaged in order to obtain upscaled coupling conditions for the REV model. The latter would then pass fluxes as coupling conditions to Ω^{PNM} which then, however, would need to be distributed meaningfully among the pores at the interface.

The coupling between Ω^{FF} and Ω^{PNM} could be modified towards an averaged scheme using mortar methods [e.g., Mehmani and Balhoff, 2014]. This would allow to use a coarser free-flow grid since the pores at the interface would not have to be resolved explicitly by the free-flow model anymore. Furthermore, the formation of droplets or liquid films at the interface [e.g., Baber et al., 2016] could be included.

The velocity-slip concept for pores at the interface could be further assessed and generalized for different geometries and flow configurations.

The direct linear solver `UMFPACK` [Davis, 2004] poses a bottleneck for solving larger system due to excessive memory and CPU usage. Iterative approaches including specially tailored preconditioners [e.g., Kuchta et al., 2018] could help to increase the coupled model's efficiency. Furthermore, this would facilitate a parallelization of the numerical scheme, which is hitherto precluded by `UMFPACK`.

In addition to the monolithic fully implicit coupling scheme, decoupled sequential approaches could be considered. Different solvers optimized for each sub-model could be employed. Each domain could be treated with different time step sizes [Rybak et al., 2015] such that larger time steps are chosen for slower processes occurring, e.g., in Ω^{REV} while smaller time steps are used to capture discrete invasion processes in Ω^{PNM} . The use of the iterative coupling framework `preCICE` [Bungartz et al., 2016] could be assessed in order to realize a sequential coupling between different sub-models implemented in `DuMux` or to couple external solvers such as `OpenFOAM` to `DuMux` models.

Currently, the derivatives of the global Jacobian matrix are evaluated numerically which is prone to floating-point precision issues. Choosing unfavorable ε values for numerically calculating the derivative of a function may lead to inaccurate results that in turn lead to an increased number of Newton iterations. The effect of scaling ε adaptively is limited and problem-dependent. Automated differentiation could help to resolve this issue and improve the model's efficiency and accuracy [e.g., Griewank and Walther, 2008].

Further comparison with experiments Further micromodel experiments and high-resolution numerical simulations involving component transport, evaporation and two-phase flow should be conducted in order to validate the coupled model.

A Determination of corner half-angles for scalene triangles

Here, we briefly describe how to find a non-unique triple of corner half-angles (α, β, γ) for a scalene triangle with a prescribed shape factor G :

Using *Heron's formula* and the Law of cotangents, the area of a triangle can be expressed as

$$A = r^2 \underbrace{(\cot(\alpha) \cot(\beta) \cot(\gamma))}_c, \quad (\text{A.1})$$

where α , β , and γ are the triangle's corner half-angles and r the radius of its inscribed circle. A triangle's perimeter P is given by

$$P = \frac{2A}{r}. \quad (\text{A.2})$$

Inserting Eq. (A.2) into the definition of the shape factor $G = \frac{A}{P^2} = \frac{r^2}{4A}$ and rearranging Eq. (A.1) yields

$$c = \cot(\alpha) \cot(\beta) \cot(\gamma) = \frac{1}{4G}. \quad (\text{A.3})$$

Patzek and Silin [2001] derived a functional relationship for a sorted triple of corner half-angles $\alpha \leq \beta \leq \gamma \leq \pi/2$

$$\left(\begin{array}{l} \alpha = -\frac{1}{2}\beta + \frac{1}{2} \arcsin \left(\frac{\tan(\beta)+4G}{\tan(\beta)-4G} \sin(\beta) \right) \\ \beta \in [\beta_{min}, \beta_{max}] \\ \gamma = \pi/2 - \alpha - \beta \end{array} \right) \quad (\text{A.4})$$

such that for any $\beta \in [\beta_{min}, \beta_{max}]$ Eq. (A.3) is satisfied. β may be picked randomly between

$$\beta_{min} = \arctan \left(\frac{2}{\sqrt{3}} \cos \left(\frac{\arccos(-12\sqrt{3}G)}{3} \right) + \frac{4\pi}{3} \right) \quad (\text{A.5})$$

and

$$\beta_{max} = \arctan \left(\frac{2}{\sqrt{3}} \cos \left(\frac{\arccos(-12\sqrt{3}G)}{3} \right) \right). \quad (\text{A.6})$$

Figure A.1 shows different realizations of triangles constructed as described above for three different shape factors G , three different corner half-angles β and three different inscribed radii r . The choice of the latter just scales the total size of the triangle without altering its shape. The smaller G , the more slit-like the geometries become.

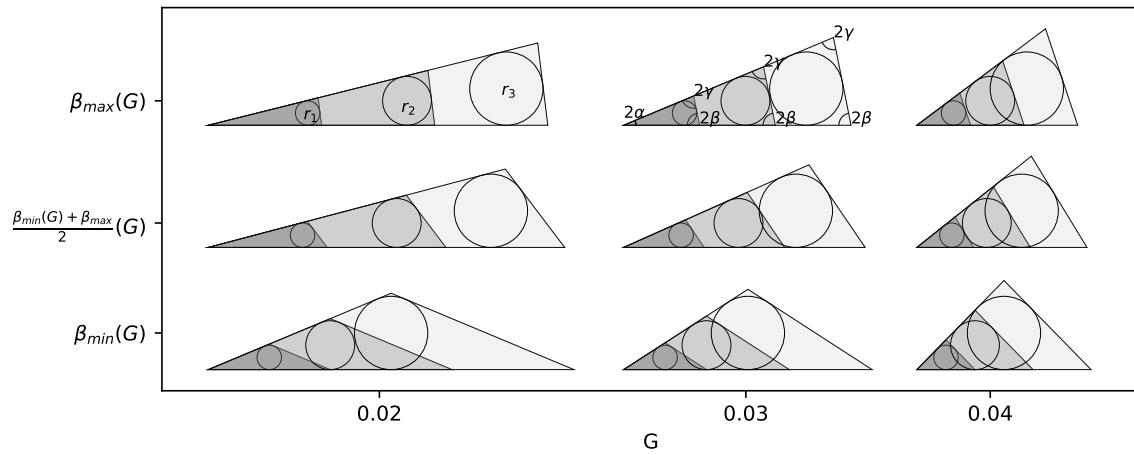


Figure A.1 – Randomly constructed triangles. Triangles featuring different shape factors G , corner half-angles β and inscribed radii r .

Equations (A.1) and (A.3) imply that for a given shape factor G , as evaluated from the actual pore geometry, the inscribed radius r and the cross-sectional area A of the equivalent triangular substitute geometry cannot be chosen independently. Since the inscribed radius r plays a crucial role in the calculation of capillary entry and snap-off pressures, as described in Section 2.4.2, r is commonly set equal to the inscribed radius of the actual geometry [Blunt, 2017]. For compositional single-phase flow, however, it might be more important to preserve the original cross-sectional area. If both parameters are of similar importance, an optimization could help to find a balance between r and A , thus also varying G .

B Derivation of the Hagen-Poiseuille equation

As explained in Section 2.4.2, standard pore-network models [Blunt, 2017] assume

- fully developed and stationary,
- creeping ($Re < 1$) and laminar

fluid flow from pore body i to j through throat ij . The throat can be considered as straight prismatic duct with a given cross-sectional area and length. For the simplest case of a tube with radius r_{ij} , single-phase flow follows the well-known Hagen-Poiseuille equation, which can be either derived from the Navier-Stokes equations in cylindrical coordinates or from a momentum balance on a discrete tube volume:

$$-\tau(2\pi r)dx + p\pi r^2 - (p + \frac{\partial p}{\partial x}dx)\pi r^2 = 0 . \quad (\text{B.1})$$

We assume that $\frac{\partial p}{\partial x}$ does not depend on the radial coordinate r and we neglect gravity. This yields for a Newtonian fluid with $\tau = -\mu\frac{\partial v}{\partial r}$ and after a division by $\mu(2\pi r)dx$

$$\frac{\partial v}{\partial r} = \frac{r}{2\mu} \frac{\partial p}{\partial x} . \quad (\text{B.2})$$

v is the velocity in axial (x) direction.

By integration over r , we get

$$v(r) = \frac{r^2}{4\mu} \frac{\partial p}{\partial x} + c_1 . \quad (\text{B.3})$$

Assuming a no-slip condition at the wall of the pipe $r = r_{ij}$ results in

$$v(r = r_{ij}) = 0 \rightarrow c_1 = -\frac{r_{ij}^2}{4\mu} \frac{\partial p}{\partial x}, \quad (\text{B.4})$$

and thus in a parabolic velocity profile

$$v(r) = \frac{r^2}{4\mu} \frac{\partial p}{\partial x} - \frac{r_{ij}^2}{4\mu} \frac{\partial p}{\partial x} = \frac{(r^2 - r_{ij}^2)}{4\mu} \frac{\partial p}{\partial x}. \quad (\text{B.5})$$

The volumetric flow Q is then given by

$$\begin{aligned} Q &= \int_0^{r_{ij}} v(r)(2\pi r)dr = \int_0^{r_{ij}} \pi \frac{(r^3 - rr_{ij}^2)}{2\mu} \frac{\partial p}{\partial x} dr \\ &= \frac{\pi}{2\mu} \left[\frac{1}{4}r^4 - \frac{1}{2}r^2r_{ij}^2 \right]_0^{r_{ij}} \frac{\partial p}{\partial x} = -\frac{\pi r_{ij}^4}{8\mu} \frac{\partial p}{\partial x}, \end{aligned} \quad (\text{B.6})$$

which leads to Eq. (2.37).

Bibliography

- M. Aghighi and J. Gostick. Pore network modeling of phase change in PEM fuel cell fibrous cathode. *Journal of Applied Electrochemistry*, 47(12):1323–1338, 2017. doi:10.1007/s10800-017-1126-6.
- M. S. Al-Gharbi and M. J. Blunt. Dynamic network modeling of two-phase drainage in porous media. *Physical Review E*, 71(1):016308, 2005. doi:10.1103/physreve.71.016308.
- T. Arbogast, G. Pencheva, M. F. Wheeler, and I. Yotov. A multiscale mortar mixed finite element method. *Multiscale Modeling & Simulation*, 6(1):319–346, 2007. doi:10.1137/060662587.
- R. T. Armstrong, N. Evseev, D. Koroteev, and S. Berg. Modeling the velocity field during haines jumps in porous media. *Advances in Water Resources*, 77:57–68, 2015. doi:10.1016/j.advwatres.2015.01.008.
- U. Ayachit. *The ParaView Guide: A Parallel Visualization Application*. Kitware, Inc., 2015.
- R. Aziz, V. Joekar-Niasar, and P. Martinez-Ferrer. Pore-scale insights into transport and mixing in steady-state two-phase flow in porous media. *International Journal of Multiphase Flow*, 109:51–62, 2018. doi:10.1016/j.ijmultiphaseflow.2018.07.006.
- M. Babaei and V. Joekar-Niasar. A transport phase diagram for pore-level correlated porous media. *Advances in Water Resources*, 92:23–29, 2016. doi:10.1016/j.advwatres.2016.03.014.
- K. Baber, B. Flemisch, and R. Helmig. Modeling drop dynamics at the interface between free and porous-medium flow using the mortar method.

- International Journal of Heat and Mass Transfer*, 99:660–671, 2016. doi:10.1016/j.ijheatmasstransfer.2016.04.014.
- Y. Bae and Y. I. Kim. Numerical modeling of anisotropic drag for a perforated plate with cylindrical holes. *Chemical Engineering Science*, 149:78–87, 2016. doi:10.1016/j.ces.2016.04.036.
- S. Bakke and P.-E. Øren. 3-D Pore-Scale Modelling of Sandstones and Flow Simulations in the Pore Networks. *SPE Journal*, 2(02):136–149, 1997. doi:10.2118/35479-pa.
- M. T. Balhoff and M. F. Wheeler. A predictive pore-scale model for non-darcy flow in porous media. *SPE Journal*, 14(04):579–587, 2009. doi:10.2118/110838-pa.
- M. T. Balhoff, K. E. Thompson, and M. Hjortsø. Coupling pore-scale networks to continuum-scale models of porous media. *Computers & Geosciences*, 33(3):393–410, 2007. doi:10.1016/j.cageo.2006.05.012.
- M. T. Balhoff, S. G. Thomas, and M. F. Wheeler. Mortar coupling and up-scaling of pore-scale models. *Computational Geosciences*, 12(1):15–27, 2008. doi:10.1007/s10596-007-9058-6.
- P. Bastian, M. Blatt, A. Dedner, C. Engwer, R. Klöfkorn, R. Kornhuber, M. Ohlberger, and O. Sander. A generic grid interface for parallel and adaptive scientific computing. Part II: Implementation and tests in DUNE. *Computing*, 82(2-3):121–138, 2008a. doi:10.1007/s00607-008-0004-9.
- P. Bastian, M. Blatt, A. Dedner, C. Engwer, R. Klöfkorn, M. Ohlberger, and O. Sander. A generic grid interface for parallel and adaptive scientific computing. Part I: Abstract framework. *Computing*, 82(2):103–119, 2008b. doi:10.1007/s00607-008-0003-x.
- P. Bastian, M. Blatt, A. Dedner, N.-A. Dreier, C. Engwer, R. Fritze, C. Gräser, D. Kempf, R. Klöfkorn, M. Ohlberger, and O. Sander. The DUNE Framework: Basic Concepts and Recent Developments, 2019. URL <https://arxiv.org/abs/1909.13672>. arXiv pre-print.
- P. Bauer, A. Thorpe, and G. Brunet. The quiet revolution of numerical weather prediction. *Nature*, 525(7567):47–55, 2015. doi:10.1038/nature14956.

-
- T. G. Baychev, A. P. Jivkov, A. Rabbani, A. Q. Raeini, Q. Xiong, T. Lowe, and P. J. Withers. Reliability of Algorithms Interpreting Topological and Geometric Properties of Porous Media for Pore Network Modelling. *Transport in Porous Media*, 128(1): 271–301, 2019. doi:10.1007/s11242-019-01244-8.
- J. Bear. *Dynamics of Fluids in Porous Media*. Dover Civil and Mechanical Engineering Series. Dover, 1972.
- G. S. Beavers and D. D. Joseph. Boundary conditions at a naturally permeable wall. *Journal of Fluid Mechanics*, 30(01):197–207, 1967. doi:10.1017/s0022112067001375.
- R. Benoit, P. Pellerin, N. Kouwen, H. Ritchie, N. Donaldson, P. Joe, and E. D. Soulis. Toward the Use of Coupled Atmospheric and Hydrologic Models at Regional Scale. *Monthly Weather Review*, 128(6):1681–1706, 2000. doi:10.1175/1520-0493(2000)128<1681:ttuoca>2.0.co;2.
- M. Benzi, G. H. Golub, and J. Liesen. Numerical solution of saddle point problems. *Acta numerica*, 14:1–137, 2005. doi:10.1017/s0962492904000212.
- S. Beyhaghi, Z. Xu, and K. M. Pillai. Achieving the Inside–Outside Coupling During Network Simulation of Isothermal Drying of a Porous Medium in a Turbulent Flow. *Transport in Porous Media*, 114(3):823–842, 2016. doi:10.1007/s11242-016-0746-3.
- P. Bhattad, C. S. Willson, and K. E. Thompson. Effect of Network Structure on Characterization and Flow Modeling Using X-ray Micro-Tomography Images of Granular and Fibrous Porous Media. *Transport in Porous Media*, 90(2):363–391, 2011. doi:10.1007/s11242-011-9789-7.
- T. Bierbaum. *Comparative study of a fully-implicit and a sequential solution strategy for dynamic two-phase flow pore-network models*. Master’s thesis, 2019.
- B. Bijeljic, A. Raeini, P. Mostaghimi, and M. J. Blunt. Predictions of non-Fickian solute transport in different classes of porous media using direct simulation on pore-scale images. *Physical Review E*, 87(1):013011, 2013. doi:10.1103/PhysRevE.87.013011.
- M. J. Blunt. Effects of Heterogeneity and Wetting on Relative Permeability Using Pore Level Modeling. *SPE Journal*, 2(01):70–87, 1997. doi:10.2118/36762-pa.

- M. J. Blunt. Physically-based network modeling of multiphase flow in intermediate-wet porous media. *Journal of Petroleum Science and Engineering*, 20(3-4):117–125, 1998. doi:10.1016/S0920-4105(98)00010-2.
- M. J. Blunt. *Multiphase flow in permeable media: A pore-scale perspective*. Cambridge University Press, Cambridge, 2017.
- M. J. Blunt, M. D. Jackson, M. Piri, and P. H. Valvatne. Detailed physics, predictive capabilities and macroscopic consequences for pore-network models of multiphase flow. *Advances in Water Resources*, 25(8):1069 – 1089, 2002. doi:[https://doi.org/10.1016/S0309-1708\(02\)00049-0](https://doi.org/10.1016/S0309-1708(02)00049-0).
- J. Boussinesq. Mémoire sur l'influence des frottements dans les mouvements réguliers des fluids. *J. Math. Pures Appl*, 13(377-424):21, 1868.
- H. C. Brinkman. A calculation of the viscous force exerted by a flowing fluid on a dense swarm of particles. *Flow, Turbulence and Combustion*, 1(1), 1949. doi:10.1007/bf02120313.
- W. Brutsaert. *Evaporation into the atmosphere: theory, history and applications*, volume 1. Springer Science & Business Media, 2013.
- H. Bruus. *Theoretical microfluidics*, volume 18. Oxford university press Oxford, 2008.
- Q. M. Bui and H. C. Elman. Semi-smooth Newton methods for nonlinear complementarity formulation of compositional two-phase flow in porous media. *Journal of Computational Physics*, 407:109163, Apr. 2020. doi:10.1016/j.jcp.2019.109163. URL <https://doi.org/10.1016/j.jcp.2019.109163>.
- H.-J. Bungartz, F. Lindner, B. Gatzhammer, M. Mehl, K. Scheufele, A. Shukaev, and B. Uekermann. preCICE – A fully parallel library for multi-physics surface coupling. *Computers & Fluids*, 141:250–258, 2016. doi:10.1016/j.compfluid.2016.04.003.
- M. Chandesris and D. Jamet. Jump Conditions and Surface-Excess Quantities at a Fluid/Porous Interface: A Multi-scale Approach. *Transport in Porous Media*, 78(3): 419–438, 2008. doi:10.1007/s11242-008-9302-0.
- M. Chandesris, A. D'Hueppe, B. Mathieu, D. Jamet, and B. Goyeau. Direct numerical simulation of turbulent heat transfer in a fluid-porous domain. *Physics of Fluids*, 25(12):125110, 2013. doi:10.1063/1.4851416.

-
- V. P. Chauhan, T. Stylianopoulos, Y. Boucher, and R. K. Jain. Delivery of Molecular and Nanoscale Medicine to Tumors: Transport Barriers and Strategies. *Annual Review of Chemical and Biomolecular Engineering*, 2(1):281–298, 2011. doi:10.1146/annurev-chembioeng-061010-114300.
- F. Chauvet, P. Duru, S. Geoffroy, and M. Prat. Three periods of drying of a single square capillary tube. *Physical Review Letters*, 103(12), 2009. doi:10.1103/physrevlett.103.124502.
- Z. Chen, G. Huan, and B. Li. An Improved IMPES Method for Two-Phase Flow in Porous Media. *Transport in Porous Media*, 54:361–376, 2004. doi:10.1023/B:TIPM.0000003667.86625.15.
- J. Chu, B. Engquist, M. Prodanović, and R. Tsai. A Multiscale Method Coupling Network and Continuum Models in Porous Media I: Steady-State Single Phase Flow. *Multiscale Modeling & Simulation*, 10(2):515–549, 2012. doi:10.1137/110836201.
- H. Class. *Models for non-isothermal compositional gas-liquid flow and transport in porous media*. habilitation, 2007. URL <https://elib.uni-stuttgart.de/handle/11682/316>.
- H. Class and R. Helmig. Numerical simulation of non-isothermal multiphase multicomponent processes in porous media.: 2. Applications for the injection of steam and air. *Advances in Water Resources*, 25(5):551–564, 2002. doi:10.1016/s0309-1708(02)00015-5.
- H. Class, R. Helmig, and P. Bastian. Numerical simulation of non-isothermal multiphase multicomponent processes in porous media.: 1. An efficient solution technique. *Advances in Water Resources*, 25(5):533–550, 2002. doi:10.1016/s0309-1708(02)00014-3.
- H. Class, K. Weishaupt, and O. Trötschler. Experimental and simulation study on validating a numerical model for CO₂ density-driven dissolution in water. *Water*, 12(3), 2020. doi:10.3390/w12030738.
- V. Cnudde and M. Boone. High-resolution X-ray computed tomography in geosciences: A review of the current technology and applications. *Earth-Science Reviews*, 123: 1–17, 2013. doi:10.1016/j.earscirev.2013.04.003.

- W. Dahmen, T. Gotzen, S. Müller, and M. Rom. Numerical simulation of transpiration cooling through porous material. *International Journal for Numerical Methods in Fluids*, 76(6):331–365, 2014. doi:10.1002/flid.3935.
- H. P. G. Darcy. *Les Fontaines publiques de la ville de Dijon. Exposition et application des principes à suivre et des formules à employer dans les questions de distribution d'eau, etc.* V. Dalamont, 1856.
- T. A. Davis. Algorithm 832: UMFPACK V4.3 - an unsymmetric-pattern multifrontal method. *ACM Transactions on Mathematical Software (TOMS)*, 30(2):196–199, 2004. doi:10.1145/992200.992206.
- T. Defraeye. Advanced computational modelling for drying processes – a review. *Applied Energy*, 131:323–344, 2014. doi:10.1016/j.apenergy.2014.06.027.
- T. Defraeye, B. Nicolai, D. Mannes, W. Aregawi, P. Verboven, and D. Derome. Probing inside fruit slices during convective drying by quantitative neutron imaging. *Journal of Food Engineering*, 178:198–202, 2016. doi:10.1016/j.jfoodeng.2016.01.023.
- H.-J. Diersch and O. Kolditz. Variable-density flow and transport in porous media: approaches and challenges. *Advances in Water Resources*, 25(8-12):899–944, 2002. doi:10.1016/s0309-1708(02)00063-5.
- M. Discacciati, P. Gervasio, A. Giacomini, and A. Quarteroni. The Interface Control Domain Decomposition Method for Stokes–Darcy Coupling. *SIAM Journal on Numerical Analysis*, 54(2):1039–1068, 2016. doi:10.1137/15m101854x.
- J. Donea and A. Huerta. *Finite element methods for flow problems*. Wiley, Chichester, 2003.
- C. Ericson. *Real-time collision detection*. CRC Press, Boca Raton, 2004.
- R. Eymard, J. Fuhrmann, and A. Linke. On MAC schemes on triangular delaunay meshes, their convergence and application to coupled flow problems. *Numerical Methods for Partial Differential Equations*, 30(4):1397–1424, Apr. 2014. doi:10.1002/num.21875. URL <https://doi.org/10.1002/num.21875>.
- I. Fatt. The network model of porous media I. Capillary pressure characteristics. *Trans. AIME*, 207:144–159, 1956a.

-
- I. Fatt. The network model of porous media II. Dynamic properties of a single size tube network. *Trans. AIME*, 207:160–163, 1956b.
- I. Fatt. The network model of porous media III. Dynamic properties of networks with tube radius distribution. *Trans. AIME*, 207:164–181, 1956c.
- T. Fetzer. *Coupled Free and Porous-Medium Flow Processes Affected by Turbulence and Roughness – Models, Concepts and Analysis*. dissertation, 2018. URL <http://elib.uni-stuttgart.de/handle/11682/614>.
- T. Fetzer, J. Vanderborght, K. Mosthaf, K. M. Smits, and R. Helmig. Heat and water transport in soils and across the soil-atmosphere interface: 2. Numerical analysis. *Water Resources Research*, 53(2):1080–1100, 2017. doi:10.1002/2016wr019983.
- A. Fischer. A special newton-type optimization method. *Optimization*, 24(3-4):269–284, Jan. 1992. doi:10.1080/02331939208843795.
- E. G. Flekkøy, U. Oxaal, J. Feder, and T. Jøssang. Hydrodynamic dispersion at stagnation points: Simulations and experiments. *Physical Review E*, 52(5):4952–4962, 1995. doi:10.1103/physreve.52.4952.
- B. Flemisch, M. Darcis, K. Erbertseder, B. Faigle, A. Lauser, K. Mosthaf, S. Müthing, P. Nuske, A. Tatomir, M. Wolff, and R. Helmig. DuMux: DUNE for multi- $\{$ phase, component, scale, physics, $\dots\}$ flow and transport in porous media. *Advances in Water Resources*, 34(9):1102–1112, 2011. doi:10.1016/j.advwatres.2011.03.007.
- U. Ghia, K. Ghia, and C. Shin. High-Re solutions for incompressible flow using the Navier-Stokes equations and a multigrid method0. *Journal of Computational Physics*, 48(3):387–411, 1982. doi:10.1016/0021-9991(82)90058-4.
- J. T. Gostick. Random pore network modeling of fibrous PEMFC gas diffusion media using Voronoi and Delaunay tessellations. *Journal of The Electrochemical Society*, 160(8):F731–F743, 2013. doi:10.1149/2.009308jes.
- J. T. Gostick. Versatile and efficient pore network extraction method using marker-based watershed segmentation. *Physical Review E*, 96(2), 2017. doi:10.1103/physreve.96.023307.

- B. Goyeau, D. Lhuillier, D. Gobin, and M. Velarde. Momentum transport at a fluid–porous interface. *International Journal of Heat and Mass Transfer*, 46(21): 4071–4081, 2003. doi:10.1016/s0017-9310(03)00241-2.
- C. Gräser and O. Sander. The dune-subgrid module and some applications. *Computing*, 86(4):269–290, 2009. doi:10.1007/s00607-009-0067-2.
- A. Griewank and A. Walther. *Evaluating derivatives: principles and techniques of algorithmic differentiation*, volume 105. Siam, 2008.
- C. Grüninger. *Numerical coupling of Navier-Stokes and Darcy flow for soil-water evaporation*. dissertation, 2017. URL <http://elib.uni-stuttgart.de/handle/11682/9674>.
- V. Gurau and J. A. Mann. A Critical Overview of Computational Fluid Dynamics Multiphase Models for Proton Exchange Membrane Fuel Cells. *SIAM Journal on Applied Mathematics*, 70(2):410–454, 2009. doi:10.1137/080727993.
- F. H. Harlow and J. E. Welch. Numerical calculation of time-dependent viscous incompressible flow of fluid with free surface. *The Physics of Fluids*, 8(12):2182–2189, 1965. doi:10.1063/1.1761178.
- S. M. Hassanizadeh and W. G. Gray. Derivation of conditions describing transport across zones of reduced dynamics within multiphase systems. *Water Resources Research*, 25(3):529–539, 1989. doi:10.1029/WR025i003p00529.
- S. M. Hassanizadeh and W. G. Gray. Thermodynamic basis of capillary pressure in porous media. *Water Resources Research*, 29(10):3389–3405, 1993. doi:10.1029/93wr01495.
- K. Heck, S. Ackermann, B. Becker, E. Coltman, S. Emmert, B. Flemisch, D. Gläser, C. Grüninger, T. Koch, T. Kurz, M. Lipp, F. Mohammadi, S. Scherrer, M. Schneider, G. Seitz, L. Stadler, M. Utz, A. Vescovini, F. Weinhardt, and K. Weishaupt. *Dumu^x 3.1.0*, 2019. URL <https://doi.org/10.5281/zenodo.3482428>.
- R. Helmig. *Multiphase flow and transport processes in the subsurface: a contribution to the modeling of hydrosystems*. Springer-Verlag, Berlin, 1997.

-
- Q. T. Ho, P. Verboven, S. W. Fanta, M. K. Abera, M. A. Retta, E. Herremans, T. Defraeye, and B. M. Nicolai. A Multiphase Pore Scale Network Model of Gas Exchange in Apple Fruit. *Food and Bioprocess Technology*, 7(2):482–495, 2013. doi:10.1007/s11947-012-1043-y.
- J. Hommel, A. B. Cunningham, R. Helmig, A. Ebigbo, and H. Class. Numerical investigation of microbially induced calcite precipitation as a leakage mitigation technology. *Energy Procedia*, 40:392–397, 2013. doi:10.1016/j.egypro.2013.08.045.
- R. Huber and R. Helmig. Node-centered finite volume discretizations for the numerical simulation of multiphase flow in heterogeneous porous media. *Computational Geosciences*, 4(2):141–164, 2000. doi:10.1023/a:1011559916309.
- V. A. Jambhekar, E. Mejri, N. Schröder, R. Helmig, and N. Shokri. Kinetic approach to model reactive transport and mixed salt precipitation in a coupled free-flow–porous-media system. *Transport in Porous Media*, 114(2):341–369, 2016. doi:10.1007/s11242-016-0665-3.
- D. Jamet, M. Chandesris, and B. Goyeau. On the Equivalence of the Discontinuous One- and Two-Domain Approaches for the Modeling of Transport Phenomena at a Fluid/Porous Interface. *Transport in Porous Media*, 78(3):403–418, 2008. doi:10.1007/s11242-008-9314-9.
- H. Jasak. OpenFOAM: Open source CFD in research and industry. *International Journal of Naval Architecture and Ocean Engineering*, 1(2):89–94, 2009. doi:10.2478/ijnaoe-2013-0011.
- J.-T. Jeong. Slip boundary condition on an idealized porous wall. *Physics of Fluids*, 13(7):1884–1890, 2001. doi:10.1063/1.1373680.
- Z. Jiang, K. Wu, G. Couples, M. I. J. van Dijke, K. S. Sorbie, and J. Ma. Efficient extraction of networks from three-dimensional porous media. *Water Resources Research*, 43(12), 2007. doi:10.1029/2006wr005780.
- V. Joekar-Niasar and S. M. Hassanizadeh. Effect of fluids properties on non-equilibrium capillarity effects: Dynamic pore-network modeling. *International Journal of Multiphase Flow*, 37:198–214, 2011. doi:10.1016/j.ijmultiphaseflow.2010.09.007.

- V. Joekar-Niasar and S. M. Hassanizadeh. Analysis of fundamentals of two-phase flow in porous media using dynamic pore-network models: A review. *Critical reviews in environmental science and technology*, 42(18):1895–1976, 2012a. doi:10.1080/10643389.2011.574101.
- V. Joekar-Niasar and S. M. Hassanizadeh. Uniqueness of Specific Interfacial Area–Capillary Pressure–Saturation Relationship Under Non-Equilibrium Conditions in Two-Phase Porous Media Flow. *Transport in Porous Media*, 94(2):465–486, 2012b. doi:10.1007/s11242-012-9958-3.
- V. Joekar-Niasar, S. Hassanizadeh, and A. Leijnse. Insights into the relationships among capillary pressure, saturation, interfacial area and relative permeability using pore-network modeling. *Transport in Porous Media*, 74(2):201–219, 2008. doi:10.1007/s11242-007-9191-7.
- V. Joekar-Niasar, S. M. Hassanizadeh, and H. K. Dahle. Non-equilibrium effects in capillarity and interfacial area in two-phase flow: dynamic pore-network modelling. *J. Fluid Mech.*, 655:38–71, 2010a. doi:10.1017/s0022112010000704.
- V. Joekar-Niasar, M. Prodanović, D. Wildenschild, and S. M. Hassanizadeh. Network model investigation of interfacial area, capillary pressure and saturation relationships in granular porous media. *Water Resources Research*, 46(6), 2010b. doi:10.1029/2009WR008585.
- L. Jofre, O. Lehmkuhl, J. Ventosa, F. X. Trias, and A. Oliva. Conservation Properties of Unstructured Finite-Volume Mesh Schemes for the Navier-Stokes Equations. *Numerical Heat Transfer, Part B: Fundamentals*, 65(1):53–79, 2013. doi:10.1080/10407790.2013.836335.
- K. Johannsen, S. Oswald, R. Held, and W. Kinzelbach. Numerical simulation of three-dimensional saltwater–freshwater fingering instabilities observed in a porous medium. *Advances in Water Resources*, 29(11):1690–1704, 2006. doi:10.1016/j.advwatres.2005.12.008.
- R. Jurjević. Modelling of two-dimensional laminar flow using finite element method. *International Journal for Numerical Methods in Fluids*, 31(3):601–626, 1999. doi:10.1002/(sici)1097-0363(19991015)31:3<601::aid-fld892>3.0.co;2-z.

-
- N. Jürß. *A dual pore network model for fluid and energy transport in soils considering thermal non-equilibrium*. Master's thesis, 2019.
- N. K. Karadimitriou, V. Joekar-Niasar, M. Babaei, and C. A. Shore. Critical role of the immobile zone in non-Fickian two-phase transport: A new paradigm. *Environmental science & technology*, 50(8):4384–4392, 2016. doi:10.1021/acs.est.5b05947.
- N. K. Karadimitriou, V. Joekar-Niasar, and O. G. Brizuela. Hydro-dynamic Solute Transport under Two-Phase Flow Conditions. *Scientific Reports*, 7(1), 2017. doi:10.1038/s41598-017-06748-1.
- Z. A. Khan, T. Tranter, M. Agnaou, A. Elkamel, and J. Gostick. Dual network extraction algorithm to investigate multiple transport processes in porous materials: Image-based modeling of pore and grain scale processes. *Computers & Chemical Engineering*, 123:64–77, 2019. doi:10.1016/j.compchemeng.2018.12.025.
- K. Khayrat and P. Jenny. A multi-scale network method for two-phase flow in porous media. *Journal of Computational Physics*, 342:194–210, 2017. doi:10.1016/j.jcp.2017.04.023.
- J. Kim and P. Moin. Application of a fractional-step method to incompressible Navier-Stokes equations. *Journal of Computational Physics*, 59(2):308–323, 1985. doi:10.1016/0021-9991(85)90148-2.
- T. Koch, K. Heck, N. Schröder, H. Class, and R. Helmig. A New Simulation Framework for Soil–Root Interaction, Evaporation, Root Growth, and Solute Transport. *Vadose Zone Journal*, 17(1):0, 2018. doi:10.2136/vzj2017.12.0210.
- T. Koch, D. Gläser, K. Weishaupt, S. Ackermann, M. Beck, B. Becker, S. Burbulla, H. Class, E. Coltman, S. Emmert, T. Fetzer, C. Grüninger, K. Heck, J. Hommel, T. Kurz, M. Lipp, F. Mohammadi, S. Scherrer, M. Schneider, G. Seitz, L. Stadler, M. Utz, F. Weinhardt, and B. Flemisch. DuMux 3 – an open-source simulator for solving flow and transport problems in porous media with a focus on model coupling. *Computers & Mathematics with Applications*, 2020a. doi:10.1016/j.camwa.2020.02.012.
- T. Koch, R. Helmig, and M. Schneider. A new and consistent well model for one-phase flow in anisotropic porous media using a distributed source model. *Journal of Computational Physics*, 410:109369, 2020b. doi:10.1016/j.jcp.2020.109369.

- T. Koch, M. Schneider, R. Helmig, and P. Jenny. Modeling tissue perfusion in terms of 1d-3d embedded mixed-dimension coupled problems with distributed sources. *Journal of Computational Physics*, 410:109370, 2020c. doi:10.1016/j.jcp.2020.109370.
- J. Koplik and T. Lasseter. Two-Phase Flow in Random Network Models of Porous Media. *Society of Petroleum Engineers Journal*, 25(01):89–100, 1985. doi:10.2118/11014-pa.
- S. Korteland, S. Bottero, S. M. Hassanizadeh, and C. W. J. Berentsen. What is the Correct Definition of Average Pressure? *Transport in Porous Media*, 84(1):153–175, 2009. doi:10.1007/s11242-009-9490-2.
- R. Krishna and J. Wesselingh. The Maxwell-Stefan approach to mass transfer. *Chemical Engineering Science*, 52(6):861–911, 1997. doi:10.1016/s0009-2509(96)00458-7.
- M. Kuchta, K.-A. Mardal, and M. Mortensen. Preconditioning trace coupled 3d-1d systems using fractional Laplacian. *Numerical Methods for Partial Differential Equations*, 35(1):375–393, 2018. doi:10.1002/num.22304.
- P. Kunz, I. M. Zarikos, N. K. Karadimitriou, M. Huber, U. Nieken, and S. M. Hassanizadeh. Study of Multi-phase Flow in Porous Media: Comparison of SPH Simulations with Micro-model Experiments. *Transport in Porous Media*, 114(2):581–600, 2015. doi:10.1007/s11242-015-0599-1.
- A. Laleian, A. Valocchi, and C. Werth. An Incompressible, Depth-Averaged Lattice Boltzmann Method for Liquid Flow in Microfluidic Devices with Variable Aperture. *Computation*, 3(4):600–615, 2015. doi:10.3390/computation3040600.
- J. B. Laurindo and M. Prat. Numerical and experimental network study of evaporation in capillary porous media. drying rates. *Chemical engineering science*, 53(12):2257–2269, 1998. doi:10.1016/s0009-2509(97)00348-5.
- A. Lauser. The DuMux material law framework. In *Advances in DUNE*, pages 113–128. Springer Berlin Heidelberg, 2012. doi:10.1007/978-3-642-28589-9_9.
- A. Lauser. *Theory and numerical applications of compositional multi-phase flow in porous media*. dissertation, 2014. URL <http://elib.uni-stuttgart.de/handle/11682/533>.

-
- A. Lauser, C. Hager, R. Helmig, and B. Wohlmuth. A new approach for phase transitions in miscible multi-phase flow in porous media. *Advances in Water Resources*, 34(8):957–966, 2011. doi:10.1016/j.advwatres.2011.04.021.
- W. J. Layton, F. Schieweck, and I. Yotov. Coupling fluid flow with porous media flow. *SIAM Journal on Numerical Analysis*, 40(6):2195–2218, 2002. doi:10.1137/s0036142901392766.
- P. Lehmann, S. Assouline, and D. Or. Characteristic lengths affecting evaporative drying of porous media. *Physical Review E*, 77(5), 2008. doi:10.1103/physreve.77.056309.
- J. Li and S. Sun. The Superconvergence Phenomenon and Proof of the MAC Scheme for the Stokes Equations on Non-uniform Rectangular Meshes. *Journal of Scientific Computing*, 65(1):341–362, 2014. doi:10.1007/s10915-014-9963-5.
- F. Lindner, P. Nuske, K. Weishaupt, R. Helmig, C. Mundt, and M. Pfitzner. Transpiration cooling with local thermal nonequilibrium: Model comparison in multiphase flow in porous media. *Journal of Porous Media*, 19(2):131–153, 2016. doi:10.1615/jpormedia.v19.i2.30.
- W. B. Lindquist, S.-M. Lee, D. A. Coker, K. W. Jones, and P. Spanne. Medial axis analysis of void structure in three-dimensional tomographic images of porous media. *Journal of Geophysical Research: Solid Earth*, 101(B4):8297–8310, 1996. doi:10.1029/95jb03039.
- M. Lipp and R. Helmig. A locally-refined locally-conservative quadtree finite-volume staggered-grid scheme. In G. Lamanna, S. Tonini, G. E. Cossali, and B. Weigand, editors, *Dropet Interaction and Spray Processes*. Springer, Heidelberg, Berlin, 2020.
- S. Ma, G. Mason, and N. R. Morrow. Effect of contact angle on drainage and imbibition in regular polygonal tubes. *Colloids and Surfaces A: Physicochemical and Engineering Aspects*, 117(3):273–291, 1996. doi:10.1016/0927-7757(96)03702-8.
- H. Man and X. Jing. Pore network modelling of electrical resistivity and capillary pressure characteristics. *Transport in Porous Media*, 41(3):263–285, 2000. doi:10.1023/a:1006612100346.
- M. Manhart. A zonal grid algorithm for DNS of turbulent boundary layers. *Computers & Fluids*, 33(3):435–461, 2004. doi:10.1016/s0045-7930(03)00061-6.

- G. Mason and N. R. Morrow. Capillary behavior of a perfectly wetting liquid in irregular triangular tubes. *Journal of Colloid and Interface Science*, 141(1):262–274, 1991. doi:10.1016/0021-9797(91)90321-x.
- R. P. Mayer and R. A. Stowe. Mercury porosimetry—breakthrough pressure for penetration between packed spheres. *Journal of Colloid Science*, 20(8):893–911, 1965. doi:10.1016/0095-8522(65)90061-9.
- W. McMinn and T. Magee. Principles, Methods and Applications of the Convective Drying of Foodstuffs. *Food and Bioproducts Processing*, 77(3):175–193, 1999. doi:10.1205/096030899532466.
- Y. Mehmani and M. T. Balhoff. Bridging from Pore to Continuum: A Hybrid Mortar Domain Decomposition Framework for Subsurface Flow and Transport. *Multiscale Modeling & Simulation*, 12(2):667–693, 2014. doi:10.1137/13092424x.
- Y. Mehmani and H. A. Tchelepi. Minimum requirements for predictive pore-network modeling of solute transport in micromodels. *Advances in Water Resources*, 108: 83–98, 2017. doi:10.1016/j.advwatres.2017.07.014.
- X. Miao, K. M. Gerke, and T. O. Sizonenko. A new way to parameterize hydraulic conductances of pore elements: A step towards creating pore-networks without pore shape simplifications. *Advances in Water Resources*, 105:162 – 172, 2017. doi:https://doi.org/10.1016/j.advwatres.2017.04.021.
- A. Mikelić and W. Jäger. On The Interface Boundary Condition of Beavers, Joseph, and Saffman. *SIAM Journal on Applied Mathematics*, 60(4):1111–1127, 2000. doi:10.1137/s003613999833678x.
- R. J. Millington. Gas Diffusion in Porous Media. *Science*, 130(3367):100–102, 1959. doi:10.1126/science.130.3367.100-a.
- H. K. Moffatt. Viscous and resistive eddies near a sharp corner. *Journal of Fluid Mechanics*, 18(1):1–18, 1964. doi:10.1017/s0022112064000015.
- K. Mogensen and E. H. Stenby. A dynamic two-phase pore-scale model for imbibition. *Transp. Porous Media*, 32:299–327, 1998. doi:10.1023/A:1006578721129.

-
- K. Mogensen, E. Stenby, S. Banerjee, and V. A. Barker. Comparison of Iterative Methods for Computing the Pressure Field in a Dynamic Network Model. *Transport in Porous Media*, 37(3):277–301, 1999. doi:10.1023/A:1006642203767.
- S. Most, B. Bijeljic, and W. Nowak. Evolution and persistence of cross-directional statistical dependence during finite-Péclet transport through a real porous medium. *Water Resources Research*, 52(11):8920–8937, 2016. doi:10.1002/2016WR018969.
- K. Mosthaf. *Modeling and analysis of coupled porous-medium and free flow with application to evaporation processes*. dissertation, 2014. URL <http://elib.uni-stuttgart.de/handle/11682/536>.
- K. Mosthaf, K. Baber, B. Flemisch, R. Helmig, A. Leijnse, I. Rybak, and B. Wohlmuth. A coupling concept for two-phase compositional porous-medium and single-phase compositional free flow. *Water Resour. Res.*, 47(10), 2011. doi:10.1029/2011WR010685.
- K. Mosthaf, R. Helmig, and D. Or. Modeling and analysis of evaporation processes from porous media on the REV scale. *Water Resources Research*, 50(2):1059–1079, 2014. doi:10.1002/2013wr014442.
- G. Neale and W. Nader. Practical significance of Brinkman’s extension of Darcy’s law: Coupled parallel flows within a channel and a bounding porous medium. *The Canadian Journal of Chemical Engineering*, 52(4):475–478, 1974. doi:10.1002/cjce.5450520407.
- D. A. Nield, A. Bejan, et al. *Convection in porous media*, volume 3. Springer, 2006.
- J. P. Nogues, J. P. Fitts, M. A. Celia, and C. A. Peters. Permeability evolution due to dissolution and precipitation of carbonates using reactive transport modeling in pore networks. *Water Resources Research*, 49(9):6006–6021, 2013. doi:10.1002/wrcr.20486.
- J. M. Nordbotten, M. A. Celia, H. K. Dahle, and S. M. Hassanizadeh. Interpretation of macroscale variables in Darcy's law. *Water Resources Research*, 43(8), 2007. doi:10.1029/2006wr005018.

- J. M. Nordbotten, M. A. Celia, H. K. Dahle, and S. M. Hassanizadeh. On the definition of macroscale pressure for multiphase flow in porous media. *Water Resources Research*, 44(6), 2008. doi:10.1029/2006wr005715.
- P. Nuske. *Beyond Local Equilibrium : Relaxing local equilibrium assumptions in multiphase flow in porous media*. dissertation, 2014. URL <http://elib.uni-stuttgart.de/handle/11682/614>.
- W. L. Oberkampf, T. G. Trucano, and C. Hirsch. Verification, validation, and predictive capability in computational engineering and physics. *Applied Mechanics Reviews*, 57(5):345–384, 2004. doi:10.1115/1.1767847.
- J. Ochoa-Tapia and S. Whitaker. Momentum transfer at the boundary between a porous medium and a homogeneous fluid—i. theoretical development. *International Journal of Heat and Mass Transfer*, 38(14):2635–2646, 1995a. doi:10.1016/0017-9310(94)00346-w.
- J. Ochoa-Tapia and S. Whitaker. Momentum transfer at the boundary between a porous medium and a homogeneous fluid—II. comparison with experiment. *International Journal of Heat and Mass Transfer*, 38(14):2647–2655, 1995b. doi:10.1016/0017-9310(94)00347-x.
- M. Oostrom, Y. Mehmani, P. Romero-Gomez, Y. Tang, H. Liu, H. Yoon, Q. Kang, V. Joekar-Niasar, M. Balhoff, T. Dewers, et al. Pore-scale and continuum simulations of solute transport micromodel benchmark experiments. *Computational Geosciences*, 20(4):857–879, 2016. doi:10.1007/s10596-014-9424-0.
- D. Or, P. Lehmann, E. Shahraneeni, and N. Shokri. Advances in Soil Evaporation Physics—A Review. *Vadose Zone Journal*, 12(4):0, 2013. doi:10.2136/vzj2012.0163.
- P.-E. Oren, S. Bakke, and O. Arntzen. Extending Predictive Capabilities to Network Models. *SPE Journal*, 3(04):324–336, 1998. doi:10.2118/52052-pa.
- T. W. Patzek. Verification of a Complete Pore Network Simulator of Drainage and Imbibition. In *SPE/DOE Improved Oil Recovery Symposium*. Society of Petroleum Engineers, 2000. doi:10.2118/59312-ms.

- T. W. Patzek and J. G. Kristensen. Shape Factor Correlations of Hydraulic Conductance in Noncircular Capillaries: II. Two-Phase Creeping Flow. *Journal of Colloid and Interface Science*, 236:305–317, 2001. doi:10.1006/jcis.2000.7414.
- T. W. Patzek and D. B. Silin. Shape factor and hydraulic conductance in noncircular capillaries: I. One-Phase Creeping flow. *Journal of Colloid and Interface Science*, 236:295–304, 2001. doi:10.1006/jcis.2000.7413.
- J. G. Powers, J. B. Klemp, W. C. Skamarock, C. A. Davis, J. Dudhia, D. O. Gill, J. L. Coen, D. J. Gochis, R. Ahmadov, S. E. Peckham, G. A. Grell, J. Michalakes, S. Trahan, S. G. Benjamin, C. R. Alexander, G. J. Dimego, W. Wang, C. S. Schwartz, G. S. Romine, Z. Liu, C. Snyder, F. Chen, M. J. Barlage, W. Yu, and M. G. Duda. The Weather Research and Forecasting Model: Overview, System Efforts, and Future Directions. *Bulletin of the American Meteorological Society*, 98(8):1717–1737, 2017. doi:10.1175/bams-d-15-00308.1.
- M. Prat. Pore Network Models of Drying, Contact Angle, and Film Flows. *Chemical Engineering & Technology*, 34(7):1029–1038, 2011. doi:10.1002/ceat.201100056.
- H. Princen. Capillary phenomena in assemblies of parallel cylinders. *Journal of Colloid and Interface Science*, 30(1):69–75, 1969a. doi:10.1016/0021-9797(69)90379-8.
- H. Princen. Capillary phenomena in assemblies of parallel cylinders. *Journal of Colloid and Interface Science*, 30(3):359–371, 1969b. doi:10.1016/0021-9797(69)90403-2.
- H. Princen. Capillary phenomena in assemblies of parallel cylinders. *Journal of Colloid and Interface Science*, 34(2):171–184, 1970. doi:10.1016/0021-9797(70)90167-0.
- M. Prodanović, W. Lindquist, and R. Seright. 3D image-based characterization of fluid displacement in a Berea core. *Advances in Water Resources*, 30(2):214–226, 2007. doi:10.1016/j.advwatres.2005.05.015.
- J. Proudman. IV. Notes on the motion of viscous liquids in channels. *The London, Edinburgh, and Dublin Philosophical Magazine and Journal of Science*, 28(163):30–36, 1914. doi:10.1080/14786440708635179.
- C. Qin. Water Transport in the Gas Diffusion Layer of a Polymer Electrolyte Fuel Cell: Dynamic Pore-Network Modeling. *Journal of The Electrochemical Society*, 162(9):F1036–F1046, 2015. doi:10.1149/2.0861509jes.

- A. Quarteroni, A. Manzoni, and C. Vergara. The cardiovascular system: Mathematical modelling, numerical algorithms and clinical applications. *Acta Numerica*, 26:365–590, 2017. doi:10.1017/s0962492917000046.
- T. Ransohoff and C. Radke. Laminar flow of a wetting liquid along the corners of a predominantly gas-occupied noncircular pore. *Journal of Colloid and Interface Science*, 121(2):392–401, 1988. doi:10.1016/0021-9797(88)90442-0.
- A. Raouf and S. M. Hassanizadeh. A New Method for Generating Pore-Network Models of Porous Media. *Transport in Porous Media*, 81(3):391–407, 2009. doi:10.1007/s11242-009-9412-3.
- A. Raouf and S. M. Hassanizadeh. Saturation-dependent solute dispersivity in porous media: Pore-scale processes. *Water Resources Research*, 49(4):1943–1951, 2013. doi:10.1002/wrcr.20152.
- A. Raouf, S. M. Hassanizadeh, and A. Leijnse. Upscaling Transport of Adsorbing Solutes in Porous Media: Pore-Network Modeling. *Vadose Zone Journal*, 9(3):624, 2010. doi:10.2136/vzj2010.0026.
- A. Raouf, H. Nick, T. Wolterbeek, and C. Spiers. Pore-scale modeling of reactive transport in wellbore cement under CO₂ storage conditions. *International Journal of Greenhouse Gas Control*, 11:S67–S77, 2012. doi:10.1016/j.ijggc.2012.09.012.
- P. C. Reeves and M. A. Celia. A functional relationship between capillary pressure, saturation, and interfacial area as revealed by a pore-scale network model. *Water Resources Research*, 32(8):2345–2358, 1996. doi:10.1029/96WR01105.
- R. C. Reid, J. M. Prausnitz, and B. E. Poling. *The properties of gases and liquids*. McGraw Hill Book Co., New York, NY, 4 edition, 1987.
- I. Rybak, J. Magiera, R. Helmig, and C. Rohde. Multirate time integration for coupled saturated/unsaturated porous medium and free flow systems. *Computational Geosciences*, 19(2):299–309, 2015. doi:10.1007/s10596-015-9469-8.
- Y. Saad. *Iterative methods for sparse linear systems*. SIAM, 2 edition, 2003.
- P. G. Saffman. On the boundary condition at the surface of a porous medium. *Studies in Applied Mathematics*, 50(2):93–101, 1971. doi:10.1002/sapm197150293.

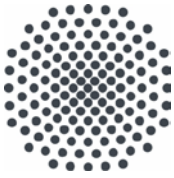
-
- O. Sander, T. Koch, N. Schröder, and B. Flemisch. The Dune FoamGrid implementation for surface and network grids. *Archive of Numerical Software*, 5(1):217–244, 2017. doi:10.11588/ans.2017.1.28490.
- T. D. Scheibe, E. M. Murphy, X. Chen, A. K. Rice, K. C. Carroll, B. J. Palmer, A. M. Tartakovsky, I. Battiato, and B. D. Wood. An analysis platform for multiscale hydrogeologic modeling with emphasis on hybrid multiscale methods. *Groundwater*, 53(1):38–56, 2015. doi:10.1111/gwat.12179.
- M. Schneider, K. Weishaupt, D. Gläser, W. M. Boon, and R. Helmig. Coupling staggered-grid and MPFA finite volume methods for free flow/porous-medium flow problems. *Journal of Computational Physics*, 401:109012, 2020. doi:10.1016/j.jcp.2019.109012.
- E. Shahraeeni, P. Lehmann, and D. Or. Coupling of evaporative fluxes from drying porous surfaces with air boundary layer: Characteristics of evaporation from discrete pores. *Water Resources Research*, 48(9), 2012. doi:10.1029/2012wr011857.
- Q. Sheng and K. Thompson. Dynamic coupling of pore-scale and reservoir-scale models for multiphase flow. *Water Resources Research*, 49(9):5973–5988, 2013. doi:10.1002/wrcr.20430.
- N. Shokri and D. Or. What determines drying rates at the onset of diffusion controlled stage-2 evaporation from porous media? *Water Resources Research*, 47(9), 2011. doi:10.1029/2010wr010284.
- S. M. Shokri-Kuehni, M. N. Rad, C. Webb, and N. Shokri. Impact of type of salt and ambient conditions on saline water evaporation from porous media. *Advances in Water Resources*, 105:154–161, 2017. doi:10.1016/j.advwatres.2017.05.004.
- D. Silin and T. Patzek. Pore space morphology analysis using maximal inscribed spheres. *Physica A: Statistical Mechanics and its Applications*, 371(2):336–360, 2006. doi:10.1016/j.physa.2006.04.048.
- G. Silva, N. Leal, and V. Semiao. Micro-PIV and CFD characterization of flows in a microchannel: Velocity profiles, surface roughness and Poiseuille numbers. *International Journal of Heat and Fluid Flow*, 29(4):1211–1220, 2008. doi:10.1016/j.ijheatfluidflow.2008.03.013.

- M. Singh and K. K. Mohanty. Dynamic modeling of drainage through three-dimensional porous materials. *Chemical Engineering Science*, 58(1):1–18, 2003. doi:10.1016/s0009-2509(02)00438-4.
- W. Somerton, J. Keese, and S. Chu. Thermal Behavior of Unconsolidated Oil Sands. *Society of Petroleum Engineers Journal*, 14(05):513–521, 1974. doi:10.2118/4506-pa.
- C. Sotgiu, B. Weigand, and K. Semmler. A turbulent heat flux prediction framework based on tensor representation theory and machine learning. *International Communications in Heat and Mass Transfer*, 95:74–79, 2018. doi:10.1016/j.icheatmasstransfer.2018.04.005.
- V. Surasani, T. Metzger, and E. Tsotsas. Consideration of heat transfer in pore network modelling of convective drying. *International journal of heat and mass transfer*, 51(9-10):2506–2518, 2008. doi:10.1016/j.ijheatmasstransfer.2007.07.033.
- V. K. Surasani, T. Metzger, and E. Tsotsas. Drying Simulations of Various 3D Pore Structures by a Nonisothermal Pore Network Model. *Drying Technology*, 28(5):615–623, 2010. doi:10.1080/07373931003788676.
- P. K. Sweby. High Resolution Schemes Using Flux Limiters for Hyperbolic Conservation Laws. *SIAM Journal on Numerical Analysis*, 21(5):995–1011, 1984. doi:10.1137/0721062.
- R. Taylor and R. Krishna. *Multicomponent mass transfer*, volume 2. John Wiley & Sons, 1993.
- A. Terzis, I. Zarikos, K. Weishaupt, G. Yang, X. Chu, R. Helmig, and B. Weigand. Microscopic velocity field measurements inside a regular porous medium adjacent to a low reynolds number channel flow. *Physics of Fluids*, 31(4):042001, 2019. doi:10.1063/1.5092169.
- K. E. Thompson. Pore-scale modeling of fluid transport in disordered fibrous materials. *AIChE Journal*, 48(7):1369–1389, 2002. doi:10.1002/aic.690480703.
- W. Thomson. 4. On the Equilibrium of Vapour at a Curved Surface of Liquid. *Proceedings of the Royal Society of Edinburgh*, 7:63–68, 1872. doi:10.1017/s0370164600041729.

-
- G. Tørå, P.-E. Øren, and A. Hansen. A Dynamic Network Model for Two-Phase Flow in Porous Media. *Transport in Porous Media*, 92(1):145–164, 2011. doi:10.1007/s11242-011-9895-6.
- E. A. Truckenbrodt. *Fluidmechanik*. Springer, Berlin, 4 edition, 1996.
- P. H. Valvatne and M. J. Blunt. Predictive pore-scale modeling of two-phase flow in mixed wet media. *Water Resources Research*, 40(7), 2004. doi:10.1029/2003WR002627.
- J. Vanderborght, T. Fetzner, K. Mosthaf, K. M. Smits, and R. Helmig. Heat and water transport in soils and across the soil-atmosphere interface: 1. Theory and different model concepts. *Water Resources Research*, 53(2):1057–1079, 2017. doi:10.1002/2016wr019982.
- M. Venturoli and E. S. Boek. Two-dimensional lattice-Boltzmann simulations of single phase flow in a pseudo two-dimensional micromodel. *Physica A: Statistical Mechanics and its Applications*, 362(1):23–29, 2006. doi:10.1016/j.physa.2005.09.006.
- P. Verboven, D. Flick, B. Nicolai, and G. Alvarez. Modelling transport phenomena in refrigerated food bulks, packages and stacks: basics and advances. *International Journal of Refrigeration*, 29(6):985–997, 2006. doi:10.1016/j.ijrefrig.2005.12.010.
- H. K. Versteeg and W. Malalasekera. *An introduction to computational fluid dynamics: the finite volume method*. Pearson Education, Harlow, 2 edition, 2007.
- A. Vescovini. *A fully implicit formulation for Navier-Stokes/Darcy coupling*. Master’s thesis, 2018.
- M. Veyskarami, A. H. Hassani, and M. H. Ghazanfari. A new insight into onset of inertial flow in porous media using network modeling with converging/diverging pores. *Computational Geosciences*, 22(1):329–346, 2017. doi:10.1007/s10596-017-9695-3.
- L. Vittoz, G. Oger, Z. Li, M. de Lefte, and D. Le Touzé. A High-Order Finite Volume Solver on Locally Refined Cartesian Meshes—Benchmark Session. In C. Cancès and P. Omnes, editors, *Finite Volumes for Complex Applications VIII - Methods and Theoretical Aspects*, pages 73–89, Cham, 2017. Springer International Publishing. doi:10.1007/978-3-319-57397-7_6.

- W. Wagner and A. Pruß. The IAPWS Formulation 1995 for the Thermodynamic Properties of Ordinary Water Substance for General and Scientific Use. *Journal of Physical and Chemical Reference Data*, 31(2):387–535, 2002. doi:10.1063/1.1461829.
- S. Wang, Q. Feng, Y. Dong, X. Han, and S. Wang. A dynamic pore-scale network model for two-phase imbibition. *Journal of Natural Gas Science and Engineering*, 26:118–129, 2015. doi:10.1016/j.jngse.2015.06.005.
- K. Weishaupt, V. Joekar-Niasar, and R. Helmig. An efficient coupling of free flow and porous media flow using the pore-network modeling approach. *Journal of Computational Physics: X*, 1:100011, 2019a. doi:10.1016/j.jcpx.2019.100011.
- K. Weishaupt, A. Terzis, I. Zarikos, G. Yang, M. de Winter, and R. Helmig. Model reduction for coupled free flow over porous media: a hybrid dimensional pore network model approach, 2019b. URL <https://arxiv.org/abs/1908.01771>. arXiv preprint.
- S. Whitaker. The Forchheimer equation: a theoretical development. *Transport in Porous media*, 25(1):27–61, 1996. doi:10.1007/BF00141261.
- S. Whitaker. *The method of volume averaging*. Springer, Dordrecht, 1999.
- F. M. White. *Viscous fluid flow*. McGraw-Hill, New York, 2 edition, 1991.
- D. Wildenschild and A. P. Sheppard. X-ray imaging and analysis techniques for quantifying pore-scale structure and processes in subsurface porous medium systems. *Advances in Water Resources*, 51:217–246, 2013. doi:10.1016/j.advwatres.2012.07.018.
- C. Xie, A. Q. Raeini, Y. Wang, M. J. Blunt, and M. Wang. An improved pore-network model including viscous coupling effects using direct simulation by the lattice Boltzmann method. *Advances in Water Resources*, 100:26–34, 2017. doi:10.1016/j.advwatres.2016.11.017.
- Q. Xiong, T. G. Baychev, and A. P. Jivkov. Review of pore network modelling of porous media: Experimental characterisations, network constructions and applications to reactive transport. *Journal of Contaminant Hydrology*, 192:101–117, 2016. doi:10.1016/j.jconhyd.2016.07.002.

-
- Z. Xu and K. M. Pillai. Modeling drying in thin porous media after coupling pore-level drying dynamics with external flow field. *Drying Technology*, 35(7):785–801, 2016. doi:10.1080/07373937.2016.1214596.
- G. Yang, B. Weigand, A. Terzis, K. Weishaupt, and R. Helmig. Numerical Simulation of Turbulent Flow and Heat Transfer in a Three-Dimensional Channel Coupled with Flow Through Porous Structures. *Transport in Porous Media*, 122(1):145–167, 2018. doi:10.1007/s11242-017-0995-9.
- G. Yang, E. Coltman, K. Weishaupt, A. Terzis, R. Helmig, and B. Weigand. On the Beavers–Joseph Interface Condition for Non-parallel Coupled Channel Flow over a Porous Structure at High Reynolds Numbers. *Transport in Porous Media*, 128(2):431–457, 2019. doi:10.1007/s11242-019-01255-5.
- A. G. Yiotis, I. N. Tsimpanogiannis, A. K. Stubos, and Y. C. Yortsos. Coupling between external and internal mass transfer during drying of a porous medium. *Water Resources Research*, 43(6), 2007. doi:10.1029/2006wr005558.
- I. V. Zenyuk, E. Medici, J. Allen, and A. Z. Weber. Coupling continuum and pore-network models for polymer-electrolyte fuel cells. *International Journal of Hydrogen Energy*, 40(46):16831–16845, 2015. doi:10.1016/j.ijhydene.2015.08.009.
- D. Zhou, M. J. Blunt, and F. M. Orr, Jr. Hydrocarbon Drainage along Corners of Noncircular Capillaries. *Journal of Colloid and Interface Science*, 187:11–21, 1997. doi:10.1006/jcis.1996.4699.



Institut für Wasser- und Umweltsystemmodellierung Universität Stuttgart

Pfaffenwaldring 61
70569 Stuttgart (Vaihingen)
Telefon (0711) 685 - 60156
Telefax (0711) 685 - 51073
E-Mail: iws@iws.uni-stuttgart.de
<http://www.iws.uni-stuttgart.de>

Direktoren

Prof. Dr. rer. nat. Dr.-Ing. András Bárdossy
Prof. Dr.-Ing. Rainer Helmig
Prof. Dr.-Ing. Wolfgang Nowak
Prof. Dr.-Ing. Silke Wieprecht

Vorstand (Stand 1.5.2019)

Prof. Dr. rer. nat. Dr.-Ing. A. Bárdossy
Prof. Dr.-Ing. R. Helmig
Prof. Dr.-Ing. W. Nowak
Prof. Dr.-Ing. S. Wieprecht
Prof. Dr. J.A. Sander Huisman
Jürgen Braun, PhD
apl. Prof. Dr.-Ing. H. Class
PD Dr.-Ing. Claus Haslauer
Stefan Haun, PhD
PD Dr.-Ing. habil. Sergey Oladyskin
Dr. rer. nat. J. Seidel
Dr.-Ing. K. Terheiden

Emeriti

Prof. Dr.-Ing. habil. Dr.-Ing. E.h. Jürgen Giesecke
Prof. Dr.h.c. Dr.-Ing. E.h. Helmut Kobus, PhD

Lehrstuhl für Wasserbau und Wassermengenwirtschaft

Leiterin: Prof. Dr.-Ing. Silke Wieprecht
Stellv.: Dr.-Ing. Kristina Terheiden
Versuchsanstalt für Wasserbau
Leiter: Stefan Haun, PhD

Lehrstuhl für Hydromechanik und Hydrosystemmodellierung

Leiter: Prof. Dr.-Ing. Rainer Helmig
Stellv.: apl. Prof. Dr.-Ing. Holger Class

Lehrstuhl für Hydrologie und Geohydrologie

Leiter: Prof. Dr. rer. nat. Dr.-Ing. András Bárdossy
Stellv.: Dr. rer. nat. Jochen Seidel
Hydrogeophysik der Vadosen Zone
(mit Forschungszentrum Jülich)
Leiter: Prof. Dr. J.A. Sander Huisman

Lehrstuhl für Stochastische Simulation und Sicherheitsforschung für Hydrosysteme

Leiter: Prof. Dr.-Ing. Wolfgang Nowak
Stellv.: PD Dr.-Ing. habil. Sergey Oladyskin

VEGAS, Versuchseinrichtung zur Grundwasser- und Altlastensanierung

Leiter: Jürgen Braun, PhD
PD Dr.-Ing. Claus Haslauer

Verzeichnis der Mitteilungshefte

- 1 Röhnisch, Arthur: *Die Bemühungen um eine Wasserbauliche Versuchsanstalt an der Technischen Hochschule Stuttgart*, und Fattah Abouleid, Abdel: *Beitrag zur Berechnung einer in lockeren Sand gerammten, zweifach verankerten Spundwand*, 1963
- 2 Marotz, Günter: *Beitrag zur Frage der Standfestigkeit von dichten Asphaltbelägen im Großwasserbau*, 1964
- 3 Gurr, Siegfried: *Beitrag zur Berechnung zusammengesetzter ebener Flächentragwerke unter besonderer Berücksichtigung ebener Stauwände, mit Hilfe von Randwert- und Lastwertmatrizen*, 1965
- 4 Plica, Peter: *Ein Beitrag zur Anwendung von Schalenkonstruktionen im Stahlwasserbau*, und Petrikat, Kurt: *Möglichkeiten und Grenzen des wasserbaulichen Versuchswesens*, 1966

- 5 Plate, Erich: *Beitrag zur Bestimmung der Windgeschwindigkeitsverteilung in der durch eine Wand gestörten bodennahen Luftschicht*, und
Röhnisch, Arthur; Marotz, Günter: *Neue Baustoffe und Bauausführungen für den Schutz der Böschungen und der Sohle von Kanälen, Flüssen und Häfen; Gestehungskosten und jeweilige Vorteile*, sowie
Unny, T.E.: *Schwingungsuntersuchungen am Kegelstrahlschieber*, 1967
- 6 Seiler, Erich: *Die Ermittlung des Anlagenwertes der bundeseigenen Binnenschiffahrtsstraßen und Talsperren und des Anteils der Binnenschifffahrt an diesem Wert*, 1967
- 7 *Sonderheft anlässlich des 65. Geburtstages von Prof. Arthur Röhnisch mit Beiträgen von*
Benk, Dieter; Breitling, J.; Gurr, Siegfried; Haberhauer, Robert; Honekamp, Hermann; Kuz, Klaus Dieter; Marotz, Günter; Mayer-Vorfelder, Hans-Jörg; Miller, Rudolf; Plate, Erich J.; Radomski, Helge; Schwarz, Helmut; Vollmer, Ernst; Wildenhahn, Eberhard; 1967
- 8 Jumikis, Alfred: *Beitrag zur experimentellen Untersuchung des Wassernachschubs in einem gefrierenden Boden und die Beurteilung der Ergebnisse*, 1968
- 9 Marotz, Günter: *Technische Grundlagen einer Wasserspeicherung im natürlichen Untergrund*, 1968
- 10 Radomski, Helge: *Untersuchungen über den Einfluß der Querschnittsform wellenförmiger Spundwände auf die statischen und rammtechnischen Eigenschaften*, 1968
- 11 Schwarz, Helmut: *Die Grenztragfähigkeit des Baugrundes bei Einwirkung vertikal gezogener Ankerplatten als zweidimensionales Bruchproblem*, 1969
- 12 Erbel, Klaus: *Ein Beitrag zur Untersuchung der Metamorphose von Mittelgebirgsschneedecken unter besonderer Berücksichtigung eines Verfahrens zur Bestimmung der thermischen Schneequalität*, 1969
- 13 Westhaus, Karl-Heinz: *Der Strukturwandel in der Binnenschifffahrt und sein Einfluß auf den Ausbau der Binnenschiffskanäle*, 1969
- 14 Mayer-Vorfelder, Hans-Jörg: *Ein Beitrag zur Berechnung des Erdwiderstandes unter Ansatz der logarithmischen Spirale als Gleitflächenfunktion*, 1970
- 15 Schulz, Manfred: *Berechnung des räumlichen Erddruckes auf die Wandung kreiszylindrischer Körper*, 1970
- 16 Mobasseri, Manoutschehr: *Die Rippenstützmauer. Konstruktion und Grenzen ihrer Standicherheit*, 1970
- 17 Benk, Dieter: *Ein Beitrag zum Betrieb und zur Bemessung von Hochwasserrückhaltebecken*, 1970
- 18 Gàl, Attila: *Bestimmung der mitschwingenden Wassermasse bei überströmten Fischbauchklappen mit kreiszylindrischem Staublech*, 1971, vergriffen
- 19 Kuz, Klaus Dieter: *Ein Beitrag zur Frage des Einsetzens von Kavitationserscheinungen in einer Düsenströmung bei Berücksichtigung der im Wasser gelösten Gase*, 1971, vergriffen
- 20 Schaak, Hartmut: *Verteilleitungen von Wasserkraftanlagen*, 1971
- 21 *Sonderheft zur Eröffnung der neuen Versuchsanstalt des Instituts für Wasserbau der Universität Stuttgart mit Beiträgen von*
Brombach, Hansjörg; Dirksen, Wolfram; Gàl, Attila; Gerlach, Reinhard; Giesecke, Jürgen; Holthoff, Franz-Josef; Kuz, Klaus Dieter; Marotz, Günter; Minor, Hans-Erwin; Petrikat, Kurt; Röhnisch, Arthur; Rueff, Helge; Schwarz, Helmut; Vollmer, Ernst; Wildenhahn, Eberhard; 1972
- 22 Wang, Chung-su: *Ein Beitrag zur Berechnung der Schwingungen an Kegelstrahlschiebern*, 1972
- 23 Mayer-Vorfelder, Hans-Jörg: *Erdwiderstandsbeiwerte nach dem Ohde-Variationsverfahren*, 1972
- 24 Minor, Hans-Erwin: *Beitrag zur Bestimmung der Schwingungsanfachungsfunktionen überströmter Stauklappen*, 1972, vergriffen
- 25 Brombach, Hansjörg: *Untersuchung strömungsmechanischer Elemente (Fluidik) und die Möglichkeit der Anwendung von Wirbelkammerelementen im Wasserbau*, 1972, vergriffen
- 26 Wildenhahn, Eberhard: *Beitrag zur Berechnung von Horizontalfilterbrunnen*, 1972

- 27 Steinlein, Helmut: *Die Eliminierung der Schwebstoffe aus Flußwasser zum Zweck der unterirdischen Wasserspeicherung, gezeigt am Beispiel der Iller*, 1972
- 28 Holthoff, Franz Josef: *Die Überwindung großer Hubhöhen in der Binnenschifffahrt durch Schwimmerhebwerke*, 1973
- 29 Röder, Karl: *Einwirkungen aus Baugrundbewegungen auf trog- und kastenförmige Konstruktionen des Wasser- und Tunnelbaues*, 1973
- 30 Kretschmer, Heinz: *Die Bemessung von Bogenstaumauern in Abhängigkeit von der Talform*, 1973
- 31 Honekamp, Hermann: *Beitrag zur Berechnung der Montage von Unterwasserpipelines*, 1973
- 32 Giesecke, Jürgen: *Die Wirbelkammertriode als neuartiges Steuerorgan im Wasserbau*, und Brombach, Hansjörg: *Entwicklung, Bauformen, Wirkungsweise und Steuereigenschaften von Wirbelkammerverstärkern*, 1974
- 33 Rueff, Helge: *Untersuchung der schwingungserregenden Kräfte an zwei hintereinander angeordneten Tiefschützen unter besonderer Berücksichtigung von Kavitation*, 1974
- 34 Röhnisch, Arthur: *Einpreßversuche mit Zementmörtel für Spannbeton - Vergleich der Ergebnisse von Modellversuchen mit Ausführungen in Hüllwellrohren*, 1975
- 35 *Sonderheft anlässlich des 65. Geburtstages von Prof. Dr.-Ing. Kurt Petrikat mit Beiträgen von:* Brombach, Hansjörg; Erbel, Klaus; Flinspach, Dieter; Fischer jr., Richard; Gál, Attila; Gerlach, Reinhard; Giesecke, Jürgen; Haberhauer, Robert; Hafner Edzard; Hausenblas, Bernhard; Horlacher, Hans-Burkhard; Hutarew, Andreas; Knoll, Manfred; Krummet, Ralph; Marotz, Günter; Merkle, Theodor; Miller, Christoph; Minor, Hans-Erwin; Neumayer, Hans; Rao, Syamala; Rath, Paul; Rueff, Helge; Ruppert, Jürgen; Schwarz, Wolfgang; Topal-Gökceli, Mehmet; Vollmer, Ernst; Wang, Chung-su; Weber, Hans-Georg; 1975
- 36 Berger, Jochum: *Beitrag zur Berechnung des Spannungszustandes in rotationssymmetrisch belasteten Kugelschalen veränderlicher Wandstärke unter Gas- und Flüssigkeitsdruck durch Integration schwach singulärer Differentialgleichungen*, 1975
- 37 Dirksen, Wolfram: *Berechnung instationärer Abfluvorgänge in gestauten Gerinnen mittels Differenzenverfahren und die Anwendung auf Hochwasserrückhaltebecken*, 1976
- 38 Horlacher, Hans-Burkhard: *Berechnung instationärer Temperatur- und Wärmespannungsfelder in langen mehrschichtigen Hohlzylindern*, 1976
- 39 Hafner, Edzard: *Untersuchung der hydrodynamischen Kräfte auf Baukörper im Tiefwasserbereich des Meeres*, 1977, ISBN 3-921694-39-6
- 40 Ruppert, Jürgen: *Über den Axialwirbelkammerverstärker für den Einsatz im Wasserbau*, 1977, ISBN 3-921694-40-X
- 41 Hutarew, Andreas: *Beitrag zur Beeinflussbarkeit des Sauerstoffgehalts in Fließgewässern an Abstürzen und Wehren*, 1977, ISBN 3-921694-41-8, vergriffen
- 42 Miller, Christoph: *Ein Beitrag zur Bestimmung der schwingungserregenden Kräfte an unterströmten Wehren*, 1977, ISBN 3-921694-42-6
- 43 Schwarz, Wolfgang: *Druckstoßberechnung unter Berücksichtigung der Radial- und Längsverschiebungen der Rohrwandung*, 1978, ISBN 3-921694-43-4
- 44 Kinzelbach, Wolfgang: *Numerische Untersuchungen über den optimalen Einsatz variabler Kühlsysteme einer Kraftwerkskette am Beispiel Oberrhein*, 1978, ISBN 3-921694-44-2
- 45 Barczewski, Baldur: *Neue Meßmethoden für Wasser-Luftgemische und deren Anwendung auf zweiphasige Auftriebsstrahlen*, 1979, ISBN 3-921694-45-0
- 46 Neumayer, Hans: *Untersuchung der Strömungsvorgänge in radialen Wirbelkammerverstärkern*, 1979, ISBN 3-921694-46-9
- 47 Elalfy, Youssef-Elhassan: *Untersuchung der Strömungsvorgänge in Wirbelkammerdioden und -drosseln*, 1979, ISBN 3-921694-47-7
- 48 Brombach, Hansjörg: *Automatisierung der Bewirtschaftung von Wasserspeichern*, 1981, ISBN 3-921694-48-5
- 49 Geldner, Peter: *Deterministische und stochastische Methoden zur Bestimmung der Selbstdichtung von Gewässern*, 1981, ISBN 3-921694-49-3, vergriffen

- 50 Mehlhorn, Hans: *Temperaturveränderungen im Grundwasser durch Brauchwassereinleitungen*, 1982, ISBN 3-921694-50-7, vergriffen
- 51 Hafner, Edzard: *Rohrleitungen und Behälter im Meer*, 1983, ISBN 3-921694-51-5
- 52 Rinnert, Bernd: *Hydrodynamische Dispersion in porösen Medien: Einfluß von Dichteunterschieden auf die Vertikalvermischung in horizontaler Strömung*, 1983, ISBN 3-921694-52-3, vergriffen
- 53 Lindner, Wulf: *Steuerung von Grundwasserentnahmen unter Einhaltung ökologischer Kriterien*, 1983, ISBN 3-921694-53-1, vergriffen
- 54 Herr, Michael; Herzer, Jörg; Kinzelbach, Wolfgang; Kobus, Helmut; Rinnert, Bernd: *Methoden zur rechnerischen Erfassung und hydraulischen Sanierung von Grundwasserkontaminationen*, 1983, ISBN 3-921694-54-X
- 55 Schmitt, Paul: *Wege zur Automatisierung der Niederschlagsermittlung*, 1984, ISBN 3-921694-55-8, vergriffen
- 56 Müller, Peter: *Transport und selektive Sedimentation von Schwebstoffen bei gestautem Abfluß*, 1985, ISBN 3-921694-56-6
- 57 El-Qawasmeh, Fuad: *Möglichkeiten und Grenzen der Tropfbewässerung unter besonderer Berücksichtigung der Verstopfungsanfälligkeit der Tropfelemente*, 1985, ISBN 3-921694-57-4, vergriffen
- 58 Kirchenbaur, Klaus: *Mikroprozessorgesteuerte Erfassung instationärer Druckfelder am Beispiel seegangsbelasteter Baukörper*, 1985, ISBN 3-921694-58-2
- 59 Kobus, Helmut (Hrsg.): *Modellierung des großräumigen Wärme- und Schadstofftransports im Grundwasser*, Tätigkeitsbericht 1984/85 (DFG-Forschergruppe an den Universitäten Hohenheim, Karlsruhe und Stuttgart), 1985, ISBN 3-921694-59-0, vergriffen
- 60 Spitz, Karlheinz: *Dispersion in porösen Medien: Einfluß von Inhomogenitäten und Dichteunterschieden*, 1985, ISBN 3-921694-60-4, vergriffen
- 61 Kobus, Helmut: *An Introduction to Air-Water Flows in Hydraulics*, 1985, ISBN 3-921694-61-2
- 62 Kaleris, Vassilios: *Erfassung des Austausches von Oberflächen- und Grundwasser in horizontalebene Grundwassermodellen*, 1986, ISBN 3-921694-62-0
- 63 Herr, Michael: *Grundlagen der hydraulischen Sanierung verunreinigter Porengrundwasserleiter*, 1987, ISBN 3-921694-63-9
- 64 Marx, Walter: *Berechnung von Temperatur und Spannung in Massenbeton infolge Hydratation*, 1987, ISBN 3-921694-64-7
- 65 Koschitzky, Hans-Peter: *Dimensionierungskonzept für Sohlbelüfter in Schußrinnen zur Vermeidung von Kavitationsschäden*, 1987, ISBN 3-921694-65-5
- 66 Kobus, Helmut (Hrsg.): *Modellierung des großräumigen Wärme- und Schadstofftransports im Grundwasser*, Tätigkeitsbericht 1986/87 (DFG-Forschergruppe an den Universitäten Hohenheim, Karlsruhe und Stuttgart) 1987, ISBN 3-921694-66-3
- 67 Söll, Thomas: *Berechnungsverfahren zur Abschätzung anthropogener Temperaturanomalien im Grundwasser*, 1988, ISBN 3-921694-67-1
- 68 Dittrich, Andreas; Westrich, Bernd: *Bodenseeufererosion, Bestandsaufnahme und Bewertung*, 1988, ISBN 3-921694-68-X, vergriffen
- 69 Huwe, Bernd; van der Ploeg, Rienk R.: *Modelle zur Simulation des Stickstoffhaushaltes von Standorten mit unterschiedlicher landwirtschaftlicher Nutzung*, 1988, ISBN 3-921694-69-8, vergriffen
- 70 Stephan, Karl: *Integration elliptischer Funktionen*, 1988, ISBN 3-921694-70-1
- 71 Kobus, Helmut; Zilliox, Lothaire (Hrsg.): *Nitratbelastung des Grundwassers, Auswirkungen der Landwirtschaft auf die Grundwasser- und Rohwasserbeschaffenheit und Maßnahmen zum Schutz des Grundwassers*. Vorträge des deutsch-französischen Kolloquiums am 6. Oktober 1988, Universitäten Stuttgart und Louis Pasteur Strasbourg (Vorträge in deutsch oder französisch, Kurzfassungen zweisprachig), 1988, ISBN 3-921694-71-X

- 72 Soyeaux, Renald: *Unterströmung von Stauanlagen auf klüftigem Untergrund unter Berücksichtigung laminarer und turbulenter Fließzustände*, 1991, ISBN 3-921694-72-8
- 73 Kohane, Roberto: *Berechnungsmethoden für Hochwasserabfluß in Fließgewässern mit überströmten Vorländern*, 1991, ISBN 3-921694-73-6
- 74 Hassinger, Reinhard: *Beitrag zur Hydraulik und Bemessung von Blocksteinrampen in flexibler Bauweise*, 1991, ISBN 3-921694-74-4, vergriffen
- 75 Schäfer, Gerhard: *Einfluß von Schichtenstrukturen und lokalen Einlagerungen auf die Längsdispersion in Porengrundwasserleitern*, 1991, ISBN 3-921694-75-2
- 76 Giesecke, Jürgen: *Vorträge, Wasserwirtschaft in stark besiedelten Regionen; Umweltforschung mit Schwerpunkt Wasserwirtschaft*, 1991, ISBN 3-921694-76-0
- 77 Huwe, Bernd: *Deterministische und stochastische Ansätze zur Modellierung des Stickstoffhaushalts landwirtschaftlich genutzter Flächen auf unterschiedlichem Skalenniveau*, 1992, ISBN 3-921694-77-9, vergriffen
- 78 Rommel, Michael: *Verwendung von Kluftdaten zur realitätsnahen Generierung von Kluftnetzen mit anschließender laminar-turbulenter Strömungsberechnung*, 1993, ISBN 3-92 1694-78-7
- 79 Marschall, Paul: *Die Ermittlung lokaler Stofffrachten im Grundwasser mit Hilfe von Einbohrloch-Meßverfahren*, 1993, ISBN 3-921694-79-5, vergriffen
- 80 Ptak, Thomas: *Stofftransport in heterogenen Porenaquiferen: Felduntersuchungen und stochastische Modellierung*, 1993, ISBN 3-921694-80-9, vergriffen
- 81 Haakh, Frieder: *Transientes Strömungsverhalten in Wirbelkammern*, 1993, ISBN 3-921694-81-7
- 82 Kobus, Helmut; Cirpka, Olaf; Barczewski, Baldur; Koschitzky, Hans-Peter: *Versuchseinrichtung zur Grundwasser- und Altlastensanierung VEGAS, Konzeption und Programmrahmen*, 1993, ISBN 3-921694-82-5
- 83 Zang, Weidong: *Optimaler Echtzeit-Betrieb eines Speichers mit aktueller Abflußregenerierung*, 1994, ISBN 3-921694-83-3, vergriffen
- 84 Franke, Hans-Jörg: *Stochastische Modellierung eines flächenhaften Stoffeintrages und Transports in Grundwasser am Beispiel der Pflanzenschutzmittelproblematik*, 1995, ISBN 3-921694-84-1
- 85 Lang, Ulrich: *Simulation regionaler Strömungs- und Transportvorgänge in Karstaquiferen mit Hilfe des Doppelkontinuum-Ansatzes: Methodenentwicklung und Parameteridentifikation*, 1995, ISBN 3-921694-85-X, vergriffen
- 86 Helmig, Rainer: *Einführung in die Numerischen Methoden der Hydromechanik*, 1996, ISBN 3-921694-86-8, vergriffen
- 87 Cirpka, Olaf: *CONTRACT: A Numerical Tool for Contaminant Transport and Chemical Transformations - Theory and Program Documentation -*, 1996, ISBN 3-921694-87-6
- 88 Haberlandt, Uwe: *Stochastische Synthese und Regionalisierung des Niederschlages für Schmutzfrachtberechnungen*, 1996, ISBN 3-921694-88-4
- 89 Croisé, Jean: *Extraktion von flüchtigen Chemikalien aus natürlichen Lockergesteinen mittels erzwungener Luftströmung*, 1996, ISBN 3-921694-89-2, vergriffen
- 90 Jorde, Klaus: *Ökologisch begründete, dynamische Mindestwasserregelungen bei Ausleitungskraftwerken*, 1997, ISBN 3-921694-90-6, vergriffen
- 91 Helmig, Rainer: *Gekoppelte Strömungs- und Transportprozesse im Untergrund - Ein Beitrag zur Hydrosystemmodellierung-*, 1998, ISBN 3-921694-91-4, vergriffen
- 92 Emmert, Martin: *Numerische Modellierung nichtisothermer Gas-Wasser Systeme in porösen Medien*, 1997, ISBN 3-921694-92-2
- 93 Kern, Ulrich: *Transport von Schweb- und Schadstoffen in staugeregelten Fließgewässern am Beispiel des Neckars*, 1997, ISBN 3-921694-93-0, vergriffen
- 94 Förster, Georg: *Druckstoßdämpfung durch große Luftblasen in Hochpunkten von Rohrleitungen* 1997, ISBN 3-921694-94-9

- 95 Cirpka, Olaf: *Numerische Methoden zur Simulation des reaktiven Mehrkomponententransports im Grundwasser*, 1997, ISBN 3-921694-95-7, vergriffen
- 96 Färber, Arne: *Wärmetransport in der ungesättigten Bodenzone: Entwicklung einer thermischen In-situ-Sanierungstechnologie*, 1997, ISBN 3-921694-96-5
- 97 Betz, Christoph: *Wasserdampfdestillation von Schadstoffen im porösen Medium: Entwicklung einer thermischen In-situ-Sanierungstechnologie*, 1998, SBN 3-921694-97-3
- 98 Xu, Yichun: *Numerical Modeling of Suspended Sediment Transport in Rivers*, 1998, ISBN 3-921694-98-1, vergriffen
- 99 Wüst, Wolfgang: *Geochemische Untersuchungen zur Sanierung CKW-kontaminierter Aquifere mit Fe(0)-Reaktionswänden*, 2000, ISBN 3-933761-02-2
- 100 Sheta, Hussam: *Simulation von Mehrphasenvorgängen in porösen Medien unter Einbeziehung von Hysterese-Effekten*, 2000, ISBN 3-933761-03-4
- 101 Ayros, Edwin: *Regionalisierung extremer Abflüsse auf der Grundlage statistischer Verfahren*, 2000, ISBN 3-933761-04-2, vergriffen
- 102 Huber, Ralf: *Compositional Multiphase Flow and Transport in Heterogeneous Porous Media*, 2000, ISBN 3-933761-05-0
- 103 Braun, Christopherus: *Ein Upscaling-Verfahren für Mehrphasenströmungen in porösen Medien*, 2000, ISBN 3-933761-06-9
- 104 Hofmann, Bernd: *Entwicklung eines rechnergestützten Managementsystems zur Beurteilung von Grundwasserschadensfällen*, 2000, ISBN 3-933761-07-7
- 105 Class, Holger: *Theorie und numerische Modellierung nichtisothermer Mehrphasenprozesse in NAPL-kontaminierten porösen Medien*, 2001, ISBN 3-933761-08-5
- 106 Schmidt, Reinhard: *Wasserdampf- und Heißluftinjektion zur thermischen Sanierung kontaminierter Standorte*, 2001, ISBN 3-933761-09-3
- 107 Josef, Reinhold: *Schadstoffextraktion mit hydraulischen Sanierungsverfahren unter Anwendung von grenzflächenaktiven Stoffen*, 2001, ISBN 3-933761-10-7
- 108 Schneider, Matthias: *Habitat- und Abflussmodellierung für Fließgewässer mit unscharfen Berechnungsansätzen*, 2001, ISBN 3-933761-11-5
- 109 Rathgeb, Andreas: *Hydrodynamische Bemessungsgrundlagen für Lockerdeckwerke an überströmbaren Erddämmen*, 2001, ISBN 3-933761-12-3
- 110 Lang, Stefan: *Parallele numerische Simulation instationärer Probleme mit adaptiven Methoden auf unstrukturierten Gittern*, 2001, ISBN 3-933761-13-1
- 111 Appt, Jochen; Stumpp Simone: *Die Bodensee-Messkampagne 2001, IWS/CWR Lake Constance Measurement Program 2001*, 2002, ISBN 3-933761-14-X
- 112 Heimerl, Stephan: *Systematische Beurteilung von Wasserkraftprojekten*, 2002, ISBN 3-933761-15-8, vergriffen
- 113 Iqbal, Amin: *On the Management and Salinity Control of Drip Irrigation*, 2002, ISBN 3-933761-16-6
- 114 Silberhorn-Hemminger, Annette: *Modellierung von Kluftaquifersystemen: Geostatistische Analyse und deterministisch-stochastische Kluftgenerierung*, 2002, ISBN 3-933761-17-4
- 115 Winkler, Angela: *Prozesse des Wärme- und Stofftransports bei der In-situ-Sanierung mit festen Wärmequellen*, 2003, ISBN 3-933761-18-2
- 116 Marx, Walter: *Wasserkraft, Bewässerung, Umwelt - Planungs- und Bewertungsschwerpunkte der Wasserbewirtschaftung*, 2003, ISBN 3-933761-19-0
- 117 Hinkelmann, Reinhard: *Efficient Numerical Methods and Information-Processing Techniques in Environment Water*, 2003, ISBN 3-933761-20-4
- 118 Samaniego-Eguiguren, Luis Eduardo: *Hydrological Consequences of Land Use / Land Cover and Climatic Changes in Mesoscale Catchments*, 2003, ISBN 3-933761-21-2
- 119 Neunhäuserer, Lina: *Diskretisierungsansätze zur Modellierung von Strömungs- und Transportprozessen in geklüftet-porösen Medien*, 2003, ISBN 3-933761-22-0
- 120 Paul, Maren: *Simulation of Two-Phase Flow in Heterogeneous Poros Media with Adaptive Methods*, 2003, ISBN 3-933761-23-9

- 121 Ehret, Uwe: *Rainfall and Flood Nowcasting in Small Catchments using Weather Radar*, 2003, ISBN 3-933761-24-7
- 122 Haag, Ingo: *Der Sauerstoffhaushalt staugeregelter Flüsse am Beispiel des Neckars - Analysen, Experimente, Simulationen -*, 2003, ISBN 3-933761-25-5
- 123 Appt, Jochen: *Analysis of Basin-Scale Internal Waves in Upper Lake Constance*, 2003, ISBN 3-933761-26-3
- 124 Hrsg.: Schrenk, Volker; Batereau, Katrin; Barczewski, Baldur; Weber, Karolin und Koschitzky, Hans-Peter: *Symposium Ressource Fläche und VEGAS - Statuskolloquium 2003, 30. September und 1. Oktober 2003*, 2003, ISBN 3-933761-27-1
- 125 Omar Khalil Ouda: *Optimisation of Agricultural Water Use: A Decision Support System for the Gaza Strip*, 2003, ISBN 3-933761-28-0
- 126 Batereau, Katrin: *Sensorbasierte Bodenluftmessung zur Vor-Ort-Erkundung von Schadensherden im Untergrund*, 2004, ISBN 3-933761-29-8
- 127 Witt, Oliver: *Erosionsstabilität von Gewässersedimenten mit Auswirkung auf den Stofftransport bei Hochwasser am Beispiel ausgewählter Stauhaltungen des Oberrheins*, 2004, ISBN 3-933761-30-1
- 128 Jakobs, Hartmut: *Simulation nicht-isothermer Gas-Wasser-Prozesse in komplexen Kluft-Matrix-Systemen*, 2004, ISBN 3-933761-31-X
- 129 Li, Chen-Chien: *Deterministisch-stochastisches Berechnungskonzept zur Beurteilung der Auswirkungen erosiver Hochwasserereignisse in Flusstauhaltungen*, 2004, ISBN 3-933761-32-8
- 130 Reichenberger, Volker; Helmig, Rainer; Jakobs, Hartmut; Bastian, Peter; Niessner, Jennifer: *Complex Gas-Water Processes in Discrete Fracture-Matrix Systems: Up-scaling, Mass-Conservative Discretization and Efficient Multilevel Solution*, 2004, ISBN 3-933761-33-6
- 131 Hrsg.: Barczewski, Baldur; Koschitzky, Hans-Peter; Weber, Karolin; Wege, Ralf: *VEGAS - Statuskolloquium 2004*, Tagungsband zur Veranstaltung am 05. Oktober 2004 an der Universität Stuttgart, Campus Stuttgart-Vaihingen, 2004, ISBN 3-933761-34-4
- 132 Asie, Kemal Jabir: *Finite Volume Models for Multiphase Multicomponent Flow through Porous Media*. 2005, ISBN 3-933761-35-2
- 133 Jacoub, George: *Development of a 2-D Numerical Module for Particulate Contaminant Transport in Flood Retention Reservoirs and Impounded Rivers*, 2004, ISBN 3-933761-36-0
- 134 Nowak, Wolfgang: *Geostatistical Methods for the Identification of Flow and Transport Parameters in the Subsurface*, 2005, ISBN 3-933761-37-9
- 135 Süß, Mia: *Analysis of the influence of structures and boundaries on flow and transport processes in fractured porous media*, 2005, ISBN 3-933761-38-7
- 136 Jose, Surabhin Chackiath: *Experimental Investigations on Longitudinal Dispersive Mixing in Heterogeneous Aquifers*, 2005, ISBN: 3-933761-39-5
- 137 Filiz, Fulya: *Linking Large-Scale Meteorological Conditions to Floods in Mesoscale Catchments*, 2005, ISBN 3-933761-40-9
- 138 Qin, Minghao: *Wirklichkeitsnahe und recheneffiziente Ermittlung von Temperatur und Spannungen bei großen RCC-Staumauern*, 2005, ISBN 3-933761-41-7
- 139 Kobayashi, Kenichiro: *Optimization Methods for Multiphase Systems in the Subsurface - Application to Methane Migration in Coal Mining Areas*, 2005, ISBN 3-933761-42-5
- 140 Rahman, Md. Arifur: *Experimental Investigations on Transverse Dispersive Mixing in Heterogeneous Porous Media*, 2005, ISBN 3-933761-43-3
- 141 Schrenk, Volker: *Ökobilanzen zur Bewertung von Altlastensanierungsmaßnahmen*, 2005, ISBN 3-933761-44-1
- 142 Hundecha, Hirpa Yeshewatesfa: *Regionalization of Parameters of a Conceptual Rainfall-Runoff Model*, 2005, ISBN: 3-933761-45-X
- 143 Wege, Ralf: *Untersuchungs- und Überwachungsmethoden für die Beurteilung natürlicher Selbstreinigungsprozesse im Grundwasser*, 2005, ISBN 3-933761-46-8

- 144 Breiting, Thomas: *Techniken und Methoden der Hydroinformatik - Modellierung von komplexen Hydrosystemen im Untergrund*, 2006, ISBN 3-933761-47-6
- 145 Hrsg.: Braun, Jürgen; Koschitzky, Hans-Peter; Müller, Martin: *Ressource Untergrund: 10 Jahre VEGAS: Forschung und Technologieentwicklung zum Schutz von Grundwasser und Boden*, Tagungsband zur Veranstaltung am 28. und 29. September 2005 an der Universität Stuttgart, Campus Stuttgart-Vaihingen, 2005, ISBN 3-933761-48-4
- 146 Rojanschi, Vlad: *Abflusskonzentration in mesoskaligen Einzugsgebieten unter Berücksichtigung des Sickerraumes*, 2006, ISBN 3-933761-49-2
- 147 Winkler, Nina Simone: *Optimierung der Steuerung von Hochwasserrückhaltebeckensystemen*, 2006, ISBN 3-933761-50-6
- 148 Wolf, Jens: *Räumlich differenzierte Modellierung der Grundwasserströmung alluvialer Aquifere für mesoskalige Einzugsgebiete*, 2006, ISBN: 3-933761-51-4
- 149 Kohler, Beate: *Externe Effekte der Laufwasserkraftnutzung*, 2006, ISBN 3-933761-52-2
- 150 Hrsg.: Braun, Jürgen; Koschitzky, Hans-Peter; Stuhmann, Matthias: *VEGAS-Statuskolloquium 2006*, Tagungsband zur Veranstaltung am 28. September 2006 an der Universität Stuttgart, Campus Stuttgart-Vaihingen, 2006, ISBN 3-933761-53-0
- 151 Niessner, Jennifer: *Multi-Scale Modeling of Multi-Phase - Multi-Component Processes in Heterogeneous Porous Media*, 2006, ISBN 3-933761-54-9
- 152 Fischer, Markus: *Beanspruchung eingerdeter Rohrleitungen infolge Austrocknung bindiger Böden*, 2006, ISBN 3-933761-55-7
- 153 Schneck, Alexander: *Optimierung der Grundwasserbewirtschaftung unter Berücksichtigung der Belange der Wasserversorgung, der Landwirtschaft und des Naturschutzes*, 2006, ISBN 3-933761-56-5
- 154 Das, Tapash: *The Impact of Spatial Variability of Precipitation on the Predictive Uncertainty of Hydrological Models*, 2006, ISBN 3-33761-57-3
- 155 Bielinski, Andreas: *Numerical Simulation of CO₂ sequestration in geological formations*, 2007, ISBN 3-933761-58-1
- 156 Mödinger, Jens: *Entwicklung eines Bewertungs- und Entscheidungsunterstützungssystems für eine nachhaltige regionale Grundwasserbewirtschaftung*, 2006, ISBN 3-933761-60-3
- 157 Manthey, Sabine: *Two-phase flow processes with dynamic effects in porous media - parameter estimation and simulation*, 2007, ISBN 3-933761-61-1
- 158 Pozos Estrada, Oscar: *Investigation on the Effects of Entrained Air in Pipelines*, 2007, ISBN 3-933761-62-X
- 159 Ochs, Steffen Oliver: *Steam injection into saturated porous media – process analysis including experimental and numerical investigations*, 2007, ISBN 3-933761-63-8
- 160 Marx, Andreas: *Einsatz gekoppelter Modelle und Wetterradar zur Abschätzung von Niederschlagsintensitäten und zur Abflussvorhersage*, 2007, ISBN 3-933761-64-6
- 161 Hartmann, Gabriele Maria: *Investigation of Evapotranspiration Concepts in Hydrological Modelling for Climate Change Impact Assessment*, 2007, ISBN 3-933761-65-4
- 162 Kebede Gurmessa, Tesfaye: *Numerical Investigation on Flow and Transport Characteristics to Improve Long-Term Simulation of Reservoir Sedimentation*, 2007, ISBN 3-933761-66-2
- 163 Trifković, Aleksandar: *Multi-objective and Risk-based Modelling Methodology for Planning, Design and Operation of Water Supply Systems*, 2007, ISBN 3-933761-67-0
- 164 Göttinger, Jens: *Distributed Conceptual Hydrological Modelling - Simulation of Climate, Land Use Change Impact and Uncertainty Analysis*, 2007, ISBN 3-933761-68-9
- 165 Hrsg.: Braun, Jürgen; Koschitzky, Hans-Peter; Stuhmann, Matthias: *VEGAS – Kolloquium 2007*, Tagungsband zur Veranstaltung am 26. September 2007 an der Universität Stuttgart, Campus Stuttgart-Vaihingen, 2007, ISBN 3-933761-69-7
- 166 Freeman, Beau: *Modernization Criteria Assessment for Water Resources Planning; Klamath Irrigation Project, U.S.*, 2008, ISBN 3-933761-70-0

- 167 Dreher, Thomas: *Selektive Sedimentation von Feinstschwebstoffen in Wechselwirkung mit wandnahen turbulenten Strömungsbedingungen*, 2008, ISBN 3-933761-71-9
- 168 Yang, Wei: *Discrete-Continuous Downscaling Model for Generating Daily Precipitation Time Series*, 2008, ISBN 3-933761-72-7
- 169 Kopecki, Ianina: *Calculational Approach to FST-Hemispheres for Multiparametrical Benthos Habitat Modelling*, 2008, ISBN 3-933761-73-5
- 170 Brommundt, Jürgen: *Stochastische Generierung räumlich zusammenhängender Niederschlagszeitreihen*, 2008, ISBN 3-933761-74-3
- 171 Papafotiou, Alexandros: *Numerical Investigations of the Role of Hysteresis in Heterogeneous Two-Phase Flow Systems*, 2008, ISBN 3-933761-75-1
- 172 He, Yi: *Application of a Non-Parametric Classification Scheme to Catchment Hydrology*, 2008, ISBN 978-3-933761-76-7
- 173 Wagner, Sven: *Water Balance in a Poorly Gauged Basin in West Africa Using Atmospheric Modelling and Remote Sensing Information*, 2008, ISBN 978-3-933761-77-4
- 174 Hrsg.: Braun, Jürgen; Koschitzky, Hans-Peter; Stuhmann, Matthias; Schrenk, Volker: *VEGAS-Kolloquium 2008 Ressource Fläche III*, Tagungsband zur Veranstaltung am 01. Oktober 2008 an der Universität Stuttgart, Campus Stuttgart-Vaihingen, 2008, ISBN 978-3-933761-78-1
- 175 Patil, Sachin: *Regionalization of an Event Based Nash Cascade Model for Flood Predictions in Ungauged Basins*, 2008, ISBN 978-3-933761-79-8
- 176 Assteerawatt, Anongnart: *Flow and Transport Modelling of Fractured Aquifers based on a Geostatistical Approach*, 2008, ISBN 978-3-933761-80-4
- 177 Karnahl, Joachim Alexander: *2D numerische Modellierung von multifraktionalem Schwebstoff- und Schadstofftransport in Flüssen*, 2008, ISBN 978-3-933761-81-1
- 178 Hiester, Uwe: *Technologieentwicklung zur In-situ-Sanierung der ungesättigten Bodenzone mit festen Wärmequellen*, 2009, ISBN 978-3-933761-82-8
- 179 Laux, Patrick: *Statistical Modeling of Precipitation for Agricultural Planning in the Volta Basin of West Africa*, 2009, ISBN 978-3-933761-83-5
- 180 Ehsan, Saqib: *Evaluation of Life Safety Risks Related to Severe Flooding*, 2009, ISBN 978-3-933761-84-2
- 181 Prohaska, Sandra: *Development and Application of a 1D Multi-Strip Fine Sediment Transport Model for Regulated Rivers*, 2009, ISBN 978-3-933761-85-9
- 182 Kopp, Andreas: *Evaluation of CO₂ Injection Processes in Geological Formations for Site Screening*, 2009, ISBN 978-3-933761-86-6
- 183 Ebigbo, Anozie: *Modelling of biofilm growth and its influence on CO₂ and water (two-phase) flow in porous media*, 2009, ISBN 978-3-933761-87-3
- 184 Freiboth, Sandra: *A phenomenological model for the numerical simulation of multiphase multicomponent processes considering structural alterations of porous media*, 2009, ISBN 978-3-933761-88-0
- 185 Zöllner, Frank: *Implementierung und Anwendung netzfreier Methoden im Konstruktiven Wasserbau und in der Hydromechanik*, 2009, ISBN 978-3-933761-89-7
- 186 Vasin, Milos: *Influence of the soil structure and property contrast on flow and transport in the unsaturated zone*, 2010, ISBN 978-3-933761-90-3
- 187 Li, Jing: *Application of Copulas as a New Geostatistical Tool*, 2010, ISBN 978-3-933761-91-0
- 188 AghaKouchak, Amir: *Simulation of Remotely Sensed Rainfall Fields Using Copulas*, 2010, ISBN 978-3-933761-92-7
- 189 Thapa, Pawan Kumar: *Physically-based spatially distributed rainfall runoff modelling for soil erosion estimation*, 2010, ISBN 978-3-933761-93-4
- 190 Wurms, Sven: *Numerische Modellierung der Sedimentationsprozesse in Retentionsanlagen zur Steuerung von Stoffströmen bei extremen Hochwasserabflussereignissen*, 2011, ISBN 978-3-933761-94-1

- 191 Merkel, Uwe: *Unsicherheitsanalyse hydraulischer Einwirkungen auf Hochwasserschutzdeiche und Steigerung der Leistungsfähigkeit durch adaptive Strömungsmodellierung*, 2011, ISBN 978-3-933761-95-8
- 192 Fritz, Jochen: *A Decoupled Model for Compositional Non-Isothermal Multiphase Flow in Porous Media and Multiphysics Approaches for Two-Phase Flow*, 2010, ISBN 978-3-933761-96-5
- 193 Weber, Karolin (Hrsg.): *12. Treffen junger WissenschaftlerInnen an Wasserbauinstituten*, 2010, ISBN 978-3-933761-97-2
- 194 Bliedernicht, Jan-Geert: *Probability Forecasts of Daily Areal Precipitation for Small River Basins*, 2011, ISBN 978-3-933761-98-9
- 195 Hrsg.: Koschitzky, Hans-Peter; Braun, Jürgen: *VEGAS-Kolloquium 2010 In-situ-Sanierung - Stand und Entwicklung Nano und ISCO -*, Tagungsband zur Veranstaltung am 07. Oktober 2010 an der Universität Stuttgart, Campus Stuttgart-Vaihingen, 2010, ISBN 978-3-933761-99-6
- 196 Gafurov, Abror: *Water Balance Modeling Using Remote Sensing Information - Focus on Central Asia*, 2010, ISBN 978-3-942036-00-9
- 197 Mackenberg, Sylvia: *Die Quellstärke in der Sickerwasserprognose: Möglichkeiten und Grenzen von Labor- und Freilanduntersuchungen*, 2010, ISBN 978-3-942036-01-6
- 198 Singh, Shailesh Kumar: *Robust Parameter Estimation in Gauged and Ungauged Basins*, 2010, ISBN 978-3-942036-02-3
- 199 Doğan, Mehmet Onur: *Coupling of porous media flow with pipe flow*, 2011, ISBN 978-3-942036-03-0
- 200 Liu, Min: *Study of Topographic Effects on Hydrological Patterns and the Implication on Hydrological Modeling and Data Interpolation*, 2011, ISBN 978-3-942036-04-7
- 201 Geleta, Habtamu Itafa: *Watershed Sediment Yield Modeling for Data Scarce Areas*, 2011, ISBN 978-3-942036-05-4
- 202 Franke, Jörg: *Einfluss der Überwachung auf die Versagenswahrscheinlichkeit von Staustufen*, 2011, ISBN 978-3-942036-06-1
- 203 Bakimchandra, Oinam: *Integrated Fuzzy-GIS approach for assessing regional soil erosion risks*, 2011, ISBN 978-3-942036-07-8
- 204 Alam, Muhammad Mahboob: *Statistical Downscaling of Extremes of Precipitation in Mesoscale Catchments from Different RCMs and Their Effects on Local Hydrology*, 2011, ISBN 978-3-942036-08-5
- 205 Hrsg.: Koschitzky, Hans-Peter; Braun, Jürgen: *VEGAS-Kolloquium 2011 Flache Geothermie - Perspektiven und Risiken*, Tagungsband zur Veranstaltung am 06. Oktober 2011 an der Universität Stuttgart, Campus Stuttgart-Vaihingen, 2011, ISBN 978-3-933761-09-2
- 206 Haslauer, Claus: *Analysis of Real-World Spatial Dependence of Subsurface Hydraulic Properties Using Copulas with a Focus on Solute Transport Behaviour*, 2011, ISBN 978-3-942036-10-8
- 207 Dung, Nguyen Viet: *Multi-objective automatic calibration of hydrodynamic models – development of the concept and an application in the Mekong Delta*, 2011, ISBN 978-3-942036-11-5
- 208 Hung, Nguyen Nghia: *Sediment dynamics in the floodplain of the Mekong Delta, Vietnam*, 2011, ISBN 978-3-942036-12-2
- 209 Kuhlmann, Anna: *Influence of soil structure and root water uptake on flow in the unsaturated zone*, 2012, ISBN 978-3-942036-13-9
- 210 Tuhtan, Jeffrey Andrew: *Including the Second Law Inequality in Aquatic Ecodynamics: A Modeling Approach for Alpine Rivers Impacted by Hydropeaking*, 2012, ISBN 978-3-942036-14-6
- 211 Tolossa, Habtamu: *Sediment Transport Computation Using a Data-Driven Adaptive Neuro-Fuzzy Modelling Approach*, 2012, ISBN 978-3-942036-15-3

- 212 Tatomir, Alexandru-Bodgan: *From Discrete to Continuum Concepts of Flow in Fractured Porous Media*, 2012, ISBN 978-3-942036-16-0
- 213 Erbertseder, Karin: *A Multi-Scale Model for Describing Cancer-Therapeutic Transport in the Human Lung*, 2012, ISBN 978-3-942036-17-7
- 214 Noack, Markus: *Modelling Approach for Interstitial Sediment Dynamics and Reproduction of Gravel Spawning Fish*, 2012, ISBN 978-3-942036-18-4
- 215 De Boer, Cjestmir Volkert: *Transport of Nano Sized Zero Valent Iron Colloids during Injection into the Subsurface*, 2012, ISBN 978-3-942036-19-1
- 216 Pfaff, Thomas: *Processing and Analysis of Weather Radar Data for Use in Hydrology*, 2013, ISBN 978-3-942036-20-7
- 217 Lebreuz, Hans-Henning: *Addressing the Input Uncertainty for Hydrological Modeling by a New Geostatistical Method*, 2013, ISBN 978-3-942036-21-4
- 218 Darcis, Melanie Yvonne: *Coupling Models of Different Complexity for the Simulation of CO₂ Storage in Deep Saline Aquifers*, 2013, ISBN 978-3-942036-22-1
- 219 Beck, Ferdinand: *Generation of Spatially Correlated Synthetic Rainfall Time Series in High Temporal Resolution - A Data Driven Approach*, 2013, ISBN 978-3-942036-23-8
- 220 Guthke, Philipp: *Non-multi-Gaussian spatial structures: Process-driven natural genesis, manifestation, modeling approaches, and influences on dependent processes*, 2013, ISBN 978-3-942036-24-5
- 221 Walter, Lena: *Uncertainty studies and risk assessment for CO₂ storage in geological formations*, 2013, ISBN 978-3-942036-25-2
- 222 Wolff, Markus: *Multi-scale modeling of two-phase flow in porous media including capillary pressure effects*, 2013, ISBN 978-3-942036-26-9
- 223 Mosthaf, Klaus Roland: *Modeling and analysis of coupled porous-medium and free flow with application to evaporation processes*, 2014, ISBN 978-3-942036-27-6
- 224 Leube, Philipp Christoph: *Methods for Physically-Based Model Reduction in Time: Analysis, Comparison of Methods and Application*, 2013, ISBN 978-3-942036-28-3
- 225 Rodríguez Fernández, Jhan Ignacio: *High Order Interactions among environmental variables: Diagnostics and initial steps towards modeling*, 2013, ISBN 978-3-942036-29-0
- 226 Eder, Maria Magdalena: *Climate Sensitivity of a Large Lake*, 2013, ISBN 978-3-942036-30-6
- 227 Greiner, Philipp: *Alkoholinjektion zur In-situ-Sanierung von CKW Schadensherden in Grundwasserleitern: Charakterisierung der relevanten Prozesse auf unterschiedlichen Skalen*, 2014, ISBN 978-3-942036-31-3
- 228 Lauser, Andreas: *Theory and Numerical Applications of Compositional Multi-Phase Flow in Porous Media*, 2014, ISBN 978-3-942036-32-0
- 229 Enzenhöfer, Rainer: *Risk Quantification and Management in Water Production and Supply Systems*, 2014, ISBN 978-3-942036-33-7
- 230 Faigle, Benjamin: *Adaptive modelling of compositional multi-phase flow with capillary pressure*, 2014, ISBN 978-3-942036-34-4
- 231 Oladyshkin, Sergey: *Efficient modeling of environmental systems in the face of complexity and uncertainty*, 2014, ISBN 978-3-942036-35-1
- 232 Sugimoto, Takayuki: *Copula based Stochastic Analysis of Discharge Time Series*, 2014, ISBN 978-3-942036-36-8
- 233 Koch, Jonas: *Simulation, Identification and Characterization of Contaminant Source Architectures in the Subsurface*, 2014, ISBN 978-3-942036-37-5
- 234 Zhang, Jin: *Investigations on Urban River Regulation and Ecological Rehabilitation Measures, Case of Shenzhen in China*, 2014, ISBN 978-3-942036-38-2
- 235 Siebel, Rüdiger: *Experimentelle Untersuchungen zur hydrodynamischen Belastung und Standsicherheit von Deckwerken an überströmbaren Erddämmen*, 2014, ISBN 978-3-942036-39-9

- 236 Baber, Katherina: *Coupling free flow and flow in porous media in biological and technical applications: From a simple to a complex interface description*, 2014, ISBN 978-3-942036-40-5
- 237 Nuske, Klaus Philipp: *Beyond Local Equilibrium — Relaxing local equilibrium assumptions in multiphase flow in porous media*, 2014, ISBN 978-3-942036-41-2
- 238 Geiges, Andreas: *Efficient concepts for optimal experimental design in nonlinear environmental systems*, 2014, ISBN 978-3-942036-42-9
- 239 Schwenck, Nicolas: *An XFEM-Based Model for Fluid Flow in Fractured Porous Media*, 2014, ISBN 978-3-942036-43-6
- 240 Chamorro Chávez, Alejandro: *Stochastic and hydrological modelling for climate change prediction in the Lima region, Peru*, 2015, ISBN 978-3-942036-44-3
- 241 Yulizar: *Investigation of Changes in Hydro-Meteorological Time Series Using a Depth-Based Approach*, 2015, ISBN 978-3-942036-45-0
- 242 Kretschmer, Nicole: *Impacts of the existing water allocation scheme on the Limarí watershed – Chile, an integrative approach*, 2015, ISBN 978-3-942036-46-7
- 243 Kramer, Matthias: *Luftbedarf von Freistrahlturbinen im Gegendruckbetrieb*, 2015, ISBN 978-3-942036-47-4
- 244 Hommel, Johannes: *Modeling biogeochemical and mass transport processes in the subsurface: Investigation of microbially induced calcite precipitation*, 2016, ISBN 978-3-942036-48-1
- 245 Germer, Kai: *Wasserinfiltration in die ungesättigte Zone eines makroporösen Hanges und deren Einfluss auf die Hangstabilität*, 2016, ISBN 978-3-942036-49-8
- 246 Hörning, Sebastian: *Process-oriented modeling of spatial random fields using copulas*, 2016, ISBN 978-3-942036-50-4
- 247 Jambhekar, Vishal: *Numerical modeling and analysis of evaporative salinization in a coupled free-flow porous-media system*, 2016, ISBN 978-3-942036-51-1
- 248 Huang, Yingchun: *Study on the spatial and temporal transferability of conceptual hydrological models*, 2016, ISBN 978-3-942036-52-8
- 249 Kleinknecht, Simon Matthias: *Migration and retention of a heavy NAPL vapor and remediation of the unsaturated zone*, 2016, ISBN 978-3-942036-53-5
- 250 Kwakye, Stephen Oppong: *Study on the effects of climate change on the hydrology of the West African sub-region*, 2016, ISBN 978-3-942036-54-2
- 251 Kissinger, Alexander: *Basin-Scale Site Screening and Investigation of Possible Impacts of CO₂ Storage on Subsurface Hydrosystems*, 2016, ISBN 978-3-942036-55-9
- 252 Müller, Thomas: *Generation of a Realistic Temporal Structure of Synthetic Precipitation Time Series for Sewer Applications*, 2017, ISBN 978-3-942036-56-6
- 253 Grüninger, Christoph: *Numerical Coupling of Navier-Stokes and Darcy Flow for Soil-Water Evaporation*, 2017, ISBN 978-3-942036-57-3
- 254 Suroso: *Asymmetric Dependence Based Spatial Copula Models: Empirical Investigations and Consequences on Precipitation Fields*, 2017, ISBN 978-3-942036-58-0
- 255 Müller, Thomas; Mosthaf, Tobias; Gunzenhauser, Sarah; Seidel, Jochen; Bárdossy, András: *Grundlagenbericht Niederschlags-Simulator (NiedSim3)*, 2017, ISBN 978-3-942036-59-7
- 256 Mosthaf, Tobias: *New Concepts for Regionalizing Temporal Distributions of Precipitation and for its Application in Spatial Rainfall Simulation*, 2017, ISBN 978-3-942036-60-3
- 257 Fenrich, Eva Katrin: *Entwicklung eines ökologisch-ökonomischen Vernetzungsmodells für Wasserkraftanlagen und Mehrzweckspeicher*, 2018, ISBN 978-3-942036-61-0
- 258 Schmidt, Holger: *Microbial stabilization of lotic fine sediments*, 2018, ISBN 978-3-942036-62-7

- 259 Fetzer, Thomas: *Coupled Free and Porous-Medium Flow Processes Affected by Turbulence and Roughness – Models, Concepts and Analysis*, 2018, ISBN 978-3-942036-63-4
- 260 Schröder, Hans Christoph: *Large-scale High Head Pico Hydropower Potential Assessment*, 2018, ISBN 978-3-942036-64-1
- 261 Bode, Felix: *Early-Warning Monitoring Systems for Improved Drinking Water Resource Protection*, 2018, ISBN 978-3-942036-65-8
- 262 Gebler, Tobias: *Statistische Auswertung von simulierten Talsperrenüberwachungsdaten zur Identifikation von Schadensprozessen an Gewichtsstaumauern*, 2018, ISBN 978-3-942036-66-5
- 263 Harten, Matthias von: *Analyse des Zuppinger-Wasserrades – Hydraulische Optimierungen unter Berücksichtigung ökologischer Aspekte*, 2018, ISBN 978-3-942036-67-2
- 264 Yan, Jieru: *Nonlinear estimation of short time precipitation using weather radar and surface observations*, 2018, ISBN 978-3-942036-68-9
- 265 Beck, Martin: *Conceptual approaches for the analysis of coupled hydraulic and geomechanical processes*, 2019, ISBN 978-3-942036-69-6
- 266 Haas, Jannik: *Optimal planning of hydropower and energy storage technologies for fully renewable power systems*, 2019, ISBN 978-3-942036-70-2
- 267 Schneider, Martin: *Nonlinear Finite Volume Schemes for Complex Flow Processes and Challenging Grids*, 2019, ISBN 978-3-942036-71-9
- 268 Most, Sebastian Christopher: *Analysis and Simulation of Anomalous Transport in Porous Media*, 2019, ISBN 978-3-942036-72-6
- 269 Buchta, Rocco: *Entwicklung eines Ziel- und Bewertungssystems zur Schaffung nachhaltiger naturnaher Strukturen in großen sandgeprägten Flüssen des norddeutschen Tieflandes*, 2019, ISBN 978-3-942036-73-3
- 270 Thom, Moritz: *Towards a Better Understanding of the Biostabilization Mechanisms of Sediment Beds*, 2019, ISBN 978-3-942036-74-0
- 271 Stolz, Daniel: *Die Nullspannungstemperatur in Gewichtsstaumauern unter Berücksichtigung der Festigkeitsentwicklung des Betons*, 2019, ISBN 978-3-942036-75-7
- 272 Rodriguez Pretelin, Abelardo: *Integrating transient flow conditions into groundwater well protection*, 2020, ISBN: 978-3-942036-76-4
- 273 Weishaupt, Kilian: *Model Concepts for Coupling Free Flow with Porous Medium Flow at the Pore-Network Scale: From Single-Phase Flow to Compositional Non-Isothermal Two-Phase Flow*, 2020, ISBN: 978-3-942036-77-1

Die Mitteilungshefte ab der Nr. 134 (Jg. 2005) stehen als pdf-Datei über die Homepage des Instituts: www.iws.uni-stuttgart.de zur Verfügung.